VERLAG DER TECHNISCHEN UNIVERSITÄT GRAZ

Daniel Schöllhammer

Unified modelling and higher-order accurate analysis of curved shells and membranes

MONOGRAPHIC SERIES TU GRAZ
STRUCTURAL ANALYSIS

Daniel Schöllhammer

Unified modelling and higher-order accurate analysis of curved shells and membranes

Monographic Series TU Graz

Structural Analysis

Monographic Series TU Graz

Structural Analysis

Daniel Schöllhammer

Unified modelling and higher-order accurate analysis of curved shells and membranes

---

This work is based on the dissertation *“Unified modelling and higher-order accurate analysis of curved shells and membranes”*, presented at Graz University of Technology, Institute of Structural Analysis in 2021.

Supervision / Assessment:

Thomas-Peter Fries (Graz University of Technology)
Peter Hansbo (Jönköping University)

Cover photo	Gernot Beer
Cover layout	Verlag der Technischen Universität Graz
Print	DATAFORM Media Ges.m.b.H.

www.tugraz-verlag.at

Print
ISBN 978-3-85125-813-4

E-Book
ISBN 978-3-85125-814-1
DOI 10.3217/978-3-85125-813-4

Abstract

The thesis introduces a generalized modelling and higher-order accurate analysis of curved shells and structural membranes. In the modelling of curved, thin-walled structures, a dimensional reduction from the 3D shell body to its 2D mid-surface is a key step. Mathematically, this results in partial differential equations (PDEs) on manifolds embedded in the three-dimensional space.

In the classical approach of modelling shells and membranes, the mid-surface is defined explicitly by a (piecewise) parametrization. Such a parametrization inherently defines curvilinear coordinates which are employed in all classical models. However, the mid-surface may also be defined implicitly by means of (multiple) level-set functions and curvilinear coordinates on the surface are not available. Therefore, the classical models of shells and membranes do not extend to this situation.

In this thesis, the classical models such as linear Kirchhoff-Love shell, linear Reissner-Mindlin shell, and structural membranes undergoing large deformations are reformulated in the frame of the tangential differential calculus (TDC) including all relevant mechanical aspects. The major advantage of this reformulation is that the employed surface operators and geometrical quantities are defined in the global Cartesian coordinate system so that curvilinear coordinates are not necessarily required. The resulting models are valid independently of the concrete geometry definition, enabling the analysis of explicitly and implicitly defined shells and membranes in a unified sense. Hence, the reformulated PDEs are more general than the classical theories and naturally yield a symbolic notation, whereas the classical approach is typically formulated in index notation.

For the numerical treatment, the reformulated boundary value problems are applicable to two fundamentally different numerical approaches. On the one hand, one may use the classical Surface FEM where the geometry is discretized by two-dimensional surface elements. On the other hand, it also applies to recent Trace FEM which is a fictitious domain method (FDM) for PDEs on manifolds. In the Trace FEM, three major issues of FDMs have to be addressed properly in order to enable higher-order accuracy: (i) the accurate integration of the implicitly defined geometry, (ii) the stabilization of the stiffness matrix, and (iii) the enforcement of essential boundary conditions.

The obtained shell and membrane models are discretized by higher-order accurate Surface and Trace FEM. In addition to the well-known benchmarks with reference or exact (manufactured) solutions, new benchmarks which enable higher-order convergence rates in the analysis are proposed. The convergence is also confirmed in the residual errors, i.e., in the strong form of the equilibrium. Provided that the involved mechanical fields are sufficiently smooth, optimal orders of convergence are achieved for linear shells and non-linear membranes for both Surface and Trace FEM.

Zusammenfassung

Das Ziel der vorliegenden Arbeit ist eine verallgemeinerte Formulierung von Schalen- und Membranproblemen und deren Analyse mit Genauigkeit höherer Ordnung. In der Modellierung von dünnwandigen Tragwerken ist die Reduktion vom 3D-Körper auf die gekrümmte 2D-Mittelfläche ein wesentlicher Aspekt. Die Modellgleichungen werden dann als partielle Differentialgleichungen (PDGen) auf Mannigfaltigkeiten (Oberflächen) formuliert, die im dreidimensionalen Raum eingebettet sind.

In der klassischen Modellierung von Schalen und Membranen ist die Mittelfläche explizit über eine (stückweise) Parametrisierung definiert. Diese Parametrisierung definiert automatisch krummlinige Koordinaten, welche in allen klassischen Modellen verwendet werden. Oberflächen können jedoch auch implizit über (mehrere) Level-set Funktionen angegeben werden und krummlinige Koordinaten sind in diesem Fall nicht verfügbar. Aus diesem Grund sind die klassischen Modelle von Schalen und Membranen nicht auf implizit definierte Geometrien anwendbar.

In dieser Dissertation werden die klassischen Modelle, wie die lineare Kirchhoff-Love Schale, lineare Reissner-Mindlin Schale und nicht-lineare Membran, mit Hilfe des Tangential Differential Calculus (TDC) neu formuliert. Die resultierenden Oberflächenoperatoren und geometrischen Größen sind dann im globalen kartesischen Koordinatensystem definiert und daher werden krummlinige Koordinaten nicht zwingend benötigt. Daraus folgt, dass die erhaltenen Schalen- und Membranmodelle unabhängig von der tatsächlichen Geometriedefinition (explizit oder implizit) wohl definiert sind und die Analyse in einer vereinheitlichten Beschreibung ermöglicht wird. In diesem Sinne sind die neu formulierten PDGen allgemeiner und führen auf eine symbolische Notation, während die klassische Formulierung typischerweise die Indexnotation verwendet.

Für die numerische Lösung der reformulierten Randwertprobleme sind zwei fundamental unterschiedliche Finite Elemente Methoden (FEM) anwendbar. Auf der einen Seite die klassische Surface FEM, bei der die Geometrie und das Randwertproblem durch 2D-Oberflächenelemente diskretisiert wird. Alternativ können auch innovative Finite Elemente Methoden wie die Trace FEM eingesetzt werden. Diese Methode ist eine Fictitious Domain Method (FDM) für PDGen auf Mannigfaltigkeiten. Wie bei jeder FDM muss auch bei der Trace FEM besondere Aufmerksamkeit auf die: (i) Integration, (ii) Stabilisierung und (iii) das Aufbringen von Randbedingungen gelegt werden.

Die neuen Schalen- und Membranformulierungen werden mit der Surface und Trace FEM mit Genauigkeit höherer Ordnung diskretisiert. Zusätzlich zu den etablierten Benchmarkbeispielen mit Referenzlösungen oder exakten (analytisch vorgegebenen) Lösungen werden neue Testfälle, welche Konvergenzordnungen höherer Ordnung ermöglichen, vorgeschlagen. Darüber hinaus, ist Konvergenz auch in den Residualfehlern (Fehler in der starken Form des Gleichgewichts) bestätigt. Vorausgesetzt, dass die Lösung eine hinreichend hohe Glattheit besitzt, können optimale Konvergenzordnungen für lineare Schalen und nicht-lineare Membranen in beiden numerischen Methoden, Surface und Trace FEM, gezeigt werden.

Acknowledgements

At first and foremost I wish to express my profound gratitude to my supervisor Univ.-Prof. Dr.-Ing. habil. Thomas-Peter Fries for his guidance and support through the whole process. His curiosity and enthusiasm in the field of computational engineering is truly inspiring. It was a privilege to work with him and I will always be thankful for the opportunity to be a part of the Institute of Structural Analysis.

In addition, I would like to thank and acknowledge the effort of Prof. Peter Hansbo for his truly appreciated comments and for providing his time to examine the thesis.

I also want to thank all of my great colleagues at the Institute of Structural Analysis, in particular, Christian Dünser and Richard Schussnig. It was a pleasure to work with them.

Moreover, I would like to thank my colleague and friend Dominik Pölz from the Institute of Applied Mechanics for all discussions about my research, his research and related topics, which increased my interests and insights in this field of engineering.

On a personal level, I want to thank my family and friends for their support at all times.

Last, but certainly not least, I would like to express my great gratitude to Sandra for her emotional support and continuous encouragement through the whole process of the thesis.

This accomplishment would not have been possible without this great support. Thank you.

Contents

1 Introduction

Curved shells and membranes are outstanding structural elements and occur in various fields of engineering and nature. Common applications in technology are in automotive, aerospace, biomedical and civil-engineering [27], [58], [145]. In Fig. 1.1, examples of shells and membranes in nature and technology are illustrated. A characteristic feature of curved shells and membranes is that these 3D structures are typically thin-walled, meaning that one dimension, i.e., the thickness, is significantly smaller compared to the other two spatial expansions. The curved shape enables transverse loadings to be carried by membrane actions and thus the whole cross section of the shell or membrane body is fully activated. Hence, the resulting structure may be typically light-weight and results in an extremely efficient structural component with high bearing capacity. On the other hand, the large slenderness causes a pronounced sensitivity against imperfections of both geometry and loading. Therefore, a sufficiently accurate analysis of their behaviour is of utmost interest for successful applications in technology.

(a) Nautilus shell [45] **(b)** L'Oceanogràfic, Spain [87] **(c)** ASU SkySong, USA [86]

Fig. 1.1: Shells and membranes in nature and technology.

1.1 Geometry definition

In the modelling of thin-walled structures, a key step is the dimensional reduction from the 3D shell body to its mid-surface Γ. As a result, the shell can be completely described by a curved surface embedded in the physical space with given thickness t. For the mechanical modelling and mathematical description, the mid-surface Γ has to be well-defined, regular, sufficiently smooth, orientable and typically bounded. Such a surface may also be called a two-dimensional *manifold* in the three-dimensional space. Given that it is possible to compute the first fundamental form at *all* points, this is a Riemannian manifold of codimension 1. The first fundamental form provides a metric to measure arc-lengths, angles and areas on the surface. More mathematical details regarding the required properties which are necessary for the analysis and calculus are given in [16], [42], [52], [138].

There are two fundamentally different methodologies for the definition of suitable surfaces. One approach is to parametrize the mid-surface, resulting into an *explicit* surface definition. The parametrization is a smooth, continuous map $\boldsymbol{\chi}$ from some 2D parameter space to the possibly curved surface Γ embedded in $\mathbb{R}^3$. In Fig. 1.2 an example of a parametrized surface is shown. The rectangular domain $\hat{\Omega}$ represents the parameter space and with the map $\boldsymbol{\chi}$, the curved surface Γ is defined. Hence, every point $\boldsymbol{r}^* \in \hat{\Omega}$ has a *unique* counterpart $\boldsymbol{x}^* \in \Gamma$. The curvilinear coordinates (grey lines) on the surface Γ are implied by the mapped coordinates $\boldsymbol{r} = [r, s]^{\mathrm{T}}$ in the parameter space $\hat{\Omega}$.

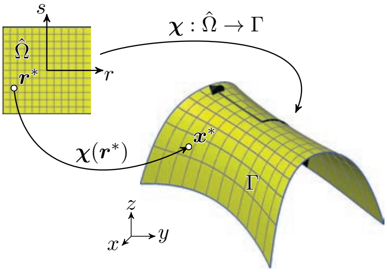

Fig. 1.2: Explicitly defined surface with curvilinear coordinates modelling a curved roof.

Alternatively, the surface Γ may also be represented *implicitly* by means of level-set functions. A level-set function is a scalar-valued function $\phi : \mathbb{R}^3 \rightarrow \mathbb{R}$ and one can define the surface implicitly by $\Gamma := \{\boldsymbol{x} \in \mathbb{R}^3 : \phi(\boldsymbol{x}) = c\}$, with some given constant $c \in \mathbb{R}$. In practice, the constant is often set to zero ($c = 0$), the surface is then defined by the *zero-isosurface* of the level-set function ϕ. This procedure is labelled as the level-set method and was first introduced by Osher and Sethian in the context of interface capturing [114]. An overview of applications and advancements of the method is presented in the recent review paper [71]. For the implicit definition of *bounded* surfaces, one may either restrict $\boldsymbol{x}$ to a subset $\tilde{\Omega} \subset \mathbb{R}^3$ or introduce additional level-set functions whose intersections with the zero-isosurfaces uniquely define the boundaries. Employing this concept, the mid-surface of the shell is defined by a *master* level-set function ϕ and the boundaries are given by the intersection of ϕ with *slave* (additional) level-set functions ψ_i, $i \in \mathbb{N}$. In Fig. 1.3, different examples of bounded implicitly defined surfaces are illustrated. The yellow surface represents the zero-isosurface of ϕ and the transparent surfaces are the zero-isosurfaces of ψ_i. The blue lines indicate the boundary of the surface.

1.2 Mechanical and mathematical modelling of shells

The mechanical modelling of shells and membranes has a rich legacy starting in the early 19^{th} century. The first attempts of modelling membranes may be traced back to the work of Lamé and Clapeyron in 1828, see [137, pp. 115-117] and [145] for details. Taking the

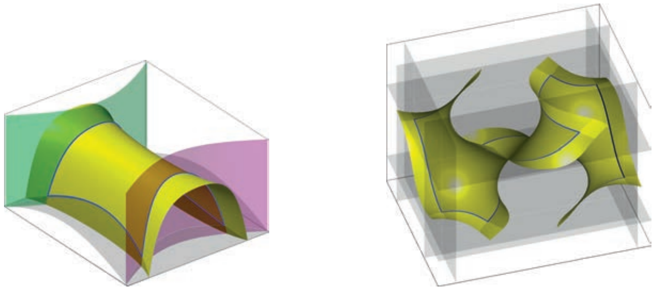

(a) curved roof **(b)** gyroid

Fig. 1.3: Implicit representation of bounded surfaces: (a) curved roof, and (b) gyroid.

flexural rigidity into account, this leads to models of plates and shells which are able to carry transversal loads by bending actions. The elastic behaviour of thin shells is based on the Kirchhoff assumptions from 1850 [96] which have been extended to shells by Love in 1888 [101]. The major assumption is that the shell is *thin*. In the context of curved shells, it is found that the product of thickness t and the largest curvature of the surface $\kappa_{\max}$ are relevant and a shell can be considered as thin if $t\kappa_{\max} \ll 1$. Further assumptions are: (1) straight lines that are normal to the mid-surface prior to deformation remain straight and normal to the deformed mid-surface, and experience no change in length, and (2) direct stress acting in normal direction of the shell mid-surface is negligible [145, p. 13]. When modelling moderately thick shells, one has to alleviate the assumptions on the shell kinematics, which results in the Reissner-Mindlin or first-order shear deformation theory [118]. The important difference is that transverse shear deformations are considered, which results in a further rotation of the normal vector independent of the mid-surface displacement. As a consequence, straight lines normal to the undeformed mid-surface remain straight after the deformation but not necessarily orthogonal to the deformed mid-surface. During the last century, these two theories have been further developed based on different mechanical assumptions by numerous scientists. Detailed historical reviews of the development of shell and membrane theories are presented in [14], [145] and excellent overviews of classical shell and membrane theories are given, e.g., in [14], [33], [94], [132], [133] or in the textbooks [7], [15], [27], [30], [31], [116], [139], [145].

The mathematical modelling of the equilibrium equations results in boundary value problems (BVPs) where partial differential equations (PDEs) are formulated on the mid-surface of the structure. For structural membranes, this results into a vector-valued, second-order surface PDE for the unknown mid-surface displacement. Also in the Kirchhoff-Love shell equations, the only unknown field is the deflection of the mid-surface. However, the incorporation of bending actions results into a fourth-order PDE for the equilibrium equations and higher continuity requirements need to be satisfied. Furthermore, the description of mechanical meaningful boundary conditions requires special attention [7], [125]. As mentioned above, allowing transverse shear deformations lead to the Reissner-Mindlin shell theory, where the continuity requirements are relaxed compared to the Kichhoff-Love shell. There, the equilibrium equations are a set of two vector-valued, second-order PDEs for the unknown fields, i.e., the mid-surface displacement and rotation of the normal vector.

Independently of the concrete model, the classical approach of modelling thin-walled structures is to formulate the PDEs in curvilinear coordinates resulting from a parametrization of the mid-surface [14]. All geometric quantities (normal vectors, curvatures, etc.) and differential surface operators (gradients, divergence, etc.), which are the key ingredients for modelling physical phenomena on curved surfaces are based on the two-dimensional, curvilinear *local* coordinates living on the manifold. Co- and contravariant base vectors and Christoffel symbols result naturally. *It is important to note, however, that the classical models are not applicable to implicitly defined geometries because there, no curvilinear coordinates are available.* A parametrization of a surface is not unique, hence there are infinitely many maps which result in the same curved surface. Obviously, the physical modelling must be independent of a concrete parametrization, which suggests the existence of a parametrization-free formulation. Note that there is a difference between “a model which holds for any parametrization, i.e., for any curvilinear coordinates” and a model “which does not necessarily need curvilinear coordinates”. While the first applies only to parametric definitions, the second applies to both parametric and implicit descriptions.

A parametrization-fee (or coordinate-free) framework which allows to define the geometric quantities and surface operators independently of curvilinear coordinates is established by the tangential differential calculus (TDC). There, these operators are defined based on the global Cartesian coordinate system which is the case in both explicit and implicit surface definitions. In this sense, the TDC-based approach is more general than approaches based on local coordinates, which are restricted to explicit surface descriptions. The TDC may be traced back to Gurtin and Murdoch in [79]. In flow and transport applications on curved surfaces, the general coordinate-free definition of the BVPs is a standard for a long time [42], [49], [52], [62], [90], thus enabling the analysis of PDEs on implicitly defined manifolds. However, in the field of structural analysis, the TDC is not as established, although the reformulation of classical (curvilinear) models for shells and membranes is a crucial preliminary step in order to enable the analysis of implicitly defined shells and membranes—the most important goal of this thesis is to establish the TDC also in shell and membrane mechanics. The TDC in structural mechanics was employed for curved beams in [84], Kirchhoff plates with arbitrary orientation in $\mathbb{R}^3$ in [82] and Kirchhoff-Love shells are considered in [37]–[40] with a mathematical focus and in [99], [113], [143] from an engineering perspective, however, only with focus on displacements. Curved membranes in the frame of the TDC are considered in [79], [81], [83]. A recast in the frame of the TDC including all relevant mechanical aspects for Kirchhoff-Love shells is presented in [125], for Reissner-Mindlin shells in [127], for linear membranes in [81] and for large deformation membranes in [66], [83].

1.3 Numerical treatment of surface PDEs

Apart from thin-walled structures, many challenging applications in engineering and natural sciences are characterized by physical phenomena taking place on curved surfaces in the three-dimensional space. There are numerous examples for transport and flow phenomena on biomembranes or bubble surfaces [75], [140]. Phenomena on surfaces may also be coupled to processes in the surrounding volume such as in surfactant transport, hydraulic fracturing, reinforced structures etc. As an additional challenge, the surfaces may be moving [50], [56], [141], i.e., the domain of interest changes. The modelling of such phenomena naturally leads to BVPs where PDEs are formulated on manifolds. For the solution of such models, tailored numerical methods are needed.

The first application of the finite element method (FEM) for the solution of the Laplace-Beltrami operator on manifolds was reported in 1988 by Dziuk [49]. Since then, the topic has attracted a tremendous research interest leading to a variety of numerical methods for PDEs on surfaces existing today, see, e.g., [16], [52] for an overview. The most straightforward approach is to generate surface meshes on the manifold and extend the finite element method in a straightforward way. As a consequence, the surface elements automatically provide curvilinear coordinates resulting from the map of the two-dimensional reference element. The resulting method may be labelled *Surface FEM*, see, e.g., [42], [65], and is applicable to BVPs on manifolds which are based on curvilinear coordinates (the classical approach, still standard in shell mechanics) as well as the TDC (the standard approach for transport and flows on manifolds). It is obvious that the Surface FEM is inherently linked to parametrized surfaces, no matter whether there is a global map from the parameter space or an atlas of maps as provided by the surface elements.

However, as discussed before, the BVP may also be set up based on an implicit description in which case the TDC has to be used as curvilinear coordinates are not available. It is now possible to obtain the solution on *all* iso-surfaces of the involved level-set functions (not only on the zero level-set) [19], [51]. Then, the problem is naturally set up in the three-dimensional space embedding the manifolds, i.e., volumetric elements and shape functions are employed. However, typically only the solution on *one* iso-surface, say the zero-isosurface, is sought. One may then restrict the surrounding domain to a narrow band around the manifold [12], [36], [55]. There are interesting similarities to phase field and diffuse interface approaches [117]. A recent approach is to collapse the narrow band to the manifold itself. Then, shape functions of the volumetric background elements are used, however, the integration takes place on the trace of the manifold only. The resulting approaches are fictitious domain methods (FDMs) and are labelled TraceFEM [16], [72], [74], [108], [109], [119], [124]. This may also be called Cut FEM which, in the last years, has become a popular FDM enabling higher-order accuracy [21], [22], [24]. When using the Cut FEM for the solution of PDEs on manifolds as done herein, the method becomes analogous to the Trace FEM [26], [28]. This recent finite element technique is fundamentally different compared to standard Surface FEM approaches, see, e.g., [42], [52], [62], [65].

Elevating the order of the employed shape functions leads to the p-version of the finite element method (p-FEM) [48]. The advantages of the p-FEM are higher-order accurate and efficient approximations of BVPs. For a successful application of the p-FEM, the geometry must be accurately represented by higher-order elements and the involved fields should be sufficiently smooth. The use of higher-order elements in both the Surface and the Trace FEM, is of particular importance in this thesis. For both the Surface and the Trace FEM, higher-order approximations of PDEs on manifolds have been reported in different contexts before: For explicit (handcrafted or automatically generated) surface meshes in [42], [61], [65] and in the context of the Trace FEM in [66], [92], [100], [119], [129]. Adaptivity is considered, e.g., in [43], [44]. If the geometry is defined by *multiple* level-set functions, we refer to [66], [129] and for *one* level-set function, we refer to [91], [92], [100].

In the following, the major differences of the Surface FEM and the Trace FEM are outlined.

1. Firstly, the differences in the geometry definition are emphasized. In the Trace FEM, the (shell) surfaces are implicitly defined by means of (multiple) level-set functions, see Fig. 1.3. In the context of Surface FEM, the geometry is usually given through an atlas of *element-wise* local maps, implying local curvilinear coordinates, see Fig. 1.4(b). Note that a parametrization is *only* available in the explicit case and is, in general, not available in implicitly defined geometries.
2. Secondly, the mesh generation and the location of the degrees of freedom (DOFs) are considered. In the Trace FEM the domain of interest, i.e., the surface Γ, is embedded in a three-dimensional background mesh. The 3D background mesh may consist of higher-order Lagrange elements into which the domain of interest is completely immersed. Neither the shell surface nor the shell boundary have to conform to the background mesh. There is one master level-set function whose zero-isosurface implies the surface and additional slave level-set functions imply the boundaries. The set of cut elements is labelled *active* mesh and is visualized in Fig. 1.4(a) where cubic tetrahedral elements are used as an example. For the numerical simulation, the DOFs are located at the nodes of the active mesh, which are clearly *not* on the mid-surface of the shell. The corresponding shape functions are those of the active mesh and are restricted to the trace. This means that for the integration of the weak form, the 3D shape functions are only evaluated on the zero-isosurface of the master level-set function. In contrast, in the Surface FEM a boundary conforming surface mesh, see Fig. 1.4(b), is defined through an atlas of element-wise local maps and the DOFs are located at nodes of the surface mesh which are on the discrete mid-surface of the shell. The corresponding shape functions are the 2D shape functions living only on the surface mesh. The location of the DOFs and the different dimensionality of the shape functions are the most important differences between the two finite element techniques.
3. Lastly, integration points need to be placed on the shell mid-surface for the integration of the weak form. In the case of the Trace FEM, this requires the identification of the zero-isosurface which is not a trivial task especially when a higher-order accurate integration scheme is desired [63]–[66], [100], [102], further details are given below. Regarding the Surface FEM, standard Gauß integration rules are applicable and mapped from the reference to the surface elements in the usual manner.

As mentioned above, the Trace FEM is a fictitious domain method and the following three well-known implementational aspects require special attention: (i) integration of the weak form, (ii) stabilization and, (iii) enforcement of essential boundary conditions. Regarding the integration of the weak form, suitable integration points with higher-order accuracy for multiple level-set functions have to be provided. Herein, the approach which

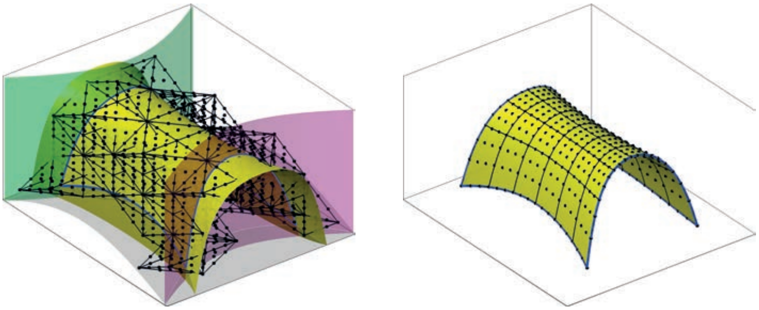
(a) meshes in the Trace FEM **(b)** meshes in the Surface FEM

Fig. 1.4: Examples of employed meshes in the numerical treatment of surface PDEs. (a) The set of cut three-dimensional background elements are labelled as active mesh and their nodes imply the DOFs for the Trace FEM, and (b) conforming surface mesh consisting of cubic 2D Lagrange elements for the Surface FEM.

naturally extends to multiple level-set functions as outlined by the author and coworkers in [63]–[66] is employed. Other higher-order integration schemes for implicitly defined surfaces with *one* level-set function are presented, e.g., in [100], [102]. A stabilization of the stiffness matrix is necessary due to small supports caused by unfavourable cut scenarios and the restriction of the 3D shape functions to the trace. An overview and analysis of the different stabilization techniques in the Trace FEM is presented in [109] and a recent approach where two stabilizations techniques, i.e., face stabilization of the cut elements and the normal derivative stabilization on the zero-isosurface, are combined is presented in [98]. Herein, the "normal derivative volume stabilization" first introduced for scalar-valued problems in [26], [73] and for vector-valued problems in [74], [107] is used. The advantage of this particular stabilization technique is that it is suitable for higher-order accuracy, a straightforward implementation and a rather flexible choice of the stabilization parameter. The essential boundary conditions need to be enforced in a weak manner due to the fact that a strong enforcement by prescribing nodal values does not apply (because the nodes of the background mesh are not on the shell boundary). In principle, there are different approaches to enforce the boundary conditions weakly. The penalty method is robust and straightforwardly implemented [6]. The main advantages are the built-in linear independence of the constraints and auxiliary fields are not required. The drawbacks are variational inconsistence and conditioning issues. One alternative is the Lagrange multiplier method [5], [23], [144]. Although the Lagrange multipliers are variationally consistent, additional degrees of freedom are introduced and the well posedness of the augmented system of equations is not guaranteed. Furthermore, in the case of FDMs, the discretization of the Lagrange multiplier fields can become a challenging task depending on the cut scenarios. A consistent approach without auxiliary fields is Nitsche's method [104]. This method has been developed to be a standard choice in FDMs due to these advantages. The original approach from [104] has been adopted to various applications for enforcing essential boundary conditions, see, e.g., [11], [57], [59],

[66], [80], [120], [129] and coupling, see, e.g., [1], [77], [78], [121]. Different variants of Nitsche's method have been developed, i.e., the symmetric and non-symmetric version. The first version does not change the symmetry of the discrete bilinear form. However, additional stabilization terms are required in order to recover positive definiteness [59]. In contrast, the non-symmetric version of Nitsche's method does not require an additional stabilization term for imposing boundary conditions [20], [76], [78], [129].

1.4 Discretization of thin-walled structures

The focus is now shifted from numerical methods applied to generic PDEs on surfaces to the situation of shells and membranes. For the numerical treatment of Kirchhoff-Love shells, it is crucial to consider continuity requirements due to the variational index 2 [14]. In other words, the employed functions need to be at least in the function space $\mathcal{H}^2$, which is the space of functions with square integrable first *and* second derivatives. This requires continuous first derivatives across the element borders. Unfortunately, on unstructured, general meshes it is not possible to achieve a C^1-continuous discrete surface in a conventional sense when local polynomials are employed as shape functions [2]. A different approach based on subdivision surfaces is presented in [33]. The complications resulting from the continuity requirements when neglecting the transverse shear deformations are a major obstacle for conventional Surface FEM approaches. However, employing spline-based, isogeometric formulations, the continuity requirements are easily met. The isogeometric analysis (IGA) as proposed by Hughes et al. [34], [88], has been applied to Kirchhoff-Love shells by Kiendl et al. [94]. The curvilinear coordinates which are implied by the map from the parameter space to the physical space of the NURBS patch and the high continuity are a perfect fit for the analysis of Kirchhoff-Love shells. Other successful implementations of the Kirchhoff-Love shell model may be found, e.g., in [32], [33], [94], [103], [125], [135].

As mentioned above, taking transverse shear deformations into account leads to the well-known Reissner-Mindlin shell. An advantage of this model is that the corresponding variational index is 1 and only C^0-continuity in a finite element analysis is required, enabling standard Surface FEM (based on Lagrange elements). A general overview of successful implementations of Reissner-Mindlin shells is given, e.g., in [8], [97], [142]. In the context of IGA, Reissner-Mindlin shells are considered in, e.g., [10], [127]. Furthermore, in [46], [47] an approach with exactly calculated shell directors in the frame of IGA is presented. Isogeometric collocation for the Reissner-Mindllin shell is presented in [95]. On the other hand, the model often suffers from locking phenomena for increasingly thin shells which may require further measures in the numerical treatment. Hierarchical shell formulations which efficiently eliminate transverse shear locking have been introduced in [53], [105], [106]. A mixed displacement approach which also eliminates membrane locking is elaborated in [13], [146].

Successful discretization of shells with FDMs are rather scarce compared to the Surface FEM. For instance, linear membranes have been introduced for Cut FEM in [28]. A recent pre-print where a C^1-continuous Trace FEM approach for Kirchhoff-Love shells with boundary conforming background meshes is presented in [69]. Higher-order accurate

Trace FEM approaches are presented by the author and coworkers for linear Reissner-Mindlin shells in [129].

Concerning structural membranes, one may employ standard Surface FEM procedures [14]. As the equilibrium is formulated in a second-order PDE, C^0-continuous discretization of the mid-surface is sufficient. Large displacement membranes are presented in [89]. For a TDC-based modelling of large deformation membranes with the Surface FEM, we emphasize the work in [83] and within the Trace FEM [66].

1.5 Scope and objectives of the thesis

The scope of the thesis is to reformulate classical shell and membrane models based on the TDC and to develop a higher-order accurate numerical framework for the analysis of explicitly and implicitly defined thin-walled structures. The mathematical and mechanical modelling of shells and membranes leads to surface PDEs on manifolds embedded in the physical space.

The classical approach of modelling shells and membranes is to formulate the PDEs in curvilinear coordinates which are implied by a parametrization. Consequently, the classical theory is limited to explicitly defined surfaces. Herein, the equilibrium equations are recast in the frame of the TDC where the employed surface operators and geometric quantities are based on the global Cartesian coordinate system. With this reformulation, the crucial requirement of a parametrization is circumvented and the obtained BVPs in strong and weak form are well-defined independently of the concrete surface definition. In this sense, the reformulated shell and membrane equations are generalized and a unified formulation for explicitly and implicitly defined structures is presented. Based on this, the obtained BVPs may be discretized with standard Surface FEM or with recent finite element techniques such as the Trace FEM or the Cut FEM. Moreover, the resulting equations are formulated in symbolic notation which results in a more compact presentation of the formulas, whereas the classical theory typically employs index notation.

For the approximation of the PDEs on surfaces, higher-order accurate Surface and Trace FEM are first investigated on a model problem in order to analyse the properties and differences of the methods in a simplified setting. The implementational aspects are described in detail. Next, the weak forms of the equilibrium equations of thin-walled structures are discretized with the higher-order Surface and Trace FEM. The numerical results confirm optimal higher-order accuracy of the two FEM approaches, independently of the mechanical model and provided that the involved mechanical fields are sufficiently smooth.

The novelty of the thesis is a complete reformulation of classical shell and membrane models including all relevant mechanical quantities in the frame of the TDC. This enables the unified description of the BVPs for parametric *and* implicit surfaces. For the first time, a higher-order Trace FEM is applied to shells and large deformation membranes. Numerical benchmarks, which enable higher-order convergence rates of thin-walled structures are proposed. Furthermore, the concept of residual errors in code verification is employed in order to perform a strict benchmarking for general test cases without the need of reference displacements, analytical or manufactured solutions.

The contributions of the thesis have been published in the following 7 peer-reviewed journal articles: [131], [129], [66], [127], [125], [65] [64] and 8 conference proceedings: [130], [67], [128], [124], [126], [123], [122], [68].

1.6 Outline of the thesis

Following this introduction, Chapter 2 introduces the geometry definitions, important geometrical quantities and the employed surface differential operators in the frame of the TDC. In Chapter 3, discretization methods for surface PDEs are introduced. In particular, the key ingredients such as the involved functions spaces, employed shape functions and meshes are defined for both Surface and Trace FEM. Major implementational aspects such as (i) numerical integration, (ii) stabilization and (iii) treatment of essential boundary conditions are elaborated and compared in detail. Furthermore, the methodologies of Surface and Trace FEM are compared on a model problem. In Chapter 4, we focus on the linear Kirchhoff-Love shell. The shell model is recast in the frame of the TDC and mechanically meaningful boundary conditions are outlined. The obtained shell model is discretized with an IGA approach (closely related to the Surface FEM) and is successfully verified on a set of benchmarks. In Chapter 5, analogous to the previous chapter, the Reissner-Mindlin shell theory is reformulated. The resulting BVP is discretized with IGA for parametrized surfaces and with a higher-order accurate Trace FEM for implicitly defined shell geometries. The discrete modelling of the rotation of the normal vector is elaborated in detail for both situations, Surface and Trace FEM. Benchmarks are performed with both finite element methodologies and the numerical results confirm optimal orders of convergence for both methods provided that the involved fields are sufficiently smooth. Chapter 6 extends the reformulation of BVPs to non-linear problems. In particular, large deformation membranes within the finite strain theory are considered in the frame of the TDC. The obtained BVP is discretized with Surface and Trace FEM and the numerical results confirm the higher-order accuracy also in case of non-linear problems. Finally, in Chapter 7, the present work is summarized and future work and applications are sketched.

2 Preliminaries

This thesis is devoted to thin-walled structures such as shells and membranes. The geometries are represented by curved surfaces in the three-dimensional space plus additional information on the thickness. In this chapter, we first focus on the geometry definition including all relevant quantities such as normal vectors and curvature. Next, differential operators such as surface gradients of scalars, vectors, and tensors are defined. Furthermore, Green's formula on manifolds is presented. The geometric and differential operators are formulated on the surface employing a framework where *only* Cartesian base vectors are required and no curvilinear coordinates are needed. This framework is called the tangential differential calculus (TDC), see, e.g., [41], [52], [62], [83], [125].

The major content of this chapter follows our own articles in [65], [125], [127], [129].

2.1 Geometry definition

Shells (and membranes) are thin-walled structures with thickness t, with one dimension being significantly smaller compared to the other two dimensions. Then, the shell can be reduced to its mid-surface Γ which is embedded in the physical space $\mathbb{R}^3$. In the context of thin-walled structures, the mid-surface may also be called reference surface. The surface represents a two-dimensional manifold in the three-dimensional space, hence, a manifold with codimension 1.

The surface Γ shall be possibly curved, sufficiently smooth, orientable, connected and bounded by $\partial\Gamma$. There are two fundamentally different approaches to the definition of surfaces, explicitly and implicitly. For *explicit* definitions, there is a bijective map $\boldsymbol{\chi}(\boldsymbol{r}) : \hat{\Omega} \rightarrow \Gamma$ from the parameter space $\hat{\Omega} \subset \mathbb{R}^2$ to the real domain $\Gamma \subset \mathbb{R}^3$. Hence, the surface is given by a parametrization or *parametrized*. In Fig. 2.1(a) an example of a global parametrization is illustrated. As a result of the map, there exist curvilinear coordinates on the surface giving rise to co- and contravariant base vectors and the notation of Christoffel symbols. In the context of Surface FEM, the parametrization is rather defined through an atlas of element-wise local maps, see Section 3.1 for details.

Alternatively, surfaces may also be defined *implicitly* by means of (multiple) level-set functions following the level-set method, see Fig. 2.1(b). The important difference is that in this case, there are no curvilinear coordinates on the surface, hence, no natural base vectors and Christoffel symbols. However, as already seen in Fig. 2.1, the *same* surface may be defined in a parametrized or implicit manner. Hence, geometry related quantities such as normal vectors and curvature must be identical and computable in both situations.

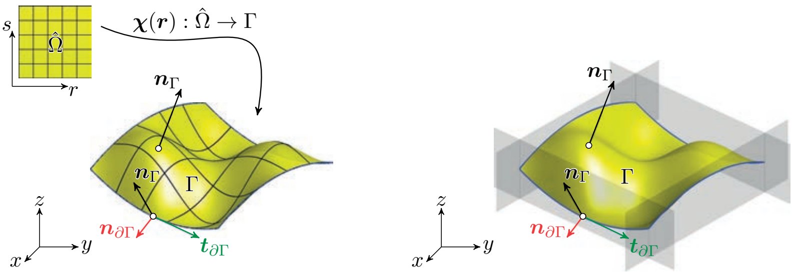

(a) explicit **(b)** implicit

Fig. 2.1: Examples of bounded surfaces Γ embedded in the physical space $\mathbb{R}^3$: (a) Explicitly defined surface by a map $\chi(\boldsymbol{r})$, (b) implicitly defined surface implied by a master level-set function $\phi(\boldsymbol{x}) = 0$ (yellow) and slave level-set functions ψ_i for the boundary definition (gray).

Let there be a master level-set function $\phi(\boldsymbol{x}) : \mathbb{R}^3 \to \mathbb{R}$ whose zero-isosurface defines the (unbounded) mid-surface of the shell in $\mathbb{R}^3$, see Fig. 2.2(a) and 2.2(b). The boundaries of the shell $\partial\Gamma_i$ are defined by additional *slave* level-set functions ψ_i with $i \in \omega_\psi = \{1, \dots, n_{\text{Slaves}}\}$, see Fig. 2.2(c), where the blue lines indicate the boundary of the shell $\partial\Gamma$. For the sake of simplicity, all slave level-set functions feature the same orientation, i.e., positive inside the domain and negative outside. The bounded mid-surface Γ and the boundaries $\partial\Gamma_i$ of the shell are then defined by

$$\Gamma := \left\{ \phi(\boldsymbol{x}) = 0 \ \wedge \ \psi_i(\boldsymbol{x}) > 0 \ \forall \ \boldsymbol{x} \in \mathbb{R}^3, i \in \omega_\psi \right\} \ , \tag{2.1}$$

$$\partial\Gamma_i := \left\{ \boldsymbol{x} \in \bar{\Gamma} \ : \ \psi_i(\boldsymbol{x}) = 0 \right\} \ , \tag{2.2}$$

where $\bar{\Gamma}$ is the closure of Γ and the union of all boundaries define $\partial\Gamma := \bigcup_{i\in\omega_\psi} \partial\Gamma_i$. Slave level-set functions are not necessarily needed when the master level-set function is restricted to some bounded domain of definition $\Omega^* \subset \mathbb{R}^3$ in Eq. 2.1 rather than $\mathbb{R}^3$.

For any surface Γ, there exists a unit normal vector $\boldsymbol{n}_\Gamma = [n_x, n_y, n_z]^\mathrm{T} \in \mathbb{R}^3$, see Fig. 2.1. The representation of the normal vector depends on whether the surface is based on a parametrization or not. In the parametrized case, the normal vector is determined by the normalized cross-product of the tangent vectors living in the shell surface and given by the columns of the Jacobi-matrix $\mathbf{J}(\boldsymbol{r}) = {}^{\partial\chi}/_{\partial\boldsymbol{r}} \in \mathbb{R}^{3\times 2}$,

$$\boldsymbol{n}_\Gamma = \frac{[\mathbf{J}]_{i1} \times [\mathbf{J}]_{i2}}{\|[\mathbf{J}]_{i1} \times [\mathbf{J}]_{i2}\|} \quad \text{with } i = 1, 2, 3 \ . \tag{2.3}$$

Along the boundary $\partial\Gamma$ there exists the local triad $(\boldsymbol{n}_\Gamma, \boldsymbol{t}_{\partial\Gamma}, \boldsymbol{n}_{\partial\Gamma})$ consisting of the normal vector, associated tangent vector and co-normal vector, see Fig. 2.1(a). The associated tangent vector $\boldsymbol{t}_{\partial\Gamma} \in \mathbb{R}^3$ is pointing along $\partial\Gamma$ which can be directly obtained through the mapping of the tangent vector $\hat{\boldsymbol{t}}_{\partial\Gamma}$ in the parameter space to the physical space. The co-normal vector $\boldsymbol{n}_{\partial\Gamma}$ at $\partial\Gamma$ points “outwards” and is perpendicular to the boundary yet

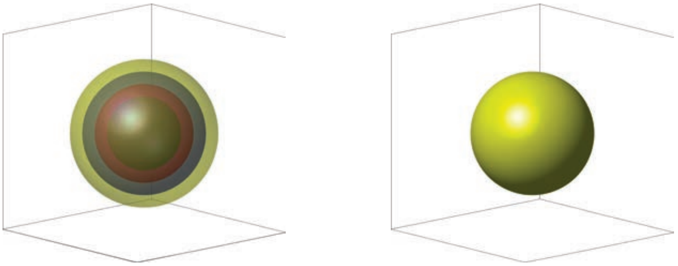

(a) isosurfaces of ϕ **(b)** implicit shell mid-surface

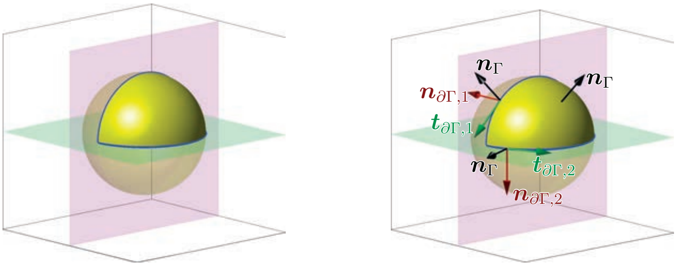

(c) some bounded shell mid-surface **(d)** normal vector and local triads

Fig. 2.2: Implicit definition of a (bounded) spherical shell: $\phi(\boldsymbol{x}) = \|\boldsymbol{x}\| - r, \psi_1(\boldsymbol{x}) = x, \psi_2(\boldsymbol{x}) = z$. (a) The colors represent different isosurfaces of ϕ, (b) implicit shell mid-surface defined by the zero-isosurface of ϕ, (c) definition of boundaries with additional slave level-set functions ψ_1 (purple) and ψ_2 (green), and (d) normal (black), co-normal (red) and tangent (green) vectors.

in the tangent space $T_p\Gamma$. It is defined as

$$\boldsymbol{n}_{\partial\Gamma}(\boldsymbol{x}) = \boldsymbol{t}_{\partial\Gamma}(\boldsymbol{x}) \times \boldsymbol{n}_{\Gamma}(\boldsymbol{x}) \ , \tag{2.4}$$

see Fig. 2.1(a). In the implicit case, the normal vector of the shell is given through the normalized gradient of the master level-set function ϕ

$$\boldsymbol{n}_{\Gamma}(\boldsymbol{x}) = \frac{\nabla\phi(\boldsymbol{x})}{\|\nabla\phi(\boldsymbol{x})\|} \ . \tag{2.5}$$

The associated tangent vector $\boldsymbol{t}_{\partial\Gamma,i}$ is defined by the normalized cross product of the corresponding slave level-set function ψ_i and the master level-set function ϕ

$$\boldsymbol{t}_{\partial\Gamma,i}(\boldsymbol{x}) = \frac{\nabla\psi_i(\boldsymbol{x}) \times \nabla\phi(\boldsymbol{x})}{\|\nabla\psi_i(\boldsymbol{x}) \times \nabla\phi(\boldsymbol{x})\|} \ , \quad \boldsymbol{x} \in \partial\Gamma_i \ . \tag{2.6}$$

The orientation of the tangent vector $\boldsymbol{t}_{\partial\Gamma,i}$ is defined through the orientation of the slave level-set function ψ_i. Finally, the co-normal vector, in accordance with Eq. 2.4 for the explicit case, is

$$\boldsymbol{n}_{\partial\Gamma,i}(\boldsymbol{x}) = \boldsymbol{t}_{\partial\Gamma,i}(\boldsymbol{x}) \times \boldsymbol{n}_{\Gamma}(\boldsymbol{x})\,, \quad \boldsymbol{x} \in \partial\Gamma_i\ . \tag{2.7}$$

For an illustration, see Fig. 2.2(d), where the normal vector $\boldsymbol{n}_{\Gamma}$ and the local triad $(\boldsymbol{n}_{\Gamma}, \boldsymbol{n}_{\partial\Gamma,i}, \boldsymbol{t}_{\partial\Gamma,i})$ at the boundaries are visualized for an implicitly defined spherical shell. For the formal proof of equivalence of both geometry definitions, i.e., explicit and implicit, we refer to, e.g., [52].

2.2 Tangential differential calculus (TDC)

The TDC provides a framework to define differential operators using the global Cartesian coordinate system and is applicable to both explicit and implicit surface definitions. It may be traced back to Gurtin and Murdoch in [79]. The concept of the TDC from a more mathematical point of view is considered in detail, see, e.g., [39], [41], [42], [52], [85], [90] and applications with a focus in engineering may be found in, e.g., [62], [81]–[84], [125], [127]. More classical approaches to differential geometry are based on local coordinate systems and Christoffel symbols, see, e.g., [27], [31], [138]. However, they rely on the parametrized definition of surfaces and are not straightforwardly applicable to the implicit definition. In this sense, the TDC-based definition of geometric and differential operators on surfaces is more general. In the following, the employed surface operators and other important relations and quantities needed in this work are briefly presented in the frame of the TDC. For the sake of brevity, we restrict ourselves to the case of surfaces embedded in the three dimensional space. However, the shown relations and definitions may be adopted to other situations accordingly (e.g., curved lines embedded in 2D or 3D), see, e.g., [66].

2.2.1 Projection operators

On the manifold Γ, the projection operator $\mathbf{Q}(\boldsymbol{x}) \in \mathbb{R}^{3\times 3}$ is based on the normal vector

$$\mathbf{Q}(\boldsymbol{x}) = \boldsymbol{n}_{\Gamma}(\boldsymbol{x}) \otimes \boldsymbol{n}_{\Gamma}(\boldsymbol{x})\ . \tag{2.8}$$

It projects an arbitrary vector $\boldsymbol{v}(\boldsymbol{x}) : \Gamma \to \mathbb{R}^3$ in normal direction of Γ. The operator $\otimes$ is the dyadic product of two vectors. There holds $\mathbf{Q} \cdot \boldsymbol{n}_{\Gamma} = \boldsymbol{n}_{\Gamma}$, $\mathbf{Q} = \mathbf{Q}^{\mathrm{T}}$, and $\mathbf{Q} \cdot \mathbf{Q} = \mathbf{Q}$. Instead, the projection operator $\mathbf{P}(\boldsymbol{x}) \in \mathbb{R}^{3\times 3}$ is defined as

$$\mathbf{P}(\boldsymbol{x}) = \mathbb{I} - \mathbf{Q}(\boldsymbol{x}) \tag{2.9}$$

and projects arbitrary vectors into the tangent space $T_P\Gamma$. There holds $\mathbf{P} \cdot \boldsymbol{n}_{\Gamma} = \mathbf{0}$, $\mathbf{P} = \mathbf{P}^{\mathrm{T}}$, and $\mathbf{P} \cdot \mathbf{P} = \mathbf{P}$. The projection of a vector field $\boldsymbol{v}(\boldsymbol{x}) : \Gamma \to \mathbb{R}^3$ onto the tangent plane is given by

$$\boldsymbol{v}_t = \mathbf{P} \cdot \boldsymbol{v} \quad \in T_P\Gamma\ , \tag{2.10}$$

where $\boldsymbol{v}_t$ is tangential, i.e., $\boldsymbol{v}_t \cdot \boldsymbol{n}_\Gamma = 0$. The double projection of a second-order tensor function $\boldsymbol{A}(\boldsymbol{x}) : \Gamma \to \mathbb{R}^{3\times 3}$ leads to an in-plane tensor and is defined as

$$\boldsymbol{A}_t = \mathbf{P} \cdot \boldsymbol{A} \cdot \mathbf{P} \quad \in T_P\Gamma \ , \tag{2.11}$$

with the properties $\boldsymbol{A}_t = \mathbf{P} \cdot \boldsymbol{A}_t \cdot \mathbf{P}$ and $\boldsymbol{A}_t \cdot \boldsymbol{n}_\Gamma = \boldsymbol{n}_\Gamma^{\mathrm{T}} \cdot \boldsymbol{A}_t = \mathbf{0}$.

2.2.2 Differential operators

Tangential gradient of scalar-, vector-, tensor-valued functions

The tangential gradient ∇_Γ of a scalar-valued function $u(\boldsymbol{x}) : \Gamma \to \mathbb{R}$ on the manifold is defined as

$$\nabla_\Gamma u(\boldsymbol{x}) = \mathbf{P}(\boldsymbol{x}) \cdot \nabla \tilde{u}(\boldsymbol{x}) \ , \ \nabla_\Gamma u(\boldsymbol{x}) \in \mathbb{R}^{3\times 1} \ , \ \boldsymbol{x} \in \Gamma \ , \tag{2.12}$$

where ∇ is the standard gradient operator in the physical space and $\tilde{u}$ is a smooth extension of u in a neighbourhood $\mathcal{U}$ of the manifold Γ (note that the particular choice of extension does not affect the tangential gradient [41]). Alternatively, $\tilde{u}$ is given as a function in global coordinates $\tilde{u}(\boldsymbol{x}) : \mathbb{R}^3 \to \mathbb{R}$ and only evaluated at the manifold $\tilde{u}_{|\Gamma} = u$.

For parametrized surfaces defined by the map $\boldsymbol{\chi}(\boldsymbol{r})$, and a given scalar function $u(\boldsymbol{r}) : \hat{\Omega} \to \mathbb{R}$, the tangential gradient can be determined without explicitly computing an extension $\tilde{u}$ using

$$\nabla_\Gamma u(\boldsymbol{x}) = \mathbf{J}^+(\boldsymbol{r}) \cdot \nabla_{\boldsymbol{r}} u(\boldsymbol{r}) \ , \tag{2.13}$$

with $\boldsymbol{x} = \boldsymbol{\chi}(\boldsymbol{r})$ and $\mathbf{J}^+ = \mathbf{J} \cdot \mathbf{G}^{-1} \in \mathbb{R}^{3\times 2}$ is the Moore–Penrose inverse of $\mathbf{J}$ and $\mathbf{G} = \mathbf{J}^{\mathrm{T}} \cdot \mathbf{J}$ is the metric tensor or the first fundamental form. The operator $\nabla_{\boldsymbol{r}}$ is the gradient with respect to the reference coordinates. The components of the tangential gradient are denoted by

$$\nabla_\Gamma u = \begin{bmatrix} \partial_x^\Gamma u \\ \partial_y^\Gamma u \\ \partial_z^\Gamma u \end{bmatrix} = \begin{bmatrix} u_{,x}^\Gamma \\ u_{,y}^\Gamma \\ u_{,z}^\Gamma \end{bmatrix} \ , \tag{2.14}$$

representing first-order partial tangential derivatives. An important property of $\nabla_\Gamma u$ is that the tangential gradient of a scalar-valued function is in the tangent space of the surface $\nabla_\Gamma u \in T_P\Gamma$, i.e., $\nabla_\Gamma u \cdot \boldsymbol{n}_\Gamma = 0$. When using the Surface FEM, see Section 3.1, to solve BVPs on surfaces, one may use Eq. 2.13 to compute tangential gradients of the shape functions. If, on the other hand, the Trace FEM is used, see Section 3.2, one may employ Eq. 2.12.

Consider a vector-valued function $\boldsymbol{v}(\boldsymbol{x}) : \Gamma \to \mathbb{R}^3$ and apply to each component of $\boldsymbol{v}$ the tangential gradient for scalars. This leads to the *directional* gradient of $\boldsymbol{v}$ and is defined as

$$\nabla_\Gamma^{\mathrm{dir}} \boldsymbol{v}(\boldsymbol{x}) = \nabla_\Gamma^{\mathrm{dir}} \begin{bmatrix} v_x(\boldsymbol{x}) \\ v_y(\boldsymbol{x}) \\ v_z(\boldsymbol{x}) \end{bmatrix} = \begin{bmatrix} \partial_x^\Gamma v_x & \partial_y^\Gamma v_x & \partial_z^\Gamma v_x \\ \partial_x^\Gamma v_y & \partial_y^\Gamma v_y & \partial_z^\Gamma v_y \\ \partial_x^\Gamma v_z & \partial_y^\Gamma v_z & \partial_z^\Gamma v_z \end{bmatrix} . \tag{2.15}$$

Note that the directional gradient is *not* in the tangent space of the surface, in general. A projection of the directional gradient to the tangent space leads to the *covariant* gradient of $\boldsymbol{v}$ and is defined as

$$\nabla_\Gamma^{\mathrm{cov}} \boldsymbol{v} = \mathbf{P} \cdot \nabla_\Gamma^{\mathrm{dir}} \boldsymbol{v} \tag{2.16}$$

which is an in-plane tensor, i.e., $\nabla_\Gamma^{\mathrm{cov}} \boldsymbol{v} \in T_P\Gamma$. The covariant gradient often appears in the modelling of physical phenomena on manifolds, i.e., in the governing equations. In contrast, the directional gradient appears naturally in product rules or divergence theorems on manifolds.

For a second-order tensor function $\mathbf{A}(\boldsymbol{x}) : \Gamma \to \mathbb{R}^{3\times 3}$, the partial directional gradient with respect to x_i is defined as

$$\nabla_{\Gamma,i}^{\mathrm{dir}} \mathbf{A} = \partial_{x_i}^\Gamma \mathbf{A} = \begin{bmatrix} \partial_{x_i}^\Gamma A_{11} & \partial_{x_i}^\Gamma A_{12} & \partial_{x_i}^\Gamma A_{13} \\ \partial_{x_i}^\Gamma A_{21} & \partial_{x_i}^\Gamma A_{22} & \partial_{x_i}^\Gamma A_{23} \\ \partial_{x_i}^\Gamma A_{31} & \partial_{x_i}^\Gamma A_{32} & \partial_{x_i}^\Gamma A_{33} \end{bmatrix} , \tag{2.17}$$

with $i = 1, 2, 3$. The directional gradient of the tensor function is then defined as

$$\nabla_\Gamma^{\mathrm{dir}} \mathbf{A} = \left(\nabla_{\Gamma,1}^{\mathrm{dir}} \mathbf{A} \quad \nabla_{\Gamma,2}^{\mathrm{dir}} \mathbf{A} \quad \nabla_{\Gamma,3}^{\mathrm{dir}} \mathbf{A} \right) . \tag{2.18}$$

The covariant partial derivative is determined by projecting the partial directional derivative onto the tangent space

$$\nabla_{\Gamma,i}^{\mathrm{cov}} \mathbf{A} = \mathbf{P} \cdot \nabla_{\Gamma,i}^{\mathrm{dir}} \mathbf{A} \cdot \mathbf{P} . \tag{2.19}$$

Second-order tangential derivatives

Next, second-order derivatives of scalar-valued functions are considered. The directional second-order gradient of a scalar function u is defined by

$$\begin{aligned} \left[\mathbf{He}^{\mathrm{dir}}\right]_{ij} (u(\boldsymbol{x})) &= \partial_{x_j}^{\Gamma,\mathrm{dir}} \left(\partial_{x_i}^\Gamma u(\boldsymbol{x}) \right) = u_{,ji}^{\mathrm{dir}} , \\ \mathbf{He}^{\mathrm{dir}}(u(\boldsymbol{x})) &= \begin{bmatrix} \partial_{xx}^\Gamma u & \partial_{yx}^\Gamma u & \partial_{zx}^\Gamma u \\ \partial_{xy}^\Gamma u & \partial_{yy}^\Gamma u & \partial_{zy}^\Gamma u \\ \partial_{xz}^\Gamma u & \partial_{yz}^\Gamma u & \partial_{zz}^\Gamma u \end{bmatrix} = \nabla_\Gamma^{\mathrm{dir}} \left(\nabla_\Gamma u(\boldsymbol{x}) \right) , \end{aligned} \tag{2.20}$$

where $\mathbf{He}^{\mathrm{dir}}$ is the directional Hessian matrix which is *not* symmetric in the case of curved manifolds [41], i.e., $u_{,ij}^{\mathrm{dir}} \neq u_{,ji}^{\mathrm{dir}}$. For the case of implicitly defined surfaces and a given scalar function in the physical space, $\mathbf{He}^{\mathrm{dir}}$ can be directly computed by employing the relation from Eq. A.37

$$\begin{aligned}\mathbf{He}^{\mathrm{dir}}(u(\boldsymbol{x})) &= \nabla_{\Gamma}^{\mathrm{dir}}\left(\nabla_{\Gamma}u(\boldsymbol{x})\right) = \nabla_{\Gamma}^{\mathrm{dir}}\left(\mathbf{P}\cdot\nabla\tilde{u}\right)\\ &= \left[\nabla_{\Gamma,1}^{\mathrm{dir}}\mathbf{P}\cdot\nabla\tilde{u} \quad \nabla_{\Gamma,2}^{\mathrm{dir}}\mathbf{P}\cdot\nabla\tilde{u} \quad \nabla_{\Gamma,3}^{\mathrm{dir}}\mathbf{P}\cdot\nabla\tilde{u}\right] + \nabla_{\Gamma}^{\mathrm{cov}}\nabla\tilde{u}\ .\end{aligned} \tag{2.21}$$

For the case of parametrized surfaces and a given scalar function in the reference space, the directional Hessian-matrix can be determined by

$$\begin{aligned}\mathbf{He}^{\mathrm{dir}}(u) &= \nabla_{\Gamma}^{\mathrm{dir}}\left(\mathbf{J}^{+}\cdot\nabla_{\boldsymbol{r}}u\right)\\ &= \left[\mathbf{J}^{+}_{,r}\cdot\nabla_{\boldsymbol{r}}u \quad \mathbf{J}^{+}_{,s}\cdot\nabla_{\boldsymbol{r}}u\right]\cdot\mathbf{J}^{+^{\mathrm{T}}} + \mathbf{J}^{+}\cdot\nabla_{\boldsymbol{r}}\left(\nabla_{\boldsymbol{r}}u\right)\cdot\mathbf{J}^{+^{\mathrm{T}}}\ ,\end{aligned} \tag{2.22}$$

where $\mathbf{J}^{+}_{,r_i}$ denotes the partial derivative of $\mathbf{J}^{+}$ with respect to r_i. The covariant counterpart is

$$\mathbf{He}^{\mathrm{cov}}(u) = \nabla_{\Gamma}^{\mathrm{cov}}\left(\nabla_{\Gamma}u\right) = \mathbf{P}\cdot\nabla_{\Gamma}^{\mathrm{dir}}\left(\nabla_{\Gamma}u\right) = \mathbf{P}\cdot\mathbf{He}^{\mathrm{dir}}(u)\ . \tag{2.23}$$

In contrast to $\mathbf{He}^{\mathrm{dir}}$, $\mathbf{He}^{\mathrm{cov}}$ is symmetric and an in-plane tensor [138]. In the special case of flat surfaces embedded in $\mathbb{R}^3$, the directional and covariant Hessian matrices are equal.

Tangential divergence operators

The divergence operator of a vector-valued function $\boldsymbol{v}(\boldsymbol{x}):\Gamma\to\mathbb{R}^3$ is given as

$$\mathrm{div}_{\Gamma}\boldsymbol{v}(\boldsymbol{x}) = \nabla_{\Gamma}^{\mathrm{dir}}\cdot\boldsymbol{v}(\boldsymbol{x}) = \mathrm{tr}\left(\nabla_{\Gamma}^{\mathrm{dir}}\boldsymbol{v}(\boldsymbol{x})\right) = \mathrm{tr}\left(\nabla_{\Gamma}^{\mathrm{cov}}\boldsymbol{v}(\boldsymbol{x})\right) \tag{2.24}$$

and the divergence of a matrix or tensor-valued function $\mathbf{A}(\boldsymbol{x}):\Gamma\to\mathbb{R}^{3\times3}$, is

$$\mathrm{div}_{\Gamma}\mathbf{A}(\boldsymbol{x}) = \begin{bmatrix}\mathrm{div}_{\Gamma}\left[A_{11},\ A_{12},\ A_{13}\right]\\ \mathrm{div}_{\Gamma}\left[A_{21},\ A_{22},\ A_{23}\right]\\ \mathrm{div}_{\Gamma}\left[A_{31},\ A_{32},\ A_{33}\right]\end{bmatrix}\ . \tag{2.25}$$

Note that $\mathrm{div}_{\Gamma}\mathbf{A}$ is, in general, not a tangential vector. It is only tangential if the surface is flat *and* $\mathbf{A}$ is an in-plane tensor.

Weingarten map and curvature

The Weingarten map is defined as [41], [90]

$$\mathbf{H} = \nabla_{\Gamma}^{\mathrm{dir}}\boldsymbol{n}_{\Gamma} = \nabla_{\Gamma}^{\mathrm{cov}}\boldsymbol{n}_{\Gamma} \tag{2.26}$$

and is related to the second fundamental form in differential geometry. The Weingarten map is a symmetric, in-plane tensor and its two non-zero eigenvalues are associated with the principal curvatures

$$\kappa_{1,2} = -\,\mathrm{eig}(\mathbf{H})\ . \tag{2.27}$$

The minus in Eq. 2.27 is due to fact that the Weingarten map is defined with the "outward" unit normal vector instead of the "inward" unit normal vector, which leads to positive curvatures of a sphere and is, in general, a matter of definition. The third eigenvalue is zero, because $\mathbf{H}$ is an in-plane tensor. The corresponding eigenvectors $\boldsymbol{t}_1$, $\boldsymbol{t}_2$ and $\boldsymbol{n}_\Gamma$ are perpendicular as $\mathbf{H}$ is symmetric. In Fig. 2.3, the osculating circles with the radii $r_i = {}^1\!/\!_{\kappa_i}$ and the eigenvectors at a point $\boldsymbol{P}$ are shown.

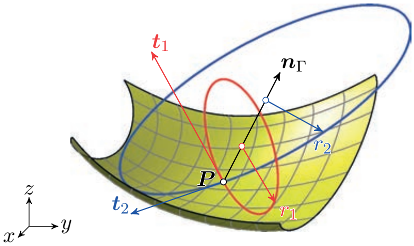

Fig. 2.3: Osculating circles (blue, red) and eigenvectors ($\boldsymbol{t}_1$, $\boldsymbol{t}_2$, $\boldsymbol{n}_\Gamma$) of $\mathbf{H}$ at point $\boldsymbol{P}$ on a surface embedded in $\mathbb{R}^3$.

The Gauß curvature is defined as the product of the principal curvatures $K = \prod_{i=1}^2 \kappa_i$ and the mean curvature is introduced as $\varkappa = \mathrm{tr}(\mathbf{H}) = -(\kappa_1 + \kappa_2)$.

Divergence theorems in terms of tangential operators

The divergence theorem or Green's formula for a scalar-valued function $f \in C^1(\Gamma)$ and a vector-valued function $\boldsymbol{v} \in C^1(\Gamma)^3$ are defined as in [39], [41]

$$\begin{aligned}\int_\Gamma f \,\mathrm{div}_\Gamma \boldsymbol{v} \;\mathrm{d}A = &-\int_\Gamma \nabla_\Gamma f \cdot \boldsymbol{v} \;\mathrm{d}A + \int_\Gamma \varkappa f \left(\boldsymbol{v} \cdot \boldsymbol{n}_\Gamma\right) \;\mathrm{d}A \\ &+ \int_{\partial\Gamma} f \boldsymbol{v} \cdot \boldsymbol{n}_{\partial\Gamma} \;\mathrm{d}s \;,\end{aligned} \tag{2.28}$$

where $C^1(\Gamma)$ is the space of functions on Γ which are at least once continuously differentiable. The term with the mean curvature $\varkappa$ is vanishing if the vector $\boldsymbol{v}$ is tangential, then $\boldsymbol{v} \cdot \boldsymbol{n}_\Gamma = 0$. In extension to Eq. 2.28, Green's formula for second-order tensor functions $\mathbf{A} \in C^1(\Gamma)^{3\times 3}$, is

$$\begin{aligned}\int_\Gamma \boldsymbol{v} \cdot \mathrm{div}_\Gamma \mathbf{A} \;\mathrm{d}A = &-\int_\Gamma \nabla_\Gamma^{\mathrm{dir}} \boldsymbol{v} : \mathbf{A} \;\mathrm{d}A + \int_\Gamma \varkappa \boldsymbol{v} \cdot \left(\mathbf{A} \cdot \boldsymbol{n}_\Gamma\right) \;\mathrm{d}A \\ &+ \int_{\partial\Gamma} \boldsymbol{v} \cdot \left(\mathbf{A} \cdot \boldsymbol{n}_{\partial\Gamma}\right) \;\mathrm{d}s \;,\end{aligned} \tag{2.29}$$

where $\nabla_\Gamma^{\mathrm{dir}} \boldsymbol{v} : \mathbf{A} = \mathrm{tr}(\nabla_\Gamma^{\mathrm{dir}} \boldsymbol{v} \cdot \mathbf{A}^\mathrm{T})$ and $:$ is the contraction operator. In the case of in-plane tensors, i.e., $\mathbf{A}_t = \mathbf{P} \cdot \mathbf{A}_t \cdot \mathbf{P}$, the term with the mean curvature $\varkappa$ vanishes due to $\mathbf{A}_t \cdot \boldsymbol{n}_\Gamma = \mathbf{0}$ and we also have $\nabla_\Gamma^{\mathrm{dir}} \boldsymbol{v} : \mathbf{A}_t = \nabla_\Gamma^{\mathrm{cov}} \boldsymbol{v} : \mathbf{A}_t$. In addition, a summary of product rules, useful relations and properties of important quantities which are employed in the following chapters, are presented in Appendix A.

3 Discretization and numerical methods for surface PDEs

Many challenging applications in engineering and natural sciences are characterized by physical phenomena taking place on curved surfaces in the physical space. The modelling of such phenomena naturally leads to boundary value problems (BVPs) where partial differential equations (PDEs) are formulated on manifolds. For the solution of such models, customized numerical methods are needed which discretize the continuous weak forms of the particular problem. In principle, there are two fundamentally different finite element approaches, i.e., the Surface FEM and the Trace FEM, which are outlined in the following. The key ingredients for both approaches are defined with emphasis on the numerical integration, stabilization and enforcement of essential boundary conditions. The two introduced finite element approaches are applied to a model problem to investigate the performance and the properties of the methods.

The major content of this chapter follows our own articles in [65], [129].

3.1 Surface FEM

The Surface FEM as described in [42], [52] is the classical approach for the approximation of BVPs on manifolds. It was first proposed by Dziuk [49] for heat flows on curved surfaces. In the approximation of shells and membranes, it became the standard approach [14], [30], [31], even, until the Trace FEM was recently proposed, the only available FEM-approach [28], [66], [129].

The starting point for the outline of the Surface FEM is a discretization of the domain of interest based on a surface mesh in $\mathbb{R}^3$, see Fig. 3.1(a), composed by (curved) two-dimensional finite elements. Each element implies a piecewise parametrization of the surface and is thus inherently linked to the classical definition of shell BVPs based on curvilinear coordinates.

In the following, the major ingredients of the Surface FEM are defined: (i) the test and trial function spaces, (ii) higher-order accurate quadrature of the weak form, and (iii) enforcement of essential boundary conditions.

3.1.1 Function spaces

As mentioned above, in the context of the Surface FEM, the domain is typically defined through an atlas of element-wise local maps. Let there exist a map $\boldsymbol{\chi}_T : \bar{T} \to T \cap \Gamma$

from the 2D reference element $\bar{T}$ to the physical element T with the properties $\boldsymbol{\chi}_T \in C^l(\bar{T}, \mathbb{R}^3)$, $\boldsymbol{\chi}$ is bijective and rank $\nabla\boldsymbol{\chi} = 2$ on $\bar{T}$. C^l is the space of l-times continuously differentiable functions. The map $\boldsymbol{\chi}_T$ is called a local parametrization and $\boldsymbol{\chi}_T^{-1}$ is labelled local chart. The set of all local parametrizations is denoted as τ_χ. The union of all local parametrizations leads to a C^l-atlas of element-wise local maps and defines $\Gamma := \cup_{\boldsymbol{\chi}\in\tau_\chi}\boldsymbol{\chi}$, see Fig. 3.1(a). The local maps are often defined as $\boldsymbol{\chi}_T(\boldsymbol{r}) := \sum_i N_i(\boldsymbol{r})\cdot\boldsymbol{x}_i,\ \boldsymbol{r} \in \bar{T}, \boldsymbol{x}_i \in T$ being nodal coordinates. Associated to the reference element, there is a fixed set of basis functions $\{N_i^k(\boldsymbol{r})\}$, with $i \in \hat{\omega} = \{1, \ldots, n_{\text{nodes}}\}$, where n_{nodes} are the number of nodes per element. The basis functions are the Lagrange basis functions, i.e., $N_i^k(\boldsymbol{r}_j) = \delta_{ij}$ and $N_i^k(\boldsymbol{r}) \in \mathbb{P}_{\text{tri}}^k(\bar{T})$ or $\mathbb{Q}^k(\bar{T})$, where $\mathbb{P}_{\text{tri}}^k\left(\bar{T}\right)$ is the polynomial basis in a triangular element and $\mathbb{Q}_k\left(\bar{T}\right)$ in a quadrilateral element, both being of complete order k. The set τ_Γ of all surface elements T defines the surface mesh $\Gamma^h := \cup_{T\in\tau_\Gamma}T$. The employed Lagrange basis functions are $C^\infty(\bar{T})$ inside the elements but only $C^0(\Gamma^h)$. Therefore, the discrete surface Γ^h is defined through a C^0-atlas, i.e., $\Gamma^h \in C^0$ across the element edges. Based on that, a general finite element space on Γ^h with the polynomial degree k is defined by

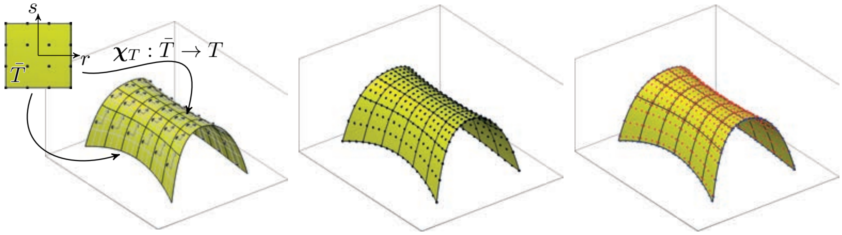

(a) atlas of local parametrizations **(b)** surface mesh and DOFs **(c)** integration points in the physical elements

Fig. 3.1: Example of a parametrized surface Γ^h: (a) Collection of local parametrizations $\boldsymbol{\chi}_T \in \tau_\chi$, (b) conforming surface mesh consisting of quadrilateral, cubic 2D Lagrange elements with black dots being the nodes, and (c) integration points for the Surface FEM obtained by standard Gauß-Legendre integration rules.

$$\mathcal{Q}_{\Gamma,h}^k = \left\{u^h \in C^0\left(\Gamma^h\right) \mid u^h \circ \boldsymbol{\chi}_T \in \mathbb{P}_{\text{tri}}^k\left(\bar{T}\right) \text{ or } \mathbb{Q}^k\left(\bar{T}\right), T \in \tau_\Gamma\right\} \subset \mathcal{H}^1(\Gamma^h), \tag{3.1}$$

where $\mathcal{H}^1$ is the Sobolev space of functions with square integrable first derivatives. In order to further specify the employed finite element functions, the connectivity of the mesh needs to be discussed. The nodes of the surface mesh are labelled as $j \in \omega = \{1, \ldots, n\}$ with n being the total number of nodes in the mesh. The set of elements T which share the same node j is labelled as τ_j and the corresponding reference node numbers are uniquely defined by $i = i(T, j) \in \hat{\omega}, T \in \tau_j, j \in \omega$. The nodal basis functions

$M_j^k(\boldsymbol{x})$ which span the function space $\mathcal{Q}_{\Gamma,h}^k$ are then defined as

$$M_j^k(\boldsymbol{x}) = \begin{cases} N_i^k(\boldsymbol{\chi}_T^{-1}(\boldsymbol{x})) & \text{for } \boldsymbol{x} \in T, T \in \tau_j, i = i(T,j) \\ 0 & \text{for } \boldsymbol{x} \in \Gamma^h \backslash \cup_{T \in \tau_j} T \end{cases} , j \in \omega \ . \tag{3.2}$$

Note that τ_j is the support of the shape function $M_j^k(\boldsymbol{x})$. Employing the same order k for the mapping $\boldsymbol{\chi}_T$ and the shape functions $M_j^k(\boldsymbol{x})$ leads to the well-known isoparametric concept and every function $u^h \in \mathcal{Q}_{\Gamma,h}^k$ takes the form

$$u^h(\boldsymbol{x}) = \sum_{j=1}^{n} M_j^k(\boldsymbol{x}) \hat{u}_j, \quad \boldsymbol{x} \in \Gamma^h, \hat{u}_j \in \mathbb{R} \ , \tag{3.3}$$

where $\hat{u}_j$ are the nodal values. Later on, in the analysis, the nodal values imply the degrees of freedom (DOFs) and are directly located at the nodes of the elements $T \in \Gamma^h$, see Fig. 3.1(b). For further information regarding the definition of higher-order surface finite element spaces, we refer to [42], [52], [93].

3.1.2 Higher-order accurate quadrature on parametrized surfaces

Secondly, for the higher-order accurate numerical integration of the discrete weak form in the Surface FEM, one may employ the same numerical integration schemes, e.g., Newton-Cotes, Gauß-Legendre, which are applied in standard 2D finite element applications, see, e.g., [144]. The only difference compared to the flat case results from the mapping $\boldsymbol{\chi}_T$. In particular, the integration points and weights are mapped from the 2D reference element $\bar{T}$ to the physical element T which is embedded in $\mathbb{R}^3$. In detail, the integration points in the reference element $\bar{\boldsymbol{x}}_{\mathrm{IP},i} \in \bar{T}$ are mapped to the physical element T with $\boldsymbol{x}_{\mathrm{IP},i} = \boldsymbol{\chi}_T(\bar{\boldsymbol{x}}_{\mathrm{IP},i}) \in T$, $i = 1, \ldots, n_Q$ being the number of integration points per element. The integration weights $\bar{w}_i$ are mapped with $\boldsymbol{w}_i = \bar{\boldsymbol{w}}_i \cdot \det(\mathbf{G}(\bar{\boldsymbol{x}}_{\mathrm{IP},i}))$, with $\mathbf{G} = \mathbf{J}^{\mathrm{T}} \cdot \mathbf{J}$ being the first fundamental form. In Fig. 3.1(c), the mapped integration points (red points) on the surface Γ^h and the integration points on the boundary (blue points) are visualized. For further details regarding the numerical integration of explicitly defined surfaces, we refer to, e.g., [144].

3.1.3 Essential boundary conditions

Lastly, in the Surface FEM, the essential boundary conditions may be, in principle, enforced in a strong sense by directly prescribing nodal values or in a weak sense by modifying the weak form with additional constraints. The major advantages of the strong enforcement are its simplicity in the implementation, consistency and robustness. On the other hand, one of the disadvantages is that the strong enforcement is limited to interpolatory shape functions and less complex boundary conditions. For instance, if the boundary conditions of a Kirchhoff plate or Kirchhoff-Love shell are to be strongly enforced and a standard displacement-based formulation is employed, it is only possible to directly prescribe the displacements, and the rotations along the possibly curved Dirichlet boundary are not accessible, in general. Furthermore, it is not possible to enforce rotated supports in a certain direction. Therefore, the strong enforcement of essential boundary conditions in the context of thin-walled structures is limited to simple cases. Enforcing the essential boundary conditions weakly overcomes this limitation, and all physically meaningful boundary conditions may be enforced. However, the implementational effort increases depending on the particular method and special attention regarding the stability and consistency is required. A detailed discussion of different strategies of weakly imposed essential boundary conditions is presented in Section 3.2.4 and a comparison of these different approaches is presented on a model problem in Section 3.3.2.

3.2 Trace FEM

The recently proposed Trace FEM [108], [110], [119] may be seen as a fictitious domain method for surface PDEs, where the domain of interest is completely immersed in a background domain $\Omega_{\mathrm{B}} \subset \mathbb{R}^3$. Usually, this approach is related to implicit surface definitions and a parametrization of Γ is neither available nor needed. In the context of thin-walled structures, the domain of interest is the implicitly defined mid-surface Γ. For examples of discretizations of surface PDEs with a trace finite element approach we refer to, e.g., [72], [74], [108]–[110], [119], [124], [129]. Just as for the Surface FEM, it remains to define for the Trace FEM, (i) the employed function spaces which are provided by the 3D background mesh and require stabilization, (ii) the integration of the weak form, and (iii) the enforcement of boundary conditions. The situation is closely related to general discussions of fictitious domain methods where stabilization, integration and enforcement of boundary conditions in the presence of cut elements also pose a major challenge for the successful realisation.

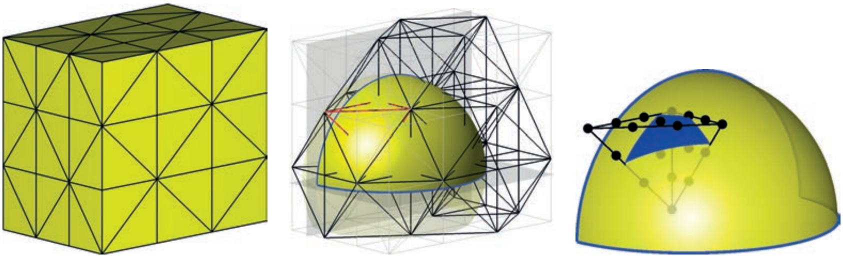

(a) background mesh Ω_{B} **(b)** active background mesh Ω_h^{Γ} **(c)** cut element T

Fig. 3.2: (a) Generic background mesh consisting of higher-order tetrahedral Lagrange elements which completely immerses the surface Γ, (b) active mesh consisting only of cut elements (black edges), and (c) degrees of freedom and intersection with the implicitly defined mid-surface (blue surface) for one specific active element.

3.2.1 Function spaces

Firstly, a background mesh Ω_B into which the domain of interest is completely immersed is generated, see Fig. 3.2(a). Without loss of generality, the mesh can be defined by a set τ_B of 3D elements and is not restricted to a certain element type. Herein, the background mesh consists of tetrahedral elements T of complete order $k \geq 1$. The background mesh is then defined by $\Omega_\mathrm{B} := \bigcup_{T \in \tau_\mathrm{B}} T \in C^0$.

The finite element function space of the background mesh Ω_B is implied by the three-dimensional elements rather than two-dimensional as for the Surface FEM. Associated to the reference element $\bar{T}$, there is a fixed set of basis functions $\{N_i^k(\boldsymbol{r})\}$, with $i = 1, \ldots, n_\mathrm{nodes}$ being the number of nodes per element. The shape functions are Lagrange basis functions, i.e., $N_i^k(\boldsymbol{r}_j) = \delta_{ij}$ and $N_i^k(\boldsymbol{r}) \in \mathbb{P}^k_\mathrm{tet}(\bar{T})$, where $\mathbb{P}^k_\mathrm{tet}(\bar{T})$ is the polynomial basis for 3D tetrahedral Lagrange elements of complete order k. With an atlas of element-wise local maps from the 3D reference element to the 3D physical elements $\boldsymbol{\chi}_T : \bar{T} \to T$, with $\boldsymbol{\chi}_T(\boldsymbol{r}) := \sum_i N_i^k(\boldsymbol{r})\boldsymbol{x}_i$, $\boldsymbol{r} \in \bar{T}$, $\boldsymbol{x}_i \in T$, where $\boldsymbol{x}_i$ are the nodal coordinates, a general finite element space is then defined as

$$\mathcal{Q}^k_{\Omega_\mathrm{B},h} := \left\{ v^h \in C^0(\Omega_\mathrm{B}) \mid v^h \circ \boldsymbol{\chi}_T \in \mathbb{P}^k_\mathrm{tet}\left(\bar{T}\right), T \in \tau_\mathrm{B} \right\} \subset \mathcal{H}^1(\Omega_\mathrm{B}) \, . \tag{3.4}$$

Analogously as above, this space is spanned by the nodal basis $\{M_j^k(\boldsymbol{x})\}$ with the shape functions of the 3D elements and employing the isoparametric concept, every function $v^h \in \mathcal{Q}^k_{\Omega_\mathrm{B},h}$ takes the form

$$v^h(\boldsymbol{x}) = \sum_{j=1}^{n} M_j^k(\boldsymbol{x})\hat{v}_j, \quad \boldsymbol{x} \in \Omega_\mathrm{B}, \hat{v}_j \in \mathbb{R} \, . \tag{3.5}$$

Next, the implicitly defined surface Γ is defined by a master level-set function ϕ plus additional slave level-set functions ψ_i for the boundary, see Section 2.1. The continuous level-set functions (ϕ, ψ_i) are interpolated by the shape functions $\{M_l^k(\boldsymbol{x})\}$ of the background mesh based on their nodal values, i.e., $\hat{\phi}_i = \phi(\boldsymbol{x}_i), \hat{\psi}_{j,i} = \psi_j(\boldsymbol{x}_i)$. This means that the level-set data is only needed at the nodes of the background mesh Ω_B. The discrete shell mid-surface Γ^h is then implied by ϕ^h and the discrete boundaries of the shell $\partial\Gamma^h$ may be defined either through the discrete slave level-set functions ψ_i^h or the boundary of the background mesh. In the following, the discrete boundary is only defined with additional slave level-set functions, otherwise the overall approach would be limited to a boundary conforming background mesh. The discrete normal vector $\boldsymbol{n}_\Gamma^h$ and the discrete local triad at the boundaries $(\boldsymbol{n}_\Gamma^h, \boldsymbol{n}_{\partial\Gamma}^h, \boldsymbol{t}_{\partial\Gamma}^h)$ are evaluated on the discrete zero-isosurface of ϕ^h. For the computation of the normal vector and local triads, one may employ the exact gradients of the level-set functions (ϕ, ψ_i) or, alternatively, the interpolated level-set functions (ϕ^h, ψ_i^h). Herein, the latter approach based on the interpolated level-set data is used, resulting in

$$\boldsymbol{n}_\Gamma^h(\boldsymbol{x}) = \frac{\nabla\phi^h(\boldsymbol{x})}{\|\nabla\phi^h(\boldsymbol{x})\|} \, , \; \boldsymbol{t}_{\partial\Gamma,i}^h(\boldsymbol{x}) = \frac{\nabla\psi_i^h(\boldsymbol{x}) \times \nabla\phi^h(\boldsymbol{x})}{\|\nabla\psi_i^h(\boldsymbol{x}) \times \nabla\phi^h(\boldsymbol{x})\|} \, , \; \boldsymbol{n}_{\partial\Gamma,i}^h = \boldsymbol{t}_{\partial\Gamma,i}^h(\boldsymbol{x}) \times \boldsymbol{n}_\Gamma^h(\boldsymbol{x}) \, , \tag{3.6}$$

where $\boldsymbol{x} \in \Gamma^h \cup \partial\Gamma^h$. The projectors $\mathbf{P}$ and $\mathbf{Q}$ are then computed by means of the discrete normal vector $\boldsymbol{n}^h_\Gamma$. Consequently, the gradients of (ϕ^h, ψ^h_i) are not exact and an additional source of error is added. However, the level-set functions are interpolated using quasi-uniform, higher-order background elements and it is shown in the numerical results in Section 5.3 and Section 6.3 that optimal convergence rates are achieved. Thus, the additional error caused by employing interpolated rather than exact level-set data is often acceptable.

The set of elements with a non-empty intersection with Γ^h is denoted by $\tau^\Gamma_{\Omega,h}$ and defines the active mesh $\Omega^\Gamma_h := \underset{T\in\tau^\Gamma_{\Omega,h}}{\cup} T \subset \Omega_B$, see Fig. 3.2(b). The definition of the active mesh is a crucial task, because the nodes of the *active* mesh imply the degrees of freedom (DOFs) in the numerical simulation. As an example, the nodes of the red element in Fig. 3.2(b) and the intersection with the zero-isosurface of the master level-set function are visualized in Fig. 3.2(c).

Lastly, the Trace FEM function space $\mathcal{T}_h$ is established by the restriction of a "higher-dimensional finite element space" of the *active* mesh Ω^Γ_h to the discrete zero-isosurface Γ^h. The finite element space of the active mesh $\mathcal{Q}^k_{\Omega^\Gamma_h}$ is defined in a similar manner as $\mathcal{Q}^k_{\Omega_\mathrm{B},h}$ in Eq. 3.4, but contains only *cut* background elements. A general Trace FEM function space $\mathcal{T}_h$ is then defined as

$$\mathcal{T}_h = \left\{ v^h \in \mathcal{Q}^k_{\Omega^\Gamma_h} \ : \ v^h|_{\Gamma^h} \in \mathcal{H}^1(\Gamma^h) \right\} \subset \mathcal{H}^1(\Omega^\Gamma_h) \ . \tag{3.7}$$

As mentioned above, the Trace FEM is a fictitious domain method and, compared to standard surface finite element approaches, see Section 3.1, three well-known challenges arise which are further outlined below: (i) integration of the weak form on the discrete zero-isosurface and its boundaries, (ii) stabilization of the stiffness matrix due to the restriction of the shape functions to the trace and small supports due to unfavourable cut scenarios and (iii) the enforcement of essential boundary conditions. In the following, these challenges are addressed in detail enabling a higher-order Trace FEM approach.

3.2.2 Higher-order accurate integration in cut background elements

The numerical integration of the domain of interest, i.e., the zero-isosurface of ϕ^h, is a non-trivial task, in particular with higher-order accuracy. Herein, we employ the integration strategy as outlined by the author and coworkers in [63]–[66]. An adoption of this approach in the context of finite cell methods and spline based boundary representations is reported in [134]. The advantages of this approach are an optimal higher-order accurate integration and a natural extension to multiple level-set functions. In this approach, the placement of the integration points on the discrete zero-isosurface is based on a higher-order accurate, recursive reconstruction in the cut *reference* element. That is, the surface is reconstructed by higher-order surface elements. It is important that the reconstructed surface elements are *only* used for the generation of integration points in the 3D reference element and may be interpreted as an integration cell. In Fig. 3.3, an overview of the procedure is illustrated. The yellow surface is the implicitly defined zero-isosurface of ϕ^h and is restricted by additional slave level-set functions ψ^h_i (green and purple surfaces). In Fig. 3.3(b), the cut scenario and integration points in the reference space of the red element from Fig. 3.3(a) are visualized. In Fig. 3.3(c), the integration points in the physical domain (red) and on the boundaries (blue) are shown. For further information and details, we refer to [63], [64].

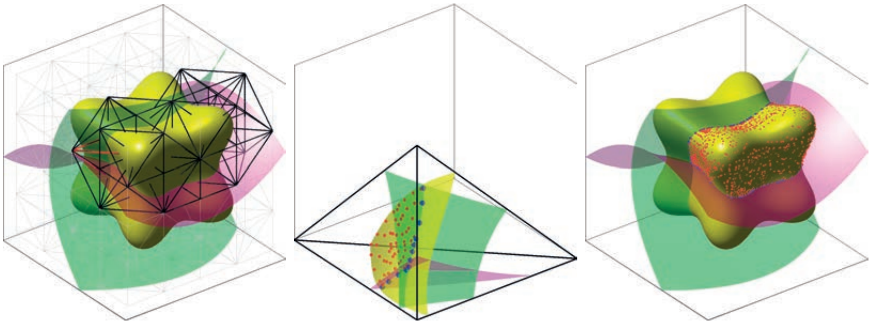

(a) active background elements **(b)** integration points in reference element **(c)** integration points in physical elements

Fig. 3.3: (a) Active, (black) elements in a background mesh are intersected by Γ^h, (b) integration points in one 3D reference element based on a (recursive) decomposition w.r.t. the master level-set function ϕ^h and further restriction to the slave level-set functions ψ_i^h, and (c) integration points in the physical domain (red points) and integration points on the boundary (blue points) $\partial\Gamma^h$.

Alternatively, a numerical integration scheme which is also suitable for higher-order is presented in [100]. The numerical integration is based on a higher-order accurate lift of a linear reconstruction of the zero-isosurface. However, the extension to multiple level-set functions, where the zero-isosurface of the master level-set function is restricted with additional slave level-set functions has not been addressed so far. A different approach which does not rely on decompositions is based on moment fitting and is presented for implicit surfaces in [102]. In a recent contribution this approach has been efficiently applied to non-linear 2D and 3D problems in [18].

3.2.3 Stabilization

Due to the restriction of the shape functions to the trace, see Eq. 3.7, the shape functions on the manifold only form a *frame*, which is, in general, not a *basis* [109], [119]. In Fig. 3.4, the consequences of the restriction to the trace of the manifold is visualized for a simple example: Let us consider a 1D manifold (blue line) embedded in three bilinear, quadrilateral 2D elements, see Fig. 3.4(a). Furthermore, a constant function on the manifold (black line) shall be interpolated based on the nodal values of the active background mesh. As shown in Fig. 3.4(b), the choice of the nodal values in order to interpolate the function on the manifold is not unique. In particular, three different configurations, which share the same values on the manifold are visualized. Therefore,

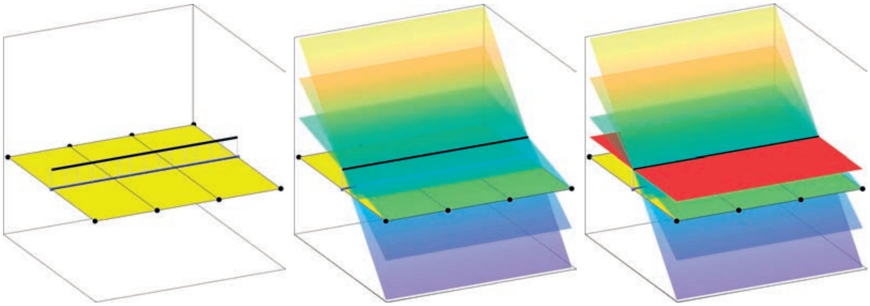

(a) overview **(b)** interpolation **(c)** stabilization

Fig. 3.4: Background meshes do not uniquely define a (constant) function on the zero level-set: (a) The black line is a constant, scalar-valued function on the manifold (blue line), which is embedded in three, bi-linear quadrilateral background elements, (b) different possibilities for the interpolation of the function on the manifold (trace), and (c) the stabilization adds a constraint in normal direction of the manifold resulting in a unique interpolation (red surface).

a suitable stabilization term needs to be added to the discrete weak form, otherwise the obtained linear system of equations does not have a unique solution w.r.t. the nodal values. In addition to the restriction, depending on unfavourable cut scenarios of cut background elements, unbounded small contributions to the stiffness matrix may occur, which causes an ill-conditioned system of linear equations.

The used stabilization technique addresses both issues and is introduced for scalar-valued problems in [26], [73]. This stabilization technique is called "normal derivative volume stabilization". In [74], [107], the stabilization is applied to vector-valued problems. The stabilization term added to each unknown field in the discrete weak form is

$$s_h(\boldsymbol{u}^h, \boldsymbol{v}^h) := \rho \int_{\Omega_h^\Gamma} \left(\nabla \boldsymbol{u}^h \cdot \boldsymbol{n}_\Gamma^{e,h} \right) \cdot \left(\nabla \boldsymbol{v}^h \cdot \boldsymbol{n}_\Gamma^{e,h} \right) \, \mathrm{d}V \ , \tag{3.8}$$

where $\boldsymbol{n}_\Gamma^{e,h}(\boldsymbol{x}) = \frac{\nabla \phi^h(\boldsymbol{x})}{\|\nabla \phi^h(\boldsymbol{x})\|}, \boldsymbol{x} \in \Omega_h^\Gamma$ is a sufficiently smooth extension of the normal vector $\boldsymbol{n}_\Gamma^h$ at the zero-isosurface of ϕ^h. It is noteworthy, that the integral is performed over the whole active background mesh and is not restricted to the trace. However, the integrand is sufficiently smooth and, therefore, a standard numerical integration scheme w.r.t. the *active* elements is applicable, i.e., a standard 3D Gauß-Legendre rule. By adding this constraint to the linear system of equations, the resulting system features a unique solution, see Fig. 3.4(c). It is recommended in [73] that the stabilization parameter shall be chosen within the following range

$$h \lesssim \rho \lesssim h^{-1} \ , \tag{3.9}$$

where h is the element size of the elements in the active mesh. This stabilization technique is suitable for higher-order shape functions, does not change the sparsity pattern of the stiffness matrix, and only first-order derivatives are needed. In addition, the implementation is straightforward and the choice of the stabilization parameter is rather flexible. Other stabilization techniques are presented in [26], [109]. A recent approach where two stabilization techniques, i.e., face stabilization of the cut elements and the normal derivative stabilization on the zero-isosurface, are combined is presented in [98].

3.2.4 Essential boundary conditions

As outlined in [66], the enforcement of essential boundary conditions is a challenging task in FDMs and, hence also in the Trace FEM, due to the fact that it is not possible to directly prescribe nodal values of the active background elements. The situation in the case of shells may be quite delicate due to complex boundary conditions, e.g., membrane support, symmetry support, clamped edges, etc., and, therefore, the treatment of boundary conditions requires special attention.

A popular strategy for weakly enforcing essential boundary conditions is the penalty method [6]. The main advantages of the penalty method are the built-in linear independence of the constraints which maintains the positive definiteness of the stiffness matrix and the straightforward implementation. On the other hand, the overall approach is variationally inconsistent and suffers from the interplay between the accuracy and violation of the constraint conditions, in particular if optimal higher-order convergence rates are desired. In addition, the conditioning of the stiffness matrix may cause further complications. One alternative is the Lagrange multiplier method [5], [23], [144]. Although the Lagrange multipliers are variationally consistent, additional degrees of freedom are introduced and the well posedness of the augmented system of equations is not guaranteed. Furthermore, in the context of fictitious domain methods (FDMs) the discretization of the Lagrange multiplier fields may become a cumbersome task depending on the cut scenarios.

As an alternative approach, Nitsche's method [104] has been developed to be a standard choice in FDMs because Nitsche's method is variationally consistent, suitable for higher-order and does not require the discretization of auxiliary fields. The original approach from [104] has been adopted to various applications for enforcing essential boundary conditions, see, e.g., [11], [57], [59], [66], [80], [120], [129] and coupling, see, e.g., [1], [77], [78], [121]. In principal, there are two different versions of Nitsche's method. The symmetric version of Nitsche's method requires an additional stabilization to ensure positive definiteness [59]. The choice of the stabilization parameter is rather crucial because if it is too large, the overall approach degenerates to a penalty method and, otherwise, the stability is lost [35], [78]. In contrast, the non-symmetric version of Nitsche's method does not require an additional stabilization term for imposing boundary conditions [20], [76], [78]. The weak points of the non-symmetric version are that the resulting system of equations is not symmetric and the theoretical error estimates in the L^2-norm of the primal variables are suboptimal [3], [20]. Nevertheless, we prefer the non-symmetric version of Nitsche's method because the obtained results are, in fact, optimal (also in the L^2-norm similar to the results in [20], [121]) and the absence of an additional stabilization term compared to the symmetric Nitsche method is very beneficial. It is noted that, a direct solver is employed herein, and, therefore, the non-symmetry of the system of equations does not pose any problems. A detailed comparison of these different approaches is presented for a model problem in Section 3.3.2.

3.3 Comparison of Surface FEM and Trace FEM

In this section, the above introduced finite element approaches, i.e., Surface FEM and Trace FEM, are compared based on a simple model problem: the Poisson's equation on surfaces [49], [65]. In particular, the accuracy of the numerical integration, accuracy w.r.t. degrees of freedom, convergence behaviour and the treatment of essential boundary conditions is elaborated in detail.

The complete boundary value problem in strong form for the Poisson equation, formulated in the frame of the TDC, on a surface Γ embedded in $\mathbb{R}^3$ states that we seek $u : \Gamma \to \mathbb{R}$ such that:

$$\begin{aligned} -\Delta_\Gamma u &= f \quad \text{on} \quad \Gamma, && (3.10a)\\ u|_{\partial\Gamma_\mathrm{D}} &= \hat{g} \quad \text{on} \quad \partial\Gamma_\mathrm{D}, && (3.10b)\\ \boldsymbol{n}_{\partial\Gamma} \cdot \nabla_\Gamma u|_{\partial\Gamma_\mathrm{N}} &= \hat{t} \quad \text{on} \quad \partial\Gamma_\mathrm{N}, && (3.10c)\end{aligned}$$

where $\Delta_\Gamma u = \mathrm{div}_\Gamma(\nabla_\Gamma u)$ and $f \in L^2(\Gamma)$ is a source function. In case of bounded surfaces, the boundary $\partial\Gamma$ is divided into two non-overlapping parts, i.e., the Dirichlet boundary $\partial\Gamma_\mathrm{D}$ and the Neumann boundary $\partial\Gamma_\mathrm{N}$. For a closed (compact) manifold, where no boundary exists, one needs an additional condition for the problem to be well-posed. Therefore, typically the zero mean constraint is imposed,

$$\int_\Gamma u \, \mathrm{d}s = 0. \tag{3.11}$$

In the classical approach, employing curvilinear coordinates, the Laplace-Beltrami operator is defined as [52]

$$\Delta_\Gamma u(\boldsymbol{\chi}(\boldsymbol{r})) = \frac{1}{\sqrt{\det(\mathbf{G}(\boldsymbol{r}))}} \sum_{i,j=1}^{2} \frac{\partial}{\partial r_j} \left(G^{ij}(\boldsymbol{r}) \sqrt{\det(\mathbf{G}(\boldsymbol{r}))} \, \frac{\partial u}{\partial r_i}(\boldsymbol{r}) \right) , \tag{3.12}$$

where $\boldsymbol{r} = [r_1, r_2]^\mathrm{T}$ are coordinates in the parameter space, $\mathbf{G}$ is the first fundamental form, see Section 2.2.2 and G^{ij} is the contravariant form of $\mathbf{G} = [G_{ij}]$ with $[G^{ij}] = \mathbf{G}^{-1}$. It is readily seen that this definition in the classical approach is *only* applicable to explicitly defined surfaces where a parametrization is available. In addition, the contravariant entries of the first fundamental form are needed explicitly. Despite the restriction to parametrized surfaces the overall notation appears to be more cumbersome in comparison to the equivalent operators in the frame of the TDC, see Section 2.2.2. Following this rationale, the formulation of the surface operators in curvilinear coordinates does not provide concrete advantages and, therefore, only the formulation in the frame of the TDC is employed herein.

The strong form is converted to the weak form employing the Galerkin-Bubnov method. In detail, Eq. 3.10a is multiplied with a suitable test function v, which will be specified below, and integrated over the domain Γ. Employing Eq. 2.28, the continuous weak form of the Poisson problem is achieved: Find $u \in \mathcal{V}_g$ such that

$$\int_\Gamma \nabla_\Gamma v \cdot \nabla_\Gamma u \, \mathrm{d}A = \int_\Gamma v f \, \mathrm{d}A + \int_{\partial\Gamma_\mathrm{N}} v \hat{t} \, \mathrm{d}s \qquad \forall v \in \mathcal{V}_0 \ , \tag{3.13}$$

with

$$\mathcal{V}_g = \left\{ u \in \mathcal{H}^1(\Gamma) \ : \ u|_{\partial\Gamma_\mathrm{D}} = \hat{g} \right\} , \tag{3.14}$$

$$\mathcal{V}_0 = \left\{ v \in \mathcal{H}^1(\Gamma) \ : \ v|_{\partial\Gamma_\mathrm{D}} = 0 \right\} \qquad \text{for manifolds with boundary,} \tag{3.15}$$

$$\mathcal{V}_0 = \left\{ v \in \mathcal{H}^1(\Gamma) \ : \ \int_\Gamma v \, \mathrm{d}s = 0 \right\} \qquad \text{for closed manifolds.} \tag{3.16}$$

The existence and uniqueness of the solution of the BVP is shown in [25], [52]. In case of compact manifolds, the zero mean constraint is enforced by a Lagrange multiplier.

In the following, the continuous weak form is discretized with the Surface and the Trace FEM. For the comparison of the two finite element approaches, two numerical experiments are performed. In detail, in the convergence analyses, the following error measures are employed

$$\varepsilon_\Gamma := \frac{\left| \int_{\Gamma^h} 1 \mathrm{d}A - \int_\Gamma 1 \mathrm{d}A \right|}{\int_\Gamma 1 \mathrm{d}A} \qquad \ldots \quad \text{area error} \ , \tag{3.17}$$

$$\varepsilon_{\partial\Gamma_\mathrm{D}} := \frac{\left| \int_{\partial\Gamma^h_\mathrm{D}} 1 \mathrm{d}s - \int_{\partial\Gamma_\mathrm{D}} 1 \mathrm{d}s \right|}{\int_{\partial\Gamma_\mathrm{D}} 1 \mathrm{d}s} \qquad \ldots \quad \text{boundary error} \ , \tag{3.18}$$

$$\varepsilon^2_{L^2} := \frac{\int_{\Gamma^h} (u^h - u_\mathrm{ex})^2 \, \mathrm{d}A}{\int_{\Gamma^h} u^2_\mathrm{ex} \, \mathrm{d}A} \qquad \ldots \quad L^2\text{-error} \ , \tag{3.19}$$

$$\varepsilon^2_{H^1} := \frac{\int_{\Gamma^h} (u^h - u_\mathrm{ex})^2 + \sum_{i=1}^3 \left(\partial_i^\Gamma u^h - \partial_i^\Gamma u_\mathrm{ex} \right)^2 \, \mathrm{d}A}{\int_{\Gamma^h} u^2 + \sum_{i=1}^3 (\partial_i^\Gamma u_\mathrm{ex})^2 \, \mathrm{d}A} \qquad \ldots \quad H^1\text{-error} \ , \tag{3.20}$$

$$\varepsilon^2_\mathrm{res} := \sum_{T \in \tau} \frac{\int_T \left(\Delta_\Gamma u^h + f \right)^2 \, \mathrm{d}A}{\int_T f^2 \, \mathrm{d}A} \qquad \ldots \quad \text{residual error} \ , \tag{3.21}$$

$$\varepsilon^2_{L^2, \partial\Gamma^h_\mathrm{D}} := \frac{\int_{\partial\Gamma^h_\mathrm{D}} (u^h - \hat{g})^2 \, \mathrm{d}s}{\int_{\partial\Gamma^h_\mathrm{D}} \hat{g}^2 \, \mathrm{d}s} \qquad \ldots \quad \text{error in DirBCs} \ , \tag{3.22}$$

where the subscript “ex” indicates the analytical (exact) solution. The first two error measures, i.e., Eqs. 3.17 and 3.18, are the integration error w.r.t. the surface and Dirichlet boundary. Eqs. 3.19 and 3.20, are the classical relative L^2- and H^1-errors with the experimental orders of convergence (EOC) $\mathcal{O}(p+1)$ and $\mathcal{O}(p)$, where p is the polynomial order of the trial and test functions w.r.t. the element size h. Next, Eq. 3.21 is the residual error, which measures the summed element-wise L^2-error in the strong form. It is noteworthy, that for the evaluation of the residual error of the Poisson equation, second-order derivatives are required. Therefore, only convergence of higher-order elements with $p \geq 2$ can be expected and the EOC is $\mathcal{O}(p-1)$. However, this error measure enables a rigorous verification of the proposed approach and only requires a sufficiently smooth solution. The concept of residual errors may be particularly useful in situations where an analytical solution is not available, for instance in case of complex geometries or when more challenging PDEs are considered so that analytical solutions are hardly available, see, e.g., [62], [66], [125], [127], [129]. Lastly, in Eq. 3.22, the L^2-error in the Dirichlet boundary conditions (DirBCs) is computed. This error measure may be interesting when different methods of weak enforcement of essential boundary conditions are compared.

3.3.1 Example 1: Compact manifold

In the first example the Poisson equation is solved on a full torus, i.e., compact manifold, and is taken from [26], [72]. The problem is defined in Fig. 3.5. The yellow surface is the torus and is denoted by Γ which is either defined by a parametrization $\boldsymbol{x}(\phi, \theta) : \hat{\Omega} \to \Gamma$ or implicitly by the zero-isosurface of ϕ, i.e., $\Gamma = \{\boldsymbol{x} \in \mathbb{R}^3 : \phi(\boldsymbol{x}) = 0\}$. The analytical solution u_{ex} satisfies the zero mean constraint and the source term f is determined by the method of manufactured solution.

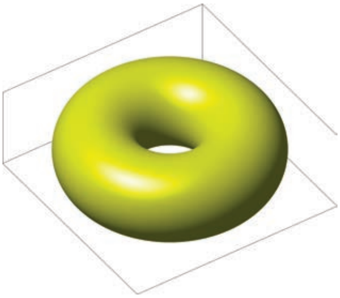

Geometry: Torus

$$\boldsymbol{x}(\phi, \theta) = R \begin{bmatrix} \cos(\phi) \\ \sin(\phi) \\ 0 \end{bmatrix} + r \begin{bmatrix} \cos(\phi)\cos(\theta) \\ \sin(\phi)\cos(\theta) \\ \sin(\theta) \end{bmatrix}$$

$$\phi(\boldsymbol{x}) = \sqrt{\left(\sqrt{x^2+y^2} - R\right)^2 + z^2} - r$$

$R = 1, \; r = 0.6$

$(\phi, \theta) \in [0, 2\pi)^2$ are torus coordinates

Analytical solution: $u_{\mathrm{ex}}(\boldsymbol{x}) = (\sin(3\phi)\cos(3\theta + \phi))$

Source term:

$$\begin{aligned} f(\boldsymbol{x}) = r^{-2}&(9\sin(3\phi)\cos(3\theta+\phi) + (R + r\cos(\theta))^{-2} \\ &(10\sin(3\phi)\cos(3\theta+\phi) + 6\cos(3\phi)\sin(3\theta+\phi)) \\ &+ (r(R + r\cos(\theta)))^{-1}(3\sin(\theta)\sin(3\phi)\sin(3\theta+\phi)) \\ &+ u_{\mathrm{ex}}(\boldsymbol{x}(\phi, \theta)) \end{aligned}$$

Fig. 3.5: Definition of the torus problem.

The discrete weak form of the Poisson equation, see Eq. 3.13, with the Surface FEM, employing the explicit geometry definition, where the discrete surface Γ^h is defined by an atlas of element-wise local maps $\boldsymbol{\chi}_T$, reads as follows: Given source term f on Γ^h, find $u^h \in \mathcal{S}^h_{S,u}$ such that for all test functions $v^h \in \mathcal{V}^h_{S,u}$ there holds in $\Gamma^h := \cup_{\boldsymbol{\chi} \in \tau_\chi} \boldsymbol{\chi}$

$$\int_{\Gamma^h} \nabla_\Gamma v^h \cdot \nabla_\Gamma u^h \, \mathrm{d}A = \int_{\Gamma^h} v^h f \, \mathrm{d}A \; , \tag{3.23}$$

with $\mathcal{S}^h_{S,u} = \{u^h \in \mathcal{Q}^k_{\Gamma,h} : \int_{\Gamma^h} u^h \, \mathrm{d}A = 0\}$ and $\mathcal{V}^h_{S,u} = \mathcal{S}^h_{S,u}$.

The discrete weak form of the same problem with the Trace FEM approach employing the implicitly defined geometry reads as follows: Given stabilization parameter $\rho \in \mathbb{R}^+$ and source term f on Γ^h, find the solution $u^h \in \mathcal{S}^h_{T,u}$ such that for all test functions

$v^h \in \mathcal{V}^h_{T,u}$ there holds in $\Gamma^h := \{\boldsymbol{x} \in \mathbb{R}^3 : \phi^h(\boldsymbol{x}) = 0\}$

$$\int_{\Gamma^h} \nabla_\Gamma v^h \cdot \nabla_\Gamma u^h \, \mathrm{d}A + \rho \int_{\Omega^\Gamma_h} \left(\nabla u^h \cdot \boldsymbol{n}^{e,h}_\Gamma\right) \left(\nabla v^h \cdot \boldsymbol{n}^{e,h}_\Gamma\right) \, \mathrm{d}V = \int_{\Gamma^h} v^h f \, \mathrm{d}A \,, \tag{3.24}$$

with $\mathcal{S}^h_{T,u} = \{u^h \in \mathcal{T}_h : \int_{\Gamma^h} u^h \, \mathrm{d}A = 0\}$ and $\mathcal{V}^h_{T,u} = \mathcal{S}^h_{T,u}$.

The focus of the first test case is a comparison on the accuracy of the numerical integration w.r.t. the element size h which is proportional to an element scale factor $h \sim {}^1\!/\!_n$ and number of integration points n_Q. The convergence is investigated in the error norms: (i) ε_{L^2}, (ii) ε_{H^1}, and (iii) $\varepsilon_{\mathrm{res}}$. In the numerical studies, the element scale factor n is varied between $4 \leq n \leq 128$ and the orders p are varied as $1 \leq p \leq 6$ for the Surface FEM and the Trace FEM, respectively. The stabilization parameter ρ in the Trace FEM is set to $\rho = {}^1\!/\!_h$ for all presented results.

In Fig. 3.6, surface meshes consisting of quadrilateral, third-order Lagrange elements with different element scale factors n are illustrated as an example. The black lines on the surface indicate the element boundaries and the black dots are the nodes. In Fig. 3.7, the background meshes (grey coloured elements) and the active meshes, i.e., only cut elements, for the Trace FEM are illustrated for different element scale factors n. In particular, the meshes in Fig. 3.7 are consisting of third-order tetrahedral Lagrange elements. The yellow surface indicates the discrete zero-isosurface of ϕ^h. For a better visualization, the nodes of the active mesh are omitted for the finer levels of refinement. In Fig. 3.8, the numerical solutions with both finite element approaches are presented for two specific meshes. The colours on the surface indicate the approximate solution of the problem. In Fig. 3.8(b), only the active mesh is visualized.

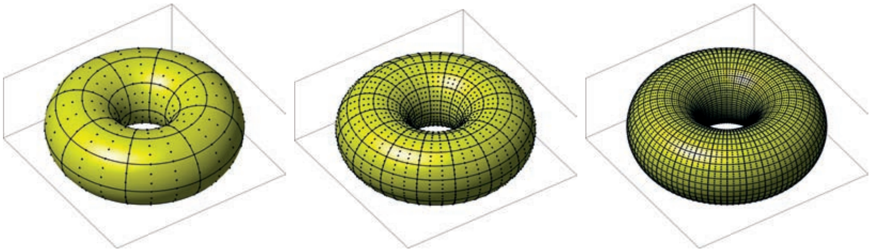

(a) $n = 8$ **(b)** $n = 16$ **(c)** $n = 32$

Fig. 3.6: Surface meshes, which are used in the Surface FEM, consisting of higher-order Lagrange elements. As an example, third-order quadrilateral elements with different element scale factors: (a) $n = 8$, (b) $n = 16$, and (c) $n = 32$ are shown.

Firstly, the total number of elements n_{Elem} and the total number of integration points n_Q w.r.t. element size ${}^1\!/\!_n$ and the ansatz orders p are compared in Fig. 3.9. A direct comparison of the surface meshes and the active meshes for the Trace FEM reveal that for this particular geometry the number of elements and integrations points is approximately one order of magnitude higher for the Trace FEM than for the Surface FEM. However,

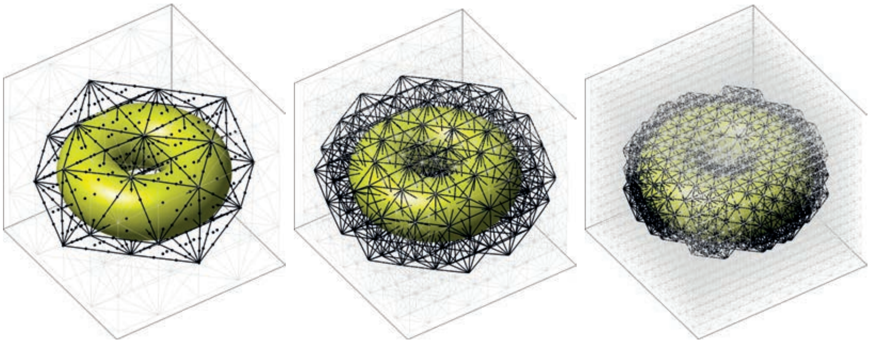

(a) $n = 4$ **(b)** $n = 8$ **(c)** $n = 16$

Fig. 3.7: Background and active meshes, which are used in the Trace FEM, consisting of higher-order tetrahedral Lagrange elements. As an example, cubic elements with different element scale factors: (a) $n = 4$, (b) $n = 8$, and (c) $n = 16$ are shown.

it can be seen that for both approaches the number of elements and integrations points increase with quadratic order, which is as expected when surfaces embedded in the physical space are considered. The number of integration points n_Q w.r.t. the order p behaves in the Trace FEM analogously to the Surface FEM where, for each order, the number of integration points increases by a certain factor. Note that the total number of elements n_{Elem} (black dotted line) is independent of the polynomial order p. In conclusion, the possible recursive refinement in case of complex cut scenarios, which causes additional integration points, does not increase the expected order. Therefore, both approaches behave asymptotically equally in terms of number of active elements and number of integration points.

Secondly, the accuracy of the numerical area integration is elaborated. Therefore, the relative integration error as defined in Eq. 3.17 is computed. The exact area of the torus is given with $A_{\text{ex}} = \int_\Gamma 1 \, \mathrm{d}A = 4\pi^2 r R$. In Fig. 3.10, the accuracy of the numerical integration for the explicitly and implicitly defined geometry is illustrated. In Fig. 3.10(a) and Fig. 3.10(b), the integration error for the explicit and implicit situation as a function of the element size $1/n$ is presented. The thin, dotted lines indicate the theoretical optimal order of converge $\mathcal{O}(p + 1)$ which is achieved for both situations and all orders p. As shown in Fig. 3.9, the number of integration points for the implicit geometry definition w.r.t. element size $1/n$ is higher than the explicit geometry definition. Nevertheless, the integration error w.r.t. n_Q is lower when surface meshes are employed, as seen in Fig. 3.10(c). However, the computed results are excellent and optimal convergence rates are achieved for both, explicit and implicit geometries, which is a crucial factor when higher-order convergence rates are desired.

Next, the convergence in the above defined error norms, i.e., ε_{L^2}, ε_{H^1}, ε_{res} are shown in Fig. 3.11 for the Surface FEM approach and in Fig. 3.12 for the Trace FEM approach, both w.r.t. element size $1/n$. It can be concluded that in all considered error norms, the optimal orders of convergence are achieved. Note that in the residual errors,

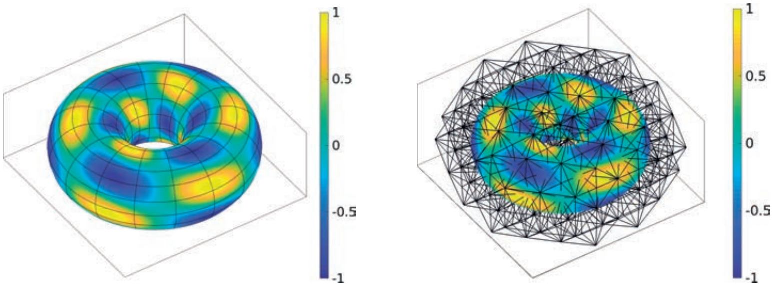

(a) Surface FEM **(b)** Trace FEM

Fig. 3.8: Numerical solution u^h of the torus problem. (a) u^h obtained with the Surface FEM with $n = 16, p = 3$, and (b) u^h obtained with the Trace FEM with $n = 8, p = 3$.

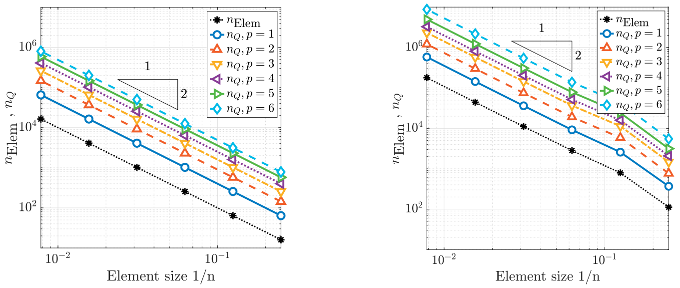

(a) surface meshes **(b)** active meshes

Fig. 3.9: Total number of elements n_{nElem} and integration points n_Q: (a) Surface meshes which are employed in the Surface FEM, and (b) active meshes which are used in the Trace FEM.

see Fig. 3.11(c) and Fig. 3.12(c), a convergence order of $\mathcal{O}(p-1)$ is expected. Therefore, it is not surprising that the linear elements do not converge in this error measure. Nevertheless, the higher orders $p \geq 2$ converge with optimal order.

Lastly, the error per degree of freedom is compared between the Surface and Trace FEM. Although optimal convergence rates are achieved in all error norms w.r.t. element size $^1/_n$, it can be seen in Fig. 3.13 that the efficiency w.r.t. the number of DOFs n_{DOF} is higher for the Surface FEM than for Trace FEM. The same phenomena has also been observed for the numerical integration w.r.t. n_Q, see Fig. 3.10(c).

Summarising the obtained results for the torus problem, it can be concluded that the performances of the Surface FEM and the Trace FEM are excellent and optimal convergence rates are achieved in all error norms and for all orders. In the direct comparison of the two approaches, the Surface FEM is more accurate w.r.t. n_Q and n_{DOF} than the Trace FEM. However, in the Surface FEM, the construction of a conforming higher-order accurate surface mesh is, in general, not a trivial task and may be seen as a drawback

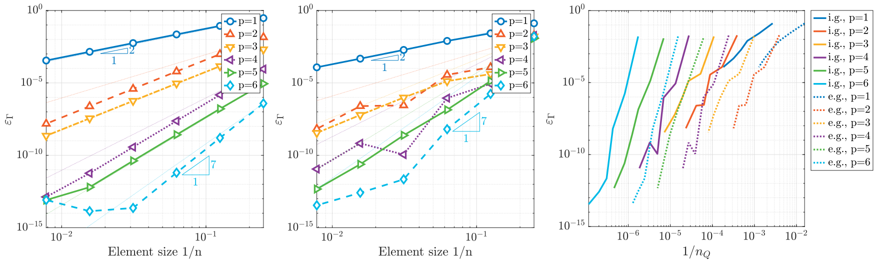

(a) explicit geometry (e.g.) **(b)** implicit geomery (i.g.) **(c)** accuarcy per integration point

Fig. 3.10: Accuracy of the numerical integration of the torus surface. (a) Explicitly defined discrete surface, (b) discrete zero-isosurface of ϕ^h w.r.t. element size $^1/_n$, and (c) efficency of the numerical integration w.r.t. total number of integration points $^1/_{n_Q}$.

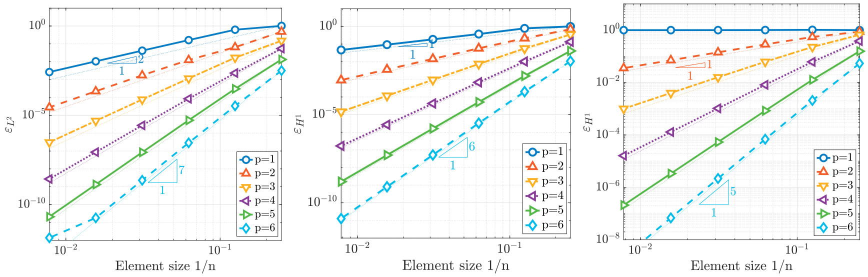

(a) L^2-error **(b)** H^1-error **(c)** residual error

Fig. 3.11: Results of the convergence analyses employing the Surface FEM approach.

of the Surface FEM, especially if the domain is moving or the topology of the surface changes. The Trace FEM is a FDM and, therefore, meshing comes without extra costs as simple, often structured background meshes may be employed. Although the accuracy per DOF is less than in the Surface FEM, the convergence orders are still optimal. From an implementational point of view, one major drawback might be that the higher-order accurate integration of the discrete weak form is more challenging compared to the Surface FEM, but with the approach sketched in Section 3.2.2, a completely automatic, robust procedure for higher-order accurate integration of (bounded) zero-isosurfaces is available. Furthermore, the employed stabilization technique is straightforward in the implementation and is suitable for higher-order. Lastly, the treatment of essential boundary conditions shall be elaborated in the following example.

3.3.2 Example 2: Bounded manifold

In the second example a hyperbolic surface with bumps is considered and is taken from [65]. The problem is defined in Fig. 3.14 and in contrast to the first test case, a bounded

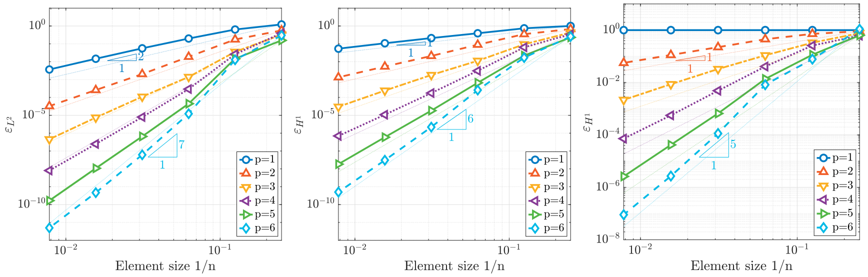

(a) L^2-error **(b)** H^1-error **(c)** residual error

Fig. 3.12: Results of the convergence analyses employing the Trace FEM approach.

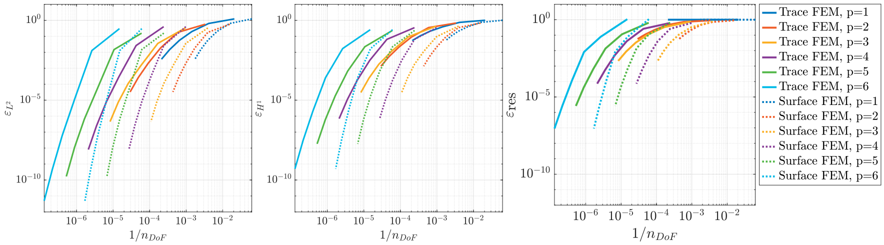

(a) L^2-error **(b)** H^1-error **(c)** residual error

Fig. 3.13: Error norms ε_{L^2}, ε_{H^1}, ε_{res} for both Surface and Trace FEM w.r.t. the total number of DOFs.

surface is considered. The source term is again computed by the method of manufactured solutions. The domain for the Surface FEM is explicity defined by a map $\boldsymbol{x}(\boldsymbol{r}) : \hat{\Omega} \rightarrow \Gamma$ and for the Trace FEM the domain is implicitly defined by means of multiple level-set functions $\Gamma = \{\boldsymbol{x} \in \mathbb{R}^3 : \phi(\boldsymbol{x}) = 0 \wedge \psi_i(\boldsymbol{x}) > 0\}$ with $i \in \{1, \ldots, 4\}$.

The focus in this example is on a comparison of the treatment of essential boundary conditions with the Surface and Trace FEM. In Section 3.2.4, different methods for the enforcement of essential boundary conditions are outlined. In the following, these different approaches: (1) strong enforcement (via nodal values), (2) Lagrange multiplier, (3) penalty method, (4) symmetric version of Nitsche's method and (5) non-symmetric version of Nitsche's method are employed in the Surface and Trace FEM. Each of these approaches yield different discrete weak forms in the Surface and Trace FEM. Note that the strong enforcement and the Lagrange multiplier method is exclusively used in the Surface FEM as they are not (straightforwardly) applicable to the Trace FEM.

Analogously to above, the convergence analyses are performed with a varying element scale factor n between $4 \leq n \leq 128$ and the order is varied as $1 \leq p \leq 6$. Furthermore, the stabilization parameter ρ for the Trace FEM is set to $\rho = {}^{1}/_{h}$. This set of parameters is applied to all discrete weak forms below. As error measures, the error norms from

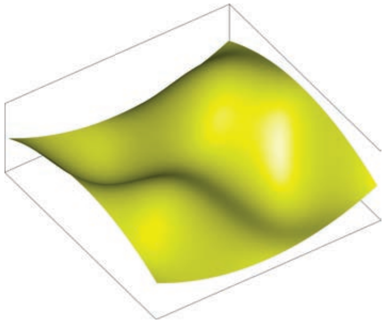

Geometry: Hyperbolic surface with bumps

$$\boldsymbol{x}(r,s) = \begin{bmatrix} r \\ s \\ t(r,s) \end{bmatrix}$$

$$t(r,s) = 0.5(r^2 - s^2) + 0.15\sin(2\pi r)\sin(2\pi s)$$

$$(r,s) \in [-0.5, 0.5]^2$$

$$\phi(\boldsymbol{x}) = t(x,y) - z$$

$$\psi_1(\boldsymbol{x}) = 0.5 - x,\ \ \psi_2(\boldsymbol{x}) = x - 0.5$$

$$\psi_3(\boldsymbol{x}) = 0.5 - y,\ \ \psi_4(\boldsymbol{x}) = y - 0.5$$

Analytical solution: $u_{\text{ex}}(\boldsymbol{x}) = \sin\left[\pi\,(x - 0.5)\right]\sin\left[\pi\,(y - 0.5)\right]$

Fig. 3.14: Definition of the hyperbolic surface with bumps problem.

Eq. 3.17 to Eq. 3.22 are computed, yet only the most meaningful results are presented here.

In Fig. 3.15, the numerical solutions according to the Surface and Trace FEM are illustrated for two specific meshes. The boundary conditions are enforced weakly with non-symmetric version of Nitsche's method, see Section 3.3.2.4. Similar as above, the colours on the surface indicate the approximate solution of the problem.

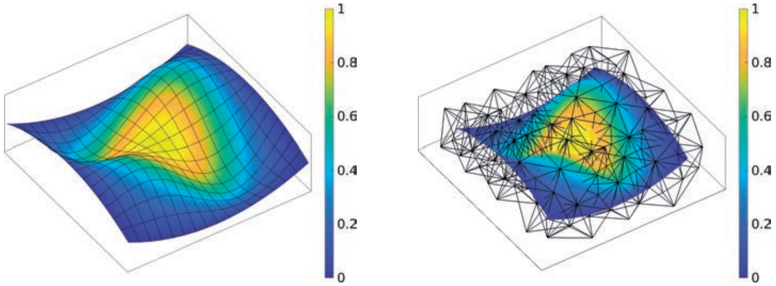

(a) Surface FEM **(b)** Trace FEM

Fig. 3.15: Numerical solution u^h of the hyperbolic surface with bumps problem. The essential boundary conditions are enforced with non-symmetric version of Nitsche's method. (a) u^h obtained with the Surface FEM with $n = 16, p = 3$, and (b) u^h obtained with the Trace FEM with $n = 16, p = 3$.

3.3.2.1 Strong enforcement and Lagrange multipliers

As mentioned above, the strong enforcement and the Lagrange multiplier approach are only applied to the Surface FEM. In principle, the Lagrange multiplier approach may be also employed within the Trace FEM, but a suitable discretization of the auxiliary fields is not trivial as the boundary of the domain is within the three-dimensional background mesh. One approach is to define a boundary conforming line mesh living *only* on the Dirichlet boundary $\partial\Gamma^h_{\mathrm{D}}$ and employ the nodes and corresponding shape functions as Lagrange multipliers. However, if the elements of the Lagrange multipliers are aligned with the elements of the active mesh, which simplifies the numerical integration along the boundary significantly, conditioning issues may occur due to small supports in case of non-favourable cut scenarios. Furthermore, the definition of a boundary conforming mesh within a FDM contradicts the main advantages of FDMs. Another approach which has been used in a recent pre-print [69], is to use the shape functions of the active mesh and restrict them only to the Dirichlet boundary. However, this requires additional stabilization and due to this increase in complexity, this is excluded from the present comparison.

In the following, the discrete weak forms for the strong enforcement of essential boundary conditions and the Lagrange multiplier method within the Surface FEM are introduced. Enforcing the essential boundary conditions in a strong sense, the discrete weak form reads as follows: Given source term f on Γ^h, boundary conditions $\hat{g}$ on $\partial\Gamma^h_{\mathrm{D}}$ and $\hat{t}$ on $\partial\Gamma^h_{\mathrm{N}}$, find $u^h \in \mathcal{S}^h_{S,g}$ such that for all test functions $v^h \in \mathcal{V}^h_{S,0}$ there holds in Γ^h

$$\int_{\Gamma^h} \nabla_\Gamma v^h \cdot \nabla_\Gamma u^h \,\mathrm{d}A = \int_{\Gamma^h} v^h f \,\mathrm{d}A + \int_{\partial\Gamma^h_{\mathrm{N}}} v^h \hat{t} \,\mathrm{d}s \ , \tag{3.25}$$

with $\mathcal{S}^h_{S,g} = \{u^h \in \mathcal{Q}^k_{\Gamma,h} : u^h|_{\partial\Gamma^h_{\mathrm{D}}} = \hat{g}\}$ and $\mathcal{V}^h_{S,0} = \{v^h \in \mathcal{Q}^k_{\Gamma,h} : v^h|_{\partial\Gamma^h_{\mathrm{D}}} = 0\}$.

Enforcing the Dirichlet boundary conditions with Lagrange multipliers converts the discrete weak form to a saddle point problem and the Lagrange multiplier field needs to be carefully discretized in order to ensure a unique solution [5]. The discrete weak form reads as follows: Given source term f on Γ^h, boundary conditions $\hat{g}$ on $\partial\Gamma^h_{\mathrm{D}}$ and $\hat{t}$ on $\partial\Gamma^h_{\mathrm{N}}$, find the solution $u^h \in \mathcal{Q}^k_{\Gamma,h}$ and the Lagrange multipliers $\lambda^h_u \in \mathcal{L}^h_{S,\lambda}$ such that for all test functions $(v^h_u, v^h_\lambda) \in \mathcal{Q}^k_{\Gamma,h} \times \mathcal{V}^h_{S,\lambda}$ there holds in Γ^h

$$\begin{aligned} \int_{\Gamma^h} \nabla_\Gamma v^h_u \cdot \nabla_\Gamma u^h \,\mathrm{d}A + \int_{\partial\Gamma^h_{\mathrm{D}}} v^h_u \lambda^h_u \,\mathrm{d}s &= \int_{\Gamma^h} v^h_u f \,\mathrm{d}A + \int_{\partial\Gamma^h_{\mathrm{N}}} v^h_u \hat{t} \,\mathrm{d}s \ , \\ \int_{\partial\Gamma^h_{\mathrm{D}}} v^h_\lambda u^h \,\mathrm{d}s &= \int_{\partial\Gamma^h_{\mathrm{D}}} v^h_\lambda \hat{g} \,\mathrm{d}s \ , \end{aligned} \tag{3.26}$$

with $\mathcal{L}^h_{S,\lambda} = \mathcal{V}^h_{S,\lambda} = \{\lambda^h_u|_{\partial\Gamma^h_{\mathrm{D}}} : \lambda^h_u \in \mathcal{Q}^k_{\Gamma,h}\}$. Note that the restriction of λ^h_u to $\partial\Gamma^h_{\mathrm{D}}$ is in the sense of a trace. As mentioned above, with the Lagrange multipliers the augmented problem in Eq. 3.26 has a saddle point structure and a completely arbitrary choice of the discrete function spaces is precluded [59]. As well-known, the Babuška-Brezzi condition [4], [17], [60] must be satisfied in order to obtain useful solutions in all involved fields. Herein, a common approach for the discrete Lagrange multipliers in the context of finite element methods with conforming meshes is employed. In particular, the shape functions which are used for the interpolation of u^h are restricted to the Dirichlet boundary $\partial\Gamma^h_{\mathrm{D}}$. According to [59], this choice satisfies the discrete inf-sup condition. Further details and other approaches of suitable discretizations of the Lagrange multipliers are given in, e.g., [5], [59].

The results of the convergence analyses are presented for both methods in Fig. 3.16 for the L^2-error. For both approaches, optimal orders of convergence are achieved, which

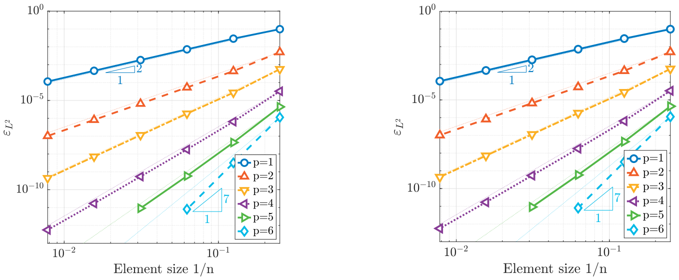

(a) strong enforcement **(b)** Lagrange multiplier

Fig. 3.16: L^2-errors in Γ^h of the hyperbolic surface with bumps problem with: (a) Strong enforcement, and (b) Lagrange multipliers.

holds also for the H^1-error and the residual error. The strong enforcement may be seen as a good reference because the DOFs at $\partial\Gamma^h_{\mathrm{D}}$ are directly prescribed with the exact solution. However, the Lagrange multiplier approach performs equally well in this direct comparison. In conclusion, when a stable and robust discretization of the auxiliary fields is available, one may prefer the Lagrange multiplier approach because in the case of vector-valued problems this approach is more general and more complex boundary conditions, e.g., symmetry boundary conditions, may be enforced in a straightforward manner.

3.3.2.2 Penalty method

The penalty method is applied to both finite element approaches and the implementation is in principle straightforward and robust. However, the additional terms in the discrete weak form are inconsistent and suffer from the interplay between accuracy and violation of the constraint conditions. In the following, the consequences on the choice of the penalty parameter in both approaches are elaborated in detail.

Employing the Surface FEM, the discrete weak form reads as follows: Given penalty parameter $\alpha \in \mathbb{R}^+$, source term f on Γ^h, boundary conditions $\hat{g}$ on $\partial\Gamma^h_{\mathrm{D}}$ and $\hat{t}$ on $\partial\Gamma^h_{\mathrm{N}}$, find the solution $u^h \in \mathcal{Q}^k_{\Gamma,h}$ such that for all test functions $v^h \in \mathcal{Q}^k_{\Gamma,h}$ there holds in Γ^h

$$\int_{\Gamma^h} \nabla_\Gamma v^h \cdot \nabla_\Gamma u^h \,\mathrm{d}A + \alpha \int_{\partial\Gamma^h_{\mathrm{D}}} v^h u^h \,\mathrm{d}s = \int_{\Gamma^h} v^h f \,\mathrm{d}A + \int_{\partial\Gamma^h_{\mathrm{N}}} v^h \hat{t} \,\mathrm{d}s + \alpha \int_{\partial\Gamma^h_{\mathrm{D}}} v^h \hat{g} \,\mathrm{d}s \; . \tag{3.27}$$

For the Trace FEM, the discrete weak form reads as follows: Given penalty parameter $\alpha \in \mathbb{R}^+$, stabilization parameter $\rho \in \mathbb{R}^+$, source term f on Γ^h, boundary conditions $\hat{g}$ on $\partial\Gamma^h_{\mathrm{D}}$ and $\hat{t}$ on $\partial\Gamma^h_{\mathrm{N}}$, find the solution $u^h \in \mathcal{T}_h$ such that for all test functions $v^h \in \mathcal{T}_h$

there holds in Γ^h

$$\begin{aligned}&\int_{\Gamma^h} \nabla_\Gamma v^h \cdot \nabla_\Gamma u^h \, \mathrm{d}A + \alpha \int_{\partial\Gamma^h_\mathrm{D}} v^h u^h \, \mathrm{d}s + \rho \int_{\Omega^\Gamma_h} \left(\nabla u^h \cdot \boldsymbol{n}^{e,h}_\Gamma\right) \left(\nabla v^h \cdot \boldsymbol{n}^{e,h}_\Gamma\right) \, \mathrm{d}V \\ &= \int_{\Gamma^h} v^h f \, \mathrm{d}A + \int_{\partial\Gamma^h_\mathrm{N}} v^h \hat{t} \, \mathrm{d}s + \alpha \int_{\partial\Gamma^h_\mathrm{D}} v^h \hat{g} \, \mathrm{d}s \; .\end{aligned} \tag{3.28}$$

In the convergence analyses, the penalty parameter α is varied between $10^2 \leq \alpha \leq 10^{16}$ with an interval of two orders of magnitude. In Fig. 3.17, partial results of the convergence studies are presented. In particular, the L^2-error is visualized for the Surface and Trace FEM with $\alpha = 10^{10}$. It can clearly be seen that for the lower orders $p \leq 2$ the convergence rates are optimal $\mathcal{O}(p+1)$. Furthermore, for an error level of about 10^{-8}, a further convergence is not be observed which is caused by a non-optimal choice of the penalty parameter. The results in the H^1-error and residual error are analogous and are omitted for brevity. The convergence behaviour can be improved with increasing penalty parameters but at a certain point, the inconsistency of the additional terms and the conditioning of the stiffness matrix prevent higher-order convergence rates. In the following, the situation for $p = 4$ is investigated. In detail, the L^2-error in the domain, see Eq. 3.19, L^2-error in the boundary conditions, see Eq. 3.22, and the conditioning for different parameters of α are presented. The condition numbers are computed with the MATLAB function *condest*, which estimates the 1-norm condition number. In Fig. 3.18 and Fig. 3.19, the results are illustrated. Depending on α, convergence up to a certain error level can be observed, see Fig. 3.18(a) and Fig. 3.19(a). This seems to be directly correlated to the error in the essential boundary conditions, see Fig. 3.18(b) and Fig. 3.19(b). Furthermore, the condition numbers are typically dominated by α and the expected growth of quadratic order can only be observed for $\alpha \leq 10^4$, which is too low for proper convergence in this particular situation, see Fig. 3.18(c) and Fig. 3.19(c).

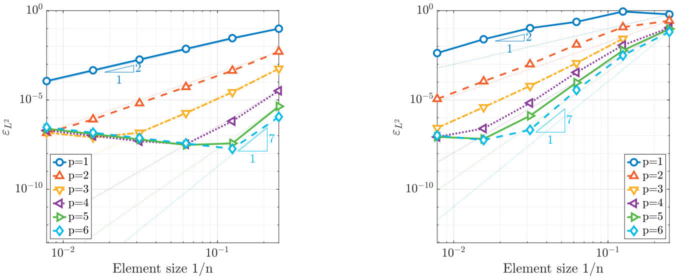

(a) Surface FEM **(b)** Trace FEM

Fig. 3.17: L^2-errors in Γ^h of the hyperbolic surface with bumps problem with penalty method and $\alpha = 10^{10}$: (a) Surface FEM, and (b) Trace FEM.

In the direct comparison of the penalty method in the Surface and Trace FEM, the expected behaviour of the penalty approach, i.e., convergence only up to a certain error level, can be observed for both finite element approaches. The major advantages of

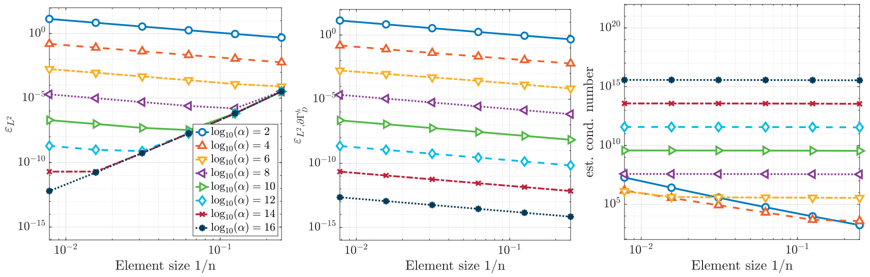

(a) L^2-error in Γ^h **(b)** L^2-error on $\partial\Gamma^h_{\mathrm{D}}$ **(c)** condition number

Fig. 3.18: Convergence for the Surface FEM with $p = 4$ for different parameters of α: (a) L^2-error in the domain, (b) L^2-error in the boundary conditions, and (c) estimated condition numbers.

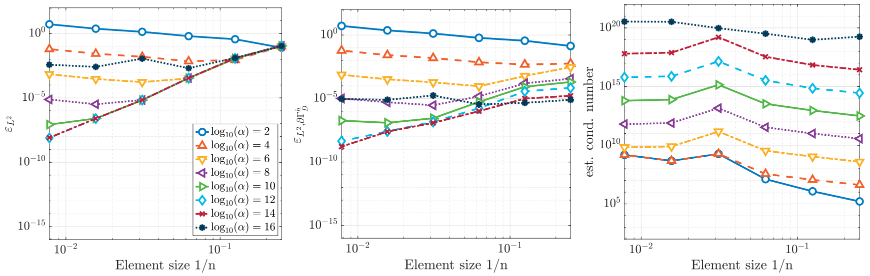

(a) L^2-error in Γ^h **(b)** L^2-error on $\partial\Gamma^h_{\mathrm{D}}$ **(c)** condition number

Fig. 3.19: Convergence for the Trace FEM with $p = 4$ for different parameters of α: (a) L^2-error in the domain, (b) L^2-error in the boundary conditions, and (c) estimated condition numbers.

the method are that a discretization of auxiliary fields is not necessary and the resulting method is stable and very robust. Depending on the particular application, in the context of Trace FEM, these advantages may be more important which makes the penalty method a reliable choice, especially if only lower orders are considered.

3.3.2.3 Symmetric version of Nitsche's method

Next, the symmetric version of Nitsche's method is employed for both finite element approaches. The major advantage of Nitsche's method is that auxiliary fields are not needed and the overall method is consistent. The additional Nitsche terms for Poisson's equation, see Eq. 3.10a, are

$$\int_{\partial\Gamma^h_{\mathrm{D}}} \left(u^h - \hat{g}\right) \nabla_\Gamma v^h \cdot \boldsymbol{n}^h_{\partial\Gamma} \,\mathrm{d}s \;, \tag{3.29}$$

which are added to the RHS of the obtained discrete weak form. The term $\nabla_\Gamma v^h \cdot \boldsymbol{n}^h_{\partial\Gamma}$ is the energy conjugated quantity to the primal variable at the Dirichlet boundary $\partial\Gamma^h_{\mathrm{D}}$. Furthermore, it can clearly be seen that these additional terms are consistent, i.e., the new terms are vanishing if the exact solution is inserted. However, the symmetric version of Nitsche's method is not elliptic without a suitable stabilization. Therefore, additional stabilization terms are added in order to ensure coercivity of the discrete weak form. The structure of the stabilization is analogously to the penalty terms in Section 3.3.2.2 and are added to the RHS of the discrete weak form

$$\rho_N \int_{\partial\Gamma^h_{\mathrm{D}}} v^h \left(\hat{g} - u^h\right) \mathrm{d}s \ . \tag{3.30}$$

The required stabilization parameter ρ_N is typically several orders of magnitude lower than the penalty parameters from above. The stabilization parameter need to be high enough in order to ensure coercivity. On the other hand, if ρ_N is too large, the overall approach may degenerate to the penalty method from above. Therefore, a suitable choice of ρ_N is crucial within this approach. One may manually set the stabilization ρ_N, yet a more advanced approach is to solve a global or local element-wise generalized eigenvalue problem, see, e.g., [35], [57], [59]. The global generalized eigenvalue problem results in slightly lower stabilization parameters than the local approach, although the computational cost increases significantly and the influence on the accuracy is often minor [120]. Herein, the stabilization parameters are determined by the solution of a local, generalized eigenvalue for each element $T \in \tau_{\partial\Gamma^h_{\mathrm{D}}}$ where $\tau_{\partial\Gamma^h_{\mathrm{D}}} = \{T \cap \partial\Gamma^h_{\mathrm{D}} \neq \emptyset\}$

$$\mathbf{A}_T \cdot \boldsymbol{x} = \Lambda_T \mathbf{B}_T \cdot \boldsymbol{x} \ , \tag{3.31}$$

with

$$[\mathbf{A}_T]_{ij} = \int_{T\cap\partial\Gamma^h_{\mathrm{D}}} \left(\nabla_\Gamma M_i \cdot \boldsymbol{n}^h_{\partial\Gamma}\right)\left(\nabla_\Gamma M_j \cdot \boldsymbol{n}^h_{\partial\Gamma}\right) \mathrm{d}s \ , \tag{3.32}$$

$$[\mathbf{B}_T]_{ij} = \int_{T\cap\Gamma^h} \nabla_\Gamma M_i \cdot \nabla_\Gamma M_j \, \mathrm{d}A \ , \tag{3.33}$$

where M_i, M_j are the employed shape functions. Based on the obtained eigenvalues for an element T the stabilization parameter for this element is set to

$$\rho_{N,T} = 2\max(\Lambda_T) \ . \tag{3.34}$$

Note that in case of boundary conforming elements, which is the case in the Surface FEM, or boundary conforming cells, only boundary DOFs shall be considered [120, p. 822].

The discrete weak form with the Surface FEM and the symmetric version of Nitsche's method, employing the local element-wise stabilization, reads as follows: Given stabilization parameter $\rho_{N,T} \in \mathbb{R}^+ \ \forall\, T \in \tau_{\partial\Gamma^h_{\mathrm{D}}}$, source term f on Γ^h, boundary conditions $\hat{g}$ on $\partial\Gamma^h_{\mathrm{D}}$ and $\hat{t}$ on $\partial\Gamma^h_{\mathrm{N}}$, find the solution $u^h \in \mathcal{Q}^k_{\Gamma,h}$ such that for all test functions $v^h \in \mathcal{Q}^k_{\Gamma,h}$

there holds in Γ^h

$$\begin{aligned}
&\int_{\Gamma^h} \nabla_\Gamma v^h \cdot \nabla_\Gamma u^h \, \mathrm{d}A - \int_{\partial\Gamma^h_\mathrm{D}} v^h \nabla_\Gamma u^h \cdot \boldsymbol{n}^h_{\partial\Gamma} \, \mathrm{d}s - \int_{\partial\Gamma^h_\mathrm{D}} u^h \nabla_\Gamma v^h \cdot \boldsymbol{n}^h_{\partial\Gamma} \, \mathrm{d}s \\
&+ \sum_{T \in \tau_{\partial\Gamma^h_\mathrm{D}}} \rho_{N,T} \int_{T \cap \partial\Gamma^h_\mathrm{D}} v^h u^h \, \mathrm{d}s \\
&= \int_{\Gamma^h} v^h f \, \mathrm{d}A + \int_{\partial\Gamma^h_\mathrm{N}} v^h \hat{t} \, \mathrm{d}s - \int_{\partial\Gamma^h_\mathrm{D}} \hat{g} \nabla_\Gamma v^h \cdot \boldsymbol{n}^h_{\partial\Gamma} \, \mathrm{d}s + \sum_{T \in \tau_{\partial\Gamma^h_\mathrm{D}}} \rho_{N,T} \int_{T \cap \partial\Gamma^h_\mathrm{D}} v^h \hat{g} \, \mathrm{d}s \; .
\end{aligned} \tag{3.35}$$

For the Trace FEM, the discrete weak form reads as follows: Given stabilization parameters $(\rho, \rho_{N,T}) \in \mathbb{R}^+, T \in \tau_{\partial\Gamma^h_\mathrm{D}}$, source term f on Γ^h, boundary conditions $\hat{g}$ on $\partial\Gamma^h_\mathrm{D}$ and $\hat{t}$ on $\partial\Gamma^h_\mathrm{N}$, find the solution $u^h \in \mathcal{T}_h$ such that for all test functions $v^h \in \mathcal{T}_h$ there holds in Γ^h

$$\begin{aligned}
&\int_{\Gamma^h} \nabla_\Gamma v^h \cdot \nabla_\Gamma u^h \, \mathrm{d}A - \int_{\partial\Gamma^h_\mathrm{D}} v^h \nabla_\Gamma u^h \cdot \boldsymbol{n}^h_{\partial\Gamma} \, \mathrm{d}s - \int_{\partial\Gamma^h_\mathrm{D}} u^h \nabla_\Gamma v^h \cdot \boldsymbol{n}^h_{\partial\Gamma} \, \mathrm{d}s \\
&+ \sum_{T \in \tau_{\partial\Gamma^h_\mathrm{D}}} \rho_{N,T} \int_{T \cap \partial\Gamma^h_\mathrm{D}} v^h u^h \, \mathrm{d}s + \rho \int_{\Omega^\Gamma_h} \left(\nabla u^h \cdot \boldsymbol{n}^{e,h}_\Gamma \right) \left(\nabla v^h \cdot \boldsymbol{n}^{e,h}_\Gamma \right) \, \mathrm{d}V \\
&= \int_{\Gamma^h} v^h f \, \mathrm{d}A + \int_{\partial\Gamma^h_\mathrm{N}} v^h \hat{t} \, \mathrm{d}s - \int_{\partial\Gamma^h_\mathrm{D}} \hat{g} \nabla_\Gamma v^h \cdot \boldsymbol{n}^h_{\partial\Gamma} \, \mathrm{d}s + \sum_{T \in \tau_{\partial\Gamma^h_\mathrm{D}}} \rho_{N,T} \int_{T \cap \partial\Gamma^h_\mathrm{D}} v^h \hat{g} \, \mathrm{d}s \; .
\end{aligned} \tag{3.36}$$

The convergence study is performed with the set of parameters as defined above for both Surface and Trace FEM. In Fig. 3.20(a) and Fig. 3.21(a), the L^2-error in Γ^h is visualized for both approaches. It can be seen that for both approaches optimal convergence rates are achieved after the pre-asymptotic region. This holds also for the H^1-error and the residual error. In Fig. 3.20(b) and Fig. 3.21(b), the error in the essential boundary conditions is shown. It is noteworthy to emphasize that in comparison to the other approaches, i.e., strong enforcement, Lagrange multiplier and penalty method, the enforcement of boundary conditions is rather weak which results in higher errors in $\varepsilon_{L^2,\partial\Gamma^h_\mathrm{D}}$, especially at coarse levels. In case of the Surface FEM, the achieved order of convergence is $\mathcal{O}(p+1)$. The situation in the Trace FEM is slightly different. Only for $p \leq 4$ the order of convergence is $\mathcal{O}(p+1)$ and for the higher orders $p = (5, 6)$ a converge order of roughly $\mathcal{O}(5)$ can be observed. Nevertheless, the suboptimal order of convergence for $p = (5, 6)$ at the Dirichlet boundary which is basically the trace of the L^2-error in the domain, does not hinder optimal convergence rates in ε_{L^2} and other error measures in the domain, see Fig. 3.21(a).

As mentioned above, the stabilization parameters $\rho_{N,T}$ are obtained by an element-wise, generalized eigenvalue problem. In Fig. 3.20(c) and Fig. 3.21(c), the largest stabilization parameters are presented. In case of the Surface FEM, the range between largest and smallest stabilization parameter is almost negligible. Furthermore, the stabilization parameters for the Surface FEM are between $10^1 \leq \max \rho_{N,T} \leq 10^4$ and, as already mentioned, several orders of magnitude lower compared to the penalty method, which are required for optimal convergence rates, e.g., $\alpha = 10^{16}$ for $p = 4$. In case of the Trace FEM, the situation is different because the obtained stabilization parameter depends on

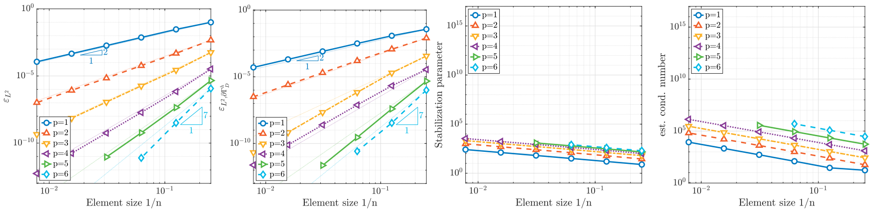

(a) L^2-error in Γ^h **(b)** L^2-error on $\partial\Gamma^h_{\mathrm{D}}$ **(c)** stab. parameter **(d)** condition number

Fig. 3.20: Convergence with the Surface FEM employing the symmetric version of Nitsche's method: (a) L^2-error in the domain, (b) L^2-error in the boundary conditions, (c) maximum stabilization parameters $\max \rho_{N,T}$, and (d) estimated condition numbers.

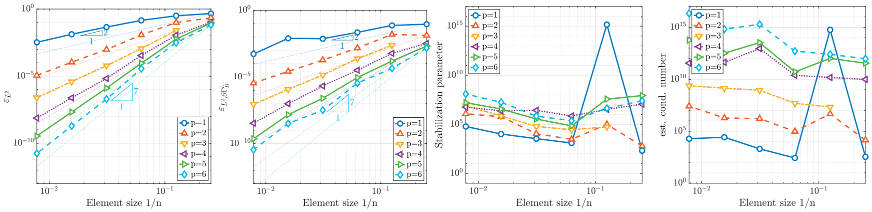

(a) L^2-error in Γ^h **(b)** L^2-error on $\partial\Gamma^h_{\mathrm{D}}$ **(c)** stab. parameter **(d)** condition number

Fig. 3.21: Convergence with the Trace FEM employing the symmetric version of Nitsche's method: (a) L^2-error in the domain, (b) L^2-error in the boundary conditions, (c) maximum stabilization parameters $\max \rho_{N,T}$, and (d) estimated condition numbers.

the cut scenario and might be unbounded. This problem has been analysed in detail in [35] and the suggested workaround is to employ a user defined limit, which prevents unbounded stabilization parameters. Alternatively, the gradient jump penalty method as proposed in [21] may also remedy the situation. In this method, the Nitsche stabilization parameter is independent of the concrete cut scenario and the issue of unbounded stabilization parameters may be circumvented. Herein, the use defined limit $\rho_{N,T,\max} = 10^{15}$ is employed. In Fig. 3.21(c), such an unfavourable cut scenario is shown, and the stabilization parameter for this level $n = 8, p = 1$ is set to $\rho_{N,T} = \rho_{N,T,\max}$ for at least one element. Therefore, the stabilization parameters are between $10^3 \leq \max \rho_{N,T} \leq \rho_{N,T,\max}$ depending on the cut scenario. The resulting method is then rather a hybrid between Nitsche's method and the penalty method. Lastly, in Fig. 3.20(d) and Fig. 3.21(d), the estimated condition numbers are presented. In case of the Surface FEM, the condition numbers behave as expected. In case of the Trace FEM, the condition numbers are highly influenced by the obtained stabilization parameters. In conclusions, the symmetric version of Nitsche's method performs excellent within the Surface FEM and the presented element-wise stabilization. In case of the Trace FEM, the symmetric version is less robust and tends to degenerate to the penalty method in case of unfavourable cut scenarios. Nevertheless, the symmetric version of Nitsche's method is a consistent approach and if one obtains suitable stabilization parameters, this approach is a reliable method for both Surface and Trace FEM.

3.3.2.4 Non-symmetric version of Nitsche's method

Lastly, the non-symmetric version of Nitsche's method is investigated for the weak enforcement of essential boundary conditions. In the non-symmetric version, the Nitsche's terms from Eq. 3.29 are multiplied by -1

$$-\int_{\partial\Gamma^h_{\mathrm{D}}} \left(u^h - \hat{g}\right) \nabla_\Gamma v^h \cdot \boldsymbol{n}^h_{\partial\Gamma} \, \mathrm{d}s \ , \tag{3.37}$$

leading to a non-symmetric system of equations. The major advantage is that the resulting discrete weak form does not require an additional stabilization. The discrete weak form with the Surface FEM reads as follows: Given source term f on Γ^h, boundary conditions $\hat{g}$ on $\partial\Gamma^h_{\mathrm{D}}$ and $\hat{t}$ on $\partial\Gamma^h_{\mathrm{N}}$, find the solution $u^h \in \mathcal{Q}^k_{\Gamma,h}$ such that for all test functions $v^h \in \mathcal{Q}^k_{\Gamma,h}$ there holds in Γ^h

$$\begin{aligned}
&\int_{\Gamma^h} \nabla_\Gamma v^h \cdot \nabla_\Gamma u^h \, \mathrm{d}A - \int_{\partial\Gamma^h_{\mathrm{D}}} v^h \nabla_\Gamma u^h \cdot \boldsymbol{n}^h_{\partial\Gamma} \, \mathrm{d}s + \int_{\partial\Gamma^h_{\mathrm{D}}} u^h \nabla_\Gamma v^h \cdot \boldsymbol{n}^h_{\partial\Gamma} \, \mathrm{d}s \\
&= \int_{\Gamma^h} v^h f \, \mathrm{d}A + \int_{\partial\Gamma^h_{\mathrm{N}}} v^h \hat{t} \, \mathrm{d}s + \int_{\partial\Gamma^h_{\mathrm{D}}} \hat{g} \nabla_\Gamma v^h \cdot \boldsymbol{n}^h_{\partial\Gamma} \, \mathrm{d}s \ .
\end{aligned} \tag{3.38}$$

For the Trace FEM, the discrete weak form reads as follows: Given stabilization parameter $\rho \in \mathbb{R}^+$, source term f on Γ^h, boundary conditions $\hat{g}$ on $\partial\Gamma^h_{\mathrm{D}}$ and $\hat{t}$ on $\partial\Gamma^h_{\mathrm{N}}$, find the solution $u^h \in \mathcal{T}_h$ such that for all test functions $v^h \in \mathcal{T}_h$ there holds in Γ^h

$$\begin{aligned}
&\int_{\Gamma^h} \nabla_\Gamma v^h \cdot \nabla_\Gamma u^h \, \mathrm{d}A - \int_{\partial\Gamma^h_{\mathrm{D}}} v^h \nabla_\Gamma u^h \cdot \boldsymbol{n}^h_{\partial\Gamma} \, \mathrm{d}s + \int_{\partial\Gamma^h_{\mathrm{D}}} u^h \nabla_\Gamma v^h \cdot \boldsymbol{n}^h_{\partial\Gamma} \, \mathrm{d}s \\
&+ \rho \int_{\Omega^\Gamma_h} \left(\nabla u^h \cdot \boldsymbol{n}^{e,h}_\Gamma\right) \left(\nabla v^h \cdot \boldsymbol{n}^{e,h}_\Gamma\right) \, \mathrm{d}V \\
&= \int_{\Gamma^h} v^h f \, \mathrm{d}A + \int_{\partial\Gamma^h_{\mathrm{N}}} v^h \hat{t} \, \mathrm{d}s - \int_{\partial\Gamma^h_{\mathrm{D}}} \hat{g} \nabla_\Gamma v^h \cdot \boldsymbol{n}^h_{\partial\Gamma} \, \mathrm{d}s \ .
\end{aligned} \tag{3.39}$$

The convergence analyses are performed with the same set of parameters than above. In the following, the L^2-error in Γ^h, L^2-error on $\partial\Gamma^h_{\mathrm{D}}$ and the condition number are presented for both finite element approaches. The results of the Surface FEM, see Fig. 3.22, are almost identical compared to the symmetric version of Nitsche's method. The convergence rates are optimal in all investigated error norms and in the direct comparison with the symmetric version, the errors are lower in general. The condition numbers are almost indistinguishable.

For the Trace FEM, see Fig. 3.23, the situation is analogously, optimal convergence rates are achieved in the L^2- , H^1- and residual-errors. The convergence in the error of the essential boundary conditions is similar as in the symmetric version. The condition numbers are not disturbed by an additional stabilization and in comparison to the symmetric version, the condition numbers are lower.

In conclusion, the convergence behaviour of the non-symmetric version of Nitsche's

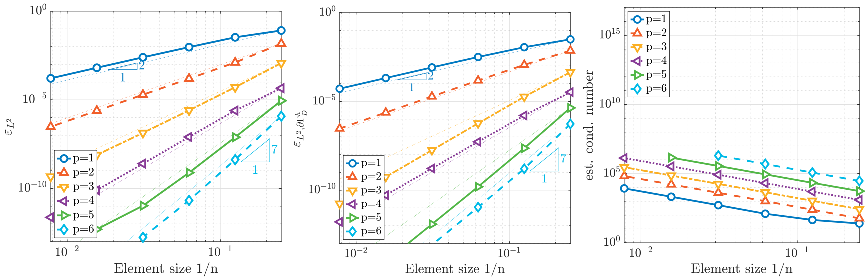

(a) L^2-error in Γ^h **(b)** L^2-error on $\partial\Gamma^h_\mathrm{D}$ **(c)** condition number

Fig. 3.22: Convergence with the Surface FEM employing the non-symmetric version of Nitsche's method: (a) L^2-error in the domain, (b) L^2-error in the boundary conditions, and (c) estimated condition numbers.

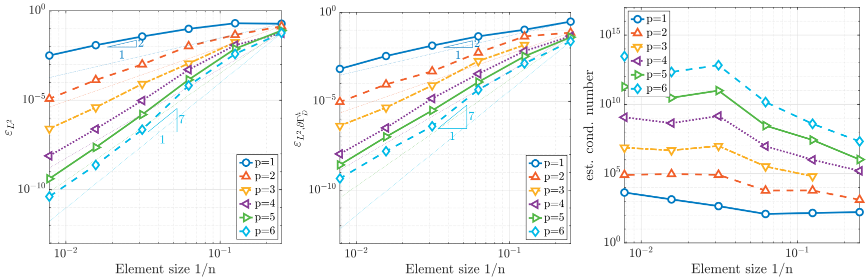

(a) L^2-error in Γ^h **(b)** L^2-error on $\partial\Gamma^h_\mathrm{D}$ **(c)** condition number

Fig. 3.23: Convergence with the Trace FEM employing the non-symmetric version of Nitsche's method: (a) L^2-error in the domain, (b) L^2-error in the boundary conditions, and (c) estimated condition numbers.

method is similar compared to the symmetric counterpart. However, in the theoretical error estimates, suboptimal convergence rates in the primal variable could be expected, see [3], [20]. Nevertheless, optimal convergence rates in L^2-error have been observed in all cases, confirming results in [20], [121]. The absence of an additional stabilization, significantly improves the robustness of the overall approach, especially in the context of FDMs. The drawback of a non-symmetric system of equations is less important for direct solvers as employed herein.

3.3.2.5 Conclusion

Comparing all presented approaches for the treatment of essential boundary conditions in the Surface and Trace FEM we conclude the following:

In case of the Surface FEM, all presented approaches perform as expected. In case of scalar-valued problems or simple boundary conditions, the strong enforcement may be preferred due to its simplicity and robustness. In case of more complex boundary conditions, e.g., directional supports or symmetry boundary conditions, the Lagrange multiplier approach or the non-symmetric version of Nitsche's method are reliable methods to achieve higher-order accurate results. When lower-order results are sufficient, the penalty method may be preferred. The overhead of the additional stabilization for the symmetric version of Nitsche's method may only be justified if a symmetric system of equations is desired and a consistent approach without auxiliary fields shall be employed.

For the Trace FEM, the situation is different. First of all, the strong enforcement is, except in special cases, not applicable. A suitable discretization of the Lagrange multiplier field is a major, non-trivial task. In terms of robustness, the penalty method may be preferred, although the choice of a suitable penalty parameter in combination with higher-order can become tricky. The symmetric version of Nitsche's method may degenerate to a hybrid between Nitsche's method and penalty method due to unfavourable cut scenarios. In contrast, the non-symmetric version of Nitsche's method is also consistent, but without additional stabilization terms. Furthermore, it also offers the flexibility to enforce all physically meaningful boundary conditions, which outweighs the drawback of theoretically suboptimal convergence rates in the primal variable and the presence of a non-symmetric system of equations. In particular, for many practical situations, optimal convergence rates have indeed been reported. Therefore, the non-symmetric version of Nitsche's method is preferred in the following in the context of the Trace FEM.

4 Linear Kirchhoff-Love shells

The Kirchhoff-Love shell theory is recast in the frame of the TDC including all mechanical quantities such as moments, normal and shear forces. The boundary conditions of the Kirchhoff-Love shell are elaborated in detail. As a consequence of the reformulation in the TDC, there is no need for a parametrization of the shell geometry implying curvilinear surface coordinates as used in the classical shell theory. Therefore, the proposed TDC-based formulation also applies to shell geometries which are zero-isosurfaces as in the level-set method where no parametrization is available in general. For the discretization, the TDC-based formulation may be used based on surface meshes implying element-wise parametrizations, hence, in the context of the Surface FEM. Then, the results are equivalent to those obtained based on the classical theory. However, it may also be used in recent finite element approaches such as the Trace FEM and Cut FEM. Herein, the obtained shell BVP is discretized with isogeometric analysis (for continuity reasons), being a special variant of the Surface FEM, and the essential boundary conditions are enforced with Lagrange multipliers and the non-symmetric version of Nitsche's method. The resulting discrete weak forms are presented including all relevant terms. The proposed approach is carefully verified with classical and new benchmarks. Higher-order convergence rates are achieved when the physical fields are sufficiently smooth.

The major content of this chapter follows our own articles in [125], [131].

4.1 Governing equations

In this section, we derive the linear Kirchhoff-Love shell theory in the frame of tangential operators based on a global Cartesian coordinate system. We restrict ourselves to infinitesimal deformations, which means that the reference and spatial configuration are indistinguishable. Furthermore, a linear elastic material governed by Hooke's law is assumed. As usual in the Kirchhoff-Love shell theory, the transverse shear strains and the change of curvature in the material law are neglected, which restricts the model to thin shells ($t\kappa_{\max} \ll 1$) [7], [14], [145].

With these assumptions, an analytical pre-integration with respect to the thickness leads to stress resultants such as normal forces and bending moments. The equilibrium in strong form is then expressed in terms of the stress resultants. Finally, the transverse shear forces may be identified via equilibrium considerations.

4.1.1 Kinematics

The mid-surface Γ of the shell is a sufficiently smooth manifold embedded in the physical space $\mathbb{R}^3$. A point on the mid-surface is denoted as $\boldsymbol{x}_\Gamma \in \Gamma \subset \mathbb{R}^3$ and may be defined explicitly or implicitly, see Section 2.1. With the unit-normal vector $\boldsymbol{n}_\Gamma$, a point in the domain of the shell Ω of thickness t is defined by

$$\boldsymbol{x} = \boldsymbol{x}_\Gamma + \zeta \boldsymbol{n}_\Gamma \ , \tag{4.1}$$

with ζ being the thickness parameter and $|\zeta| \leq {}^{t}\!/\!_{2}$. Alternatively, if the mid-surface is defined implicitly with a signed distance function $\phi_{\mathrm{SDF}}(\boldsymbol{x})$ the domain of the shell Ω is defined by

$$\Omega = \left\{ \boldsymbol{x} \in \mathbb{R}^3 : |\phi_{\mathrm{SDF}}(\boldsymbol{x})| \leq \frac{t}{2} \right\} \ . \tag{4.2}$$

In this case the mid-surface Γ is the zero-isosurface of $\phi(\boldsymbol{x})$, see Eq. 2.1. The zero-isosurface may then be bounded by additional slave level-set functions as described in Section 2.1. Independent of the concrete surface definition, the overall displacement of a point $\boldsymbol{P} \in \Omega$ is the difference between the spatial and reference configuration

$$\boldsymbol{u}_\Omega(\boldsymbol{x}) = \bar{\boldsymbol{P}}(\boldsymbol{x}) - \boldsymbol{P}(\boldsymbol{x}) \ ,$$

which takes the form

$$\boldsymbol{u}_\Omega(\boldsymbol{x}_\Gamma, \zeta) = \boldsymbol{u}(\boldsymbol{x}_\Gamma) + \zeta \boldsymbol{w}(\boldsymbol{x}_\Gamma) \ . \tag{4.3}$$

There, $\boldsymbol{u}(\boldsymbol{x}_\Gamma) : \Gamma \to \mathbb{R}^3$ is the displacement field of the mid-surface and $\boldsymbol{w}(\boldsymbol{x}_\Gamma) \in T_P\Gamma$ is the difference vector, as illustrated in Fig. 4.1. Without transverse shear strains, the difference vector $\boldsymbol{w}$ expressed in terms of the TDC is defined as in [39],

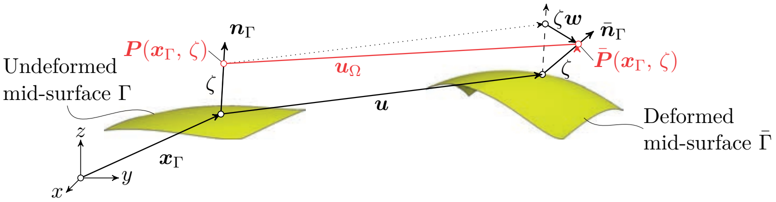

Fig. 4.1: Displacements $\boldsymbol{u}_\Omega$, $\boldsymbol{u}$ and $\boldsymbol{w}$ of the shell.

$$\boldsymbol{w}(\boldsymbol{x}_\Gamma) = -\left[\nabla_\Gamma^{\mathrm{dir}} \boldsymbol{u} + (\nabla_\Gamma^{\mathrm{dir}} \boldsymbol{u})^{\mathrm{T}}\right] \cdot \boldsymbol{n}_\Gamma = \mathbf{H} \cdot \boldsymbol{u} - \nabla_\Gamma(\boldsymbol{u} \cdot \boldsymbol{n}_\Gamma) \ . \tag{4.4}$$

As readily seen in the equation above, the difference vector $\boldsymbol{w}$ is tangential. Alternatively, the difference vector $\boldsymbol{w}$ may also be rewritten in terms of partial tangential derivatives of $\boldsymbol{u}$ and the normal vector $\boldsymbol{n}_\Gamma$ as

$$\boldsymbol{w}(\boldsymbol{x}_\Gamma) = \mathbf{H} \cdot \boldsymbol{u} - \nabla_\Gamma(\boldsymbol{u} \cdot \boldsymbol{n}_\Gamma) = - \begin{bmatrix} \boldsymbol{u}^{\mathrm{dir}}_{,x} \cdot \boldsymbol{n}_\Gamma \\ \boldsymbol{u}^{\mathrm{dir}}_{,y} \cdot \boldsymbol{n}_\Gamma \\ \boldsymbol{u}^{\mathrm{dir}}_{,z} \cdot \boldsymbol{n}_\Gamma \end{bmatrix} \ . \tag{4.5}$$

Consequently, the displacement field of the shell continuum is only a function of the mid-surface displacement $\boldsymbol{u}$, the unit normal vector $\boldsymbol{n}_\Gamma$ and the thickness parameter ζ. The surface gradient of $\boldsymbol{u}_\Omega(\boldsymbol{x})$ is given by

$$\begin{aligned}\nabla_\Gamma^{\mathrm{dir}} \boldsymbol{u}_\Omega(\boldsymbol{x}) &= \mathbf{P} \cdot \frac{\partial \boldsymbol{u}_\Omega(\boldsymbol{x})}{\partial \boldsymbol{x}} \cdot \frac{\partial \boldsymbol{x}}{\partial \boldsymbol{x}_\Gamma} \\ &= \mathbf{P} \cdot (\nabla \tilde{\boldsymbol{u}} + \nabla \zeta \otimes \boldsymbol{w} + \zeta \nabla \tilde{\boldsymbol{w}}) \cdot (\mathbb{I} + \zeta \mathbf{H}) \\ &= \left(\nabla_\Gamma^{\mathrm{dir}} \boldsymbol{u} + \boldsymbol{n}_\Gamma \otimes \boldsymbol{w} + \zeta \nabla_\Gamma^{\mathrm{dir}} \boldsymbol{w}\right) \cdot (\mathbb{I} + \zeta \mathbf{H}) \ ,\end{aligned} \tag{4.6}$$

with $\mathbf{H} = \nabla_\Gamma^{\mathrm{dir}} \boldsymbol{n}_\Gamma$ being the Weingarten map and $\mathbf{P}$ being the projector introduced in Section 2.2.1 (not to be confused with some point $\boldsymbol{P}$ on the surface mentioned above). Note that the gradient of the thickness parameter ζ can be identified as the normal vector $\boldsymbol{n}_\Gamma$ if the deformations in thickness direction are neglected. The second term $(\mathbb{I} + \zeta \mathbf{H})$ in Eq. 4.6 is the inverse of the shell shifter [14], which is a second order tensor. The equivalent expression in local coordinates is $\sum_{i=1}^3 \boldsymbol{G}^i \otimes \boldsymbol{A}_i$, where $\boldsymbol{G}^i$ are the contravariant base vectors in the shell continuum and $\boldsymbol{A}_i$ the covariant base vectors on the surface [14].

The linearised strain tensor $\boldsymbol{\varepsilon}_\Gamma$ is defined by the symmetric part of the surface gradient of $\boldsymbol{u}_\Omega$

$$\boldsymbol{\varepsilon}_\Gamma(\boldsymbol{x}) = \frac{1}{2}\left[\nabla_\Gamma^{\mathrm{dir}} \boldsymbol{u}_\Omega + (\nabla_\Gamma^{\mathrm{dir}} \boldsymbol{u}_\Omega)^{\mathrm{T}}\right] = \boldsymbol{\varepsilon}_\Gamma^{\mathrm{P}}(\boldsymbol{x}) + \boldsymbol{\varepsilon}_\Gamma^{\mathrm{S}}(\boldsymbol{x}) \tag{4.7}$$

and is split into an in-plane strain $\boldsymbol{\varepsilon}_\Gamma^{\mathrm{P}}$ and a transverse shear strain $\boldsymbol{\varepsilon}_\Gamma^{\mathrm{S}}$. Neglecting higher-order terms in thickness direction, as usual in the classical theory [14], the in-plane strain is defined by [125]

$$\boldsymbol{\varepsilon}_\Gamma^{\mathrm{P}} = \mathbf{P} \cdot \boldsymbol{\varepsilon}_\Gamma^{\mathrm{dir}} \cdot \mathbf{P} \tag{4.8}$$

$$= \boldsymbol{\varepsilon}_{\Gamma,\,\mathrm{Mem}}^{\mathrm{P}} + \zeta \boldsymbol{\varepsilon}_{\Gamma,\,\mathrm{Bend}}^{\mathrm{P}} \tag{4.9}$$

which is divided into a membrane and bending strain. The in-plane membrane strain becomes

$$\boldsymbol{\varepsilon}_{\Gamma,\,\mathrm{Mem}}^{\mathrm{P}}(\boldsymbol{u}) = \frac{1}{2}\left[\nabla_\Gamma^{\mathrm{cov}} \boldsymbol{u} + (\nabla_\Gamma^{\mathrm{cov}} \boldsymbol{u})^{\mathrm{T}}\right] \ , \tag{4.10}$$

and the bending strain is

$$\begin{aligned}\boldsymbol{\varepsilon}_{\Gamma,\,\mathrm{Bend}}^{\mathrm{P}}(\boldsymbol{u}) &= \frac{1}{2}\left[\mathbf{H} \cdot \nabla_\Gamma^{\mathrm{dir}} \boldsymbol{u} + (\nabla_\Gamma^{\mathrm{dir}} \boldsymbol{u})^{\mathrm{T}} \cdot \mathbf{H} + \nabla_\Gamma^{\mathrm{cov}} \boldsymbol{w} + (\nabla_\Gamma^{\mathrm{cov}} \boldsymbol{w})^{\mathrm{T}}\right] \\ &= -\begin{bmatrix} \boldsymbol{u}_{,xx}^{\mathrm{cov}} \cdot \boldsymbol{n}_\Gamma & \boldsymbol{u}_{,yx}^{\mathrm{cov}} \cdot \boldsymbol{n}_\Gamma & \boldsymbol{u}_{,zx}^{\mathrm{cov}} \cdot \boldsymbol{n}_\Gamma \\ & \boldsymbol{u}_{,yy}^{\mathrm{cov}} \cdot \boldsymbol{n}_\Gamma & \boldsymbol{u}_{,zy}^{\mathrm{cov}} \cdot \boldsymbol{n}_\Gamma \\ \mathrm{sym} & & \boldsymbol{u}_{,zz}^{\mathrm{cov}} \cdot \boldsymbol{n}_\Gamma \end{bmatrix} \ ,\end{aligned} \tag{4.11}$$

where $\nabla_\Gamma^{\mathrm{cov}} \boldsymbol{w} = -\left[\boldsymbol{u}_{,ij}^{\mathrm{cov}} \cdot \boldsymbol{n}_\Gamma + (\nabla_\Gamma^{\mathrm{dir}} \boldsymbol{u})^{\mathrm{T}} \cdot \mathbf{H}\right]$. The transverse shear strain is defined in a similar manner as in [84]

$$\boldsymbol{\varepsilon}_{\Gamma}^{\mathrm{S}}(\boldsymbol{u},\,\boldsymbol{w}) = \mathbf{Q}\cdot\boldsymbol{\varepsilon}_{\Gamma} + \boldsymbol{\varepsilon}_{\Gamma}\cdot\mathbf{Q} = \mathbf{0} \tag{4.12}$$

and vanishes due to the kinematic assumptions from above. The resulting membrane and bending strain in Eq. 4.10 and Eq. 4.11 are equivalent compared to the classical theory, e.g., [7]. In the case of flat shell structures as considered in [82] the membrane strain is only a function of the tangential displacement $\boldsymbol{u}_t = \mathbf{P}\cdot\boldsymbol{u}$ and the bending strain only depends on the normal displacement $u_n = \boldsymbol{u}\cdot\boldsymbol{n}_{\Gamma}$, which simplifies the overall kinematics significantly. Moreover, the normal vector $\boldsymbol{n}_{\Gamma}$ is constant and the difference vector simplifies to $\boldsymbol{w}(\boldsymbol{x}_{\Gamma}) = -\nabla_{\Gamma}u_n$.

4.1.2 Constitutive equations and stress resultants

As already mentioned above, the shell is assumed to be linear elastic and, as usual for thin structures, plane stress is presumed. The in-plane stress tensor $\boldsymbol{\sigma}_{\Gamma}$ is defined as

$$\begin{aligned}\boldsymbol{\sigma}_{\Gamma}(\boldsymbol{x}_{\Gamma},\,\zeta) &= \mathbf{P}\cdot[2\mu\boldsymbol{\varepsilon}_{\Gamma} + \lambda\mathrm{tr}(\boldsymbol{\varepsilon}_{\Gamma})\mathbb{I}]\cdot\mathbf{P} \\ &= \mathbf{P}\cdot\left[2\mu\boldsymbol{\varepsilon}_{\Gamma}^{\mathrm{dir}} + \lambda\mathrm{tr}(\boldsymbol{\varepsilon}_{\Gamma}^{\mathrm{dir}})\mathbb{I}\right]\cdot\mathbf{P}\ ,\end{aligned} \tag{4.13}$$

where $\mu = \frac{E}{2(1+\nu)}$ and $\lambda = \frac{E\nu}{(1-\nu^2)}$ are the Lamé constants and $\boldsymbol{\varepsilon}_{\Gamma}^{\mathrm{dir}}$ is the directional strain tensor from Eq. 4.8. With this identity the in-plane stress tensor can be computed only with the directional strain tensor

$$\boldsymbol{\varepsilon}_{\Gamma}^{\mathrm{dir}} = \boldsymbol{\varepsilon}_{\Gamma,\mathrm{Mem}}^{\mathrm{dir}}(\boldsymbol{u}) + \zeta\boldsymbol{\varepsilon}_{\Gamma,\mathrm{Bend}}^{\mathrm{dir}}(\boldsymbol{w})\ , \tag{4.14}$$

with

$$\begin{aligned}\boldsymbol{\varepsilon}_{\Gamma,\mathrm{Mem}}^{\mathrm{dir}} &= \frac{1}{2}(\nabla_{\Gamma}^{\mathrm{dir}}\boldsymbol{u} + (\nabla_{\Gamma}^{\mathrm{dir}}\boldsymbol{u})^{\mathrm{T}})\ , \\ \boldsymbol{\varepsilon}_{\Gamma,\mathrm{Bend}}^{\mathrm{dir}} &= -\begin{bmatrix}\boldsymbol{u}_{,xx}^{\mathrm{dir}}\cdot\boldsymbol{n}_{\Gamma} & \frac{1}{2}(\boldsymbol{u}_{,yx}^{\mathrm{dir}} + \boldsymbol{u}_{,xy}^{\mathrm{dir}})\cdot\boldsymbol{n}_{\Gamma} & \frac{1}{2}(\boldsymbol{u}_{,zx}^{\mathrm{dir}} + \boldsymbol{u}_{,xz}^{\mathrm{dir}})\cdot\boldsymbol{n}_{\Gamma} \\ & \boldsymbol{u}_{,yy}^{\mathrm{dir}}\cdot\boldsymbol{n}_{\Gamma} & \frac{1}{2}(\boldsymbol{u}_{,zy}^{\mathrm{dir}} + \boldsymbol{u}_{,yz}^{\mathrm{dir}})\cdot\boldsymbol{n}_{\Gamma} \\ \mathrm{sym} & & \boldsymbol{u}_{,zz}^{\mathrm{dir}}\cdot\boldsymbol{n}_{\Gamma}\end{bmatrix}\ ,\end{aligned}$$

which is, from an implementational point of view, an advantage because covariant derivatives are not needed explicitly. In contrast to the classical theory, the in-plane stress tensor expressed in terms of the TDC does not require the computation of the metric coefficients in the material law. Therefore, the resulting stress tensor does not rely on a parametrization of the mid-surface and the shell analysis based on implicitly defined surfaces is enabled.

The stress tensor is only a function of the mid-surface displacement vector $\boldsymbol{u}$, the difference vector $\boldsymbol{w}(\boldsymbol{u})$ and the thickness parameter ζ. This enables an analytical pre-integration with respect to the thickness and stress resultants can be identified. The following quantities are equivalent to the stress resultants in the classical theory [7], [133], but they are expressed in terms of the TDC using a global Cartesian coordinate system.

The symmetric moment tensor $\mathbf{m}_\Gamma$ is defined as

$$\mathbf{m}_\Gamma = \int_{-t/2}^{t/2} \zeta \boldsymbol{\sigma}_\Gamma(\boldsymbol{u},\, \zeta)\; \mathrm{d}\zeta = \frac{t^3}{12} \boldsymbol{\sigma}_\Gamma(\boldsymbol{\varepsilon}^{\mathrm{P}}_{\Gamma,\mathrm{Bend}}) = \mathbf{P} \cdot \mathbf{m}^{\mathrm{dir}}_\Gamma \cdot \mathbf{P} \;, \tag{4.15}$$

which results in the components

$$\begin{aligned}
\left[\mathbf{m}^{\mathrm{dir}}_\Gamma\right]_{11} &= -D_\mathrm{B} \left(\boldsymbol{u}^{\mathrm{dir}}_{,xx} + \nu \boldsymbol{u}^{\mathrm{dir}}_{,yy} + \nu \boldsymbol{u}^{\mathrm{dir}}_{,zz}\right) \cdot \boldsymbol{n}_\Gamma \;, \\
\left[\mathbf{m}^{\mathrm{dir}}_\Gamma\right]_{22} &= -D_\mathrm{B} \left(\boldsymbol{u}^{\mathrm{dir}}_{,yy} + \nu \boldsymbol{u}^{\mathrm{dir}}_{,xx} + \nu \boldsymbol{u}^{\mathrm{dir}}_{,zz}\right) \cdot \boldsymbol{n}_\Gamma \;, \\
\left[\mathbf{m}^{\mathrm{dir}}_\Gamma\right]_{33} &= -D_\mathrm{B} \left(\boldsymbol{u}^{\mathrm{dir}}_{,zz} + \nu \boldsymbol{u}^{\mathrm{dir}}_{,xx} + \nu \boldsymbol{u}^{\mathrm{dir}}_{,yy}\right) \cdot \boldsymbol{n}_\Gamma \;, \\
\left[\mathbf{m}^{\mathrm{dir}}_\Gamma\right]_{12} &= -D_\mathrm{B} \, \frac{1-\nu}{2} (\boldsymbol{u}^{\mathrm{dir}}_{,yx} + \boldsymbol{u}^{\mathrm{dir}}_{,xy}) \cdot \boldsymbol{n}_\Gamma \;, \\
\left[\mathbf{m}^{\mathrm{dir}}_\Gamma\right]_{13} &= -D_\mathrm{B} \, \frac{1-\nu}{2} (\boldsymbol{u}^{\mathrm{dir}}_{,zx} + \boldsymbol{u}^{\mathrm{dir}}_{,xz}) \cdot \boldsymbol{n}_\Gamma \;, \\
\left[\mathbf{m}^{\mathrm{dir}}_\Gamma\right]_{23} &= -D_\mathrm{B} \, \frac{1-\nu}{2} (\boldsymbol{u}^{\mathrm{dir}}_{,zy} + \boldsymbol{u}^{\mathrm{dir}}_{,yz}) \cdot \boldsymbol{n}_\Gamma \;,
\end{aligned}$$

where $D_\mathrm{B} = \frac{Et^3}{12(1-\nu^2)}$ is the flexural rigidity of the shell. The moment tensor $\mathbf{m}_\Gamma$ is symmetric and an in-plane tensor. Therefore, one of the three eigenvalues is zero and the two non-zero eigenvalues of $\mathbf{m}_\Gamma$ are the principal bending moments m_1 and m_2. The principal moments are in agreement with the eigenvalues of the moment tensor in the classical setting, see [7]. For the effective normal force tensor $\tilde{\mathbf{n}}_\Gamma$ we have

$$\tilde{\mathbf{n}}_\Gamma = \int_{-t/2}^{t/2} \boldsymbol{\sigma}_\Gamma(\boldsymbol{u},\, \zeta)\; \mathrm{d}\zeta = t \boldsymbol{\sigma}_\Gamma(\boldsymbol{\varepsilon}^{\mathrm{P}}_{\Gamma,\mathrm{Mem}}) = \mathbf{P} \cdot \mathbf{n}^{\mathrm{dir}}_\Gamma \cdot \mathbf{P} \;, \tag{4.16}$$

with the components

$$\begin{aligned}
\left[\mathbf{n}^{\mathrm{dir}}_\Gamma\right]_{11} &= D_\mathrm{M} \left[u^\Gamma_{x,x} + \nu(u^\Gamma_{y,y} + u^\Gamma_{z,z})\right] \;, \\
\left[\mathbf{n}^{\mathrm{dir}}_\Gamma\right]_{22} &= D_\mathrm{M} \left[u^\Gamma_{y,y} + \nu(u^\Gamma_{x,x} + u^\Gamma_{z,z})\right] \;, \\
\left[\mathbf{n}^{\mathrm{dir}}_\Gamma\right]_{33} &= D_\mathrm{M} \left[u^\Gamma_{z,z} + \nu(u^\Gamma_{x,x} + u^\Gamma_{y,y})\right] \;, \\
\left[\mathbf{n}^{\mathrm{dir}}_\Gamma\right]_{12} &= D_\mathrm{M} \left[\frac{1-\nu}{2}(u^\Gamma_{x,y} + u^\Gamma_{y,x})\right] \;, \\
\left[\mathbf{n}^{\mathrm{dir}}_\Gamma\right]_{13} &= D_\mathrm{M} \left[\frac{1-\nu}{2}(u^\Gamma_{x,z} + u^\Gamma_{z,x})\right] \;, \\
\left[\mathbf{n}^{\mathrm{dir}}_\Gamma\right]_{23} &= D_\mathrm{M} \left[\frac{1-\nu}{2}(u^\Gamma_{y,z} + u^\Gamma_{z,y})\right] \;,
\end{aligned}$$

where $D_\mathrm{M} = \frac{Et}{1-\nu^2}$. Similar to the moment tensor, the two non-zero eigenvalues of $\tilde{\mathbf{n}}_\Gamma$ are in agreement with those of the effective normal force tensor expressed in local coordinates. Note that for curved shells this tensor is *not* the physical normal force tensor. This tensor only appears in the variational formulation, see Section 4.2. The physical normal force tensor $\mathbf{n}^{\mathrm{real}}_\Gamma$ is defined by

$$\mathbf{n}^{\mathrm{real}}_\Gamma = \tilde{\mathbf{n}}_\Gamma + \mathbf{H} \cdot \mathbf{m}_\Gamma \tag{4.17}$$

and is, in general, not symmetric but also has one zero eigenvalue. The occurrence of the zero eigenvalues in $\mathbf{m}_\Gamma$, $\tilde{\mathbf{n}}_\Gamma$ and $\mathbf{n}_\Gamma^{\text{real}}$ is due to fact that these tensors are in-plane tensors, i.e., $\mathbf{m}_\Gamma \cdot \boldsymbol{n}_\Gamma = \boldsymbol{n}_\Gamma^{\text{T}} \cdot \mathbf{m}_\Gamma = \mathbf{0}$. The normal vector $\boldsymbol{n}_\Gamma$ is the corresponding eigenvector to the zero eigenvalue and the other two eigenvectors are tangential. It is noted that the vectors and tensors defined in the frame of the TDC live in the three-dimensional space. In contrast, in the classical theory based on curvilinear coordinates, these are quanitites given in two dimensions.

4.1.3 Equilibrium

4.1.3.1 Equilibrium in strong form

Based on the stress resultants from above, one obtains the equilibrium for a curved shell in terms of the TDC using a global Cartesian coordinate system in strong form as

$$\text{div}_\Gamma \mathbf{n}_\Gamma^{\text{real}} + \boldsymbol{n}_\Gamma \text{div}_\Gamma(\mathbf{P} \cdot \text{div}_\Gamma \mathbf{m}_\Gamma) + \mathbf{H} \cdot \text{div}_\Gamma \mathbf{m}_\Gamma = -\boldsymbol{f} \ , \tag{4.18}$$

with $\boldsymbol{f}$ being the load vector per area on the mid-surface Γ. In the classical theory, see, e.g., [7], the force equilibrium is often split into tangential and normal direction

$$\mathbf{P} \cdot \text{div}_\Gamma \mathbf{n}_\Gamma^{\text{real}} + \mathbf{H} \cdot \text{div}_\Gamma \mathbf{m}_\Gamma = -\boldsymbol{f}_t \ , \tag{4.19}$$

$$-\mathbf{H} : \mathbf{n}_\Gamma^{\text{real}} + \text{div}_\Gamma(\mathbf{P} \cdot \text{div}_\Gamma \mathbf{m}_\Gamma) = -f_n \ . \tag{4.20}$$

Expanding the physical normal force tensor $\text{div}_\Gamma \mathbf{n}_\Gamma^{\text{real}}$, converts the equilibrium from Eq. 4.18 to

$$\text{div}_\Gamma \tilde{\mathbf{n}}_\Gamma + \boldsymbol{n}_\Gamma \text{div}_\Gamma(\mathbf{P} \cdot \text{div}_\Gamma \mathbf{m}_\Gamma) + 2\mathbf{H} \cdot \text{div}_\Gamma \mathbf{m}_\Gamma + \sum_{i,k=1}^{3} [\partial x_i^\Gamma \mathbf{H}]_{jk} [\mathbf{m}_\Gamma]_{ki} = -\boldsymbol{f} \ . \tag{4.21}$$

The obtained equilibrium does not rely on a parametrization of the mid-surface, but in the presence of a parametrization it becomes equivalent to the equilibrium in local coordinates [7], [139]. From this point of view, the reformulation of the linear Kirchhoff-Love shell equations in terms of the TDC may be seen as a generalization, because it holds for explicit *and* implicit geometry definitions. With boundary conditions, as shown in detail in Section 4.1.3.3, the complete fourth-order boundary value problem (BVP) is defined.

Based on the equilibrium in Eq. 4.18, the transverse shear force vector $\boldsymbol{q}$ is defined as

$$\boldsymbol{q} = \mathbf{P} \cdot \text{div}_\Gamma \mathbf{m}_\Gamma \ . \tag{4.22}$$

Note that in the special case of *flat* Kirchhoff-Love shells embedded in $\mathbb{R}^3$, the divergence of an in-plane tensor is a tangential vector, as already mentioned in Section 2.2. Therefore, the definition of the transverse shear force vector in [82] is in agreement with the obtained transverse shear force vector herein.

4.1.3.2 Equilibrium in weak form

The equilibrium in strong form is converted to a weak form by multiplying Eq. 4.18 with a suitable test function $\boldsymbol{v}$ and integrating over the domain, leading to

$$\begin{aligned} -\int_\Gamma \boldsymbol{v} \cdot \{ &\mathrm{div}_\Gamma \tilde{\mathbf{n}}_\Gamma + \boldsymbol{n}_\Gamma \mathrm{div}_\Gamma (\mathbf{P} \cdot \mathrm{div}_\Gamma \mathbf{m}_\Gamma) + 2\mathbf{H} \cdot \mathrm{div}_\Gamma \mathbf{m}_\Gamma \\ &+ [\partial x_i^\Gamma \mathbf{H}]_{jk} [\mathbf{m}_\Gamma]_{ki} \} \, \mathrm{d}A = \int_\Gamma \boldsymbol{v} \cdot \boldsymbol{f} \, \mathrm{d}A \ . \end{aligned} \tag{4.23}$$

With Green's formula from Section 2.2, we introduce the continuous weak form of the equilibrium: Find $\boldsymbol{u} \in \mathcal{V}^{\mathrm{KL}} : \Gamma \to \mathbb{R}^3$ such that

$$a(\boldsymbol{u}, \, \boldsymbol{v}) = \langle \boldsymbol{F}, \, \boldsymbol{v} \rangle \quad \forall \, \boldsymbol{v} \in \mathcal{V}^{\mathrm{KL}} \ , \tag{4.24}$$

with

$$\begin{aligned} a(\boldsymbol{u}, \, \boldsymbol{v}) &= \int_\Gamma \nabla_\Gamma^{\mathrm{dir}} \boldsymbol{v} : \tilde{\mathbf{n}}_\Gamma - \boldsymbol{\varepsilon}_{\Gamma,\mathrm{B}}^{\mathrm{dir}}(\boldsymbol{v}) : \mathbf{m}_\Gamma \, \mathrm{d}A, \\ \langle \boldsymbol{F}, \, \boldsymbol{v} \rangle &= \int_\Gamma \boldsymbol{f} \cdot \boldsymbol{v} \, \mathrm{d}A - \int_{\partial\Gamma_\mathrm{N}} \nabla_\Gamma^{\mathrm{dir}} (\boldsymbol{v} \cdot \boldsymbol{n}_\Gamma) \cdot (\mathbf{m}_\Gamma \cdot \boldsymbol{n}_{\partial\Gamma}) \\ &\qquad - 2(\mathbf{H} \cdot \boldsymbol{v}) \cdot (\mathbf{m}_\Gamma \cdot \boldsymbol{n}_{\partial\Gamma}) - \boldsymbol{v} \cdot (\tilde{\mathbf{n}}_\Gamma \cdot \boldsymbol{n}_{\partial\Gamma}) \\ &\qquad - (\boldsymbol{v} \cdot \boldsymbol{n}_\Gamma) \, (\mathbf{P} \cdot \mathrm{div}_\Gamma \mathbf{m}_\Gamma \cdot \boldsymbol{n}_{\partial\Gamma}) \ \mathrm{d}s \ . \end{aligned}$$

The corresponding function spaces are

$$\mathcal{V}^{\mathrm{KL}} = \{ \boldsymbol{u} : \Gamma \to \mathbb{R}^3 \mid \boldsymbol{u} \in [\mathcal{H}^1(\Gamma)]^3 : \boldsymbol{u}_{,ji} \cdot \boldsymbol{n}_\Gamma \in [\mathcal{L}^2(\Gamma)]^3 \} \ , \tag{4.25}$$

$$\mathcal{V}_0^{\mathrm{KL}} = \{ \boldsymbol{v} \in \mathcal{V}^{\mathrm{KL}}(\Gamma) : \boldsymbol{v}|_{\partial\Gamma_\mathrm{D}} = \mathbf{0} \} \ , \tag{4.26}$$

where the Dirichlet boundary is labelled $\partial\Gamma_\mathrm{D}$ and the Neumann boundary $\partial\Gamma_\mathrm{N}$. Following this procedure has the advantage that the boundary terms naturally occur and directly allow to consider for mechanically meaningful boundary conditions.

4.1.3.3 Boundary conditions

As well-known in the classical Kirchhoff-Love shell theory, special attention has to be paid to the boundary conditions. In the following, the boundary terms of the weak form in Eq. 4.24 are rearranged in order to derive the effective boundary forces.

Using Eqs. (4.17) and (4.4), we have

$$\begin{aligned} -\int_{\partial\Gamma_\mathrm{N}} &\nabla_\Gamma^{\mathrm{dir}} (\boldsymbol{v} \cdot \boldsymbol{n}_\Gamma) \cdot (\mathbf{m}_\Gamma \cdot \boldsymbol{n}_{\partial\Gamma}) - 2(\mathbf{H} \cdot \boldsymbol{v}) \cdot (\mathbf{m}_\Gamma \cdot \boldsymbol{n}_{\partial\Gamma}) \\ &- \boldsymbol{v} \cdot (\tilde{\mathbf{n}}_\Gamma \cdot \boldsymbol{n}_{\partial\Gamma}) - (\boldsymbol{v} \cdot \boldsymbol{n}_\Gamma) \, (\mathbf{P} \cdot \mathrm{div}_\Gamma \mathbf{m}_\Gamma \cdot \boldsymbol{n}_{\partial\Gamma}) \ \mathrm{d}s \ = \\ \int_{\partial\Gamma_\mathrm{N}} &\boldsymbol{v} \cdot (\mathbf{n}_\Gamma^{\mathrm{real}} \cdot \boldsymbol{n}_{\partial\Gamma}) + \boldsymbol{w}(\boldsymbol{v}) \cdot (\mathbf{m}_\Gamma \cdot \boldsymbol{n}_{\partial\Gamma}) \\ &+ (\boldsymbol{v} \cdot \boldsymbol{n}_\Gamma) \cdot (\mathbf{P} \cdot \mathrm{div}_\Gamma \mathbf{m}_\Gamma \cdot \boldsymbol{n}_{\partial\Gamma}) \ \mathrm{d}s \ . \end{aligned} \tag{4.27}$$

As already mentioned above, the difference vector $\boldsymbol{w}$ is a tangential vector. Consequently, the difference vector at the boundary may be expressed in terms of the tangential vectors $\boldsymbol{t}_{\partial\Gamma}$ and $\boldsymbol{n}_{\partial\Gamma}$

$$\boldsymbol{w}(\boldsymbol{v}) = \underbrace{[\mathbf{H} \cdot \boldsymbol{v} - \nabla_\Gamma(\boldsymbol{v} \cdot \boldsymbol{n}_\Gamma)] \cdot \boldsymbol{n}_{\partial\Gamma}}_{\omega_{\boldsymbol{t}_{\partial\Gamma}}} \boldsymbol{n}_{\partial\Gamma} + \underbrace{[\mathbf{H} \cdot \boldsymbol{v} - \nabla_\Gamma(\boldsymbol{v} \cdot \boldsymbol{n}_\Gamma)] \cdot \boldsymbol{t}_{\partial\Gamma}}_{\omega_{\boldsymbol{n}_{\partial\Gamma}}} \boldsymbol{t}_{\partial\Gamma} \ , \tag{4.28}$$

where $\omega_{\boldsymbol{t}_{\partial\Gamma}}$ may be interpreted as rotation along the boundary and $\omega_{\boldsymbol{n}_{\partial\Gamma}}$ is the rotation in co-normal direction, when the test function $\boldsymbol{v}$ is interpreted as a displacement, see Fig. 4.2(a). Analogously to the difference vector, the expressions $\mathbf{n}_\Gamma^{\mathrm{real}} \cdot \boldsymbol{n}_{\partial\Gamma}$ and $\mathbf{m}_\Gamma \cdot \boldsymbol{n}_{\partial\Gamma}$ in Eq. 4.27 are decomposed in a similar manner

$$\mathbf{n}_\Gamma^{\mathrm{real}} \cdot \boldsymbol{n}_{\partial\Gamma} = \underbrace{(\mathbf{n}_\Gamma^{\mathrm{real}} \cdot \boldsymbol{n}_{\partial\Gamma}) \cdot \boldsymbol{t}_{\partial\Gamma}}_{p_{\boldsymbol{t}_{\partial\Gamma}}} \boldsymbol{t}_{\partial\Gamma} + \underbrace{(\mathbf{n}_\Gamma^{\mathrm{real}} \cdot \boldsymbol{n}_{\partial\Gamma}) \cdot \boldsymbol{n}_{\partial\Gamma}}_{p_{\boldsymbol{n}_{\partial\Gamma}}} \boldsymbol{n}_{\partial\Gamma} \ , \tag{4.29}$$

$$\mathbf{m}_\Gamma \cdot \boldsymbol{n}_{\partial\Gamma} = \underbrace{(\mathbf{m}_\Gamma \cdot \boldsymbol{n}_{\partial\Gamma}) \cdot \boldsymbol{n}_{\partial\Gamma}}_{m_{\boldsymbol{t}_{\partial\Gamma}}} \boldsymbol{n}_{\partial\Gamma} + \underbrace{(\mathbf{m}_\Gamma \cdot \boldsymbol{n}_{\partial\Gamma}) \cdot \boldsymbol{t}_{\partial\Gamma}}_{m_{\boldsymbol{n}_{\partial\Gamma}}} \boldsymbol{t}_{\partial\Gamma} \ . \tag{4.30}$$

The term $p_{\boldsymbol{n}_\Gamma} = \mathbf{P} \cdot \mathrm{div}_\Gamma \mathbf{m}_\Gamma \cdot \boldsymbol{n}_{\partial\Gamma}$ represents the resultant force in normal direction. Inserting these expressions in Eq. 4.27, the integral along the Neumann boundary simplifies to

$$\int_{\partial\Gamma_{\mathrm{N}}} \boldsymbol{v} \cdot (p_{\boldsymbol{t}_{\partial\Gamma}} \boldsymbol{t}_{\partial\Gamma} + p_{\boldsymbol{n}_{\partial\Gamma}} \boldsymbol{n}_{\partial\Gamma} + p_{\boldsymbol{n}_\Gamma} \boldsymbol{n}_\Gamma) + \omega_{\boldsymbol{t}_{\partial\Gamma}} m_{\boldsymbol{t}_{\partial\Gamma}} + \omega_{\boldsymbol{n}_{\partial\Gamma}} m_{\boldsymbol{n}_{\partial\Gamma}} \ \mathrm{d}s \ . \tag{4.31}$$

As discussed in detail, e.g., in [7], the rotation in co-normal direction $\omega_{\boldsymbol{n}_{\partial\Gamma}}$ is already prescribed with $\boldsymbol{v}|_{\partial\Gamma}$. Therefore, the term $\omega_{\boldsymbol{n}_{\partial\Gamma}} m_{\boldsymbol{n}_{\partial\Gamma}}$ is expanded and with integration by parts we obtain

$$\begin{aligned} \int_{\partial\Gamma_{\mathrm{N}}} \omega_{\boldsymbol{n}_{\partial\Gamma}} m_{\boldsymbol{n}_{\partial\Gamma}} \ \mathrm{d}s &= \int_{\partial\Gamma_{\mathrm{N}}} -\nabla_\Gamma(\boldsymbol{v} \cdot \boldsymbol{n}_\Gamma) \cdot \boldsymbol{t}_{\partial\Gamma} \, m_{\boldsymbol{n}_{\partial\Gamma}} + \mathbf{H} \cdot \boldsymbol{v} \cdot \boldsymbol{t}_{\partial\Gamma} \, m_{\boldsymbol{n}_{\partial\Gamma}} \mathrm{d}s \\ &= \int_{\partial\Gamma_{\mathrm{N}}} (\boldsymbol{v} \cdot \boldsymbol{n}_\Gamma) \cdot (\nabla_\Gamma m_{\boldsymbol{n}_{\partial\Gamma}} \cdot \boldsymbol{t}_{\partial\Gamma}) + \mathbf{H} \cdot \boldsymbol{v} \cdot \boldsymbol{t}_{\partial\Gamma} \, m_{\boldsymbol{n}_{\partial\Gamma}} \ \mathrm{d}s \\ &\quad - (\boldsymbol{v} \cdot \boldsymbol{n}_\Gamma) m_{\boldsymbol{n}_{\partial\Gamma}} \Big|_{+C}^{-C} \ , \end{aligned} \tag{4.32}$$

where $+C$ and $-C$ are points close to a corner C. The new boundary term represents the Kirchhoff forces or corner forces F_c. Note that if the boundary of the shell is smooth, the corner forces vanish. Finally, the integral over the Neumann boundary, with the "$-$" in front of Eq. 4.24 is expressed in terms of the well-known effective boundary forces and the bending moment along the boundary

$$\int_{\partial\Gamma_{\mathrm{N}}} \boldsymbol{v} \cdot (\tilde{p}_{\boldsymbol{t}_{\partial\Gamma}} \boldsymbol{t}_{\partial\Gamma} + \tilde{p}_{\boldsymbol{n}_{\partial\Gamma}} \boldsymbol{n}_{\partial\Gamma} + \tilde{p}_{\boldsymbol{n}_\Gamma} \boldsymbol{n}_\Gamma) + \omega_{\boldsymbol{t}_{\partial\Gamma}} m_{\boldsymbol{t}_{\partial\Gamma}} \ \mathrm{d}s - (\boldsymbol{v} \cdot \boldsymbol{n}_\Gamma) F_c \ , \tag{4.33}$$

with

$$\tilde{p}_{\boldsymbol{t}_{\partial\Gamma}} = p_{\boldsymbol{t}_{\partial\Gamma}} + (\mathbf{H}\cdot\boldsymbol{t}_{\partial\Gamma})\cdot\boldsymbol{t}_{\partial\Gamma}\, m_{\boldsymbol{n}_{\partial\Gamma}} \ , \tag{4.34}$$

$$\tilde{p}_{\boldsymbol{n}_{\partial\Gamma}} = p_{\boldsymbol{n}_{\partial\Gamma}} + (\mathbf{H}\cdot\boldsymbol{t}_{\partial\Gamma})\cdot\boldsymbol{n}_{\partial\Gamma}\, m_{\boldsymbol{n}_{\partial\Gamma}} \ , \tag{4.35}$$

$$\tilde{p}_{\boldsymbol{n}_{\Gamma}} = p_{\boldsymbol{n}_{\Gamma}} + \nabla_{\Gamma} m_{\boldsymbol{n}_{\partial\Gamma}}\cdot\boldsymbol{t}_{\partial\Gamma} \ . \tag{4.36}$$

In Fig. 4.2(b) the forces and bending moments along a curved boundary are illustrated. The obtained effective boundary forces and moments are in agreement with the given quantities in local coordinates [7], [139]. The mechanically useful boundary conditions are the conjugated displacements and rotations to the effective forces and moments at the boundary

(a) displacements and rotation **(b)** effective forces and bending moment

Fig. 4.2: Boundary conditions for the Kirchhoff-Love shell in terms of the local triad $(\boldsymbol{t}_{\partial\Gamma}, \boldsymbol{n}_{\partial\Gamma}, \boldsymbol{n}_{\Gamma})$: (a) Decomposition of the mid-surface displacement $\boldsymbol{u}$ and the rotation $\omega_{\boldsymbol{t}_{\partial\Gamma}}$ along the boundary, and (b) conjugated, effective forces, bending moment and corner forces at the boundary.

$$\begin{aligned}
\tilde{p}_{\boldsymbol{t}_{\partial\Gamma}} &\quad\Longleftrightarrow\quad & \boldsymbol{u}\cdot\boldsymbol{t}_{\partial\Gamma} &= u_{\boldsymbol{t}_{\partial\Gamma}} \ ,\\
\tilde{p}_{\boldsymbol{n}_{\partial\Gamma}} &\quad\Longleftrightarrow\quad & \boldsymbol{u}\cdot\boldsymbol{n}_{\partial\Gamma} &= u_{\boldsymbol{n}_{\partial\Gamma}} \ ,\\
\tilde{p}_{\boldsymbol{n}_{\Gamma}} &\quad\Longleftrightarrow\quad & \boldsymbol{u}\cdot\boldsymbol{n}_{\Gamma} &= u_{\boldsymbol{n}_{\Gamma}} \ ,\\
m_{\boldsymbol{t}_{\partial\Gamma}} &\quad\Longleftrightarrow\quad & \omega_{\boldsymbol{t}_{\partial\Gamma}} &= \left[\mathbf{H}\cdot\boldsymbol{u} - \nabla_{\Gamma}(\boldsymbol{u}\cdot\boldsymbol{n}_{\Gamma})\right]\cdot\boldsymbol{n}_{\partial\Gamma} \ ,\\
& & &= -\left[(\nabla_{\Gamma}^{\mathrm{dir}}\boldsymbol{u})^{\mathrm{T}}\cdot\boldsymbol{n}_{\Gamma}\right]\cdot\boldsymbol{n}_{\partial\Gamma} \ .
\end{aligned}$$

In conclusion, for the unknown displacement field $\boldsymbol{u}$ and the rotation $\omega_{\boldsymbol{t}_{\partial\Gamma}}$ along the boundary there exist two non-overlapping parts at the boundary of the shell $\partial\Gamma$. In particular, the Dirichlet boundary $\partial\Gamma_{\mathrm{D},i}$ and the Neumann boundary $\partial\Gamma_{\mathrm{N},i}$ with $i \in \{\boldsymbol{u}, \omega\}$. The corresponding boundary conditions are

$$\begin{aligned}
\boldsymbol{u} &= \hat{\boldsymbol{g}}_{\boldsymbol{u}} \ \text{ on } \partial\Gamma_{\mathrm{D},\boldsymbol{u}} \ ,\\
\tilde{\boldsymbol{p}} &= \hat{\boldsymbol{p}} \ \text{ on } \partial\Gamma_{\mathrm{N},\boldsymbol{u}} \ ,\\
\omega_{\boldsymbol{t}_{\partial\Gamma}} = -[\nabla_{\Gamma}^{\mathrm{dir}}\boldsymbol{u}^{\mathrm{T}}\cdot\boldsymbol{n}_{\Gamma}]\cdot\boldsymbol{n}_{\partial\Gamma} &= \hat{g}_{\omega} \ \text{ on } \partial\Gamma_{\mathrm{D},\omega} \ ,\\
m_{\boldsymbol{t}_{\partial\Gamma}} = \boldsymbol{n}_{\partial\Gamma}\cdot\mathbf{m}_{\Gamma}\cdot\boldsymbol{n}_{\partial\Gamma} &= \hat{m} \ \text{ on } \partial\Gamma_{\mathrm{N},\omega} \ ,
\end{aligned} \tag{4.37}$$

where $\hat{\boldsymbol{g}}_{\boldsymbol{u}}$ are the displacements, $\hat{\boldsymbol{p}}$ are the conjugated, effective forces to $\boldsymbol{u}$, $\hat{g}_{\omega}$ is the rotation along the boundaries and $\hat{m}$ is the conjugated bending moment to $\omega_{\boldsymbol{t}_{\partial\Gamma}}$ at their corresponding parts of the boundary. In Tab. 4.1, common support types are given. With the quantities from above, other boundary conditions (e.g., membrane support, …) may be derived accordingly.

Clamped edge	$\hat{g}_{\boldsymbol{t}_{\partial\Gamma}} = 0$	$\hat{g}_{\boldsymbol{n}_{\partial\Gamma}} = 0$	$\hat{g}_{\boldsymbol{n}_{\Gamma}} = 0$	$\hat{g}_{\omega} = 0$
Simply supported edge	$\hat{g}_{\boldsymbol{t}_{\partial\Gamma}} = 0$	$\hat{g}_{\boldsymbol{n}_{\partial\Gamma}} = 0$	$\hat{g}_{\boldsymbol{n}_{\Gamma}} = 0$	$\hat{m} = 0$
Symmetry support	$\hat{p}_{\boldsymbol{t}_{\partial\Gamma}} = 0$	$\hat{g}_{\boldsymbol{n}_{\partial\Gamma}} = 0$	$\hat{p}_{\boldsymbol{n}_{\Gamma}} = 0$	$\hat{g}_{\omega} = 0$
Free edge	$\hat{p}_{\boldsymbol{t}_{\partial\Gamma}} = 0$	$\hat{p}_{\boldsymbol{n}_{\partial\Gamma}} = 0$	$\hat{p}_{\boldsymbol{n}_{\Gamma}} = 0$	$\hat{m} = 0$

Tab. 4.1: Set of common boundary conditions for Kirchhoff-Love shells.

4.2 Discretization

The previously derived continuous weak form can be discretized with different finite element approaches such as the classical Surface FEM or more recent approaches such as the CutFEM [21], [22], [28], [54] and TraceFEM [73], [109], [111], [119]. Herein, the weak form of the BVP is discretized using isogeometric analysis (IGA) as proposed by Hughes et al. [34], [88], being closely related to Surface FEM using NURBS-based test and trial functions.

The NURBS patch T_Γ is the mid-surface of the shell and the elements T are defined by the knot spans of the patch. Linking isogeometric analysis to standard FE terminology, one may naturally refer to (i) the NURBS patch as the “mesh”, (ii) the knot spans as the “elements”, and (iii) the NURBS functions as the shape, test, and/or trial functions. The shape functions $M_j^k(\boldsymbol{x}), \boldsymbol{x} \in \Gamma$ are defined by means of the isoparametric concept and are NURBS of order k with $j = 1, \ldots, n_c$ being the number of control points. The shape functions are employed for all (physical) fields and naturally fulfil the continuity requirements of the Kirchhoff-Love BVP. We avoid the mathematical definition of NURBS and the resulting patches here because of the abundance of literature devoted to IGA and consider this as common state of the art, see, e.g., [34], [115].

The surface derivatives of the shape functions $\nabla_\Gamma M(\boldsymbol{x})$ are computed as defined in Eq. 2.13, similar to the Surface FEM [42], [52], [62], [65] using NURBS instead of Lagrange polynomials as trial and test functions. A general finite element space of order k is now defined by

$$\mathcal{N}_\Gamma^k = \left\{ u^h \in C^{k-1}(\Gamma), u^h(\boldsymbol{x}) = \sum_{j=1}^{n_c} M_j^k(\boldsymbol{x})\hat{u}_j \, , \; \hat{u}_j \in \mathbb{R} \right\} \, , \tag{4.38}$$

where the degrees of freedom $\hat{u}_j$ are stored at the control points. The shape functions of order $k \geq 2$ are in the function space $\mathcal{V}^{\mathrm{KL}}$, see Eq. 4.25. In fact, the used shape functions are in the Sobolev space $[\mathcal{H}^k(\Gamma)]^3 \subset \mathcal{V}^{\mathrm{KL}}$ iff $k \geq 2$.

The discrete displacement of the mid-surface results as $\boldsymbol{u}^h = u^{h,i}\boldsymbol{E}_i$, with $\boldsymbol{E}_i$ being Cartesian base vectors, with $i = 1, 2, 3$ and $u^{h,i} = \boldsymbol{M}^{\mathrm{T}} \cdot \hat{\boldsymbol{u}}^i$. Herein, the essential boundary conditions are enforced weakly with Lagrange multipliers or the non-symmetric version of Nitsche's method. Similar as in Section 3.3.2, both approaches lead to two different discrete weak forms which are introduced in the following.

4.2.1 Lagrange multipliers

The Lagrange multiplier field for the displacements is labelled $\boldsymbol{\lambda}^h_{\boldsymbol{u}} \in \mathbb{R}^3$ and the Lagrange multipliers for the rotation along the boundary as $\lambda^h_\omega \in \mathbb{R}$. The shape functions of $\boldsymbol{\lambda}^h_{\boldsymbol{u}}$ are defined as $M_{\lambda_{\boldsymbol{u}}} = \{M|_{\partial\Gamma_{\mathrm{D},\boldsymbol{u}}}\}$ and λ^h_ω for $M_{\lambda_\omega} = \{M|_{\partial\Gamma_{\mathrm{D},\omega}}\}$ in the sense of a trace. Note that shape functions of the Lagrange multipliers are NURBS of the same order than the shape functions of the displacements. Based on this, the following discrete trial and test functions spaces are defined

$$\mathcal{S}^{\mathrm{KL},h}_{\boldsymbol{u}} = \mathcal{V}^{\mathrm{KL},h}_{\boldsymbol{u}} = \left\{ \boldsymbol{u}^h \in \left[\mathcal{N}^k_\Gamma\right]^3 \right\} \ , \tag{4.39}$$

$$\mathcal{L}^{\mathrm{KL},h}_{\boldsymbol{\lambda}_{\boldsymbol{u}}} = \mathcal{V}^{\mathrm{KL},h}_{\boldsymbol{\lambda}_{\boldsymbol{u}}} = \left\{ \boldsymbol{\lambda}^h_{\boldsymbol{u}}|_{\partial\Gamma_{\mathrm{D},\boldsymbol{u}}} : \ \boldsymbol{\lambda}^h_{\boldsymbol{u}} \in \mathcal{S}^{\mathrm{KL},h}_{\boldsymbol{u}} \right\} \ , \tag{4.40}$$

$$\mathcal{L}^{\mathrm{KL},h}_{\lambda_\omega} = \mathcal{V}^{\mathrm{KL},h}_{\lambda_\omega} = \left\{ \lambda^h_\omega|_{\partial\Gamma_{\mathrm{D},\omega}} : \ \lambda^h_\omega \in \mathcal{N}^k_\Gamma \right\} \ . \tag{4.41}$$

The discrete weak form of the Kirchhoff-Love shell with Lagrange multipliers reads as follows: Given Young's modulus $E \in \mathbb{R}^+$, Poisson's ratio $\nu \in [0,\, 0.5]$, surface load $\boldsymbol{f}$ on Γ, traction and corner forces $(\hat{\boldsymbol{p}}, \hat{F}_c)$ on $\partial\Gamma_{\mathrm{N},\boldsymbol{u}}$, bending moments $\hat{m}$ on $\partial\Gamma_{\mathrm{N},\omega}$ and boundary conditions $\hat{\boldsymbol{g}}_{\boldsymbol{u}}$ on $\partial\Gamma_{\mathrm{D},\boldsymbol{u}}$, $\hat{g}_\omega$ on $\partial\Gamma_{\mathrm{D},\omega}$, find the displacement field $\boldsymbol{u}^h \in \mathcal{S}^{\mathrm{KL},h}_{\boldsymbol{u}}$ and the Lagrange multiplier fields $(\boldsymbol{\lambda}^h_{\boldsymbol{u}},\, \lambda^h_\omega) \in \mathcal{L}^{\mathrm{KL},h}_{\boldsymbol{\lambda}_{\boldsymbol{u}}} \times \mathcal{L}^{\mathrm{KL},h}_{\lambda_\omega}$ such that for all test functions $(\boldsymbol{v}^h,\, \boldsymbol{v}^h_{\boldsymbol{\lambda}_{\boldsymbol{u}}},\, v^h_{\lambda_\omega}) \in \mathcal{V}^{\mathrm{KL},h}_{\boldsymbol{u}} \times \mathcal{V}^{\mathrm{KL},h}_{\boldsymbol{\lambda}_{\boldsymbol{u}}} \times \mathcal{V}^{\mathrm{KL},h}_{\lambda_\omega}$, there holds in Γ

$$\begin{aligned}
\int_\Gamma \nabla^{\mathrm{dir}}_\Gamma \boldsymbol{v}^h : \tilde{\mathbf{n}}_\Gamma - \boldsymbol{\varepsilon}^{\mathrm{dir}}_{\Gamma,\mathrm{B}}(\boldsymbol{v}^h) : \mathbf{m}_\Gamma \,\mathrm{d}A + \int_{\partial\Gamma_{\mathrm{D},\boldsymbol{u}}} \boldsymbol{v}^h \cdot \boldsymbol{\lambda}^h_{\boldsymbol{u}} \,\mathrm{d}s + \int_{\partial\Gamma_{\mathrm{D},\omega}} \omega_{\boldsymbol{t}_{\partial\Gamma}}(\boldsymbol{v}^h)\, \lambda^h_\omega \,\mathrm{d}s \\
= \int_\Gamma \boldsymbol{f} \cdot \boldsymbol{v}^h \,\mathrm{d}A + \int_{\partial\Gamma_{\mathrm{N},\boldsymbol{u}}} \boldsymbol{v}^h \cdot \hat{\boldsymbol{p}} \,\mathrm{d}s + \int_{\partial\Gamma_{\mathrm{N},\omega}} \omega_{\boldsymbol{t}_{\partial\Gamma}}(\boldsymbol{v}^h) \hat{m} \,\mathrm{d}s - (\boldsymbol{v}^h \cdot \boldsymbol{n}_\Gamma)\hat{F}_c \ , \\
\int_{\partial\Gamma_{\mathrm{D},\boldsymbol{u}}} \boldsymbol{\lambda}^h_{\boldsymbol{u}} \cdot \boldsymbol{u}^h \,\mathrm{d}s = \int_{\partial\Gamma_{\mathrm{D},\boldsymbol{u}}} \boldsymbol{v}^h_{\boldsymbol{\lambda}_{\boldsymbol{u}}} \cdot \hat{\boldsymbol{g}}_{\boldsymbol{u}} \,\mathrm{d}s \ , \\
\int_{\partial\Gamma_{\mathrm{D},\omega}} \lambda^h_\omega\, \omega_{\boldsymbol{t}_{\partial\Gamma}}(\boldsymbol{u}^h) \,\mathrm{d}s = \int_{\partial\Gamma_{\mathrm{D},\omega}} v^h_{\lambda_\omega} \hat{g}_\omega \,\mathrm{d}s \ .
\end{aligned} \tag{4.42}$$

The usual assembly yields a linear system of equations in the form

$$\begin{bmatrix} \mathbf{K}_{\mathrm{Stiff}} & \mathbf{C} \\ \mathbf{C}^{\mathrm{T}} & \mathbf{0} \end{bmatrix} \cdot \begin{bmatrix} \hat{\underline{\boldsymbol{u}}} \\ \hat{\boldsymbol{\lambda}} \end{bmatrix} = \begin{bmatrix} \boldsymbol{b}_{\mathrm{Load}} \\ \boldsymbol{b}_{\boldsymbol{\lambda}} \end{bmatrix} \ , \tag{4.43}$$

with $[\hat{\underline{\boldsymbol{u}}},\, \hat{\boldsymbol{\lambda}}]^{\mathrm{T}} = [\hat{\boldsymbol{u}}_x,\, \hat{\boldsymbol{u}}_y,\, \hat{\boldsymbol{u}}_z,\, \hat{\boldsymbol{\lambda}}]$ being the sought displacements of the control points and Lagrange multipliers. Note that in the case of homogeneous Dirichlet boundary conditions, $\boldsymbol{b}_{\boldsymbol{\lambda}} = \mathbf{0}$. As usual in the context of Lagrange multiplier methods, Eq. 4.43 has a saddle point structure and the well-known Babuška-Brezzi condition [4], [17], [60] must be satisfied in order to obtain useful solutions in all involved fields. With this choice of discrete functions spaces, see Eq. 4.39 to Eq. 4.41, bounded condition numbers, unique solutions, and the expected rates of convergence for the presented test cases in Section 4.3 are observed. Based on this observations, the discrete inf-sup condition seems to be satisfied herein.

The resulting element stiffness matrix $\mathbf{K}_{\text{Elem}}$ is a 3×3 block matrix and is divided into a membrane and bending part

$$\mathbf{K}_{\text{Elem}} = \mathbf{K}_{\text{Elem,M}} + \mathbf{K}_{\text{Elem,B}} \; . \tag{4.44}$$

The membrane part is defined by

$$\mathbf{K}_{\text{Elem,M}} = t \int_\Gamma P_{ib} \cdot [\hat{\mathbf{K}}]_{bj} \; \mathrm{d}A \; , \tag{4.45}$$

$$[\hat{\mathbf{K}}]_{kj} = \mu(\delta_{kj} \boldsymbol{M}^\Gamma_{,a} \cdot \boldsymbol{M}^{\Gamma^\mathrm{T}}_{,a} + \boldsymbol{M}^\Gamma_{,j} \cdot \boldsymbol{M}^{\Gamma^\mathrm{T}}_{,k}) + \lambda \boldsymbol{M}^\Gamma_{,k} \cdot \boldsymbol{M}^{\Gamma^\mathrm{T}}_{,j} \; , \tag{4.46}$$

summation over a and b. The matrix $\hat{\mathbf{K}}$ is determined by directional first-order derivatives of the shape functions $\boldsymbol{M}$. One may recognize that the structure of the matrix $\hat{\mathbf{K}}$ is similar to the stiffness matrix of 3D linear elasticity problems, however, here only integrated on the shell surface. For the bending part we have

$$[\mathbf{K}_{\text{Elem,B}}]_{ij} = D_\mathrm{B} \int_\Gamma n_i n_j \tilde{\mathbf{K}} \; \mathrm{d}A \; , \tag{4.47}$$

$$\tilde{\mathbf{K}} = (1-\nu) \boldsymbol{M}^{\text{cov}}_{,ab} \cdot \boldsymbol{M}^{\text{cov}^\mathrm{T}}_{,ab} + \nu \boldsymbol{M}^{\text{cov}}_{,cc} \cdot \boldsymbol{M}^{\text{cov}^\mathrm{T}}_{,dd} \; . \tag{4.48}$$

A summation over a, b on the one hand and c, d on the other has to be performed. The first term of $\tilde{\mathbf{K}}$ is the contraction of the covariant Hessian matrix $\mathbf{He}^{\text{cov}}_\Gamma$ and the second term may be identified as the Bi-Laplace operator. Note that for the Bi-Laplace operator also directional derivatives may be used due to the fact that the trace of second order derivatives is invariant, although the components differ. This suggests a further rearrangement of the contraction of the covariant Hessian matrix in order to use only directional derivatives, which is preferred from an implementational point of view. The equivalent expression of $\tilde{\mathbf{K}}$ using only second-order directional derivatives is

$$\tilde{\mathbf{K}} = (1-\nu) P_{ea} \boldsymbol{M}^{\text{dir}}_{,ab} \cdot \boldsymbol{M}^{\text{dir}^\mathrm{T}}_{,be} + \nu \boldsymbol{M}^{\text{dir}}_{,cc} \cdot \boldsymbol{M}^{\text{dir}^\mathrm{T}}_{,dd} \; , \tag{4.49}$$

with summation over a, b, c and d, e as above. When the shell is given through a parametrization, the resulting element stiffness matrix in the classical theory, e.g., [33] is equivalent to the element stiffness matrix from above, but in the classical setting the computation may be found more cumbersome due to fact that the local basis vectors and the metric tensor in co- and contravariant form has to be computed. In contrast, herein, the surface gradients and second-order derivatives are first applied to the shape functions (NURBS or classical finite element functions) to obtain $\boldsymbol{M}^\Gamma_{,i}$, $\boldsymbol{M}^{\text{dir}}_{,ij}$ and $\boldsymbol{M}^{\text{cov}}_{,ij}$, which is independent of the application. In this sense, a significant part of the complexity of implementing shells is shifted to finite element technology and may be recycled for any kind of boundary value problems on curved surfaces in $\mathbb{R}^3$. Examples are transport problems [42], [49], [52] or flow problems [62], [90] on curved surfaces. We expect that future implementations in finite element software will provide frameworks for solving PDEs on manifolds and, based, e.g., on this work will also apply to shells.

With the shape functions of the Lagrange multipliers $(\boldsymbol{M}_{\lambda_{\boldsymbol{u}}}, \boldsymbol{M}_{\lambda_\omega})$, the constraint matrix $\mathbf{C}$ for simply supported edges is defined by

$$\mathbf{C} = \int_{\partial\Gamma_{\mathrm{D},\boldsymbol{u}}} \begin{bmatrix} \boldsymbol{M}\cdot\boldsymbol{M}^{\mathrm{T}}_{\lambda_{\boldsymbol{u}}} & \mathbf{0} & \mathbf{0} \\ \mathbf{0} & \boldsymbol{M}\cdot\boldsymbol{M}^{\mathrm{T}}_{\lambda_{\boldsymbol{u}}} & \mathbf{0} \\ \mathbf{0} & \mathbf{0} & \boldsymbol{M}\cdot\boldsymbol{M}^{\mathrm{T}}_{\lambda_{\boldsymbol{u}}} \end{bmatrix} \mathrm{d}s \ , \tag{4.50}$$

for clamped edges

$$\mathbf{C} = \int_{\partial\Gamma_{\mathrm{D},\boldsymbol{u}}\cap\partial\Gamma_{\mathrm{D},\omega}} \begin{bmatrix} \boldsymbol{M}\cdot\boldsymbol{M}^{\mathrm{T}}_{\lambda_{\boldsymbol{u}}} & \mathbf{0} & \mathbf{0} & (n_x n_{\partial\Gamma_i}\boldsymbol{M}^{\Gamma}_{,i})\cdot\boldsymbol{M}^{\mathrm{T}}_{\lambda_\omega} \\ \mathbf{0} & \boldsymbol{M}\cdot\boldsymbol{M}^{\mathrm{T}}_{\lambda_{\boldsymbol{u}}} & \mathbf{0} & (n_y n_{\partial\Gamma_i}\boldsymbol{M}^{\Gamma}_{,i})\cdot\boldsymbol{M}^{\mathrm{T}}_{\lambda_\omega} \\ \mathbf{0} & \mathbf{0} & \boldsymbol{M}\cdot\boldsymbol{M}^{\mathrm{T}}_{\lambda_{\boldsymbol{u}}} & (n_z n_{\partial\Gamma_i}\boldsymbol{M}^{\Gamma}_{,i})\cdot\boldsymbol{M}^{\mathrm{T}}_{\lambda_\omega} \end{bmatrix} \mathrm{d}s \ , \tag{4.51}$$

and for symmetry supports

$$\mathbf{C} = \int_{\partial\Gamma_{\mathrm{D},\boldsymbol{u}}\cap\partial\Gamma_{\mathrm{D},\omega}} \begin{bmatrix} n_{\partial\Gamma_x}\boldsymbol{M}\cdot\boldsymbol{M}^{\mathrm{T}}_{\lambda_{\boldsymbol{u}}} & (n_x n_{\partial\Gamma_i}\boldsymbol{M}^{\Gamma}_{,i})\cdot\boldsymbol{M}^{\mathrm{T}}_{\lambda_\omega} \\ n_{\partial\Gamma_y}\boldsymbol{M}\cdot\boldsymbol{M}^{\mathrm{T}}_{\lambda_{\boldsymbol{u}}} & (n_y n_{\partial\Gamma_i}\boldsymbol{M}^{\Gamma}_{,i})\cdot\boldsymbol{M}^{\mathrm{T}}_{\lambda_\omega} \\ n_{\partial\Gamma_z}\boldsymbol{M}\cdot\boldsymbol{M}^{\mathrm{T}}_{\lambda_{\boldsymbol{u}}} & (n_z n_{\partial\Gamma_i}\boldsymbol{M}^{\Gamma}_{,i})\cdot\boldsymbol{M}^{\mathrm{T}}_{\lambda_\omega} \end{bmatrix} \mathrm{d}s \ . \tag{4.52}$$

Note that all constraint matrices have three block-rows referring to the unknowns $\hat{\boldsymbol{u}}_x, \hat{\boldsymbol{u}}_y, \hat{\boldsymbol{u}}_z$.

4.2.2 Non-symmetric version of Nitsche's method

The Nitsche terms which have to be added to the weak form in order to enforce the displacements $\hat{\boldsymbol{g}}_{\boldsymbol{u}}$ and rotations $\hat{g}_\omega$ at the Dirichlet boundaries are the energy conjugated terms for the displacements and rotation at their Dirichlet boundaries

$$\int_{\partial\Gamma_{\mathrm{D},\boldsymbol{u}}} \left(\hat{\boldsymbol{g}}_{\boldsymbol{u}} - \boldsymbol{u}^h\right)\cdot\tilde{\boldsymbol{p}}(\boldsymbol{v}^h)\ \mathrm{d}s + \left(\hat{\boldsymbol{g}}_{\boldsymbol{u}} - \boldsymbol{u}^h\right)\cdot\boldsymbol{n}_\Gamma m_{\boldsymbol{n}\partial\Gamma}(\boldsymbol{v}^h)\Big|_{+C}^{-C} \ , \tag{4.53}$$

$$\int_{\partial\Gamma_{\mathrm{D},\omega}} \left[\hat{g}_\omega - \omega_{\boldsymbol{t}\partial\Gamma}(\boldsymbol{u}^h)\right] m_{\boldsymbol{t}\partial\Gamma}(\boldsymbol{v}^h)\ \mathrm{d}s \ . \tag{4.54}$$

Adding these terms to the RHS of Eq. 4.24 with the discrete displacement field $\boldsymbol{u}^h$ and its corresponding test function $\boldsymbol{v}^h$ and reordering terms yields

$$\begin{aligned} a(\boldsymbol{u}^h, \boldsymbol{v}^h) \quad & - \int_{\partial\Gamma_{\mathrm{D},\boldsymbol{u}}} \boldsymbol{v}^h\cdot\tilde{\boldsymbol{p}}(\boldsymbol{u}^h)\ \mathrm{d}s + \boldsymbol{v}^h\cdot\boldsymbol{n}_\Gamma m_{\boldsymbol{n}\partial\Gamma}(\boldsymbol{u}^h)\Big|_{+C}^{-C} \\ & + \int_{\partial\Gamma_{\mathrm{D},\boldsymbol{u}}} \boldsymbol{u}^h\cdot\tilde{\boldsymbol{p}}(\boldsymbol{v}^h)\ \mathrm{d}s - \boldsymbol{u}^h\cdot\boldsymbol{n}_\Gamma m_{\boldsymbol{n}\partial\Gamma}(\boldsymbol{v}^h)\Big|_{+C}^{-C} \\ & - \int_{\partial\Gamma_{\mathrm{D},\omega}} \omega_{\boldsymbol{t}\partial\Gamma}(\boldsymbol{v}^h) m_{\boldsymbol{t}\partial\Gamma}(\boldsymbol{u}^h)\ \mathrm{d}s + \int_{\partial\Gamma_{\mathrm{D},\omega}} \omega_{\boldsymbol{t}\partial\Gamma}(\boldsymbol{u}^h) m_{\boldsymbol{t}\partial\Gamma}(\boldsymbol{v}^h)\ \mathrm{d}s \\ = \langle \boldsymbol{F},\, \boldsymbol{v}^h\rangle & + \int_{\partial\Gamma_{\mathrm{D},\boldsymbol{u}}} \hat{\boldsymbol{g}}_{\boldsymbol{u}}\cdot\tilde{\boldsymbol{p}}(\boldsymbol{v}^h)\ \mathrm{d}s + \hat{\boldsymbol{g}}_{\boldsymbol{u}}\cdot\boldsymbol{n}_\Gamma m_{\boldsymbol{n}\partial\Gamma}(\boldsymbol{v}^h)\Big|_{+C}^{-C} \\ & \int_{\partial\Gamma_{\mathrm{D},\omega}} \hat{g}_\omega m_{\boldsymbol{t}\partial\Gamma}(\boldsymbol{v}^h)\ \mathrm{d}s \ . \end{aligned} \tag{4.55}$$

Applying integration by parts on the effective normal force $\widetilde{p}_{\boldsymbol{n}_\Gamma}$, we can get rid of the corner forces. Furthermore, a shift of the rather cumbersome derivative on the drilling moment $m_{\boldsymbol{n}_{\partial\Gamma}}$ in $\widetilde{p}_{\boldsymbol{n}_\Gamma}$, see Eq. 4.36, simplifies the obtained terms in Eq. 4.55 significantly. The resulting discrete weak form for the Kirchhoff-Love shell with the non-symmetric version of Nitsche's method reads as follows: Given Young's modulus $E \in \mathbb{R}^+$, Poisson's ratio $\nu \in [0, 0.5]$, surface load $\boldsymbol{f}$ on Γ, traction and corner forces $(\hat{\boldsymbol{p}}, \hat{F}_c)$ on $\partial\Gamma_{\text{N},\boldsymbol{u}}$, bending moments $\hat{m}$ on $\partial\Gamma_{\text{N},\omega}$ and boundary conditions $\hat{\boldsymbol{g}}_{\boldsymbol{u}}$ on $\partial\Gamma_{\text{D},\boldsymbol{u}}$, $\hat{g}_\omega$ on $\partial\Gamma_{\text{D},\omega}$, find the displacement field $\boldsymbol{u}^h \in \mathcal{S}^{\text{KL},h,N}_{\boldsymbol{u}}$ such that for all test function $\boldsymbol{v}^h \in \mathcal{V}^{\text{KL},h,N}_{\boldsymbol{u}}$, there holds in Γ

$$\begin{aligned}
&\int_\Gamma \nabla^{\text{dir}}_\Gamma \boldsymbol{v}^h : \tilde{\mathbf{n}}_\Gamma(\boldsymbol{u}^h) - \boldsymbol{\varepsilon}^{\text{dir}}_{\Gamma,\text{B}}(\boldsymbol{v}^h) : \mathbf{m}_\Gamma(\boldsymbol{u}^h)\ \mathrm{d}A \\
&\quad - \underbrace{\int_{\partial\Gamma_{\text{D},\boldsymbol{u}}} \omega_{\boldsymbol{n}_{\partial\Gamma}}(\boldsymbol{v}^h) m_{\boldsymbol{n}_{\partial\Gamma}}(\boldsymbol{u}^h) + \boldsymbol{v}^h \cdot \boldsymbol{p}(\boldsymbol{u}^h)\ \mathrm{d}s}_{\text{bound. terms due to } \boldsymbol{v} \neq \boldsymbol{0} \text{ on } \partial\Gamma_{\text{D},\boldsymbol{u}}} - \underbrace{\int_{\partial\Gamma_{\text{D},\omega}} \omega_{\boldsymbol{t}_{\partial\Gamma}}(\boldsymbol{v}^h) m_{\boldsymbol{t}_{\partial\Gamma}}(\boldsymbol{u}^h)\ \mathrm{d}s}_{\text{bound. term due to } \boldsymbol{v} \neq \boldsymbol{0} \text{ on } \partial\Gamma_{\text{D},\omega}} \\
&\quad + \underbrace{\int_{\partial\Gamma_{\text{D},\boldsymbol{u}}} \omega_{\boldsymbol{n}_{\partial\Gamma}}(\boldsymbol{u}^h) m_{\boldsymbol{n}_{\partial\Gamma}}(\boldsymbol{v}^h) + \boldsymbol{u}^h \cdot \boldsymbol{p}(\boldsymbol{v}^h)\ \mathrm{d}s}_{\text{Nitsche terms for displ. on LHS}} + \underbrace{\int_{\partial\Gamma_{\text{D},\omega}} \omega_{\boldsymbol{t}_{\partial\Gamma}}(\boldsymbol{u}^h) m_{\boldsymbol{t}_{\partial\Gamma}}(\boldsymbol{v}^h)\ \mathrm{d}s}_{\text{Nitsche term for rot. on LHS}} \\
&= \int_\Gamma \boldsymbol{f} \cdot \boldsymbol{v}^h\ \mathrm{d}A + \int_{\partial\Gamma_{\text{N},\boldsymbol{u}}} \boldsymbol{v}^h \cdot \hat{\boldsymbol{p}}\ \mathrm{d}s + \int_{\partial\Gamma_{\text{N},\omega}} \omega_{\boldsymbol{t}_{\partial\Gamma}}(\boldsymbol{v}^h)\hat{m}\ \mathrm{d}s - (\boldsymbol{v}^h \cdot \boldsymbol{n}_\Gamma)\hat{F}_c \\
&\quad + \underbrace{\int_{\partial\Gamma_{\text{D},\boldsymbol{u}}} \hat{\boldsymbol{g}}_{\boldsymbol{u}} \cdot \boldsymbol{p}(\boldsymbol{v}^h) + \omega_{\boldsymbol{n}_{\partial\Gamma}}(\hat{\boldsymbol{g}}_{\boldsymbol{u}}) m_{\boldsymbol{n}_{\partial\Gamma}}(\boldsymbol{v}^h)\ \mathrm{d}s}_{\text{Nitsche terms for displ. on RHS}} + \underbrace{\int_{\partial\Gamma_{\text{D},\omega}} \hat{g}_\omega m_{\boldsymbol{t}_{\partial\Gamma}}(\boldsymbol{v}^h)\ \mathrm{d}s}_{\text{Nitsche term for rot. on RHS}}\ ,
\end{aligned} \tag{4.56}$$

where $\boldsymbol{p}$ are the standard boundary forces from Eq. 4.31 and $(\mathcal{S}^{\text{KL},h,N}_{\boldsymbol{u}}, \mathcal{V}^{\text{KL},h,N}_{\boldsymbol{u}})$ are the discrete function spaces for the Nitsche's method with the order $k \geq 3$ in Eq. 4.39. The reason for the higher continuity requirements are that in $p_{\boldsymbol{n}_\Gamma}$, third-order derivatives of $\boldsymbol{u}^h$ occur. A detailed discussion regarding the function spaces and analysis of Nitsche's method for Kirchhoff-Love shells is presented in [11].

Circumventing the corner forces and shifting the tangent derivative on the drilling moment has already been presented for the Kirchhoff plate in [121] and is, herein, straightforwardly extended to the Kirchhoff-Love shell. Compared to [78] this may lead to a more compact implementation of the Nitsche terms because the effective boundary forces are not needed explicitly in the implementation. Another approach for the symmetric version of Nitsche's method, where the corner forces explicitly appear in the variational formulation, is presented in [11]. Note that, in case of slip supports, e.g., membrane support, or displacement constraints in a selected, arbitrary unit direction $\boldsymbol{d}$ with the magnitude $\hat{G}_d$, the involved terms for the displacement along $\partial\Gamma_{\text{D},\boldsymbol{u}}$ in Eq. 4.56 have to be converted accordingly.

The usual element assembly yields a non-symmetric, linear system of equations in the form

$$\underbrace{(\mathbf{K}_{\text{Stiff}} + \mathbf{K}_{\text{Nitsche}})}_{\mathbf{K}} \cdot \underline{\hat{\boldsymbol{u}}} = \underbrace{(\boldsymbol{b}_{\text{Load}} + \boldsymbol{b}_{\text{Nitsche}})}_{\boldsymbol{b}}\ , \tag{4.57}$$

with $\underline{\hat{\boldsymbol{u}}}$ being the sought displacements of the control points. Note that the terms $(\mathbf{K}_{\text{Stiff}}, \boldsymbol{b}_{\text{Load}})$ are identical as in Eq. 4.43 and in case of homogeneous boundary conditions, the term $\boldsymbol{b}_{\text{Nitsche}}$ vanishes.

4.3 Numerical results

In this section the obtained shell equations in the frame of the TDC are carefully verified and compared to the classical approach with different test cases. As already mentioned above, the use of the Surface FEM in this isogeometric context leads to an equivalent stiffness matrix for arbitrarily curved and flat shells. Consequently, the same convergence properties as shown, e.g., in [33], [94] are expected. In the following, the results of the convergence analyses of a flat shell embedded in $\mathbb{R}^3$, the Scordelis-Lo roof, and the pinched cylinder test (part of the shell obstacle course proposed by Belytschko et al. [9]) are shown. Furthermore, a new test case with a challenging geometry is proposed which features smooth solutions enabling higher-order convergence rates. These rates are confirmed in the residual error as no analytic solution exists, see Section 4.3.4. Other examples (e.g., pinched hemispherical shell, shells of revolution, etc.) have been considered but are omitted as these performed equally well.

In the convergence studies, NURBS patches with different orders and numbers of knot spans in each direction are employed. This is equivalent to meshes with higher-order elements and $n \in \{2, 4, 8, 16, 32\}$ elements per side are used. The orders are varied as $p \in \{2, 3, 4, 5, 6\}$, $p = 1$ is not suitable as the resulting shape functions fail the continuity requirements. In the convergence analyses, the essential boundary conditions are enforced with both the Lagrange multiplier approach and the non-symmetric version of Nitsche's method. Both methods perform as expected and give optimal convergence rates if the involved fields are sufficiently smooth. In the following, the results obtained with the Lagrange multiplier approach are presented and the analogous results with the non-symmetric version of Nitsche's method are omitted for brevity.

4.3.1 Flat shell embedded in $\mathbb{R}^3$

Following a similar rationale as in [82], as a first test case, we consider a simple quadrilateral, flat shell with the normal vector $\boldsymbol{n}_\Gamma = [-1/4, -\sqrt{3}/2, \sqrt{3}/4]^{\mathrm{T}}$ in $\mathbb{R}^3$, see Fig. 4.3. The shell is simply supported at all edges. For verification, the load vector $\boldsymbol{f}$ is split into tangential $\boldsymbol{f}_t$ and normal f_n loads. The tangential loads are obtained with the method of manufactured solutions for a given displacement field $\boldsymbol{u}_t(\boldsymbol{x}) = \left[[1, 1]^{\mathrm{T}} \cdot 1/4 \sin(\pi r) \sin(\pi s) \right] \circ \boldsymbol{\chi}^{-1}(\boldsymbol{x})$. In normal direction, a sinusoidal load $f_n(\boldsymbol{x}) = [-D \sin(\pi r) \sin(\pi s)] \circ \boldsymbol{\chi}^{-1}(\boldsymbol{x})$ is applied to the shell. Herein, $\boldsymbol{\chi}$ is an affine mapping function (rigid-body rotation) from the horizontal parameter space to the real domain. An analytic solution for the normal displacements is easily obtained with $u_n(\boldsymbol{x}) = [-(\sin(\pi r) \sin(\pi s))/(4\pi^4)] \circ \boldsymbol{\chi}^{-1}(\boldsymbol{x})$, [136]. The shell is defined with $L = 1$ and the thickness is set to $t = 0.01$. The material parameters are: Young's modulus $E = 10\,000$ and the Poisson's ratio $\nu = 0.3$.

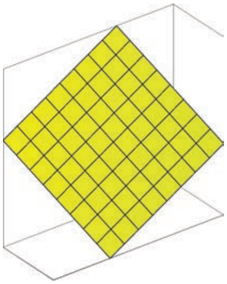

Geometry:	Quadrilateral flat shell $L = 1$ $t = 0.01$ $\boldsymbol{n}_\Gamma = [-{}^1\!/_4,\ -{}^{\sqrt{3}}\!/_2,\ {}^{\sqrt{3}}\!/_4]^\mathrm{T}$
Material parameters:	$E = 10\,000$ $\nu = 0.3$
Load:	$\boldsymbol{f}_t$ and f_n
Support:	Simple support on all edges

Fig. 4.3: Definition of flat shell problem.

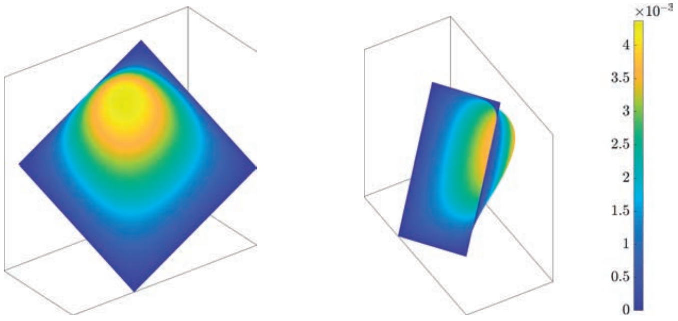

(a) front view **(b)** rotated view

Fig. 4.4: Displacement $\boldsymbol{u}$ of arbitrarily orientated flat shell, scaled by two orders of magnitude.

In Fig. 4.4, the solution of the shell is illustrated. The displacements are scaled by two orders of magnitude. The colours on the deformed surface indicate the Euclidean norm of the displacement field $\|\boldsymbol{u}\|$. In the convergence analyses, the relative L^2-error of the displacements $\boldsymbol{u}$, normal forces $\mathbf{n}_\Gamma^\mathrm{real}$, bending moments $\mathbf{m}_\Gamma$ and transverse shear forces $\mathbf{q}$ are considered. The theoretical, optimal orders of convergence w.r.t. the element size ${}^1\!/_n$ for the displacements, normal forces, bending moments and transverse shear forces are $\mathcal{O}(p+1), \mathcal{O}(p), \mathcal{O}(p-1), \mathcal{O}(p-2)$, respectively.

The results of the convergence analysis are shown in Fig. 4.5. The curves are plotted as a function of the element size ${}^1\!/_n$ (which is rather a characteristic length of the knot spans). The dotted lines indicate the theoretical optimal order of convergence. In Fig. 4.5(a), the relative L^2-error of the primal variable (displacements) is shown. Optimal higher-order convergence rates for $p \geq 3$ are achieved. In Fig. 4.5(b) to Fig. 4.5(d), the relative L^2-errors of the normal forces (membrane forces), bending moments and transverse shear forces are plotted. For all stress resultants and orders, the theoretical optimal orders of convergence are achieved. One may observe suboptimal convergence rates for $p = 2$ in the primal variable, while the convergence rates in the stress resultant are optimal. This phenomena has also been reported in [11]. It is clear that the same results were obtained

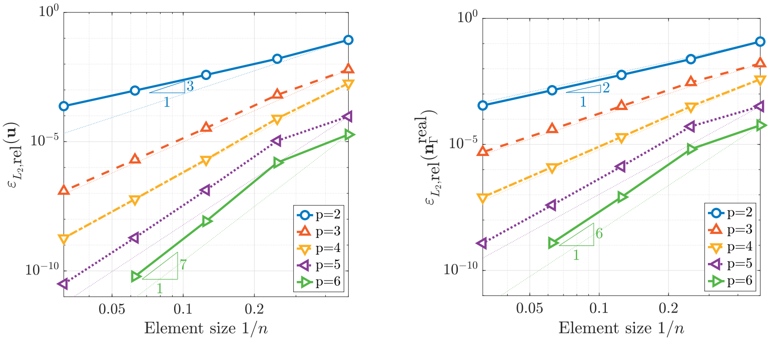

(a) relative L^2-norm of displacements $\boldsymbol{u}$

(b) relative L^2-norm of normal forces $\mathbf{n}_{\Gamma}^{\mathrm{real}}$

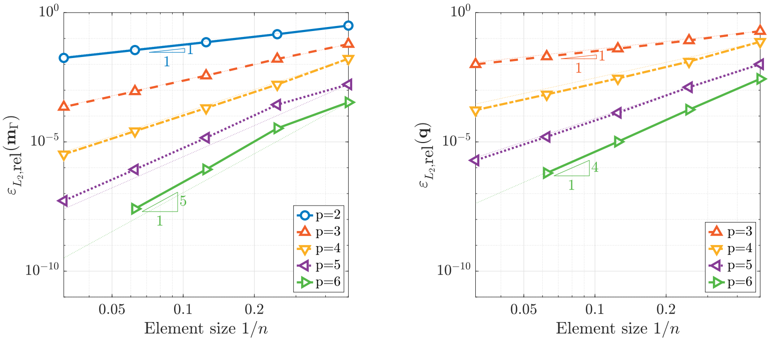

(c) relative L^2-norm of bending moments $\mathbf{m}_{\Gamma}$

(d) relative L^2-norm of transverse shear forces $\boldsymbol{q}$

Fig. 4.5: Convergence results for the rotated, flat shell.

if the results are computed for the purely two-dimensional case as, e.g., in [33].

4.3.2 Scordelis-Lo roof

The Scordelis-Lo roof is a cylindrical shell and is supported with two rigid diaphragms at the ends. The shell is loaded by gravity forces, see Fig. 4.6. The cylinder is defined with $L = 50$, $R = 25$ and the angle subtended by the roof is $\phi = 80°$. The thickness of the shell is set to $t = 0.25$. The material parameters are: Young's modulus $E = 4.32 \times 10^8$ and the Poisson's ratio $\nu = 0.0$. In contrast to the first example, the maximum vertical displacement $u_{z,\max}$ is compared to the reference solution $u_{z,\max,\mathrm{Ref}} = 0.3024$ as given in reference [9]. The largest vertical displacement occurs in the midpoint of the free edges at $[\pm R\cos(50°),\ 25,\ R\sin(50°)]^{\mathrm{T}}$.

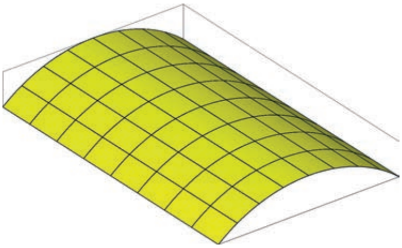

Geometry:	Cylindrical shell $L = 50$ $R = 25$ $\phi = 80°$ $t = 0.25$
Material parameters:	$E = 4.32 \times 10^8$ $\nu = 0.0$
Load:	Gravity load $\boldsymbol{f} = [0,\ 0,\ -90]^{\mathrm{T}}$
Support:	Rigid diaphragms at it ends

Fig. 4.6: Definition of Scordelis-Lo roof problem.

In Fig. 4.7(a), the numerical solution of the Scordelis-Lo roof is illustrated. The colours on the deformed surface indicate the Euclidean norm of the displacement field $\|\boldsymbol{u}\|$. The displacements are magnified by one order of magnitude. In Fig. 4.7(b), the convergence

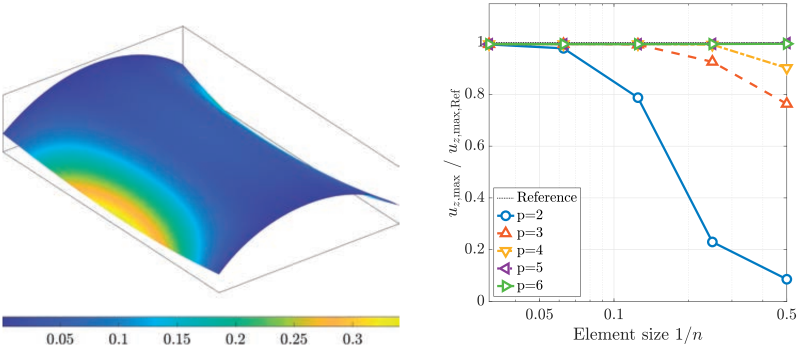

(a) displacement $\boldsymbol{u}$ **(b)** convergence

Fig. 4.7: Scordelis-Lo roof modelled as Kirchhoff-Love shell: (a) Displacement field $\boldsymbol{u}$ scaled by one order of magnitude, and (b) normalized convergence of reference displacement $u_{z,\max,\mathrm{Ref}} = 0.3024$.

of the maximum displacement $u_{z,\max}$ is plotted up to an order of $p = 6$ as a function of the element (knot span) size. It is clearly seen that the expected results are achieved, with increasing accuracy for higher-order NURBS. Due to the lack of a more accurate reference solution, it is not useful to show these results in a double-logarithmic diagram as usual for error plots. The style of presentation follows those of many other references such as, e.g., in [9], [33], [94].

4.3.3 Pinched cylinder

The next test case is a cylindrical shell pinched with two diametrically opposite unit loads located within the middle of the shell, see Fig. 4.8. The cylinder is defined with $L = 600$, $R = 300$. The thickness is set to $t = 3$. The material properties are: Young's modulus $E = 3 \times 10^6$ and the Poisson's ratio $\nu = 0.3$. The reference displacement at the loading points are $u_{\mathrm{Ref}} = 1.824\,88 \times 10^{-5}$ as given in reference [9]. Due to symmetry only one eighth of the geometry is modelled.

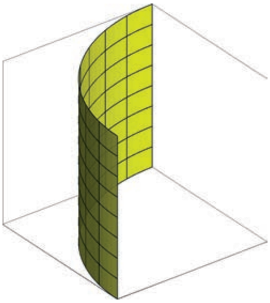

Geometry:	Cylinder (one eighth of cylinder modeled) $L/2 = 300$ $R = 300$ $\phi = 90°$ $t = 3$
Material parameters:	$E = 3 \times 10^6$ $\nu = 0.3$
Load:	Single unit forces
Support:	Rigid diaphragms at the top and symmetry boundary conditions

Fig. 4.8: Definition of the pinched cylinder problem.

In Fig. 4.9(a), the numerical solution of the pinched cylinder is illustrated with scaled displacements by a factor of 5×10^6. Similar as above, the colours on the deformed surface indicate the Euclidean norm of the displacement field $\|\boldsymbol{u}\|$.

As in the example before, in Fig. 4.9(b), the convergence to a normalized reference displacement as a function of the element size is plotted. The results confirm with the expected convergence behaviour as shown in [33], [94]. It is noted that due to the singularity in some mechanical quantities due to the single force, higher-order convergence rates are not possible here. However, the improvement for increasing the order of the NURBS is still seen in the figure. An additional grading of the elements in order to better resolve the singularity would have further improved the situation but is omitted here.

4.3.4 Flower-shaped shell

As a last example, a more complex geometry is considered, which enables smooth mechanical fields and thereby enables higher-order convergence rates. The geometry of the

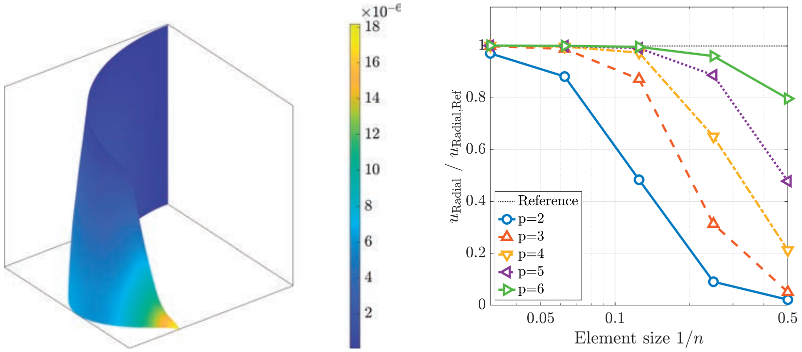

(a) displacement $\boldsymbol{u}$ **(b)** convergence

Fig. 4.9: Pinched cylinder: (a) Displacement $\boldsymbol{u}$ of one eighth of the geometry (scaled by a factor of 5×10^6), and (b) normalized convergence of reference displacement $u_{\text{Radial,Ref}} = 1.824\,88 \times 10^{-5}$ at loading points.

mid-surface is given with

$$\boldsymbol{x}_\Gamma(r,\, s) = \begin{bmatrix} (A-C)\cos(\theta) \\ (A-C)\sin(\theta) \\ 1-s^2 \end{bmatrix} \; , \tag{4.58}$$

where

$$\begin{aligned} & r,\, s \in [-1,\, 1] \; , \; A = 2.3 \; , \; B = 0.8 \; , \\ & \theta(r) = \pi(r+1) \; , \\ & C(r,\, s) = s[B + 0.3\cos(6\theta)] \; , \end{aligned}$$

and is illustrated in Fig. 4.10. On the right side of the figure, the boundary conditions and material parameters are defined. The mid-surface of the shell features varying principal curvatures and curved boundaries. The curved boundaries are clamped and

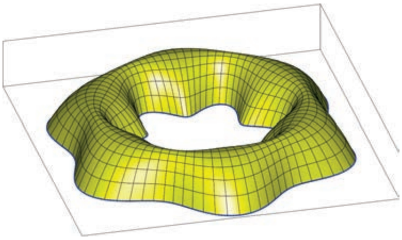

Geometry:	Flower shaped shell see Eq. 4.58 $t = 0.1\,\text{m}$
Material parameters:	$E = 1 \times 10^5\,\text{kN}\,\text{m}^{-2}$ $\nu = 0.3$
Load:	$\boldsymbol{f} = [1,\, 2,\, -10]^{\text{T}}\text{kN}\,\text{m}^{-2}$
Support:	Clamped edges at inner and outer boundary

Fig. 4.10: Definition of flower shaped shell problem for the Kirchhoff-Love shell.

the corresponding conditions (from Tab. 4.1) have to be properly enforced. An analytical solution or reference displacement is not available. Therefore, the error is measured in the strong form of the equilibrium from Eq. 4.18 which may be called residual error as done above in Section 3.3. In particular, this residual error is calculated as

$$\varepsilon^2_{\text{rel,residual}} = \frac{\int_\Gamma \left[\text{div}_\Gamma \mathbf{n}_\Gamma^{\text{real}} + \boldsymbol{n}_\Gamma \text{div}_\Gamma (\mathbf{P} \cdot \text{div}_\Gamma \mathbf{m}_\Gamma) + \mathbf{H} \cdot \text{div}_\Gamma \mathbf{m}_\Gamma + \boldsymbol{f}\right]^2 \, \mathrm{d}A}{\int_\Gamma \boldsymbol{f}^2 \, \mathrm{d}A} \,. \tag{4.59}$$

The computation of the residual error requires the evaluation of fourth-order surface derivatives. It is noteworthy that the implementation of these higher-order derivatives is not without efforts. For example, recall that mixed directional surface derivatives are not symmetric. That is, there are $3^4 = 81$ partial fourth-order derivatives. Nevertheless, provided that the displacement field is smooth enough, this error measure is a suitable quantity for the convergence analysis.

In Fig. 4.11(a), the deformed shell is illustrated. The displacement field is scaled by one order of magnitude. In Fig. 4.11(b), the results of the convergence analysis are plotted. Due to the fact that fourth-order derivatives need to be computed, at least fourth-order shape functions are required. The theoretical optimal order of convergence is $\mathcal{O}(p-3)$ if the solution is smooth enough. One may observe that higher-order convergence rates are achieved, however, rounding-off errors and the conditioning may slightly influence the convergence. Nevertheless, the results are excellent also given the fact that higher-order accurate results for shells (given in double-logarithmic error plots) are rare.

The stored elastic energy at the finest level with a polynomial order $p = 8$, which may be seen as an overkill solution, is $\mathfrak{e} = 1.7635958 \pm 1 \times 10^{-7}$ kN m. This stored elastic energy may be used for future benchmark tests, without the hassle to implement fourth-order derivatives on manifolds.

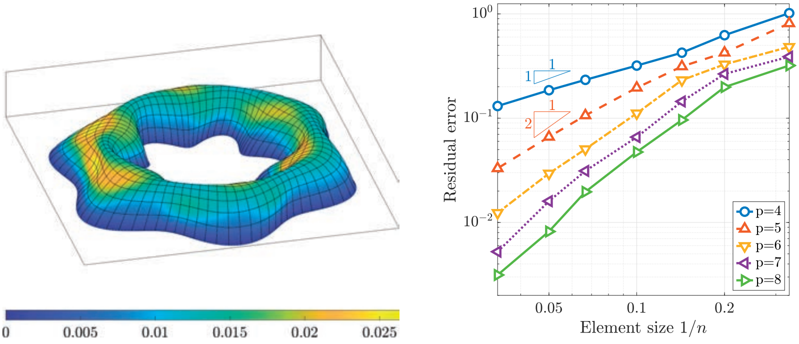

(a) displacement $\boldsymbol{u}$ **(b)** convergence

Fig. 4.11: Flower shaped shell modelled as Kirchhoff-Love shell: (a) Displacement $\boldsymbol{u}$ of flower shaped shell (scaled by one order of magnitude), and (b) residual error $\varepsilon_{\text{rel,residual}}$.

5 Linear Reissner-Mindlin shells

In this chapter, the linear Reissner-Mindlin shell, suitable to model thin and moderately thick shells, is reformulated in the frame of the TDC using a global Cartesian coordinate system. The rotation of the normal vector is modelled with a difference vector approach. As before, the reformulation includes all relevant mechanical quantities such as stress results and the computation of invariant quantities, e.g., principal moments. The resulting BVP in strong form is a set of second-order PDEs and is valid for explicitly *and* implicitly defined shells which generalizes the classical shell equations. In the numerical treatment, the shell BVP is discretized with both isogeometric analysis (IGA) as a variant of the Surface FEM on the one hand and the Trace FEM on the other. Therefore, the discrete weak forms for both finite element methods are introduced. The essential boundary conditions are enforced with Lagrange multipliers and the non-symmetric version of Nitsche's method, respectively. For the discretization of the tangential difference vector, different approaches which do not necessarily rely on a parametrization are elaborated in detail. The numerical results confirm higher-order convergence rates for both FEMs provided that the involved mechanical fields are sufficiently smooth.

The major content of this chapter follows our own articles in [127], [129].

5.1 Governing equations

In this section, we derive the linear Reissner-Mindlin shell theory or first-order shear deformation theory in the frame of tangential operators based on a global Cartesian coordinate system. As mentioned above, this has the advantage over classical shell theory that the resulting model is valid no matter whether a parametrization is available or not.

We restrict ourselves to infinitesimal deformations and rotations, which means that the reference and spatial configuration are indistinguishable. For simplicity, a linear elastic material governed by Hooke's law is assumed. In contrast to the Kirchhoff-Love shells, the additional constraint on the shell director is omitted, thus allowing transverse shear strains, leading to the well-known five-parameter shell models, e.g., [14]. Furthermore, we assume a constant shifter in the material law, which enables an analytical pre-integration in thickness direction.

Just as for the Kirchhoff-Love shells, the shell continuum Ω of thickness t may be defined implicitly with a signed distance function $\phi_{\mathrm{SDF}}(\boldsymbol{x})$,

$$\Omega = \left\{ \boldsymbol{x} \in \mathbb{R}^3 : |\phi_{\mathrm{SDF}}(\boldsymbol{x})| \leq \frac{t}{2} \right\} \ . \tag{5.1}$$

Alternatively, when the mid-surface Γ is parametrized with a map $\boldsymbol{x}_\Gamma(\boldsymbol{r})$, the domain of the shell is defined by

$$\boldsymbol{x} = \boldsymbol{x}_\Gamma + \zeta \boldsymbol{n}_\Gamma(\boldsymbol{x}_\Gamma) \ , \tag{5.2}$$

where ζ is the coordinate in thickness direction $|\zeta| \leq {}^t\!/\!_2$. Further details regarding the geometry definition are presented in Section 2.1.

5.1.1 Kinematics

For Reissner-Mindlin shells, the cross section remains straight after the deformation, but not necessarily normal to the mid-surface due to transverse shear deformations. Herein, the rotation of the normal vector is modelled with a standard difference vector formulation [53], [95]. Other approaches such as exponential maps, rotation tensors, etc. have been proposed, e.g., in [7], [14], [47], [132], [133], but are not considered here. The overall displacement of a point $\boldsymbol{P} \in \Omega$ is the difference between the spatial and reference configuration

$$\boldsymbol{u}_\Omega(\boldsymbol{x}) = \bar{\boldsymbol{P}}(\boldsymbol{x}) - \boldsymbol{P}(\boldsymbol{x}) \ ,$$

which takes the form

$$\boldsymbol{u}_\Omega(\boldsymbol{x}_\Gamma, \zeta) = \boldsymbol{u}(\boldsymbol{x}_\Gamma) + \zeta \boldsymbol{w}(\boldsymbol{x}_\Gamma) \ , \tag{5.3}$$

with $\boldsymbol{u}(\boldsymbol{x}_\Gamma) : \Gamma \to \mathbb{R}^3$ being the displacement of the mid-surface and $\boldsymbol{w}(\boldsymbol{x}_\Gamma) : \Gamma \to T_P\Gamma$ being the difference vector, describing the rotation of the normal vector. In contrast to the Kirchhoff-Love shell, transverse shear deformations $\boldsymbol{\gamma}$ are not neglected, which results in an additional rotation of the normal vector $\boldsymbol{n}_\Gamma$, as illustrated in Fig. 5.1. The difference vector $\boldsymbol{w}$ expressed in terms of the TDC is then defined as in [39], [125] with additional transverse shear deformations

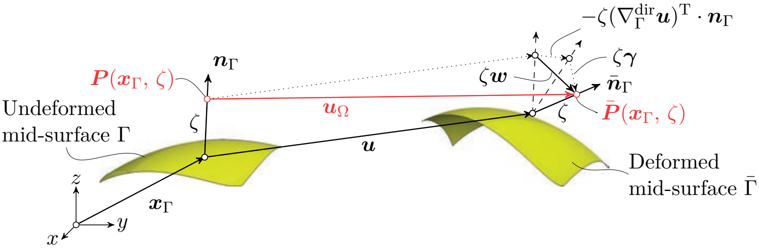

Fig. 5.1: Displacement field $\boldsymbol{u}_\Omega$ of the Reissner-Mindlin shell.

$$\boldsymbol{w}(\boldsymbol{x}_\Gamma) = -[\nabla_\Gamma^{\mathrm{dir}} \boldsymbol{u}(\boldsymbol{x}_\Gamma)]^{\mathrm{T}} \cdot \boldsymbol{n}_\Gamma + \boldsymbol{\gamma}(\boldsymbol{x}_\Gamma) \ . \tag{5.4}$$

Note that the difference vector is a tangential vector as in the classical theory. The surface gradient of $\boldsymbol{u}_\Omega(\boldsymbol{x})$ is given by

$$\begin{aligned}
\nabla_\Gamma^{\text{dir}} \boldsymbol{u}_\Omega(\boldsymbol{x}) &= \mathbf{P} \cdot \frac{\partial \boldsymbol{u}_\Omega(\boldsymbol{x})}{\partial \boldsymbol{x}} \cdot \frac{\partial \boldsymbol{x}}{\partial \boldsymbol{x}_\Gamma} \\
&= \mathbf{P} \cdot (\nabla \tilde{\boldsymbol{u}} + \nabla \zeta \otimes \boldsymbol{w} + \zeta \nabla \tilde{\boldsymbol{w}}) \cdot (\mathbb{I} + \zeta \mathbf{H}) \\
&= \left(\nabla_\Gamma^{\text{dir}} \boldsymbol{u} + \boldsymbol{n}_\Gamma \otimes \boldsymbol{w} + \zeta \nabla_\Gamma^{\text{dir}} \boldsymbol{w}\right) \cdot (\mathbb{I} + \zeta \mathbf{H}) \ .
\end{aligned}$$

with $\mathbf{H} = \nabla_\Gamma^{\text{dir}} \boldsymbol{n}_\Gamma$ being the Weingarten map and $(\mathbb{I} + \zeta \mathbf{H})$ is the inverse of the shell shifter, similar to Eq. 4.6. The linearised strain tensor $\boldsymbol{\varepsilon}_\Gamma$ is defined by the symmetric part of the surface gradient of $\boldsymbol{u}_\Omega$

$$\boldsymbol{\varepsilon}_\Gamma(\boldsymbol{x}) = \frac{1}{2} \left[\nabla_\Gamma^{\text{dir}} \boldsymbol{u}_\Omega + (\nabla_\Gamma^{\text{dir}} \boldsymbol{u}_\Omega)^{\text{T}}\right] = \boldsymbol{\varepsilon}_\Gamma^{\text{P}}(\boldsymbol{x}) + \boldsymbol{\varepsilon}_\Gamma^{\text{S}}(\boldsymbol{x}) \ , \tag{5.5}$$

and is split into an in-plane strain $\boldsymbol{\varepsilon}_\Gamma^{\text{P}}$ and a transverse shear strain $\boldsymbol{\varepsilon}_\Gamma^{\text{S}}$. Neglecting higher-order terms in thickness direction, as usual in the classical theory [14], the in-plane strain is defined by

$$\boldsymbol{\varepsilon}_\Gamma^{\text{P}} = \mathbf{P} \cdot \boldsymbol{\varepsilon}_\Gamma \cdot \mathbf{P} = \boldsymbol{\varepsilon}_{\Gamma,\,\text{Mem}}^{\text{P}} + \zeta \boldsymbol{\varepsilon}_{\Gamma,\,\text{Bend}}^{\text{P}} \ , \tag{5.6}$$

which is divided into a membrane and bending strain. The in-plane membrane strain becomes

$$\boldsymbol{\varepsilon}_{\Gamma,\,\text{Mem}}^{\text{P}}(\boldsymbol{u}) = \frac{1}{2} \left[\nabla_\Gamma^{\text{cov}} \boldsymbol{u} + (\nabla_\Gamma^{\text{cov}} \boldsymbol{u})^{\text{T}}\right] \ , \tag{5.7}$$

and the bending strain is

$$\boldsymbol{\varepsilon}_{\Gamma,\,\text{Bend}}^{\text{P}}(\boldsymbol{u}, \boldsymbol{w}) = \frac{1}{2} \left[\mathbf{H} \cdot \nabla_\Gamma^{\text{dir}} \boldsymbol{u} + (\nabla_\Gamma^{\text{dir}} \boldsymbol{u})^{\text{T}} \cdot \mathbf{H} + \nabla_\Gamma^{\text{cov}} \boldsymbol{w} + (\nabla_\Gamma^{\text{cov}} \boldsymbol{w})^{\text{T}}\right] \ . \tag{5.8}$$

The transverse shear strain is defined in a similar manner as in [84]

$$\begin{aligned}
\boldsymbol{\varepsilon}_\Gamma^{\text{S}}(\boldsymbol{u},\, \boldsymbol{w}) &= \mathbf{Q} \cdot \boldsymbol{\varepsilon}_\Gamma + \boldsymbol{\varepsilon}_\Gamma \cdot \mathbf{Q} & (5.9)\\
&= \frac{1}{2} \left[\mathbf{Q} \cdot \nabla_\Gamma^{\text{dir}} \boldsymbol{u} + (\nabla_\Gamma^{\text{dir}} \boldsymbol{u})^{\text{T}} \cdot \mathbf{Q} + \boldsymbol{n}_\Gamma \otimes \boldsymbol{w} + \boldsymbol{w} \otimes \boldsymbol{n}_\Gamma\right] \ . & (5.10)
\end{aligned}$$

When the shell surface is parametrized, the resulting strain components are equivalent compared to the classical theory in local coordinates, see, e.g., [7], [14], [53], [95]. In the case of *flat* shell structures, the membrane strain is only a function of the tangential part of the mid-surface displacement $\boldsymbol{u}_t = \mathbf{P} \cdot \boldsymbol{u}$. Since the curvature is zero in this case, the Weingarten map $\mathbf{H}$ vanishes. Therefore, the bending strain is only a function of the difference vector $\boldsymbol{w}$ and the transverse shear strain becomes a function of the normal displacement $u_n = \boldsymbol{u} \cdot \boldsymbol{n}_\Gamma$ and $\boldsymbol{w}$, resulting into the well-known Reissner-Mindlin *plate*, see, e.g., [112].

5.1.2 Constitutive equations and stress resultants

The shell is assumed to be linear elastic and, as usual for thin structures, the Lamé constants are chosen such that the normal stress in thickness direction is eliminated, hence,

$$\boldsymbol{\sigma}_\Gamma(\boldsymbol{x}) = 2\mu\boldsymbol{\varepsilon}_\Gamma(\boldsymbol{x}) + \lambda \mathrm{tr}[\boldsymbol{\varepsilon}_\Gamma(\boldsymbol{x})]\mathbb{I} \tag{5.11}$$

where $\mu = \frac{E}{2(1+\nu)}$ and $\lambda = \frac{E\nu}{1-\nu^2}$. The stress tensor is decomposed in a similar manner than above into in-plane (membrane and bending) stresses

$$\boldsymbol{\sigma}^{\mathrm{P}}_\Gamma(\boldsymbol{x}) = \mathbf{P} \cdot \left[2\mu\boldsymbol{\varepsilon}^{\mathrm{P}}_\Gamma(\boldsymbol{x}) + \lambda \mathrm{tr}[\boldsymbol{\varepsilon}^{\mathrm{P}}_\Gamma(\boldsymbol{x})]\mathbb{I}\right] \cdot \mathbf{P} \ , \tag{5.12}$$

and transverse shear stresses

$$\begin{aligned}\boldsymbol{\sigma}^{\mathrm{S}}_\Gamma(\boldsymbol{x}_\Gamma) &= 2\mu \left[\mathbf{Q} \cdot \boldsymbol{\varepsilon}^{\mathrm{S}}_\Gamma(\boldsymbol{x}_\Gamma) + \boldsymbol{\varepsilon}^{\mathrm{S}}_\Gamma(\boldsymbol{x}_\Gamma) \cdot \mathbf{Q}\right] + \lambda \mathrm{tr}\left[\boldsymbol{\varepsilon}^{\mathrm{S}}_\Gamma(\boldsymbol{x}_\Gamma)\right] \mathbf{Q} \ , \\ &= 2\mu\, \alpha_{\mathrm{s}}\, \boldsymbol{\varepsilon}^{\mathrm{S}}_\Gamma(\boldsymbol{x}_\Gamma) \ .\end{aligned} \tag{5.13}$$

As readily seen, the transverse shear stress is only a function of $\boldsymbol{x}_\Gamma$, which results in a constant transverse shear stress in thickness direction within the Reissner-Mindlin shell theory. In order to account for this, a shear correction factor α_{s} is introduced [14]. A common choice of the shear correction factor is $\alpha_{\mathrm{s}} = 5/6$. Note that due to the double projection with $\mathbf{P}$ in Eq. 5.12 of the in-plane stress, also directional gradients can be used, which is beneficial from an implementational point of view, see Eq. 4.13.

Assuming a constant shifter in the material law, the stress tensor $\boldsymbol{\sigma}_\Gamma(\boldsymbol{x})$ is only a function of the deflection of the mid-surface $\boldsymbol{u}$, the difference vector $\boldsymbol{w}$ and linear in thickness direction. This enables an analytical pre-integration with respect to the thickness and stress resultants such as effective membrane forces, bending moments, and transverse shear forces are identified. The following quantities are expressed in terms of the TDC using a global Cartesian coordinate system and are equivalent to the stress resultants in the classical theory using curvilinear coordinates, e.g., [7], [14].

The symmetric, in-plane moment tensor $\mathbf{m}_\Gamma$ is defined as

$$\mathbf{m}_\Gamma = \int_{-t/2}^{t/2} \zeta \boldsymbol{\sigma}^{\mathrm{P}}_\Gamma(\boldsymbol{x}) \ \mathrm{d}\zeta = \frac{t^3}{12}\boldsymbol{\sigma}_\Gamma(\boldsymbol{\varepsilon}^{\mathrm{P}}_{\Gamma,\mathrm{Bend}}) = \mathbf{P} \cdot \mathbf{m}^{\mathrm{dir}}_\Gamma \cdot \mathbf{P} \ , \tag{5.14}$$

resulting in the components

$$
\begin{aligned}
\left[\mathbf{m}_\Gamma^{\mathrm{dir}}\right]_{11} &= D_{\mathrm{B}}\left[w^\Gamma_{x,x} + [\mathbf{H}]_{1j}\cdot\boldsymbol{u}^{\mathrm{dir}}_{,x} + \nu(w^\Gamma_{y,y} + w^\Gamma_{z,z} + [\mathbf{H}]_{2j}\cdot\boldsymbol{u}^{\mathrm{dir}}_{,y} + [\mathbf{H}]_{3j}\cdot\boldsymbol{u}^{\mathrm{dir}}_{,z})\right] \ ,\\
\left[\mathbf{m}_\Gamma^{\mathrm{dir}}\right]_{22} &= D_{\mathrm{B}}\left[w^\Gamma_{y,y} + [\mathbf{H}]_{2j}\cdot\boldsymbol{u}^{\mathrm{dir}}_{,y} + \nu(w^\Gamma_{x,x} + w^\Gamma_{z,z} + [\mathbf{H}]_{1j}\cdot\boldsymbol{u}^{\mathrm{dir}}_{,x} + [\mathbf{H}]_{3j}\cdot\boldsymbol{u}^{\mathrm{dir}}_{,z})\right] \ ,\\
\left[\mathbf{m}_\Gamma^{\mathrm{dir}}\right]_{33} &= D_{\mathrm{B}}\left[w^\Gamma_{z,z} + [\mathbf{H}]_{3j}\cdot\boldsymbol{u}^{\mathrm{dir}}_{,z} + \nu(w^\Gamma_{x,x} + w^\Gamma_{y,y} + [\mathbf{H}]_{1j}\cdot\boldsymbol{u}^{\mathrm{dir}}_{,x} + [\mathbf{H}]_{2j}\cdot\boldsymbol{u}^{\mathrm{dir}}_{,y})\right] \ ,\\
\left[\mathbf{m}_\Gamma^{\mathrm{dir}}\right]_{12} &= D_{\mathrm{B}}\,\frac{1-\nu}{2}\left[w^\Gamma_{x,y} + w^\Gamma_{y,x} + [\mathbf{H}]_{1j}\cdot\boldsymbol{u}^{\mathrm{dir}}_{,y} + [\mathbf{H}]_{2j}\cdot\boldsymbol{u}^{\mathrm{dir}}_{,x}\right] \ ,\\
\left[\mathbf{m}_\Gamma^{\mathrm{dir}}\right]_{13} &= D_{\mathrm{B}}\,\frac{1-\nu}{2}\left[w^\Gamma_{x,z} + w^\Gamma_{z,x} + [\mathbf{H}]_{1j}\cdot\boldsymbol{u}^{\mathrm{dir}}_{,z} + [\mathbf{H}]_{3j}\cdot\boldsymbol{u}^{\mathrm{dir}}_{,x}\right] \ ,\\
\left[\mathbf{m}_\Gamma^{\mathrm{dir}}\right]_{23} &= D_{\mathrm{B}}\,\frac{1-\nu}{2}\left[w^\Gamma_{y,z} + w^\Gamma_{z,y} + [\mathbf{H}]_{2j}\cdot\boldsymbol{u}^{\mathrm{dir}}_{,z} + [\mathbf{H}]_{3j}\cdot\boldsymbol{u}^{\mathrm{dir}}_{,y}\right] \ ,
\end{aligned}
$$

with $j = 1,\ 2,\ 3$ and $D_{\mathrm{B}} = \frac{Et^3}{12(1-\nu^2)}$ being the flexural rigidity of the shell. The two non-zero eigenvalues of $\mathbf{m}_\Gamma$ are the principal moments m_1 and m_2. The effective membrane (normal) force tensor $\tilde{\boldsymbol{n}}_\Gamma$ is defined as

$$
\tilde{\mathbf{n}}_\Gamma = \int_{-t/2}^{t/2} \boldsymbol{\sigma}^{\mathrm{P}}_\Gamma(\boldsymbol{x})\ \mathrm{d}\zeta = t\boldsymbol{\sigma}_\Gamma(\boldsymbol{\varepsilon}^{\mathrm{P}}_{\Gamma,\mathrm{Mem}}) = \mathbf{P}\cdot\mathbf{n}^{\mathrm{dir}}_\Gamma\cdot\mathbf{P} \ , \tag{5.15}
$$

with components

$$
\begin{aligned}
\left[\mathbf{n}_\Gamma^{\mathrm{dir}}\right]_{11} &= D_{\mathrm{M}}\left[u^\Gamma_{x,x} + \nu(u^\Gamma_{y,y} + u^\Gamma_{z,z})\right] \ ,\\
\left[\mathbf{n}_\Gamma^{\mathrm{dir}}\right]_{22} &= D_{\mathrm{M}}\left[u^\Gamma_{y,y} + \nu(u^\Gamma_{x,x} + u^\Gamma_{z,z})\right] \ ,\\
\left[\mathbf{n}_\Gamma^{\mathrm{dir}}\right]_{33} &= D_{\mathrm{M}}\left[u^\Gamma_{z,z} + \nu(u^\Gamma_{x,x} + u^\Gamma_{y,y})\right] \ ,\\
\left[\mathbf{n}_\Gamma^{\mathrm{dir}}\right]_{12} &= D_{\mathrm{M}}\left[\frac{1-\nu}{2}(u^\Gamma_{x,y} + u^\Gamma_{y,x})\right] \ ,\\
\left[\mathbf{n}_\Gamma^{\mathrm{dir}}\right]_{13} &= D_{\mathrm{M}}\left[\frac{1-\nu}{2}(u^\Gamma_{x,z} + u^\Gamma_{z,x})\right] \ ,\\
\left[\mathbf{n}_\Gamma^{\mathrm{dir}}\right]_{23} &= D_{\mathrm{M}}\left[\frac{1-\nu}{2}(u^\Gamma_{y,z} + u^\Gamma_{z,y})\right] \ ,
\end{aligned}
$$

where $D_{\mathrm{M}} = \frac{Et}{1-\nu^2}$ is the membrane stiffness. Analogously to the moment tensor, the effective normal force tensor is also a symmetric, in-plane tensor. For curved shells, this tensor is *not* the physical normal force tensor but occurs in the weak form, see Section 5.1.3.2. Similar to the Kirchhoff-Love shell, the physical normal force tensor $\mathbf{n}^{\mathrm{real}}_\Gamma$ is defined by

$$
\mathbf{n}^{\mathrm{real}}_\Gamma = \tilde{\mathbf{n}}_\Gamma + \mathbf{H}\cdot\mathbf{m}_\Gamma
$$

and is, in general, not symmetric but features one zero eigenvalue just as $\tilde{\mathbf{n}}_\Gamma$. With Eq. 5.13, the resulting transverse shear force tensor is

$$
\mathbf{q}_\Gamma = \int_{-t/2}^{t/2} \boldsymbol{\sigma}^{\mathrm{S}}_\Gamma(\boldsymbol{x})\ \mathrm{d}\zeta = t\boldsymbol{\sigma}_\Gamma(\boldsymbol{\varepsilon}^{\mathrm{S}}_\Gamma) = 2D_{\mathrm{Shear}}\,\boldsymbol{\varepsilon}^{\mathrm{S}}_\Gamma \ , \tag{5.16}
$$

with components

$$
\begin{aligned}
[\mathbf{q}_\Gamma]_{11} &= 2D_{\text{Shear}}\left[n_x w_x + [\mathbf{Q}]_{1j}\cdot \boldsymbol{u}^{\text{dir}}_{,x}\right] \ ,\\
[\mathbf{q}_\Gamma]_{22} &= 2D_{\text{Shear}}\left[n_y w_y + [\mathbf{Q}]_{2j}\cdot \boldsymbol{u}^{\text{dir}}_{,y}\right] \ ,\\
[\mathbf{q}_\Gamma]_{33} &= 2D_{\text{Shear}}\left[n_z w_z + [\mathbf{Q}]_{3j}\cdot \boldsymbol{u}^{\text{dir}}_{,z}\right] \ ,\\
[\mathbf{q}_\Gamma]_{12} &= D_{\text{Shear}}\left[n_x w_y + n_y w_x + [\mathbf{Q}]_{1j}\cdot \boldsymbol{u}^{\text{dir}}_{,y} + [\mathbf{Q}]_{2j}\cdot \boldsymbol{u}^{\text{dir}}_{,x}\right] \ ,\\
[\mathbf{q}_\Gamma]_{13} &= D_{\text{Shear}}\left[n_x w_z + n_z w_x + [\mathbf{Q}]_{1j}\cdot \boldsymbol{u}^{\text{dir}}_{,z} + [\mathbf{Q}]_{3j}\cdot \boldsymbol{u}^{\text{dir}}_{,x}\right] \ ,\\
[\mathbf{q}_\Gamma]_{23} &= D_{\text{Shear}}\left[n_y w_z + n_z w_y + [\mathbf{Q}]_{2j}\cdot \boldsymbol{u}^{\text{dir}}_{,z} + [\mathbf{Q}]_{3j}\cdot \boldsymbol{u}^{\text{dir}}_{,y}\right] \ ,
\end{aligned}
$$

where $D_{\text{Shear}} = \alpha_{\text{s}}\mu t = \alpha_{\text{s}}\frac{Et}{2(1+\nu)}$ is the transverse shear stiffness.

5.1.3 Equilibrium

5.1.3.1 Equilibrium in strong form

Based on the stress resultants from above, one obtains the force and moment equilibrium for a curved Reissner-Mindlin shell in terms of the TDC using a global Cartesian coordinate system in strong form as

$$
\begin{aligned}
\text{div}_\Gamma \mathbf{n}^{\text{real}}_\Gamma + \mathbf{Q}\cdot\text{div}_\Gamma \mathbf{q}_\Gamma + \mathbf{H}\cdot(\mathbf{q}_\Gamma\cdot\boldsymbol{n}_\Gamma) &= -\boldsymbol{f} \ , && (5.17)\\
\mathbf{P}\cdot\text{div}_\Gamma \mathbf{m}_\Gamma - \mathbf{q}_\Gamma\cdot\boldsymbol{n}_\Gamma &= -\boldsymbol{c} \ , && (5.18)
\end{aligned}
$$

with $\boldsymbol{f}$ being the load vector per area and $\boldsymbol{c}$ being a distributed moment vector on the mid-surface Γ. One may split the force equilibrium into the tangential and normal direction

$$
\begin{aligned}
\mathbf{P}\cdot\text{div}_\Gamma \mathbf{n}^{\text{real}}_\Gamma + \mathbf{H}\cdot(\mathbf{q}_\Gamma\cdot\boldsymbol{n}_\Gamma) &= -\boldsymbol{f}_t \ , && (5.19)\\
-\mathbf{H} : \mathbf{n}^{\text{real}}_\Gamma + \boldsymbol{n}_\Gamma\cdot\text{div}_\Gamma \mathbf{q}_\Gamma &= -f_n \ . && (5.20)
\end{aligned}
$$

Alternatively, Eq. 5.17 can be rewritten in terms of the effective normal force tensor by substituting $\mathbf{n}^{\text{real}}_\Gamma$ with Eq. 4.17

$$
\text{div}_\Gamma \tilde{\mathbf{n}}_\Gamma + \mathbf{H}\cdot\text{div}_\Gamma \mathbf{m}_\Gamma + \sum_{i,j=1}^{3}[\mathbf{H}_{,i}]_{jk}[\mathbf{m}_\Gamma]_{ji} + \mathbf{Q}\cdot\text{div}_\Gamma \mathbf{q}_\Gamma + \mathbf{H}\cdot(\mathbf{q}_\Gamma\cdot\boldsymbol{n}_\Gamma) = -\boldsymbol{f} \ . \qquad (5.21)
$$

Assuming a bounded shell with boundary $\partial\Gamma$, there exist for each field (deflection of the mid-surface $\boldsymbol{u}$ and difference vector $\boldsymbol{w}$) two non-overlapping parts, the Dirichlet boundary $\partial\Gamma_{\text{D},i}$ and the Neumann boundary $\partial\Gamma_{\text{N},i}$, with $i \in \{\boldsymbol{u},\, \boldsymbol{w}\}$. The corresponding boundary conditions for the displacements $\boldsymbol{u}$ are

$$
\begin{aligned}
\boldsymbol{u} &= \hat{\boldsymbol{g}}_{\boldsymbol{u}} \text{ on } \partial\Gamma_{\text{D},\boldsymbol{u}} \ ,\\
\mathbf{n}^{\text{real}}_\Gamma\cdot\boldsymbol{n}_{\partial\Gamma} + (\boldsymbol{n}_\Gamma\cdot\mathbf{q}_\Gamma\cdot\boldsymbol{n}_{\partial\Gamma})\cdot\boldsymbol{n}_\Gamma &= \hat{\boldsymbol{p}} \ \text{ on } \partial\Gamma_{\text{N},\boldsymbol{u}} \ .
\end{aligned}
\qquad (5.22)
$$

For the rotation of the normal vector, the boundary conditions are

$$\begin{aligned} \boldsymbol{w} &= \hat{\boldsymbol{g}}_{\boldsymbol{w}} \quad \text{on } \partial\Gamma_{\mathrm{D},\boldsymbol{w}} \ , \\ \mathbf{m}_\Gamma \cdot \boldsymbol{n}_{\partial\Gamma} &= \hat{\boldsymbol{m}}_{\partial\Gamma} \ \text{on } \partial\Gamma_{\mathrm{N},\boldsymbol{w}} \ . \end{aligned} \tag{5.23}$$

In Fig. 5.2, the possible boundary conditions are illustrated. In Fig. 5.2(a), the displacement field $\boldsymbol{u}$ at the boundary is expressed in terms of the local triad ($\boldsymbol{t}_{\partial\Gamma}$, $\boldsymbol{n}_{\partial\Gamma}$, $\boldsymbol{n}_\Gamma$) and, since the difference vector is tangential, the rotation of the normal vector may be written in terms of ($\boldsymbol{t}_{\partial\Gamma}$, $\boldsymbol{n}_{\partial\Gamma}$)

$$\boldsymbol{w} = \underbrace{(\boldsymbol{w} \cdot \boldsymbol{n}_{\partial\Gamma})}_{\omega_{\boldsymbol{t}_{\partial\Gamma}}} \boldsymbol{n}_{\partial\Gamma} + \underbrace{(\boldsymbol{w} \cdot \boldsymbol{t}_{\partial\Gamma})}_{\omega_{\boldsymbol{n}_{\partial\Gamma}}} \boldsymbol{t}_{\partial\Gamma} \ , \tag{5.24}$$

where $(\omega_{\boldsymbol{t}_{\partial\Gamma}}, \omega_{\boldsymbol{n}_{\partial\Gamma}})$ are the rotations around $\boldsymbol{t}_{\partial\Gamma}$ and $\boldsymbol{n}_{\partial\Gamma}$, respectively. The decomposition of $\mathbf{m}_\Gamma \cdot \boldsymbol{n}_{\partial\Gamma} = \hat{\boldsymbol{m}}_{\partial\Gamma}$ is similar to Eq. 4.30. The conjugated forces ($\boldsymbol{p}_{\boldsymbol{t}_{\partial\Gamma}}$, $\boldsymbol{p}_{\boldsymbol{n}_{\partial\Gamma}}$, $\boldsymbol{p}_{\boldsymbol{n}_\Gamma}$) and bending moments ($\boldsymbol{m}_{\boldsymbol{t}_{\partial\Gamma}}$, $\boldsymbol{m}_{\boldsymbol{n}_{\partial\Gamma}}$) at the boundary are shown in Fig. 5.2(b). A set of common support types is given in Tab. 4.1. Other boundary conditions (e.g., membrane support, etc.) can be found, e.g., in [7].

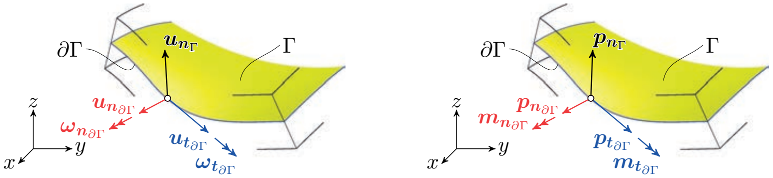

(a) displacements and rotations **(b)** forces and moments

Fig. 5.2: Decomposition of the mid-surface displacement $\boldsymbol{u}$, difference vector $\boldsymbol{w}$, forces and bending moments along the boundary $\partial\Gamma$ in terms of $\boldsymbol{t}_{\partial\Gamma}$, $\boldsymbol{n}_{\partial\Gamma}$ and $\boldsymbol{n}_\Gamma$: (a) Displacements and rotations at the boundary, and (b) forces and bending moments at the boundary.

Clamped edge	$\hat{g}_{u,\boldsymbol{t}_{\partial\Gamma}} = 0$	$\hat{g}_{u,\boldsymbol{n}_{\partial\Gamma}} = 0$	$\hat{g}_{u,\boldsymbol{n}_\Gamma} = 0$	$\hat{\omega}_{\boldsymbol{t}_{\partial\Gamma}} = 0$	$\hat{\omega}_{\boldsymbol{n}_{\partial\Gamma}} = 0$
Simply supported edge	$\hat{g}_{u,\boldsymbol{t}_{\partial\Gamma}} = 0$	$\hat{g}_{u,\boldsymbol{n}_{\partial\Gamma}} = 0$	$\hat{g}_{u,\boldsymbol{n}_\Gamma} = 0$	$\hat{m}_{\boldsymbol{t}_{\partial\Gamma}} = 0$	$\hat{m}_{\boldsymbol{n}_{\partial\Gamma}} = 0$
Symmetry support	$\hat{p}_{\boldsymbol{t}_{\partial\Gamma}} = 0$	$\hat{g}_{u,\boldsymbol{n}_{\partial\Gamma}} = 0$	$\hat{p}_{\boldsymbol{n}_\Gamma} = 0$	$\hat{\omega}_{\boldsymbol{t}_{\partial\Gamma}} = 0$	$\hat{m}_{\boldsymbol{n}_{\partial\Gamma}} = 0$
Free edge	$\hat{p}_{\boldsymbol{t}_{\partial\Gamma}} = 0$	$\hat{p}_{\boldsymbol{n}_{\partial\Gamma}} = 0$	$\hat{p}_{\boldsymbol{n}_\Gamma} = 0$	$\hat{m}_{\boldsymbol{t}_{\partial\Gamma}} = 0$	$\hat{m}_{\boldsymbol{n}_{\partial\Gamma}} = 0$

Tab. 5.1: Set of common boundary conditions for Reissner-Mindlin shells.

With the boundary conditions for the displacements and rotations, the complete second-order BVP is defined. The obtained BVP in terms of the TDC is valid in the case of implicitly and explicitly defined surfaces. In the case of parametrized shells, the equilibrium in strong form is equivalent to the strong form formulated in local coordinates [7], [95], [139]. However, because the obtained BVP does not rely on a parametrized mid-surface of the shell, the formulation in the frame of the TDC is more general.

5.1.3.2 Equilibrium in weak form

In order to convert the equilibrium in strong form to the weak form, we introduce the following function spaces

$$\mathcal{S}_{\boldsymbol{u}}^{\mathrm{RM}} = \left\{ \boldsymbol{v} \in \left[\mathcal{H}^1(\Gamma)\right]^3 : \boldsymbol{v} = \hat{\boldsymbol{g}}_{\boldsymbol{u}} \text{ on } \partial\Gamma_{\mathrm{D},\boldsymbol{u}} \right\} , \tag{5.25}$$

$$\mathcal{V}_{\boldsymbol{u}}^{\mathrm{RM}} = \left\{ \boldsymbol{v} \in \left[\mathcal{H}^1(\Gamma)\right]^3 : \boldsymbol{v} = \boldsymbol{0} \text{ on } \partial\Gamma_{\mathrm{D},\boldsymbol{u}} \right\} , \tag{5.26}$$

$$\mathcal{S}_{\boldsymbol{w}}^{\mathrm{RM}} = \left\{ \boldsymbol{v} \in \left[\mathcal{H}^1(\Gamma)\right]^3 : \boldsymbol{v} \cdot \boldsymbol{n}_\Gamma = 0 \ ; \ \boldsymbol{v} = \hat{\boldsymbol{g}}_{\boldsymbol{w}} \text{ on } \partial\Gamma_{\mathrm{D},\boldsymbol{w}} \right\} , \tag{5.27}$$

$$\mathcal{V}_{\boldsymbol{w}}^{\mathrm{RM}} = \left\{ \boldsymbol{v} \in \left[\mathcal{H}^1(\Gamma)\right]^3 : \boldsymbol{v} \cdot \boldsymbol{n}_\Gamma = 0 \ ; \ \boldsymbol{v} = 0 \text{ on } \partial\Gamma_{\mathrm{D},\boldsymbol{w}} \right\} , \tag{5.28}$$

where $\mathcal{H}^1$ is the space of functions with square integrable first derivatives. Note that the functions are 3D functions on the mid-surface, i.e., $\boldsymbol{v}(\boldsymbol{x}) : \Gamma \to \mathbb{R}^3, \boldsymbol{x} \in \Gamma \subset \mathbb{R}^3$. The non-tangential spaces $(\mathcal{S}_{\boldsymbol{u}}^{\mathrm{RM}}, \mathcal{V}_{\boldsymbol{u}}^{\mathrm{RM}})$ are employed for the trial and test functions of the mid-surface displacement, whereas the tangential function spaces $(\mathcal{S}_{\boldsymbol{w}}^{\mathrm{RM}}, \mathcal{V}_{\boldsymbol{w}}^{\mathrm{RM}})$ are used for the trial and test functions of the difference vector, which need to be tangential according to the Reissner-Mindlin kinematics. Later on for the discrete problem in the frame of the Trace FEM, these functions are defined in the physical space $\mathbb{R}^3$ and then restricted to Γ, with the additional condition that the functions need to be in $[\mathcal{H}^1(\Gamma)]^3$. It is emphasized that the definition of the functions in the higher-dimensional space and then restricting them to the trace (mid-surface) is an important difference compared to classical Surface FEM.

With the above defined function spaces, see Eq. 5.25 to Eq. 5.28, the weak form of the equilibrium reads as follows: Given Young's modulus $E \in \mathbb{R}^+$, Poisson's ratio $\nu \in [0, 0.5]$, body forces $\boldsymbol{f}$ on Γ, tractions $\hat{\boldsymbol{p}}$ on $\partial\Gamma_{\mathrm{N},\boldsymbol{u}}$, find $\boldsymbol{u} \in \mathcal{S}_{\boldsymbol{u}}^{\mathrm{RM}}$ and $\boldsymbol{w} \in \mathcal{S}_{\boldsymbol{w}}^{\mathrm{RM}}$ such that for all $\boldsymbol{v}_{\boldsymbol{u}} \in \mathcal{V}_{\boldsymbol{u}}^{\mathrm{RM}}$, there holds

$$\begin{aligned} \int_\Gamma \nabla_\Gamma^{\mathrm{dir}} \boldsymbol{v}_u : \tilde{\mathbf{n}}_\Gamma + (\mathbf{H} \cdot \nabla_\Gamma^{\mathrm{dir}} \boldsymbol{v}_u) : \mathbf{m}_\Gamma + (\mathbf{Q} \cdot \nabla_\Gamma^{\mathrm{dir}} \boldsymbol{v}_u) : \mathbf{q}_\Gamma \, \mathrm{d}A & \\ = \int_\Gamma \boldsymbol{v}_u \cdot \boldsymbol{f} \, \mathrm{d}A + \int_{\partial\Gamma_{\mathrm{N},\boldsymbol{u}}} \boldsymbol{v}_u \cdot \hat{\boldsymbol{p}} \, \mathrm{d}s \ . & \end{aligned} \tag{5.29}$$

Note that, in order to obtain Eq. 5.29, the identities $(\mathbf{H} \cdot \nabla_\Gamma^{\mathrm{dir}} \boldsymbol{v}_u) : \mathbf{m}_\Gamma = \nabla_\Gamma^{\mathrm{dir}} \boldsymbol{v}_u : (\mathbf{H} \cdot \mathbf{m}_\Gamma)$ and $[\mathbf{Q}_{,x}^\Gamma \cdot \boldsymbol{v}_u \quad \mathbf{Q}_{,y}^\Gamma \cdot \boldsymbol{v}_u \quad \mathbf{Q}_{,z}^\Gamma \cdot \boldsymbol{v}_u] : \mathbf{q}_\Gamma = \boldsymbol{v}_u^{\mathrm{T}} \cdot \mathbf{H} \cdot (\mathbf{q}_\Gamma \cdot \boldsymbol{n}_\Gamma)$ are used. As previously mentioned, in the weak form of the force equilibrium, only the effective normal force tensor appears instead of the non-symmetric, physical normal force tensor.

The weak form of the moment equilibrium reads as follows: Given Young's modulus $E \in \mathbb{R}^+$, Poisson's ratio $\nu \in [0, 0.5]$, distributed moments $\boldsymbol{c} \in T_P\Gamma$ on Γ, bending moments $\hat{\boldsymbol{m}}_{\partial\Gamma}$ on $\partial\Gamma_{\mathrm{N},\boldsymbol{w}}$, find $\boldsymbol{u} \in \mathcal{S}_{\boldsymbol{u}}^{\mathrm{RM}}$ and $\boldsymbol{w} \in \mathcal{S}_{\boldsymbol{w}}^{\mathrm{RM}}$ such that for all $\boldsymbol{v}_{\boldsymbol{w}} \in \mathcal{V}_{\boldsymbol{w}}^{\mathrm{RM}}$, there holds

$$\int_\Gamma \nabla_\Gamma^{\mathrm{dir}} \boldsymbol{v}_w : \mathbf{m}_\Gamma + \boldsymbol{v}_w \cdot (\mathbf{q}_\Gamma \cdot \boldsymbol{n}_\Gamma) \, \mathrm{d}A = \int_\Gamma \boldsymbol{v}_w \cdot \boldsymbol{c} \, \mathrm{d}A + \int_{\partial\Gamma_{\mathrm{N},\boldsymbol{w}}} \boldsymbol{v}_w \cdot \hat{\boldsymbol{m}}_{\partial\Gamma} \, \mathrm{d}s \ . \tag{5.30}$$

5.2 Discretization

In the following, the obtained continuous weak form from Section 5.1.3.2 is discretized with the Surface and the Trace FEM. For the Surface FEM, similar to Section 4.2, isogeometric analysis (IGA) is employed. It is pointed out that continuity requirements would also allow a standard finite element approach using C^0-continuous shape functions as presented in Section 3.1. Nevertheless, we prefer the use of NURBS here, for example, due to the improved convergence properties and higher smoothness of the results (including smooth forces and moments). Furthermore, the discrete weak form for a higher-order Trace FEM is presented in detail. The major ingredients of the Trace FEM are introduced in Section 3.2. The discretization of the difference vector must satisfy the tangentiality constraint which requires special attention as outlined below.

5.2.1 Surface FEM

As mentioned above, similar to the Kirchhoff-Love shell, NURBS-based shape functions are employed. The general finite element function space is defined in Eq. 4.38. The discrete displacement of the mid-surface results in $\boldsymbol{u}^h = u^{h,i}\boldsymbol{E}_i$, with $\boldsymbol{E}_i$ being Cartesian base vectors, with $i = 1, 2, 3$ and $u^{h,i} = \boldsymbol{M}_{\boldsymbol{u}}^{\mathrm{T}} \cdot \hat{\boldsymbol{u}}^i$. In contrast to $\boldsymbol{u}$, the difference vector $\boldsymbol{w}$ is a tangential vector, describing the rotation of the normal vector. The discretization of a tangential vector is, in general, not straightforward and, in the following, different strategies are examined:

(1) In the case of a parametrized surface, the covariant base vectors $\boldsymbol{A}_\alpha$, $\alpha = 1, 2$, which are by construction tangential, may be used to define the difference vector $\boldsymbol{w}^h = w^{h,\alpha}\boldsymbol{A}_\alpha$, where $w^{h,\alpha} = \boldsymbol{M}_{\boldsymbol{w}}^{\mathrm{T}} \cdot \hat{\boldsymbol{w}}^\alpha$. This approach is used in the classical five-parameter models [14], however, it does not extend to implicitly defined shell surfaces.

(2) Alternatively, the directions of the principal curvatures, which are eigenvectors of the Weingarten map $\mathbf{H}$, can be used as basis vectors. These vectors are perpendicular and also tangential by construction. This might be a reasonable choice in the case of curved, implicitly defined surfaces, where a parametrization is not available. Compared to the first approach, the crucial requirement of a parametrization is circumvented without changing the number of degrees of freedom per control point or node respectively.

(3) Another possibility is to define the difference vector in the global Cartesian coordinate system $\boldsymbol{w}^h = w^{h,i}\boldsymbol{E}_i$, with $i = 1, 2, 3$ and $w^{h,i} = \boldsymbol{M}_{\boldsymbol{w}}^{\mathrm{T}} \cdot \hat{\boldsymbol{w}}^i$ and enforce the constraint $\boldsymbol{w}^h \cdot \boldsymbol{n}_\Gamma = 0$ weakly using a Lagrange multiplier or penalty method.

(4) A variant of (3), is to project the difference vector onto the tangent space of the mid-surface $\boldsymbol{w}^h = \mathbf{P} \cdot w^{h,i}\boldsymbol{E}_i$. An advantage of this approach is that the additional Lagrange multiplier field is not needed. On the other hand, due to the projection, conditioning issues occur, which may be addressed with an additional stabilization term. This approach is employed in the Trace FEM approach, see Section 5.2.2 for details.

For the Surface FEM, the third approach, where the difference vector is globally defined and the constraint is enforced with a Lagrange multiplier, is chosen. Note that the fourth approach is also considered in the Surface FEM. The performance and convergence behaviour is analogously compared to the third approach and will be omitted for brevity. The shape functions of the discrete Lagrange multiplier $\lambda_n^h = \boldsymbol{M}_{\lambda_n}^{\mathrm{T}} \cdot \hat{\boldsymbol{\lambda}}_n$ for the constraint on the difference vector is defined in the same manner as the components of the mid-surface displacement. Furthermore, the boundary conditions shall be enforced weakly with Lagrange multipliers [144]. The shape functions of the discrete Lagrange multiplier field for the displacements are defined as $M_{\lambda_{\boldsymbol{u}}} = \{M_{\boldsymbol{u}}|_{\partial\Gamma_{\mathrm{D},\boldsymbol{u}}}\}$ and for the difference vector as $M_{\lambda_{\boldsymbol{w}}} = \{M_{\boldsymbol{w}}|_{\partial\Gamma_{\mathrm{D},\boldsymbol{w}}}\}$ in the sense of a trace.

Based on this, the following discrete trial and test functions spaces for the discrete weak form of the Reissner-Mindlin shell are defined

$$\begin{aligned}
\mathcal{S}_{\boldsymbol{u}}^{\mathrm{RM},h} &= \mathcal{V}_{\boldsymbol{u}}^{\mathrm{RM},h} = \mathcal{S}_{\boldsymbol{w}}^{\mathrm{RM},h} = \mathcal{V}_{\boldsymbol{w}}^{\mathrm{RM},h} = \left\{ \boldsymbol{v}^h \in \left[\mathcal{N}_\Gamma^k\right]^3 \right\} \,, && (5.31)\\
\mathcal{L}_{\lambda_n}^{\mathrm{RM},h} &= \mathcal{V}_{\lambda_n}^{\mathrm{RM},h} = \left\{ \lambda_n^h \in \mathcal{N}_\Gamma^k \right\} \,, && (5.32)\\
\mathcal{L}_{\boldsymbol{\lambda_u}}^{\mathrm{RM},h} &= \mathcal{V}_{\boldsymbol{\lambda_u}}^{\mathrm{RM},h} = \left\{ \boldsymbol{\lambda}_{\boldsymbol{u}}^h|_{\partial\Gamma_{\mathrm{D},\boldsymbol{u}}} :\ \boldsymbol{\lambda}_{\boldsymbol{u}}^h \in \mathcal{S}_{\boldsymbol{u}}^{\mathrm{RM},h} \right\} \,, && (5.33)\\
\mathcal{L}_{\boldsymbol{\lambda_w}}^{\mathrm{RM},h} &= \mathcal{V}_{\boldsymbol{\lambda_w}}^{\mathrm{RM},h} = \left\{ \boldsymbol{\lambda}_{\boldsymbol{w}}^h|_{\partial\Gamma_{\mathrm{D},\boldsymbol{w}}} :\ \boldsymbol{\lambda}_{\boldsymbol{w}}^h \in \mathcal{S}_{\boldsymbol{w}}^{\mathrm{RM},h} \right\} \,. && (5.34)
\end{aligned}$$

The discrete weak form of the Reissner-Mindlin shell with Lagrange multipliers for enforcing the tangentiality of the difference vector and the essential boundary conditions reads: Given Young's modulus $E \in \mathbb{R}^+$, Poisson's ratio $\nu \in [0,\, 0.5]$, surface load and moment $(\boldsymbol{f},\, \boldsymbol{c})$ on Γ, traction $\hat{\boldsymbol{p}}$ on $\partial\Gamma_{\mathrm{N},\boldsymbol{u}}$, bending moments $\hat{\boldsymbol{m}}_{\partial\Gamma}$ on $\partial\Gamma_{\mathrm{N},\boldsymbol{w}}$ and boundary conditions $\hat{\boldsymbol{g}}_{\boldsymbol{u}}$ in $\partial\Gamma_{\mathrm{D},\boldsymbol{u}}$, $\hat{\boldsymbol{g}}_{\boldsymbol{w}}$ on $\partial\Gamma_{\mathrm{D},\boldsymbol{w}}$, find the displacement field $\boldsymbol{u}^h \in \mathcal{S}_{\boldsymbol{u}}^{\mathrm{RM},h}$, the difference vector $\boldsymbol{w}^h \in \mathcal{S}_{\boldsymbol{w}}^{\mathrm{RM},h}$, and the Lagrange multiplier fields $(\lambda_n^h,\, \boldsymbol{\lambda}_{\boldsymbol{u}}^h,\, \boldsymbol{\lambda}_{\boldsymbol{w}}^h) \in \mathcal{L}_{\lambda_n}^{\mathrm{RM},h} \times \mathcal{L}_{\boldsymbol{\lambda_u}}^{\mathrm{RM},h} \times \mathcal{L}_{\boldsymbol{\lambda_w}}^{\mathrm{RM},h}$ such that for all test functions $(\boldsymbol{v}_u^h,\, \boldsymbol{v}_w^h,\, v_{\lambda_n}^h,\, \boldsymbol{v}_{\boldsymbol{\lambda_u}}^h,\, \boldsymbol{v}_{\boldsymbol{\lambda_w}}^h) \in \mathcal{V}_{\boldsymbol{u}}^{\mathrm{RM},h} \times \mathcal{V}_{\boldsymbol{w}}^{\mathrm{RM},h} \times \mathcal{V}_{\lambda_n}^{\mathrm{RM},h} \times \mathcal{V}_{\boldsymbol{\lambda_u}}^{\mathrm{RM},h} \times \mathcal{V}_{\boldsymbol{\lambda_w}}^{\mathrm{RM},h}$, there holds in Γ

$$\begin{aligned}
&\int_\Gamma \nabla_\Gamma^{\mathrm{dir}} \boldsymbol{v}_u^h : \tilde{\mathbf{n}}_\Gamma + (\mathbf{H} \cdot \nabla_\Gamma^{\mathrm{dir}} \boldsymbol{v}_u^h) : \mathbf{m}_\Gamma + (\mathbf{Q} \cdot \nabla_\Gamma^{\mathrm{dir}} \boldsymbol{v}_u^h) : \mathbf{q}_\Gamma \;\mathrm{d}A + \int_{\partial\Gamma_{\mathrm{D},\boldsymbol{u}}} \boldsymbol{v}_u^h \cdot \boldsymbol{\lambda}_{\boldsymbol{u}}^h \mathrm{d}s \\
&\qquad\qquad = \int_\Gamma \boldsymbol{v}_u^h \cdot \boldsymbol{f} \;\mathrm{d}A + \int_{\partial\Gamma_{\mathrm{N},\boldsymbol{u}}} \boldsymbol{v}_u^h \cdot \hat{\boldsymbol{p}} \;\mathrm{d}s \,, \\
&\int_\Gamma \nabla_\Gamma^{\mathrm{dir}} \boldsymbol{v}_w^h : \mathbf{m}_\Gamma + \boldsymbol{v}_w^h \cdot (\mathbf{q}_\Gamma \cdot \boldsymbol{n}_\Gamma) + \lambda_n^h (\boldsymbol{v}_w^h \cdot \boldsymbol{n}_\Gamma) \;\mathrm{d}A + \int_{\partial\Gamma_{\mathrm{D},\boldsymbol{w}}} \boldsymbol{v}_w^h \cdot \boldsymbol{\lambda}_{\boldsymbol{w}}^h \mathrm{d}s \\
&\qquad\qquad = \int_\Gamma \boldsymbol{v}_w^h \cdot \boldsymbol{c} \;\mathrm{d}\Gamma + \int_{\partial\Gamma_{\mathrm{N},\boldsymbol{w}}} \boldsymbol{v}_w^h \cdot \hat{\boldsymbol{m}}_{\partial\Gamma} \;\mathrm{d}s \,, \\
&\qquad\qquad \int_\Gamma v_{\lambda_n}^h \boldsymbol{w}^h \cdot \boldsymbol{n}_\Gamma \;\mathrm{d}A = 0 \,, \\
&\qquad\qquad \int_{\partial\Gamma_{\mathrm{D},\boldsymbol{u}}} \boldsymbol{v}_{\boldsymbol{\lambda_u}}^h \cdot \boldsymbol{u}^h \;\mathrm{d}s = \int_{\partial\Gamma_{\mathrm{D},\boldsymbol{u}}} \boldsymbol{v}_{\boldsymbol{\lambda_u}}^h \cdot \boldsymbol{g}_{\boldsymbol{u}} \;\mathrm{d}s \,, \\
&\qquad\qquad \int_{\partial\Gamma_{\mathrm{D},\boldsymbol{w}}} \boldsymbol{v}_{\boldsymbol{\lambda_w}}^h \cdot \boldsymbol{w}^h \;\mathrm{d}s = \int_{\partial\Gamma_{\mathrm{D},\boldsymbol{w}}} \boldsymbol{v}_{\boldsymbol{\lambda_w}}^h \cdot \boldsymbol{g}_{\boldsymbol{w}} \;\mathrm{d}s \,.
\end{aligned} \qquad (5.35)$$

The usual element assembly yields a linear system of equations (if displacements and rotations are prescribed) in the form

$$\begin{bmatrix} \mathbf{K}_{\boldsymbol{uu}} & \mathbf{K}_{\boldsymbol{uw}} & \mathbf{0} & \mathbf{C}_{\lambda_u} & \mathbf{0} \\ \mathbf{K}^{\mathrm{T}}_{\boldsymbol{uw}} & \mathbf{K}_{\boldsymbol{ww}} & \mathbf{C}_{\lambda_n} & \mathbf{0} & \mathbf{C}_{\lambda_w} \\ \mathbf{0} & \mathbf{C}^{\mathrm{T}}_{\lambda_n} & \mathbf{0} & \mathbf{0} & \mathbf{0} \\ \mathbf{C}^{\mathrm{T}}_{\lambda_u} & \mathbf{0} & \mathbf{0} & \mathbf{0} & \mathbf{0} \\ \mathbf{0} & \mathbf{C}^{\mathrm{T}}_{\lambda_w} & \mathbf{0} & \mathbf{0} & \mathbf{0} \end{bmatrix} \cdot \begin{bmatrix} \underline{\hat{\boldsymbol{u}}} \\ \underline{\hat{\boldsymbol{w}}} \\ \hat{\boldsymbol{\lambda}}_n \\ \underline{\hat{\boldsymbol{\lambda}}}_{\boldsymbol{u}} \\ \underline{\hat{\boldsymbol{\lambda}}}_{w} \end{bmatrix} = \begin{bmatrix} \boldsymbol{b}_{\boldsymbol{f}} \\ \boldsymbol{b}_{\boldsymbol{c}} \\ \mathbf{0} \\ \boldsymbol{b}_{\boldsymbol{\lambda}_u} \\ \boldsymbol{b}_{\boldsymbol{\lambda}_w} \end{bmatrix} , \tag{5.36}$$

with $[\underline{\hat{\boldsymbol{u}}},\ \underline{\hat{\boldsymbol{w}}},\ \hat{\boldsymbol{\lambda}}_n,\ \underline{\hat{\boldsymbol{\lambda}}}_{\boldsymbol{u}},\ \underline{\hat{\boldsymbol{\lambda}}}_{\boldsymbol{w}}]^{\mathrm{T}}$ being the sought displacements and rotations of the control points and Lagrange multipliers. The procedure for the definition of the stiffness matrices $\mathbf{K}_{ij}$ and constraint matrices $\mathbf{C}_k$ is analogously to Section 4.2 and is omitted for brevity. As usual in the context of Lagrange multiplier methods, Eq. 5.36 has a saddle point structure and the well-known Babuška-Brezzi condition [4], [17], [60] must be satisfied in order to obtain useful solutions in all involved fields. The same order of the trial and test functions are employed for all fields. With this choice of discrete functions spaces, see Eq. 5.31 to Eq. 5.34, bounded condition numbers, unique solutions, and the expected rates of convergence for the presented test cases in Section 5.3.1 are observed. Based on this observations, the discrete inf-sup condition seems to be satisfied herein.

5.2.2 Trace FEM

In this section, the continuous weak form of the equilibrium, see Eq. 5.29 and Eq. 5.30 is discretized with the Trace FEM as described above. The discrete function spaces for the trial and test functions of the mid-surface displacements are

$$\bar{\mathcal{S}}_{\boldsymbol{u}}^{\mathrm{RM},h} = \left\{ \boldsymbol{u}^h \in [\mathcal{T}_h]^3 \right\} , \tag{5.37}$$

$$\bar{\mathcal{V}}_{\boldsymbol{u}}^{\mathrm{RM},h} = \left\{ \boldsymbol{v}_u^h \in [\mathcal{T}_h]^3 \right\} , \tag{5.38}$$

with $\mathcal{T}_h$ from Eq. 3.7. Note that the corresponding function spaces in the Trace FEM for the trial and test functions are denoted with a bar in comparison to their counterpart in the Surface FEM, see Eq. 5.31.

For the discrete difference vector $\boldsymbol{w}^h$, the situation is more complicated due to the kinematic assumptions that the difference vector needs to be tangential. Different approaches for the discretization of tangent vector fields are presented in, e.g., in [91], [107], [127]. Herein, the difference vector $\boldsymbol{w}^h$ and its corresponding test function $\boldsymbol{v}_w^h$ are defined using the fourth approach in Section 5.2.1. Alternatively, one may also employ the third approach with the Lagrange multiplier for the Trace FEM similar to the above presented approach with the Surface FEM. Note that the a suitable discretization of the auxiliary field need to be available which may become a non-trivial task in the Trace FEM. The situation is analogously to the elaborated issue in Section 3.3.2.1 where Lagrange multipliers in the Trace FEM in the context of essential boundary conditions are considered. In the employed approach for the discretization of the difference vector, auxiliary fields are not required. In particular, the discrete difference vector is *first* defined in the general Trace FEM function space without the tangentiality constraint, similar to [107]. The corresponding function spaces are

$$\bar{\mathcal{S}}_{\boldsymbol{w}}^{\mathrm{RM},h} = \left\{ \boldsymbol{w}^h \in [\mathcal{T}_h]^3 \right\} \ , \tag{5.39}$$

$$\bar{\mathcal{V}}_{\boldsymbol{w}}^{\mathrm{RM},h} = \left\{ \boldsymbol{v}_w^h \in [\mathcal{T}_h]^3 \right\} \ , \tag{5.40}$$

but in the discrete weak form, see Eq. 5.45 and Eq. 5.46, only the *projected* difference vector and test functions are used, i.e., $\widetilde{\boldsymbol{w}}^h = \mathbf{P} \cdot \boldsymbol{w}^h \ , \ \widetilde{\boldsymbol{v}}_w^h = \mathbf{P} \cdot \boldsymbol{v}_w^h$. The directional and covariant gradient of the discrete, projected difference vector $\nabla_\Gamma^{\mathrm{dir}} \widetilde{\boldsymbol{w}}^h$ and $\nabla_\Gamma^{\mathrm{cov}} \widetilde{\boldsymbol{w}}^h$ can be directly computed with the product rule

$$\nabla_\Gamma^{\mathrm{dir}} \widetilde{\boldsymbol{w}}^h = \nabla_\Gamma^{\mathrm{dir}} \left(\mathbf{P} \cdot \boldsymbol{w}^h \right) = \left[\nabla_{\Gamma x}^{\mathrm{dir}} \mathbf{P} \cdot \boldsymbol{w}^h \quad \nabla_{\Gamma y}^{\mathrm{dir}} \mathbf{P} \cdot \boldsymbol{w}^h \quad \nabla_{\Gamma z}^{\mathrm{dir}} \mathbf{P} \cdot \boldsymbol{w}^h \right] + \nabla_\Gamma^{\mathrm{cov}} \boldsymbol{w}^h \ , \tag{5.41}$$

$$\nabla_\Gamma^{\mathrm{cov}} \widetilde{\boldsymbol{w}}^h = \mathbf{P} \cdot \nabla_\Gamma^{\mathrm{dir}} \widetilde{\boldsymbol{w}}^h = \mathbf{P} \cdot \left[\nabla_{\Gamma x}^{\mathrm{dir}} \mathbf{P} \cdot \boldsymbol{w}^h \quad \nabla_{\Gamma y}^{\mathrm{dir}} \mathbf{P} \cdot \boldsymbol{w}^h \quad \nabla_{\Gamma z}^{\mathrm{dir}} \mathbf{P} \cdot \boldsymbol{w}^h \right] + \nabla_\Gamma^{\mathrm{cov}} \boldsymbol{w}^h \ . \tag{5.42}$$

One may argue that in this approach, the derivatives of the projector $\mathbf{P}$ occur which involves surface derivatives of the normal vector $\boldsymbol{n}_\Gamma^h$. This does not lead to additional computational costs, because in the case of the Reissner-Mindlin shell, the Weingarten map $\mathbf{H}$ directly appears in the weak form and, therefore, the surface derivatives of the normal vector $\boldsymbol{n}_\Gamma^h$ are required anyway.

As a result of this projection, only the tangential part of $\boldsymbol{w}^h$ and $\boldsymbol{v}_w^h$ is considered in the discrete weak form and, therefore, the tangentiality constraint is built-in automatically. The employed stabilization technique, i.e., normal derivative volume stabilization, see Section 3.2.3, ensures unique nodal values and prevents an ill-conditioned system of equations due to small supports for general vector fields. However, due to the projection, the normal part of $\boldsymbol{w}^h$, i.e., $w_n^h = \boldsymbol{w}^h \cdot \boldsymbol{n}_\Gamma^h$, does not appear in the discrete weak form and, therefore, w_n^h is not unique. It is clear, that without any further measures this would lead to an ill-conditioned system of equations as a consequence. In order to address this issue, a simple and consistent additional stabilization term, similar to the penalty term in [107], is introduced

$$s_{w,h} := \rho_w \int_{\Gamma^h} \left(\boldsymbol{w}^h \cdot \boldsymbol{n}_\Gamma^h \right) \left(\boldsymbol{v}_w^h \cdot \boldsymbol{n}_\Gamma^h \right) \, \mathrm{d}A \ , \tag{5.43}$$

where ρ_w is a suitable stabilization parameter. In other words, for the stabilization of the projected, discrete difference vector $\widetilde{\boldsymbol{w}}^h$, a combination of the normal derivative volume stabilization and the above introduced stabilization term for the normal part of $\boldsymbol{w}^h$ is employed, see Eq. 5.46.

A series of numerical studies regarding the choice of the stabilization parameter ρ_w for the Reissner-Mindlin shell has been conducted on flat and curved shell geometries. In detail, the dependency on the (1) material parameter E, (2) thickness t and (3) element size on h w.r.t. the condition number of the stiffness matrix and the influence on the results were investigated. Summarizing the outcome of the numerical studies, the stabilization parameter can be chosen independently of h and, for a suitable scaling of the stabilization term, the parameter is set to

$$\rho_w = E \cdot t \ . \tag{5.44}$$

A difference of the proposed approach and the method shown in [107] is that only the projected part of the vector field, i.e., $\widetilde{\boldsymbol{w}}^h = \mathbf{P}\cdot\boldsymbol{w}^h$, is used in the discrete weak form which directly enforces the tangentiality constraint. Furthermore, the stabilization parameter used herein, which is in [91], [107] a penalty parameter, does not depend on h and only a suitable constant scaling of the stabilization term as in Eq. 5.44 is required.

The essential boundary conditions are enforced with the non-symmetric version of Nitsche's method. As mentioned before, the advantage of this method in the context of FDMs is that it does not require additional stabilization terms and the discretization of auxiliary fields such as Lagrange multipliers is not needed. Furthermore, Nitsche's method is a consistent approach to enforce essential boundary conditions which may be an advantage if higher-order convergence rates shall be achieved. Further details regarding the enforcement of essential boundary conditions within the Trace FEM are presented in Section 3.2.4. The additional terms resulting from Nitsche's method are directly added to the discrete weak form, see Eq. 5.45 and Eq. 5.46.

Based on the previous definitions, the discrete weak form of the force equilibrium in the context of the Trace FEM reads: Given Young's modulus $E \in \mathbb{R}^+$, Poisson's ratio $\nu \in [0,\, 0.5]$, body forces $\boldsymbol{f}$ on Γ^h, tractions $\hat{\boldsymbol{p}}$ on $\partial\Gamma^h_{\mathrm{N},\boldsymbol{u}}$, stabilization parameter $\rho \in \mathbb{R}^+$ and boundary conditions $\hat{\boldsymbol{g}}_{\boldsymbol{u}}$ in $\partial\Gamma_{\mathrm{D},\boldsymbol{u}}$, find the displacement fields $(\boldsymbol{u}^h, \boldsymbol{w}^h) \in \bar{\mathcal{S}}^{\mathrm{RM},h}_{\boldsymbol{u}} \times \bar{\mathcal{S}}^{\mathrm{RM},h}_{\boldsymbol{w}}$ such that for all test functions $(\boldsymbol{v}^h_u, \boldsymbol{v}^h_w) \in \bar{\mathcal{V}}^{\mathrm{RM},h}_{\boldsymbol{u}} \times \bar{\mathcal{V}}^{\mathrm{RM},h}_{\boldsymbol{w}}$ there holds in Γ^h

$$
\begin{aligned}
&\int_{\Gamma^h} \nabla^{\mathrm{dir}}_{\Gamma}\boldsymbol{v}_u : \tilde{\mathbf{n}}_\Gamma(\boldsymbol{u}^h) + (\mathbf{H}\cdot\nabla^{\mathrm{dir}}_{\Gamma}\boldsymbol{v}_u) : \mathbf{m}_\Gamma(\boldsymbol{u}^h, \widetilde{\boldsymbol{w}}^h) + (\mathbf{Q}\cdot\nabla^{\mathrm{dir}}_{\Gamma}\boldsymbol{v}_u) : \mathbf{q}_\Gamma(\boldsymbol{u}^h, \widetilde{\boldsymbol{w}}^h)\,\mathrm{d}A \\
&- \underbrace{\int_{\partial\Gamma^h_{\mathrm{D},\boldsymbol{u}}} \boldsymbol{v}_u \cdot \boldsymbol{p}(\boldsymbol{u}^h, \widetilde{\boldsymbol{w}}^h)\,\mathrm{d}s}_{\text{boundary term due to } \boldsymbol{v}^h_u \neq \boldsymbol{0} \text{ on } \partial\Gamma_{\mathrm{D},\boldsymbol{u}}} \quad + \underbrace{\int_{\partial\Gamma^h_{\mathrm{D},\boldsymbol{u}}} \boldsymbol{u}^h \cdot \boldsymbol{p}(\boldsymbol{v}^h_u, \tilde{\boldsymbol{v}}^h_w)\,\mathrm{d}s}_{\text{Nitsche term for displ. on LHS}} \\
&+ \underbrace{\rho \int_{\Omega^\Gamma_h} \left(\nabla\boldsymbol{u}^h \cdot \boldsymbol{n}^{e,h}_\Gamma\right) \cdot \left(\nabla\boldsymbol{v}^h_u \cdot \boldsymbol{n}^{e,h}_\Gamma\right)\,\mathrm{d}V}_{\text{Trace FEM stabilization, see Section 3.2.3}} \\
&= \int_{\Gamma^h} \boldsymbol{v}^h_u \cdot \boldsymbol{f}\,\mathrm{d}A + \underbrace{\int_{\partial\Gamma^h_{\mathrm{D},\boldsymbol{u}}} \hat{\boldsymbol{g}}_{\boldsymbol{u}} \cdot \boldsymbol{p}(\boldsymbol{v}^h_u, \tilde{\boldsymbol{v}}^h_w)\,\mathrm{d}s}_{\text{Nitsche term for displ. on RHS}} + \int_{\partial\Gamma^h_{\mathrm{N},\boldsymbol{u}}} \boldsymbol{v}^h_u \cdot \hat{\boldsymbol{p}}\,\mathrm{d}s\;,
\end{aligned}
\tag{5.45}
$$

where $\boldsymbol{p} = \mathbf{n}^{\mathrm{real}}_\Gamma \cdot \boldsymbol{n}^h_{\partial\Gamma} + \left(\boldsymbol{n}^h_\Gamma \cdot \mathbf{q}_\Gamma \cdot \boldsymbol{n}^h_{\partial\Gamma}\right)\boldsymbol{n}^h_\Gamma$, see Eq. 4.37, are the conjugated forces at the Dirichlet boundary $\partial\Gamma^h_{\mathrm{D},\boldsymbol{u}}$.

The discrete weak form of the moment equilibrium states: Given Young's modulus $E \in \mathbb{R}^+$, Poisson's ratio $\nu \in [0,\, 0.5]$, distributed moments $\boldsymbol{c} \in T_P\Gamma^h$ on Γ^h, bending moments $\hat{\boldsymbol{m}}_{\partial\Gamma}$ on $\partial\Gamma^h_{\mathrm{N},\boldsymbol{w}}$, stabilization parameters $(\rho, \rho_w) \in \mathbb{R}^+ \times \mathbb{R}^+$ and boundary conditions $\hat{\boldsymbol{g}}_{\boldsymbol{w}}$ on $\partial\Gamma_{\mathrm{D},\boldsymbol{w}}$, find the displacement fields $(\boldsymbol{u}^h, \boldsymbol{w}^h) \in \bar{\mathcal{S}}^{\mathrm{RM},h}_{\boldsymbol{u}} \times \bar{\mathcal{S}}^{\mathrm{RM},h}_{\boldsymbol{w}}$ such that for all test functions $(\boldsymbol{v}_u^h, \boldsymbol{v}_w^h) \in \bar{\mathcal{V}}_{\boldsymbol{u}}^{\mathrm{RM},h} \times \bar{\mathcal{V}}_{\boldsymbol{w}}^{\mathrm{RM},h}$ there holds in Γ^h

$$\begin{aligned}
&\int_{\Gamma^h} \nabla_\Gamma^{\mathrm{dir}} \tilde{\boldsymbol{v}}_w^h : \mathbf{m}_\Gamma(\boldsymbol{u}^h, \widetilde{\boldsymbol{w}}^h) + \tilde{\boldsymbol{v}}_w^h \cdot \left[\mathbf{q}_\Gamma(\boldsymbol{u}^h, \widetilde{\boldsymbol{w}}^h) \cdot \boldsymbol{n}_\Gamma \right] \, \mathrm{d}A \\
&- \underbrace{\int_{\partial\Gamma_{\mathrm{D},\boldsymbol{w}}} \tilde{\boldsymbol{v}}_w^h \cdot \boldsymbol{m}_{\partial\Gamma}(\boldsymbol{u}^h, \widetilde{\boldsymbol{w}}^h) \, \mathrm{d}s}_{\text{boundary term due to } \boldsymbol{v}_w^h \neq \mathbf{0} \text{ on } \partial\Gamma_{\mathrm{D},\boldsymbol{w}}} + \underbrace{\int_{\partial\Gamma_{\mathrm{D},\boldsymbol{w}}} \widetilde{\boldsymbol{w}}^h \cdot \boldsymbol{m}_{\partial\Gamma}(\boldsymbol{v}_u^h, \tilde{\boldsymbol{v}}_w^h) \, \mathrm{d}s}_{\text{Nitsche term for rot. on LHS}} \\
&+ \underbrace{\rho \int_{\Omega_h^\Gamma} \left(\nabla \boldsymbol{w}^h \cdot \boldsymbol{n}_\Gamma^{e,h} \right) \cdot \left(\nabla \boldsymbol{v}_w^h \cdot \boldsymbol{n}_\Gamma^{e,h} \right) \, \mathrm{d}V}_{\text{Trace FEM stabilization, see Section 3.2.3}} + \underbrace{\rho_w \int_{\Gamma^h} \left(\boldsymbol{w}^h \cdot \boldsymbol{n}_\Gamma^h \right) \left(\boldsymbol{v}_w^h \cdot \boldsymbol{n}_\Gamma^h \right) \, \mathrm{d}A}_{\text{stabilization term for } \widetilde{\boldsymbol{w}}^h} \qquad (5.46) \\
&= \int_{\Gamma^h} \boldsymbol{v}_w^h \cdot \boldsymbol{c} \, \mathrm{d}A + \underbrace{\int_{\partial\Gamma_{\mathrm{D},\boldsymbol{w}}^h} \hat{\boldsymbol{g}}_{\boldsymbol{w}} \cdot \boldsymbol{m}_{\partial\Gamma}(\boldsymbol{v}_u^h, \tilde{\boldsymbol{v}}_w^h) \, \mathrm{d}s}_{\text{Nitsche term for rot. on RHS}} + \int_{\partial\Gamma_{\mathrm{N},\boldsymbol{w}}^h} \boldsymbol{v}_w^h \cdot \hat{\boldsymbol{m}}_{\partial\Gamma} \, \mathrm{d}s \ ,
\end{aligned}$$

where $\boldsymbol{m}_{\partial\Gamma} = \mathbf{m}_\Gamma \cdot \boldsymbol{n}_{\partial\Gamma}^h$, see Eq. 4.37, are the conjugated bending moments at the Dirichlet boundary $\partial\Gamma_{\mathrm{D},\boldsymbol{w}}^h$. Note that in the implementation, one may employ the identity $\mathbf{A} : \mathbf{B} = (\mathbf{P} \cdot \mathbf{A} \cdot \mathbf{P}) : \mathbf{B}^{\mathrm{dir}}$ with $(\mathbf{A}, \mathbf{B}) \in \mathbb{R}^{3\times3}$ and $\mathbf{B} = \mathbf{P} \cdot \mathbf{B}^{\mathrm{dir}} \cdot \mathbf{P}$ in order to further simplify the obtained terms with the projected difference vector. As a result, only directional derivatives of the discrete, projected difference vector are required which simplifies the implementation significantly.

The usual element assembly w.r.t. the active elements yields a linear system of equations in the following form

$$\underbrace{\left(\mathbf{K}_{\mathrm{Stiff}} + \mathbf{K}_{\mathrm{Nitsche}} + \mathbf{K}_{\mathrm{Stab}} \right)}_{\mathbf{K}} \cdot \begin{bmatrix} \underline{\hat{\boldsymbol{u}}} \\ \underline{\hat{\boldsymbol{w}}} \end{bmatrix} = \underbrace{\left(\boldsymbol{b}_{\mathrm{Load}} + \boldsymbol{b}_{\mathrm{Nitsche}} \right)}_{\boldsymbol{b}} \ , \qquad (5.47)$$

with $[\underline{\hat{\boldsymbol{u}}}, \underline{\hat{\boldsymbol{w}}}]$ being the sought displacements and rotations of the normal vector at the nodes of the active elements. The matrix $\mathbf{K}$ and the load vector $\boldsymbol{b}$ are split into: (1) standard terms for the stiffness matrix, (2) boundary terms and (3) stabilization terms, respectively.

5.3 Numerical results

In the following, numerical results for both finite element approaches are presented. The proposed shell formulations in the frame of the TDC with the Surface and Trace FEM are applied to a set of classical and new benchmark examples. In the presented test cases, the thickness of the shell is rather thin and locking phenomena may be expected, especially in the case of low ansatz orders. However, when increasing the order p, it is well-known (and confirmed herein) that locking phenomena decrease significantly and, therefore, no further measures against locking phenomena are considered herein.

5.3.1 Surface FEM

The set of benchmark examples for the Surface FEM consists of the well-known Scordelis-Lo roof from [9], the partly clamped hyperbolic paraboloid from [8], [29] and the clamped flower shaped shell from [125]. In the convergence studies, uniform NURBS patches with different orders and numbers of knot spans in each direction are employed. This is equivalent to meshes with higher-order elements and $n \in \{2, 4, 8, 16, 32, 64, 128\}$ elements per side are used. The orders are varied as $p \in \{2, 3, 4, 5, 6\}$.

5.3.1.1 Scordelis-Lo roof

The Scordelis-Lo roof problem is presented in Section 4.3.2, see also Fig. 4.6. In Fig. 5.3(a), the numerical solution obtained with the Reissner-Mindlin shell theory of the Scordelis-Lo roof is illustrated. The displacements are magnified by one order of magnitude. The colors on the deformed surface indicate the Euclidean norm of the displacement field $\boldsymbol{u}$. In Fig. 5.3(b), the normalized convergence of the maximum displacement $u_{z,\max}$ is plotted up to polynomial order of $p = 6$ as a function of the element (knot span) size. It is clearly seen that the results improve upon increasing the order of the NURBS. The style of presentation is analogously to the test case in Section 4.3.2. Except for the order $p = 2$, the locking phenomena are not very pronounced. Hence, it is not necessary to employ graded meshes as used, e.g., in [95] in order to resolve the boundary layers.

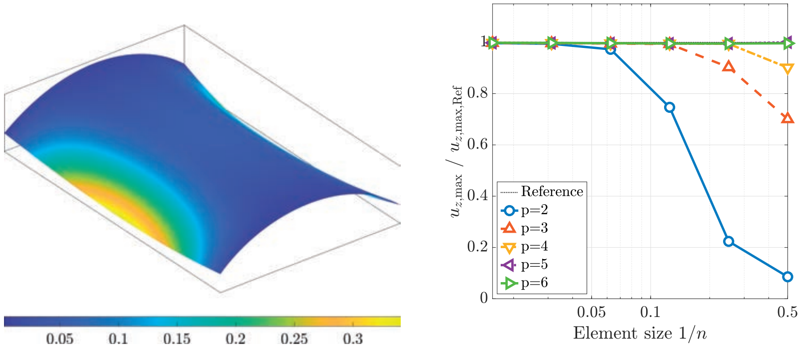

(a) displacement $\boldsymbol{u}$ **(b)** convergence

Fig. 5.3: Scordelis-Lo roof modelled as Reissner-Mindlin shell and IGA: (a) Displacement field $\boldsymbol{u}$ scaled by one order of magnitude, and (b) normalized convergence of reference displacement $u_{z,\max,\mathrm{Ref}} = 0.3024$.

5.3.1.2 Hyperbolic paraboloid

The next test case is a partly clamped hyperbolic paraboloid and is taken from [8], [29]. The shell is defined by $z = x^2 - y^2$ with $(x, y) \in [-1/2, 1/2]^2$, the thickness is set to $t = 0.01$

and is loaded by gravity, see Fig. 5.4. The edge at $x = -1/2$ is clamped and the other three edges are free. The material parameters are Young's modulus $E = 2.0 \times 10^{11}$ and Poisson's ratio $\nu = 0.3$. Similar to the example before, the displacements are compared with a reference solution. In particular, the vertical displacement at point $\boldsymbol{x}_i = (0.5,\, 0,\, 0.25)^{\mathrm{T}}$ is compared with the reference solution $u_{z,\mathrm{Ref}} = -9.3355 \times 10^{-5}$ given in [8]. In Fig. 5.5(a), the undeformed domain (grey) and the deformed shell is presented, with displacements scaled by a factor of 2000. In Fig. 5.5(b), analogously to the example before, the normalized convergence of the vertical displacement $u_{z,i}$ at point i is plotted up to polynomial order of $p = 6$ as a function of the element (knot span) size. For the lower orders $p = 2, 3$, the expected locking phenomena is more pronounced compared to the example before. Nevertheless, it is clearly seen that the accuracy for higher-order NURBS increases significantly and the behaviour of convergence is in agreement with the results shown, e.g., in [8], [95].

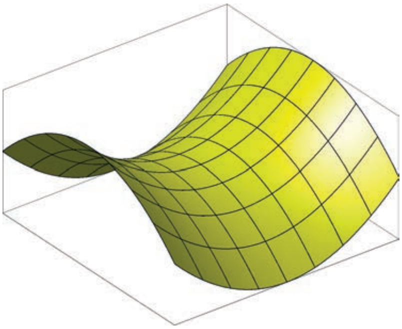

Geometry:	Hyperbolic paraboloid $L_x = L_y = 1$ (center is at origin) $z = x^2 - y^2$ $t = 0.01$
Material parameters:	$E = 2.0 \times 10^{11}$ $\nu = 0.3$ $\alpha_{\mathrm{s}} = 1.0$
Load:	Gravity load $\boldsymbol{f} = [0,\, 0,\, -8000 \cdot t]^{\mathrm{T}}$ $\boldsymbol{c} = \boldsymbol{0}$
Support:	Clamped edge at $x = -1/2$

Fig. 5.4: Definition of the hyperbolic paraboloid problem for the Reissner-Mindlin shell and IGA.

5.3.1.3 Flower-shaped shell

The geometry for this example is similar to Section 4.3.4. The surface is rather complex, but suitable to feature smooth solutions of all physical fields and, consequently, higher-order convergence rates can be achieved. In contrast to the example in Section 4.3.4, the material parameters and loading are modified. A summary of the example is shown in Fig. 5.6.

Following the same rationale as in Section 4.3.4, the force equilibrium of Eq. 5.17 and moment equilibrium of Eq. 5.18 are computed in strong form and serve as the basis to compute residual errors. In particular, the L^2-norms of the residual errors are calculated

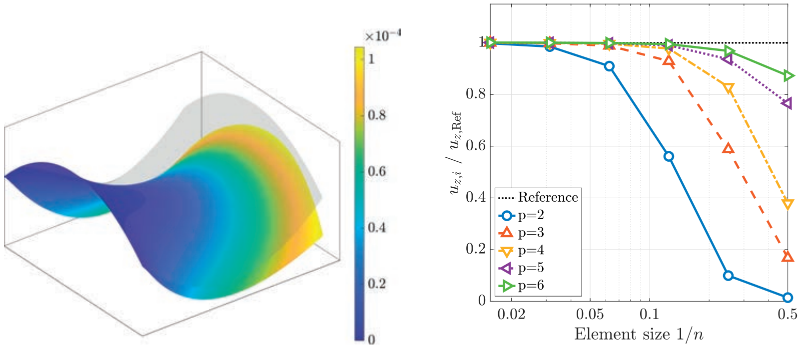

(a) displacement $\boldsymbol{u}$ **(b)** convergence

Fig. 5.5: Hyperbolic paraboloid modelled as Reissner-Mindlin shell and IGA: (a) Displacement field $\boldsymbol{u}$ scaled by 2000, and (b) normalized convergence of reference displacement $u_{z,\mathrm{Ref}} = -9.3355 \times 10^{-5}$ at point $\boldsymbol{x}_i = (0.5,\ 0,\ 0.25)^{\mathrm{T}}$.

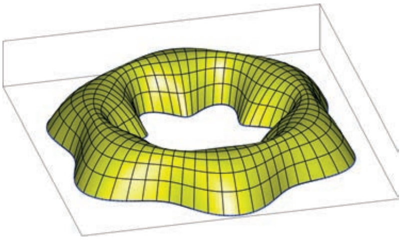

Geometry:	Flower shaped shell see Eq. 4.58 $t = 0.1$
Material parameters:	$E = 10$ $\nu = 0.3$ $\alpha_{\mathrm{s}} = 1.0$
Load:	$\boldsymbol{f} = [-1 \cdot t^3,\ -2 \cdot t^3,\ -3 \cdot t^3]^{\mathrm{T}}$ $\boldsymbol{c} = \boldsymbol{0}$
Support:	Clamped edges at inner and outer boundary

Fig. 5.6: Definition of flower-shaped shell problem for the Reissner-Mindlin shell with IGA.

as

$$\varepsilon^2_{\mathrm{rel,residual,F}} = \frac{\int_\Gamma \left[\mathrm{div}_\Gamma \mathbf{n}_\Gamma^{\mathrm{real}} + \mathbf{Q} \cdot \mathrm{div}_\Gamma \mathbf{q}_\Gamma + \mathbf{H} \cdot (\mathbf{q}_\Gamma \cdot \boldsymbol{n}_\Gamma) + \boldsymbol{f}\right]^2 \,\mathrm{d}A}{\int_\Gamma \boldsymbol{f}^2 \,\mathrm{d}A}\ , \tag{5.48}$$

$$\varepsilon^2_{\mathrm{residual,M}} = \int_\Gamma \left[\mathbf{P} \cdot \mathrm{div}_\Gamma \mathbf{m}_\Gamma - \mathbf{q}_\Gamma \cdot \boldsymbol{n}_\Gamma + \boldsymbol{c}\right]^2 \,\mathrm{d}A\ . \tag{5.49}$$

The theoretical optimal order of convergence in the residual errors is $\mathcal{O}(p-1)$ due to the presence of second-order derivatives. The numerical solution is presented in Fig. 5.7(a) and scaled by one order of magnitude. The results of the convergence study are shown in Fig. 5.7(b) and Fig. 5.7(c). The polynomial orders are varied up to $p = 6$. Due to the complex geometry and boundary layer effects, the pre-asymptotic range is rather pronounced for this particular application. Therefore, the results of the coarser levels $n \in \{2,\ 4\}$ are omitted in the results. As can be seen, the expected higher-order convergence rates are achieved in both residual errors Eq. 5.48 and Eq. 5.49. The stored elastic energy at the finest level with a polynomial order $p = 6$ is $\mathfrak{e} = 5.052\,979\,16 \times 10^{-4}$, which

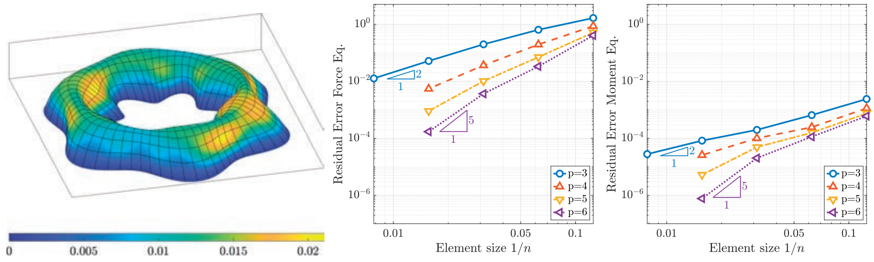

(a) displacement $\boldsymbol{u}$ **(b)** force equilibrium **(c)** moment equilibrium

Fig. 5.7: Flower shaped shell with Reissner-Mindlin shell and IGA: (a) Displacement $\boldsymbol{u}$ scaled by one order of magnitude, (b) residual error of the force equilibrium $\varepsilon_{\text{rel,residual,F}}$, and (c) residual error of the moment equilibrium $\varepsilon_{\text{residual,M}}$.

can be seen as an overkill solution. This stored elastic energy may be used for future benchmarking when the computation of the residual errors is not desired.

5.3.2 Trace FEM

The proposed numerical method for implicitly defined Reissner-Mindlin shells is tested on a set of benchmark examples, consisting of the partly clamped hyperbolic paraboloid from [8], [29], the partly clamped gyroid from [70] and a clamped flower-shaped shell inspired by [125], [127].

In the convergence studies, quasi-regular background meshes consisting of tetrahedral elements are used. For all unknown fields, i.e., $\boldsymbol{u}^h, \boldsymbol{w}^h$, and the interpolation of the level-set functions, the same order of shape functions are used. The orders are varied as $2 \leq p \leq 6$. The element size h is proportional to the factor n which is related to the number of elements and is varied between $2 \leq n \leq 128$.

In the presented examples, the stabilization parameter ρ for the normal derivative volume stabilization is set to $\rho = {}^{1000}/_{h}$ which is in accordance with the suggested range mentioned in Section 3.2.3. In order to achieve a proper scaling of the stiffness matrix, the parameter ρ_w, is set to $\rho_w = Et$, as proposed in Section 5.2.2.

5.3.2.1 Hyperbolic paraboloid

The first example is the partly clamped hyperbolic paraboloid as defined in Section 5.3.1.2. The problem with the implicitly defined shell body is defined in Fig. 5.8. The yellow surface is the zero-isosurface of the master level-set function ϕ and the grey planes are the zero-isosurfaces of the slave level-set functions ψ_j, $j \in \{1, \ldots, 4\}$, which define the boundaries of the shell. The blue line is the clamped edge of the shell. In Fig. 5.9(a), the active background mesh which contains only cut elements is shown. In Fig. 5.9(b), the corresponding integration points are illustrated, those in the domain are plotted in

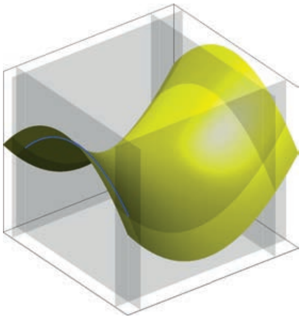

Geometry:	Hyperbolic paraboloid $\phi(\boldsymbol{x}) = x^2 - y^2 - z$ $x \in [-0.5, 0.5]$ $y \in [-0.5, 0.5]$ $t = 0.01$
Material parameters:	$E = 2.0 \times 10^{11}$ $\nu = 0.3$ $\alpha_{\mathrm{s}} = 1.0$
Load:	Gravity load $\boldsymbol{f} = [0,\ 0,\ -8000 \cdot t]^{\mathrm{T}}$ $\boldsymbol{c} = \boldsymbol{0}$
Support:	Clamped edge at $x = -1/2$
Ref. displacement:	$\lvert u_{z,i,\mathrm{Ref}} \rvert = 9.3355 \times 10^{-5}$ $\boldsymbol{x}_i = (0.5,\ 0,\ 0.25)^{\mathrm{T}}$

Fig. 5.8: Definition of the hyperbolic paraboloid problem for the Reissner-Mindlin shell with Trace FEM.

red and those on the boundaries are blue. In Fig. 5.9(c), the numerical solution of the partly clamped hyperbolic paraboloid is presented. The grey surface is the undeformed zero-isosurface and the colors on the deformed mid-surface of the shell are the Euclidean norm of the displacement field $\boldsymbol{u}$. The displacements are magnified by a factor of 2×10^3. In the convergence studies, the vertical displacement at $\boldsymbol{x}_i$ is compared with the given reference displacement. Due to the moderate complexity of the master level-set function, the numerical solution converges rather fast and the element factor n is only varied between $2 \leq n \leq 64$. In Fig. 5.10(a), the result of the convergence study is presented. In particular, the normalized displacement $u_{z,i}/u_{z,i,\mathrm{Ref}}$ is plotted as a function of the element size $h \sim 1/n$. The behaviour of the convergence is in agreement with the results shown, e.g., in [8], [95]. In particular, the expected locking behaviour is more pronounced for $p = 2$ and decreases significantly for higher orders. In the direct comparison with the results obtained with the Surface FEM (more precisely, IGA) in Section 5.3.1.2, the results w.r.t. the element scale factor n are quite similar. One may observe that for the

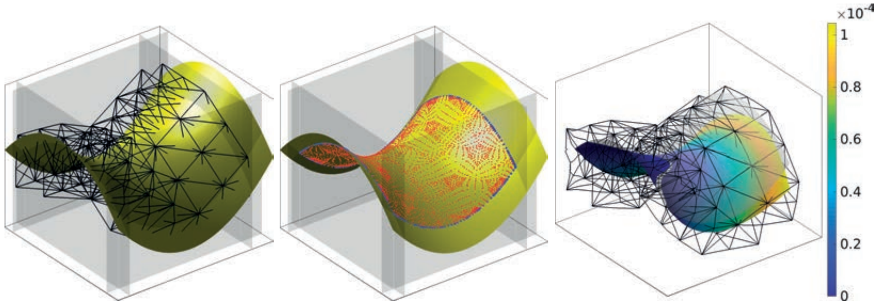

(a) active background mesh **(b)** integration points **(c)** displacement $\boldsymbol{u}$

Fig. 5.9: (a) Active background mesh, which consists only of cut elements, (b) automatically generated integration points in the domain (red) and on the boundaries (blue), and (c) deformed zero-isosurface with scaled displacements $\boldsymbol{u}$ by a factor of 2×10^3.

higher orders $p \geq 3$, the locking is less pronounced in the Trace FEM approach. The overestimation of the displacement at the coarsest level for the orders $p \in \{4, 5, 6\}$ is caused by rather large errors in the essential boundary conditions which may be traced back to a rather coarse mesh resolution. As clearly seen in Fig. 5.10(a), this phenomenon decreases rapidly with finer meshes.

In Fig. 5.10(b), the normalized, estimated condition number of the stiffness matrix is plotted as a function of the element size $h \sim {}^{1}\!/_{n}$. They are obtained with the MATLAB function *condest*. It can be seen that the condition numbers increase with quadratic order as expected for second-order PDEs. The difference between the element orders is well-known in the context of higher-order finite element approaches, see e.g., in [65].

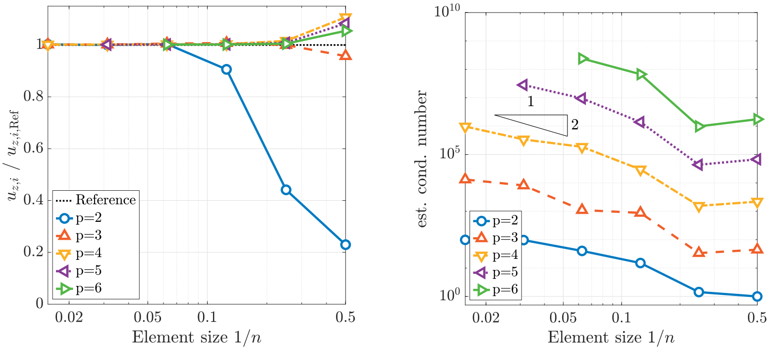

(a) convergence **(b)** condition number

Fig. 5.10: (a) Normalized convergence of reference displacement $u_{z,i,\mathrm{Ref}} = -9.3355 \times 10^{-5}$ at point $\boldsymbol{x}_i = (0.5,\, 0,\, 0.25)^{\mathrm{T}}$, (b) normalized condition numbers, the reference value is 1.0797×10^{10}, which is the condition number at $n = p = 2$.

5.3.2.2 Gyroid

The next test case is a partly clamped gyroid and is taken from [70]. The problem is defined in Fig. 5.11. Similar to above, the yellow surface is the zero-isosurface of the master level-set function ϕ, the grey planes are the zero-isosurfaces of the slave level-set functions ψ_j, $j \in \{1, \dots, 6\}$, which bound the master leve-set function. The blue curve is the clamped edge of the shell.

In contrast to [70], a factor π is inserted into the arguments of the trigonometric functions of the master level-set function, which is given in [70, Eq. 43]. Otherwise, the obtained geometry is not in agreement with the presented geometry in [70, Fig. 12]. In addition, the load is decreased by one order of magnitude in order to decrease the deformations, which shall be significantly smaller than the dimensions of the shell. Therefore, the given reference displacement needs to be scaled accordingly to 0.18812. However, in [70], a different shell model (seven-parameter shell model) is used. Herein, the classical Reissner-Mindlin shell which is often labelled as five-parameter model, is used and, therefore, we

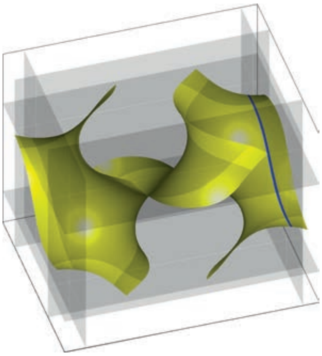

Geometry:	Gyroid $\phi(\boldsymbol{x}) = \sin(\pi x)\cos(\pi y) + \sin(\pi y)\cos(\pi z) + \sin(\pi z)\cos(\pi x)$ $x \in [0, 2]$ $y \in [-0.5, 0.5]$ $z \in [-0.5, 0.5]$ $t = 0.03$
Material parameters:	$E = 70 \times 10^9$ $\nu = 0.3$ $\alpha_\mathrm{s} = 1.0$
Load:	Gravity load $\boldsymbol{f} = [0,\ 0,\ 10^7 \cdot t]^\mathrm{T}$ $\boldsymbol{c} = \boldsymbol{0}$
Support:	Clamped edge at $x = 0$
Ref. displacement:	$\lvert u_{z,i,\mathrm{Ref}}\rvert = 0.182661$ $\boldsymbol{x}_i = (2,\ 0.5,\ -0.25)^\mathrm{T}$

Fig. 5.11: Definition of the partly clamped gyroid problem.

can expect small differences in the displacements. For the Reissner-Mindlin shell model, the converged reference displacement is 0.182661, which is a relative difference of 2.9% compared to the seven-parameter model. This can be explained by the differences in the kinematic assumptions between the two shell models. This discrepancy could be decreased with a suitable shear correction factor.

Analogously to the example above, in Fig. 5.12, the active background mesh and the corresponding integration points are shown, where the domain integrations points are plotted in red and the integration points on the boundaries are blue. The deformed zero-isosurface of the shell is plotted in a similar manner as in the first example in Fig. 5.13(a), where the colors on the surface are the Euclidean norm of the displacement field $\boldsymbol{u}$ and the grey surface indicates the undeformed zero-isosurface.

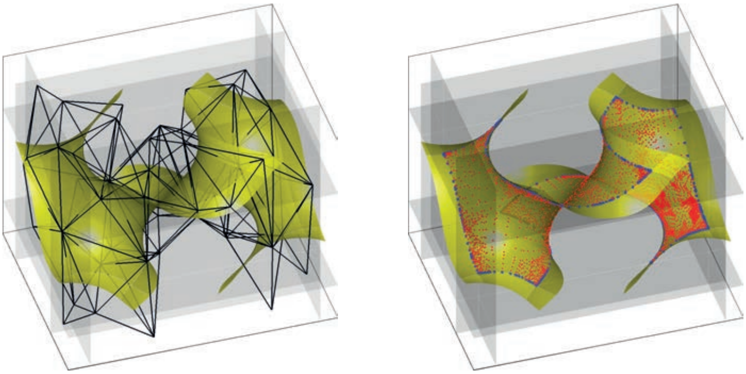

(a) active background mesh **(b)** integration points

Fig. 5.12: (a) Active background mesh, which consists only of cut elements, and (b) automatically generated integration points in the domain (red) and on the boundaries (blue).

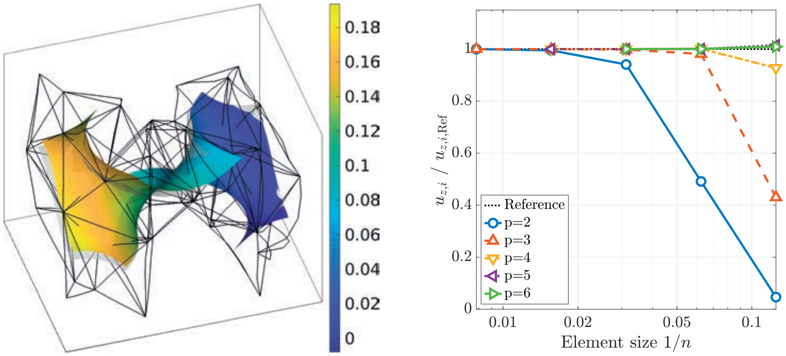

(a) displacement $\boldsymbol{u}$ **(b)** convergence

Fig. 5.13: (a) Deformed zero-isosurface, and (b) normalized convergence of reference displacement $u_{z,i,\mathrm{Ref}} = 0.182661$ at point $\boldsymbol{x}_i = (2,\, 0.5,\, -0.25)^{\mathrm{T}}$.

In the convergence study, the parameter n is varied between $8 \leq n \leq 128$. In Fig. 5.13(b), the results of the convergence analyses are presented. Similar to the first test case, the normalized displacement $u_{z,i}/u_{z,i,\mathrm{Ref}}$ is plotted as a function of the element size $h \sim 1/n$. For the lower orders $p \in \{2, 3\}$ the expected locking phenomena is more pronounced compared to the example before. Nevertheless, it is clearly seen that the accuracy for higher orders increases significantly and the behaviour of convergence is in agreement with the results shown, e.g., in [70]. The condition numbers for this example behave in a similar manner as in Fig. 5.10(b) and, therefore, a visualization is omitted for brevity.

5.3.2.3 Flower-shaped shell

The geometry of the last example is inspired from [127]. The problem is defined in Fig. 5.14. Analogously to above, the yellow surface is the zero-isosurface of the master level-set function ϕ and the intersection with the slave level-set function ψ (grey surface) defines the boundaries of the shell.

A characteristic feature of this test case is that smooth solutions in all involved fields can be expected and, therefore, optimal higher-order convergences rates are enabled. In contrast to the examples before, a reference displacement is not available for this example. For the error measurement, we employ the concept of residual errors in a similar manner than above. In particular, the summed element-wise L^2-errors of the force and moment equilibrium are computed in the convergence analyses

$$\varepsilon^2_{\mathrm{rel,residual,F}} = \sum_{T \in \tau^{\Gamma}_{\Omega,h}} \frac{\int_T \left[\mathrm{div}_\Gamma \mathbf{n}^{\mathrm{real}}_\Gamma + \mathbf{Q} \cdot \mathrm{div}_\Gamma \mathbf{q}_\Gamma + \mathbf{H} \cdot (\mathbf{q}_\Gamma \cdot \boldsymbol{n}_\Gamma) + \boldsymbol{f}\right]^2 \,\mathrm{d}A}{\int_T \boldsymbol{f}^2 \,\mathrm{d}A}\,, \tag{5.50}$$

$$\varepsilon^2_{\mathrm{residual,M}} = \sum_{T \in \tau^{\Gamma}_{\Omega,h}} \int_T \left[\mathbf{P} \cdot \mathrm{div}_\Gamma \mathbf{m}_\Gamma - \mathbf{q}_\Gamma \cdot \boldsymbol{n}_\Gamma + \boldsymbol{c}\right]^2 \,\mathrm{d}A\,. \tag{5.51}$$

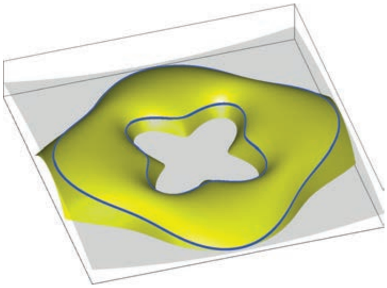

Geometry:	Flower shell $\phi(\boldsymbol{x}) = {}^1\!/\!_3 \left(1 - s^2\right) + {}^1\!/\!_{40} \left(x^2 - y^2\right) - z$ $s = \frac{r-2.3}{0.8+0.3\cos(4\theta)}$ r, θ are polar coordinates of x, y $\psi(\boldsymbol{x}) = {}^1\!/\!_{40} \left(x^2 - y^2\right) - z$ $t = 0.05$
Material parameters:	$E = 1.05 \times 10^8$ $\nu = 0.33$ $\alpha_{\mathrm{s}} = 1.0$
Load:	$\boldsymbol{f} = -10^2[1,\ 2,\ 3]^{\mathrm{T}}$ $\boldsymbol{c} = \boldsymbol{0}$
Support:	Clamped edges
Error measurement	Residual errors

Fig. 5.14: Definition of shallow flower-shaped shell problem.

For the computation of the residual errors, second-order surface derivatives are required which implies a theoretical optimal order of convergence $\mathcal{O}(p-1)$. The numerical solution of the problem is visualized in Fig. 5.15(b). The displacements are scaled by a factor of 5×10^2. The colors on the deformed zero-isosurface are the Euclidean norm of the displacement field $\boldsymbol{u}$. The corresponding integration points are shown in Fig. 5.15(a) in the same style than before.

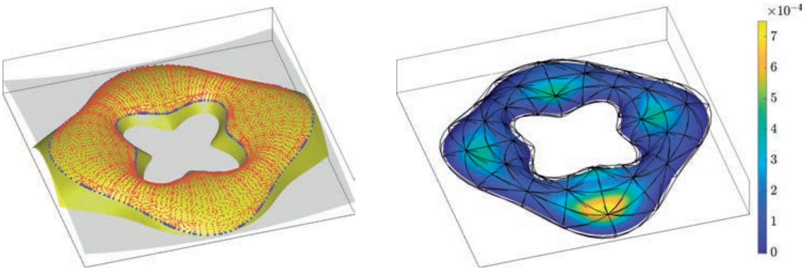

(a) integration points **(b)** displacements

Fig. 5.15: (a) Automatically generated integration points in the domain (red) and on the boundaries (blue), and (b) deformed zero-isosurface with scaled displacements $\boldsymbol{u}$ by a factor of 5×10^2.

In the convergence analyses, the parameter n is varied between $2 \leq n \leq 64$. The results are plotted in Fig. 5.16. It is noticeable that the pre-asymptotic range is more pronounced for the lower ansatz orders $p \in \{2, 3\}$. Nevertheless, it is clear that higher-order convergence rates are achieved in both residual errors of Eqs. 5.50 and 5.51. In comparison to the test case for the Reissner-Mindlin shell presented in Section 5.3.1.3, the convergence in the residual errors obtained here with the Trace FEM is very similar to the results obtained with isogeometric analysis. Note that the residual error of the moment equilibrium is the absolute, summed element-wise L^2-norm, due to $\boldsymbol{c} = \boldsymbol{0}$. When comparing $\varepsilon_{\mathrm{residual,M}}$ in Fig. 5.16(b) with results obtained by the authors in Fig. 5.7(c), the difference in the magnitudes is traced back to the material parameters and a modified geometry.

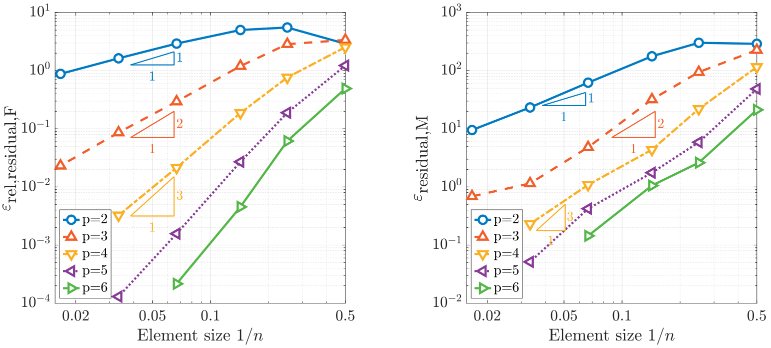

(a) force equilibrium **(b)** moment equilibrium

Fig. 5.16: (a) Residual error of the force equilibrium $\varepsilon_{\text{rel,residual,F}}$, and (b) residual error of the moment equilibrium $\varepsilon_{\text{residual,M}}$.

6 Large deformation membranes

In the following, the previously proposed approach of reformulating the equilibrium equations of shells in the frame of the TDC is extended to membranes undergoing large deformations. In the mechanical modelling of membranes, the flexural rigidity is neglected and loads can *only* be carried through in-plane (membrane) stresses. Consequently, bending moments and transverse shear stresses do not occur in the equilibrium. In contrast to shells, this automatically implies that the support forces at the boundaries must be tangential to the deformed membrane to satisfy the equilibrium.

Considering large deformations, a major difference compared to linear elasticity is that one carefully distinguishes between the undeformed (reference) configuration and the deformed (spatial) configuration. Furthermore, in the kinematics, the assumption of infinitesimal strains is abandoned. As a result of the more realistic kinematics, rigid body motions are modelled correctly and do not produce spurious stresses as in linear elasticity. The resulting strain measures are typically non-linear and, therefore, the obtained BVP results in a non-linear, vector-valued, second-order PDE where the equilibrium is to be fulfilled in the *deformed* configuration. The BVP is discretized with a higher-order Surface and Trace FEM. The numerical results show that the proposed finite strain theory yields higher-order convergence rates independent of the numerical methodology.

The major content of this chapter follows our own article in [66].

6.1 Governing equations

In this section, the governing equations of structural membranes are derived in the finite strain theory in the frame of the TDC. For the sake of simplicity, only a Saint Vernant-Kirchhoff material model is considered herein which may be seen as the simplest extension of linear elastic materials governed by Hooke's law to large deformations. The advantages of the reformulation of the membrane equations in the frame of the TDC are similar to shells. Furthermore, as shown in [66], the resulting BVP for membranes can easily be adopted to cables and ropes which, however, is omitted here for brevity.

The geometric definition of the membrane is analogously to the previous chapters. The membrane continuum Ω of thickness t can be defined implicitly with a signed distance function $\phi_{\mathrm{SDF}}(\boldsymbol{x})$,

$$\Omega = \left\{ \boldsymbol{x} \in \mathbb{R}^3 : |\phi_{\mathrm{SDF}}(\boldsymbol{x})| \leq \frac{t}{2} \right\} \ . \tag{6.1}$$

Alternatively, when the mid-surface Γ is parametrized with a map $\boldsymbol{x}_\Gamma(\boldsymbol{r})$, the domain of the membrane is defined by

$$\boldsymbol{x} = \boldsymbol{x}_\Gamma + \zeta \boldsymbol{n}_\Gamma(\boldsymbol{x}_\Gamma) \ , \tag{6.2}$$

where ζ is the coordinate in thickness direction $|\zeta| \leq {}^t\!/\!_2$. Further details regarding the geometry definition are discussed in Section 2.1. In the following, the subscript Γ in the notation of the normal vector is omitted for a more compact presentation.

6.1.1 Kinematics

As usual in finite strain theory, we consider an undeformed material configuration and a deformed spatial configuration. These are represented by $\Gamma_{\boldsymbol{X}}$ and $\Gamma_{\boldsymbol{x}}$, respectively, both are immersed in the physcial space $\mathbb{R}^3$. We follow the usual notation to relate uppercase letters in variable and operator names with the undeformed configuration and lowercase letters with the deformed one. The displacement field $\boldsymbol{u}(\boldsymbol{X})$ relates the two configurations via

$$\boldsymbol{x} = \boldsymbol{X} + \boldsymbol{u}(\boldsymbol{X}) \ , \quad \text{with } \boldsymbol{X} \in \Gamma_{\boldsymbol{X}} \subset \mathbb{R}^3 \text{ and } \boldsymbol{x} \in \Gamma_{\boldsymbol{x}} \subset \mathbb{R}^3. \tag{6.3}$$

In Fig. 6.1(a), the two configurations of a membrane undergoing large deformations are illustrated. As an example, the membrane is explicitly defined by a map $\boldsymbol{X}(\boldsymbol{r}) : \hat{\Omega} \rightarrow \Gamma_{\boldsymbol{X}}$, where the coordinates in the parameter space are labelled $\boldsymbol{r} = [r, s]^{\mathrm{T}}$. For further details regarding the explicit and implicit geometry definition, we refer to Section 2.1. In Fig. 6.1(b), the normal vectors and local triads for both configurations are illustrated.

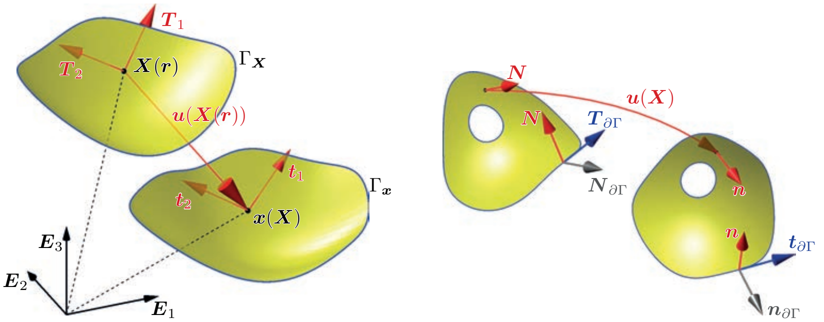

(a) def. and undef. configuration, $\Gamma_{\boldsymbol{X}}$ and $\Gamma_{\boldsymbol{x}}$ **(b)** normal vector and local triads

Fig. 6.1: (a) Undeformed and deformed configuration of a membrane undergoing large deformations with $\boldsymbol{x} = \boldsymbol{X} + \boldsymbol{u}$. (b) Normal vectors, $\boldsymbol{N}$ and $\boldsymbol{n}$, and conormal vectors, $\boldsymbol{N}_{\partial\Gamma}$ and $\boldsymbol{n}_{\partial\Gamma}$, in undeformed and deformed manifolds. The vectors $\boldsymbol{T}_{\partial\Gamma}$ and $\boldsymbol{t}_{\partial\Gamma}$ point in tangential direction along the boundary.

In the case of a *parametrized* membrane, one may easily obtain two vectors $\boldsymbol{T}_1^\star = \frac{\partial \boldsymbol{X}}{\partial r}$ and $\boldsymbol{T}_2^\star = \frac{\partial \boldsymbol{X}}{\partial s}$ from the columns of the Jacobi matrix $\mathbf{J}$, being tangential to $\Gamma_{\boldsymbol{X}}$ at a mapped point $\boldsymbol{X}$. As defined in Section 2.2.2, the first fundamental form in the undeformed configuration is $\mathbf{G} = \mathbf{J}^{\mathrm{T}} \cdot \mathbf{J}$. Normalizing $(\boldsymbol{T}_1^\star, \boldsymbol{T}_2^\star)$ gives the tangent vectors $(\boldsymbol{T}_1, \boldsymbol{T}_2)$ as visualized in Fig. 6.1(a). The tangent vectors $(\boldsymbol{t}_1, \boldsymbol{t}_2)$ in the deformed configuration are given by $\boldsymbol{t}_i = \mathbf{F}_\Gamma \cdot \boldsymbol{T}_i$, where $i = 1, 2$ and $\mathbf{F}_\Gamma$ is the surface deformation gradient which is defined in the subsequent section. Similar to Section 2.1, the cross product of the tangent vectors leads to the normal vector in the undeformed and deformed configuration

$$\boldsymbol{N} = \frac{\boldsymbol{N}^\star}{\|\boldsymbol{N}^\star\|} \qquad \text{with} \qquad \boldsymbol{N}^\star = \boldsymbol{T}_1^\star \times \boldsymbol{T}_2^\star \,, \tag{6.4}$$

$$\boldsymbol{n} = \frac{\boldsymbol{n}^\star}{\|\boldsymbol{n}^\star\|} \qquad \text{with} \qquad \boldsymbol{n}^\star = \boldsymbol{t}_1^\star \times \boldsymbol{t}_2^\star \,. \tag{6.5}$$

Next, we focus on the situation in large displacement theory for the *implicit* setup. The normal vector of the undeformed configuration is obtained by the gradient of the level-set function,

$$\boldsymbol{N}^\star(\boldsymbol{X}) = \nabla_{\boldsymbol{X}} \phi(\boldsymbol{X}) \quad \text{for } \boldsymbol{X} \in \Gamma_{\boldsymbol{X}}. \tag{6.6}$$

Let there be a displacement field $\boldsymbol{u}(\boldsymbol{X})$ which lives in the full 3-dimensional space (instead of only the manifold itself as for parametric manifolds) so that the classical gradient $\nabla_{\boldsymbol{X}} \boldsymbol{u}(\boldsymbol{X})$ is available. Note that capital subscript $\boldsymbol{X}$ in $\nabla_{\boldsymbol{X}}$ is the gradient w.r.t. the undeformed configuration. The resulting deformation gradient is

$$\mathbf{F}_\Omega(\boldsymbol{X}) = \nabla_{\boldsymbol{X}} \boldsymbol{x}(\boldsymbol{X}) = \mathbf{I} + \nabla_{\boldsymbol{X}} \boldsymbol{u}(\boldsymbol{X}) \,. \tag{6.7}$$

Based on this, one may compute the normal vector of the deformed configuration at $\boldsymbol{x} = \boldsymbol{X} + \boldsymbol{u}(\boldsymbol{X})$ as

$$\boldsymbol{n}^\star(\boldsymbol{x}) = \nabla_{\boldsymbol{x}} \phi(\boldsymbol{X}(\boldsymbol{x})) = \mathbf{F}_\Omega^{-\mathrm{T}} \cdot \boldsymbol{N}^\star \quad \text{for } \boldsymbol{x} \in \Gamma_{\boldsymbol{x}}, \tag{6.8}$$

which follows by the chain rule. Normalizing $(\boldsymbol{N}^\star, \boldsymbol{n}^\star)$ leads to the unit normal vectors $(\boldsymbol{N}, \boldsymbol{n})$ in the implicit setup as visualized in Fig. 6.1(b). The definition of the local triad on the boundary of the membrane is elaborated in Section 2.1 and is omitted here for brevity.

6.1.1.1 Tangential differential calculus in finite strain theory

Let us extend the surface operators in the TDC to the situation in the finite strain theory. In particular, the orthogonal projection operator, differential operators, surface deformation gradient etc. have to be distinguished in the deformed and undeformed configuration. Moreover, the area stretch and line stretch along the boundaries which are important in the mechanical modelling are introduced. The situation is described for both explicitly and implicitly defined membranes next.

Firstly, the projection operators $\mathbf{P}(\boldsymbol{X})$ and $\mathbf{p}(\boldsymbol{x})$ are introduced

$$\mathbf{P} = \mathbf{I} - \boldsymbol{N} \otimes \boldsymbol{N}, \tag{6.9}$$

$$\mathbf{p} = \mathbf{I} - \boldsymbol{n} \otimes \boldsymbol{n}. \tag{6.10}$$

The projector $\mathbf{P}$ at some point $\boldsymbol{X}$ maps an arbitrary vector in $\mathbb{R}^3$ to the tangent space at $\Gamma_{\boldsymbol{X}}$ (analogously for $\mathbf{p}$ in the deformed configuration). The properties of the projectors are equivalent to those discussed in Section 2.2.1.

Secondly, the differential operators in the case of *parametrized* membranes are defined. Let us consider a displacement field $\boldsymbol{u}(\boldsymbol{r})$ assuming that a point $\boldsymbol{r}$ is given which may also be seen as a function $\boldsymbol{u}(\boldsymbol{r}(\boldsymbol{X}))$ when a point $\boldsymbol{X} \in \Gamma_{\boldsymbol{X}}$ is given (and back-projected to the reference domain inverting the map $\boldsymbol{X}(\boldsymbol{r})$). We emphasize that in both cases, the displacement field only lives on the manifold $\Gamma_{\boldsymbol{X}}$. For some scalar function $f(\boldsymbol{r})$, e.g., each displacement component, the surface gradient w.r.t. the undeformed domain is

$$\nabla_{\boldsymbol{X}}^{\Gamma} f(\boldsymbol{r}) = \mathbf{J}^{+} \cdot \nabla_{\boldsymbol{r}} f(\boldsymbol{r}) \quad \Leftrightarrow \quad \begin{bmatrix} \partial_X^{\Gamma} f \\ \partial_Y^{\Gamma} f \\ \partial_Z^{\Gamma} f \end{bmatrix} = \mathbf{J}^{+} \cdot \begin{bmatrix} \partial_r f \\ \partial_s f \end{bmatrix} \tag{6.11}$$

and for vector-valued functions $\boldsymbol{u}(\boldsymbol{r}) = [u_x, u_y, u_z]^{\mathrm{T}} \in \mathbb{R}^3$, we have the *directional* surface gradient

$$\nabla_{\boldsymbol{X}}^{\Gamma,\mathrm{dir}} \boldsymbol{u}(\boldsymbol{r}) = \nabla_{\boldsymbol{X}}^{\Gamma,\mathrm{dir}} \begin{bmatrix} u_x(\boldsymbol{r}) \\ u_y(\boldsymbol{r}) \\ u_z(\boldsymbol{r}) \end{bmatrix} = \begin{bmatrix} \partial_X^{\Gamma} u_x & \partial_Y^{\Gamma} u_x & \partial_Z^{\Gamma} u_x \\ \partial_X^{\Gamma} u_y & \partial_Y^{\Gamma} u_y & \partial_Z^{\Gamma} u_y \\ \partial_X^{\Gamma} u_z & \partial_Y^{\Gamma} u_z & \partial_Z^{\Gamma} u_z \end{bmatrix} = \nabla_{\boldsymbol{r}} \boldsymbol{u}(\boldsymbol{r}) \cdot \mathbf{J}^{+\mathrm{T}}, \tag{6.12}$$

which is to be distinguished from the *covariant* surface gradient of a vector field as defined in Section 2.2.2. The related Jacobi matrix of the map from the undeformed to the deformed configuration, see Eq. 6.3, is also called *surface deformation gradient*,

$$\mathbf{F}_{\Gamma}(\boldsymbol{X}) = \nabla_{\boldsymbol{X}}^{\Gamma,\mathrm{dir}} \boldsymbol{x}(\boldsymbol{X}) = \mathbf{I} + \nabla_{\boldsymbol{X}}^{\Gamma,\mathrm{dir}} \boldsymbol{u}(\boldsymbol{X}). \tag{6.13}$$

Employing the surface deformation gradient, one may obtain the Jacobi-matrix from the reference to the deformed configuration $\mathbf{j} = \mathbf{F}_{\Gamma} \cdot \mathbf{J}$ whose columns are the tangent vectors $\boldsymbol{t}_1^{\star}$, $\boldsymbol{t}_2^{\star}$ to the deformed configuration $\Gamma_{\boldsymbol{x}}$. Furthermore, the first fundamental form is $\mathbf{g} = \mathbf{j}^{\mathrm{T}} \cdot \mathbf{j}$ and the operator $\mathbf{j}^{+} = \mathbf{j} \cdot \mathbf{g}^{-1}$ relates the classical gradient in the reference configuration with the surface gradient in the deformed configuration as $\nabla_{\boldsymbol{x}}^{\Gamma} f = \mathbf{j}^{+} \cdot \nabla_{\boldsymbol{r}} f$. The link between the surface gradients w.r.t. the undeformed and deformed configuration is accomplished with the operator $\mathbf{W}$ and defined by

$$\nabla_{\boldsymbol{x}}^{\Gamma} f = \mathbf{W} \cdot \nabla_{\boldsymbol{X}}^{\Gamma} f \ , \quad \text{with } \mathbf{W} = \mathbf{j}^{+} \cdot \left(\mathbf{J}^{+\mathrm{T}} \cdot \mathbf{J}^{+} \right)^{-1} \cdot \mathbf{J}^{+\mathrm{T}} \ . \tag{6.14}$$

This result is obtained using $\nabla_{\boldsymbol{X}}^{\Gamma} f = \mathbf{J}^{+} \cdot \nabla_{\boldsymbol{r}} f$ and $\nabla_{\boldsymbol{x}}^{\Gamma} f = \mathbf{j}^{+} \cdot \nabla_{\boldsymbol{r}} f$.

Next, the equivalent quantities for the *implicit* setup are introduced. The *surface* gradient (with respect to the undeformed configuration) of a scalar-valued function $f(\boldsymbol{X})$ with $\boldsymbol{X} \in \mathbb{R}^3$ results in

$$\nabla_{\boldsymbol{X}}^{\Gamma} f = \mathbf{P} \cdot \nabla_{\boldsymbol{X}} f. \tag{6.15}$$

As before, $\nabla_{\boldsymbol{X}} f$ is the classical gradient in the 3-dimensional space. The situation is analogous for each component u_i of a vector-valued function $\boldsymbol{u}(\boldsymbol{X})$, so that one obtains the *directional* surface gradient

$$\nabla_{\boldsymbol{X}}^{\Gamma,\mathrm{dir}}\boldsymbol{u} = \nabla_{\boldsymbol{X}}\boldsymbol{u}\cdot\mathbf{P} = \begin{bmatrix} \partial_X^\Gamma u_x & \partial_Y^\Gamma u_x & \partial_Z^\Gamma u_x \\ \partial_X^\Gamma u_y & \partial_Y^\Gamma u_y & \partial_Z^\Gamma u_y \\ \partial_X^\Gamma u_z & \partial_Y^\Gamma u_z & \partial_Z^\Gamma u_z \end{bmatrix}. \tag{6.16}$$

The definition of the covariant gradient is analogously to Section 2.2.2. The surface deformation gradient $\mathbf{F}_\Gamma$ is directly obtained with Eq. 6.14 employing the surface gradients for implicitly defined membranes. The equivalent expression of the operator $\mathbf{W}$ which relates the gradients between undeformed and deformed configuration is

$$\nabla_{\boldsymbol{x}}^\Gamma f = \mathbf{W}\cdot\nabla_{\boldsymbol{X}}^\Gamma f\ , \quad \text{with } \mathbf{W} = \mathbf{p}\cdot\mathbf{F}_\Omega^{-\mathrm{T}}. \tag{6.17}$$

Finally, we are interested in the stretch of a differential element of the membrane when undergoing the deformation. This is interpreted as an area stretch Λ inside the domain and at the boundaries as line stretch $\bar{\Lambda}$. For explicitly defined membranes the stretch measures are

$$\Lambda = \frac{\sqrt{\det\mathbf{g}}}{\sqrt{\det\mathbf{G}}} = \frac{\|\boldsymbol{n}^\star\|}{\|\boldsymbol{N}^\star\|} = \frac{\|\boldsymbol{t}_1^\star\times\boldsymbol{t}_2^\star\|}{\|\boldsymbol{T}_1^\star\times\boldsymbol{T}_2^\star\|}\ , \tag{6.18}$$

$$\bar{\Lambda} = \frac{\|\boldsymbol{t}^\star\|}{\|\boldsymbol{T}^\star\|}, \tag{6.19}$$

where $\boldsymbol{T}^\star$ is a tangent vector along the boundary and for the tangent vector in the deformed configuration follows $\boldsymbol{t}^\star = \mathbf{F}_\Gamma\cdot\boldsymbol{T}^\star$. For implicit membranes the equivalent representation of the stretch measures are

$$\Lambda = \frac{\|\nabla_{\boldsymbol{x}}\phi\|}{\|\nabla_{\boldsymbol{X}}\phi\|}\cdot\det\mathbf{F}_\Omega = \frac{\|\boldsymbol{n}^\star\|}{\|\boldsymbol{N}^\star\|}\cdot\det\mathbf{F}_\Omega\ , \tag{6.20}$$

$$\bar{\Lambda} = \frac{\|\boldsymbol{t}^\star\|}{\|\boldsymbol{T}^\star\|}\cdot\det\mathbf{F}_\Omega = \frac{\|\boldsymbol{n}_2^\star\times\boldsymbol{n}_1^\star\|}{\|\boldsymbol{N}_2^\star\times\boldsymbol{N}_1^\star\|}\cdot\det\mathbf{F}_\Omega\ , \tag{6.21}$$

where $(\boldsymbol{N}_1^\star, \boldsymbol{N}_2^\star)$ are the gradients of the master level-set and corresponding slave level-set function. The normal vectors in the deformed configuration may be obtained with Eq. 6.8.

6.1.1.2 Strain tensors

Above, a number of geometric quantities (such as normal vectors, projectors, area/line stretches, etc.) and differential operators related to (surface) gradients are introduced. It was shown how these quantities are obtained for parametrized and implicitly defined manifolds. The focus is now turned to the mechanics and the procedure follows the classical outline, however, it is based on the TDC here. It is emphasized that *all* tensors considered in the following refer to the parametric as well as implicit situation. A tensor $\mathbf{A}\in\mathbb{R}^{3\times3}$ is called “in-plane” or “tangential” to the undeformed configuration $\Gamma_{\boldsymbol{X}}$ if $\mathbf{A} = \mathbf{P}\cdot\mathbf{A}\cdot\mathbf{P}$ and to the deformed configuration $\Gamma_{\boldsymbol{x}}$ if $\mathbf{A} = \mathbf{p}\cdot\mathbf{A}\cdot\mathbf{p}$. Every in-plane (3×3)-tensor, except the null tensor, has 2 non-zero eigenvalues representing the principal mechanical quantity.

Starting point is the surface deformation gradient $\mathbf{F}_\Gamma(\boldsymbol{X})$ at $\boldsymbol{X} \in \Gamma_{\boldsymbol{X}}$, specified previously in Eq. 6.13. It may also be seen as a geometrical quantity mapping tangent vectors from the undeformed to the deformed configuration. Based on the surface deformation gradient, the directional and tangential Green-Lagrange strain tensors are defined as

$$\mathbf{E}_{\mathrm{dir}} = \frac{1}{2}\left(\mathbf{F}_\Gamma^{\mathrm{T}} \cdot \mathbf{F}_\Gamma - \mathbb{I}\right), \tag{6.22}$$

$$\mathbf{E}_{\mathrm{tang}} = \mathbf{P} \cdot \mathbf{E}_{\mathrm{dir}} \cdot \mathbf{P} \ , \tag{6.23}$$

respectively. The Euler-Almansi strain tensors are

$$\mathbf{e}_{\mathrm{dir}} = \frac{1}{2}\left[\mathbb{I} - \left(\mathbf{F}_\Gamma \cdot \mathbf{F}_\Gamma^{\mathrm{T}}\right)^{-1}\right], \tag{6.24}$$

$$\mathbf{e}_{\mathrm{tang}} = \mathbf{p} \cdot \mathbf{e}_{\mathrm{dir}} \cdot \mathbf{p} \ , \tag{6.25}$$

where $\mathbf{e}_{\mathrm{tang}}$ is tangential to the deformed configuration $\Gamma_{\boldsymbol{x}}$. As usual, there holds $\mathbf{e}_{\mathrm{dir}} = \mathbf{F}_\Gamma^{-\mathrm{T}} \cdot \mathbf{E}_{\mathrm{dir}} \cdot \mathbf{F}_\Gamma^{-1}$ (which is not true for the tangential versions of these strain tensors).

6.1.2 Constitutive equations

Conjugated stress tensors are introduced next and only the tangential versions are considered. Generally speaking, we assume some hyper-elastic material with an elastic energy function $\Psi(\mathbf{E}_{\mathrm{tang}})$ and obtain the second Piola-Kirchhoff stress tensor as $\mathbf{S} = \frac{\partial \Psi}{\partial \mathbf{E}_{\mathrm{tang}}}$. In [83] a compressible hyper-elastic material model, i.e., Mooney-Rivlin, is employed. Note that in the application of general hyper-elastic material models to thin-walled structures (membranes), one may carefully enforce the plane stress condition which is not as straightforward as in linear elasticity, for details we refer to, e.g., [83]. For simplicity, only Saint Venant-Kirchhoff solids are considered herein and the enforcement of plane stress remains analogously to linear elasticity. The second Piola-Kirchhoff stress tensor then follows

$$\begin{aligned}\mathbf{S} &= \lambda \operatorname{tr}(\mathbf{E}_{\mathrm{tang}})\,\mathbf{P} + 2\mu \mathbf{E}_{\mathrm{tang}} \\ &= \mathbf{P} \cdot \left(\lambda \operatorname{tr}(\mathbf{E}_{\mathrm{dir}})\,\mathbb{I} + 2\mu \mathbf{E}_{\mathrm{dir}}\right) \cdot \mathbf{P} \ ,\end{aligned} \tag{6.26}$$

with $\mathbf{S}$ being tangential to $\Gamma_{\boldsymbol{X}}$, λ and μ are the Lamé constants. For given Young's modulus E and Poisson's ratio ν, we have, for membranes, the modified Lamé constants $\lambda = \frac{E\nu}{1-\nu^2}$ and $\mu = \frac{E}{2(1+\nu)}$. The Cauchy stress tensor reads

$$\boldsymbol{\sigma} = \frac{1}{\Lambda} \mathbf{F}_\Gamma \cdot \mathbf{S} \cdot \mathbf{F}_\Gamma^{\mathrm{T}} \ , \tag{6.27}$$

where Λ is an area stretch for membranes when undergoing the displacement, see Section 6.1.1.1. The Cauchy stress is tangential to the deformed configuration $\Gamma_{\boldsymbol{x}}$ since $\mathbf{F}_\Gamma \cdot \mathbf{P} = \mathbf{p} \cdot \mathbf{F}_\Gamma \cdot \mathbf{P}$ and $\mathbf{P} \cdot \mathbf{F}_\Gamma^{\mathrm{T}} = \mathbf{P} \cdot \mathbf{F}_\Gamma^{\mathrm{T}} \cdot \mathbf{p}$, hence $\boldsymbol{\sigma} = \mathbf{p} \cdot \boldsymbol{\sigma} \cdot \mathbf{p}$. The first Piola-Kirchhoff stress tensor is given by

$$\mathbf{K} = \mathbf{F}_\Gamma \cdot \mathbf{S} \tag{6.28}$$

and there holds $\mathbf{K} = \mathbf{K} \cdot \mathbf{P} = \mathbf{p} \cdot \mathbf{K}$.

6.1.2.1 Relation of stress and strain tensors

For every point $\boldsymbol{X} \in \Gamma_{\boldsymbol{X}}$ and its mapped counterpart $\boldsymbol{x}(\boldsymbol{X}) \in \Gamma_{\boldsymbol{x}}$, we have the following equality,

$$\mathbf{S}(\boldsymbol{X}) : \mathbf{E}_{\text{tang}}(\boldsymbol{X}) = (\boldsymbol{\sigma}(\boldsymbol{x}) : \mathbf{e}_{\text{tang}}(\boldsymbol{x}))\, \Lambda(\boldsymbol{X}) \ , \tag{6.29}$$

where : is the contraction operator. In this sense the two stress tensors $\mathbf{S}$ and $\boldsymbol{\sigma}$ are conjugated to their related strain tensors $\mathbf{E}_{\text{tang}}$ and $\mathbf{e}_{\text{tang}}$, respectively. It is noted that

$$\mathbf{S} : \mathbf{E}_{\text{tang}} = \mathbf{S} : \mathbf{E}_{\text{dir}} \quad \text{and} \quad \boldsymbol{\sigma} : \mathbf{e}_{\text{tang}} = \boldsymbol{\sigma} : \mathbf{e}_{\text{dir}}$$

which will be important later. Furthermore, the result of these matrix contractions may also be derived by the non-zero eigenvalues S_i, $E_{\text{tang},i}$, σ_i, $e_{\text{tang},i}$, $i = 1, 2$, of the tangential tensors $\mathbf{S}$, $\mathbf{E}_{\text{tang}}$, $\boldsymbol{\sigma}$, $\mathbf{e}_{\text{tang}}$, respectively. Hence, we obtain

$$\mathbf{S} : \mathbf{E}_{\text{tang}} = \sum_{i=1}^{2} S_i\, E_{\text{tang},i} \quad \text{and} \quad \boldsymbol{\sigma} : \mathbf{e}_{\text{tang}} = \sum_{i=1}^{2} \sigma_i\, e_{\text{tang},i} \ .$$

6.1.2.2 Energy relation

An immediate consequence of Eq. 6.29 is that one may obtain the same stored potential energy of the deformed body by integrating over the undeformed or deformed configuration as follows

$$\begin{aligned} \mathfrak{e}(\boldsymbol{u}) &= \frac{t}{2} \int_{\Gamma_{\boldsymbol{x}}} \mathbf{e}_{\text{tang}}(\boldsymbol{u}) : \boldsymbol{\sigma}(\boldsymbol{u}) \ \mathrm{d}A \ , && (6.30) \\ &= \frac{t}{2} \int_{\Gamma_{\boldsymbol{X}}} \mathbf{E}_{\text{tang}}(\boldsymbol{u}) : \mathbf{S}\,(\boldsymbol{u}) \ \mathrm{d}A \ . && (6.31) \end{aligned}$$

6.1.3 Equilibrium

6.1.3.1 Equilibrium in strong form

A crucial aspect of finite strain theory is that equilibrium is to be fulfilled in the *deformed* configuration which is expressed in strong form as

$$\operatorname{div}_\Gamma \boldsymbol{\sigma}(\boldsymbol{x}) = -\boldsymbol{f}(\boldsymbol{x}) \quad \forall \boldsymbol{x} \in \Gamma_{\boldsymbol{x}} \ , \tag{6.32}$$

where $\boldsymbol{f}$ are body forces and $\operatorname{div}_\Gamma \boldsymbol{\sigma} = \nabla_{\boldsymbol{x}}^{\Gamma,\text{dir}} \cdot \boldsymbol{\sigma} = \nabla_{\boldsymbol{x}}^{\Gamma,\text{cov}} \cdot \boldsymbol{\sigma}$ is the divergence of the Cauchy stress tensor with respect to $\Gamma_{\boldsymbol{x}}$. Furthermore, we have the identity

$$\operatorname{Div}_\Gamma \mathbf{K}(\boldsymbol{X}) = \operatorname{div}_\Gamma \boldsymbol{\sigma}(\boldsymbol{x}(\boldsymbol{X}))\, \Lambda(\boldsymbol{X}) \ , \tag{6.33}$$

with $\mathrm{Div}_\Gamma \mathbf{K} = \nabla_{\boldsymbol{X}}^{\Gamma,\mathrm{dir}} \cdot \mathbf{K} = \nabla_{\boldsymbol{X}}^{\Gamma,\mathrm{cov}} \cdot \mathbf{K}$ being the divergence of the first Piola-Kirchhoff stress tensor from Eq. 6.28 with respect to $\Gamma_{\boldsymbol{X}}$. In order to transform the derivatives in the divergence operators from the undeformed to the deformed situation, use Eqs. (6.14) and (6.17) for parametric and implicit manifolds, respectively. Due to $\boldsymbol{F}(\boldsymbol{X}) = \boldsymbol{f}(\boldsymbol{x}(\boldsymbol{X}))\,\Lambda(\boldsymbol{X})$, the equilibrium in $\Gamma_{\boldsymbol{x}}$ can be stated equivalently to Eq. (6.32) based on quantities in the undeformed configuration as

$$\mathrm{Div}_\Gamma \mathbf{K}(\boldsymbol{X}) = -\boldsymbol{F}(\boldsymbol{X}) \quad \forall \boldsymbol{X} \in \Gamma_{\boldsymbol{X}} \ . \tag{6.34}$$

The domain of interest is a bounded manifold where the boundary $\partial\Gamma$ falls into the two non-overlapping parts $\partial\Gamma_\mathrm{D}$ and $\partial\Gamma_\mathrm{N}$, which holds in the deformed and undeformed configuration $\Gamma_{\boldsymbol{X}}$ and $\Gamma_{\boldsymbol{x}}$, respectively. Hence, the boundary conditions in the deformed configuration are

$$\boldsymbol{u}(\boldsymbol{x}) = \hat{\boldsymbol{g}}(\boldsymbol{x}) \text{ on } \partial\Gamma_{\boldsymbol{x},\mathrm{D}} \ , \tag{6.35}$$

$$\boldsymbol{\sigma}(\boldsymbol{x}) \cdot \boldsymbol{n}_{\partial\Gamma}(\boldsymbol{x}) = \hat{\boldsymbol{h}}(\boldsymbol{x}) \text{ on } \partial\Gamma_{\boldsymbol{x},\mathrm{N}} \ , \tag{6.36}$$

where $\hat{\boldsymbol{g}}$ are prescribed displacements and $\hat{\boldsymbol{h}}$ are tractions per length for membranes. Note that for membranes, $\hat{\boldsymbol{h}}$ must be in the tangent space of the deformed manifold in order to satisfy the equilibrium due to the absence of bending stresses or transverse shear stresses. The equivalent boundary conditions formulated in the *un*deformed configuration are

$$\boldsymbol{u}(\boldsymbol{X}) = \hat{\boldsymbol{G}}(\boldsymbol{X}) \text{ on } \partial\Gamma_{\boldsymbol{X},\mathrm{D}} \ , \tag{6.37}$$

$$\mathbf{K}(\boldsymbol{X}) \cdot \boldsymbol{N}_{\partial\Gamma}(\boldsymbol{X}) = \hat{\boldsymbol{H}}(\boldsymbol{X}) \text{ on } \partial\Gamma_{\boldsymbol{X},\mathrm{N}} \ , \tag{6.38}$$

where $\hat{\boldsymbol{G}}$ and $\hat{\boldsymbol{H}}$ have similar interpretations than before. The relation between $\hat{\boldsymbol{h}}$ and $\hat{\boldsymbol{H}}$ is $\hat{\boldsymbol{H}}(\boldsymbol{X}) = \bar{\Lambda}(\boldsymbol{X})\,\hat{\boldsymbol{h}}(\boldsymbol{x})$, where $\bar{\Lambda}$ is the line stretch along the boundary. Further information about boundary conditions for membranes are given in [27].

With the boundary conditions above, the complete second-order BVP is defined in the deformed and undeformed configuration. The obtained BVP in the frame of the TDC is valid for explicitly and implicitly defined manifolds and does not rely on curvilinear coordinates implied by a parametrization which are typically used in classical approaches, see, e.g., [27], [31]. Therefore, the proposed formulation in the frame of the TDC is more general compared to the classical theory.

6.1.3.2 Equilibrium in weak form

For stating the governing equations in weak form, the following test and trial function spaces are introduced

$$\mathcal{S}_{\boldsymbol{u}}^\mathrm{M} = \left\{ \boldsymbol{v} \in \left[\mathcal{H}^1(\Gamma_{\boldsymbol{X}})\right]^3 : \ \boldsymbol{v} = \hat{\boldsymbol{G}} \text{ on } \partial\Gamma_{\boldsymbol{X},\mathrm{D}} \right\} , \tag{6.39}$$

$$\mathcal{V}_{\boldsymbol{u}}^\mathrm{M} = \left\{ \boldsymbol{v} \in \left[\mathcal{H}^1(\Gamma_{\boldsymbol{X}})\right]^3 : \ \boldsymbol{v} = \boldsymbol{0} \text{ on } \partial\Gamma_{\boldsymbol{X},\mathrm{D}} \right\} , \tag{6.40}$$

where $\mathcal{H}^1(\Gamma_{\boldsymbol{X}})$ is the Sobolev space of functions with square integrable first derivatives in the undeformed domain $\Gamma_{\boldsymbol{X}}$. The task is to find $\boldsymbol{u} \in \mathcal{S}_{\boldsymbol{u}}^{\mathrm{M}}$ such that for all $\boldsymbol{v} \in \mathcal{V}_{\boldsymbol{u}}^{\mathrm{M}}$, there holds

$$t \int_{\Gamma_{\boldsymbol{X}}} \nabla_{\boldsymbol{X}}^{\Gamma,\mathrm{dir}} \boldsymbol{v} : \mathbf{K}\left(\boldsymbol{u}\right) \,\mathrm{d}A = t \int_{\Gamma_{\boldsymbol{X}}} \boldsymbol{v} \cdot \boldsymbol{F} \,\mathrm{d}A + \int_{\partial\Gamma_{\boldsymbol{X},\mathrm{N}}} \boldsymbol{v} \cdot \hat{\boldsymbol{H}} \,\mathrm{d}s \,. \tag{6.41}$$

In order to obtain Eq. 6.41, we applied the usual procedure for converting the strong form to a weak form: Multiply Eq. 6.34 with test functions, integrate over the domain $\Gamma_{\boldsymbol{X}}$, and apply the divergence theorem from Eq. 2.29. It is noteworthy that the curvature term from Eq. 2.29 vanishes due to $\mathbf{K} \cdot \boldsymbol{N} = \mathbf{0}$. Note that the weak form stated above is related to energy minimization in the sense that

$$\int_{\Gamma_{\boldsymbol{X}}} \nabla_{\boldsymbol{X}}^{\Gamma,\mathrm{dir}} \boldsymbol{v} : \mathbf{K}(\boldsymbol{u}) \,\mathrm{d}A = \int_{\Gamma_{\boldsymbol{X}}} \delta\mathbf{E}_{\mathrm{tang}}(\boldsymbol{u}) : \mathbf{S}(\boldsymbol{u}) \,\mathrm{d}A \;,$$

where δ is the variational operator.

6.2 Discretization

In the following, the obtained continuous weak form from Eq. 6.41 is discretized with the Surface and the Trace FEM. For the Surface FEM, C^0-continuous shape functions as defined in Section 3.1 are employed. In particular, two-dimensional higher-order Lagrange elements are used and the essential boundary conditions are enforced in a strong sense by prescribing the nodal values. Instead, for the Trace FEM as defined in Section 3.2, three-dimensional Lagrange elements are used in the background mesh. The boundary conditions are weakly enforced with the penalty method and the non-symmetric version of Nitsche's method. In Fig. 6.2, the situations of a deformed membrane discretized with Surface and Trace FEM are illustrated.

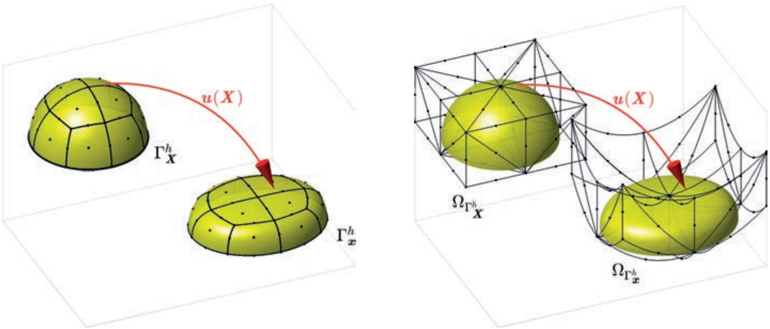

(a) Surface FEM **(b)** Trace FEM

Fig. 6.2: The situations of discretized domains and their corresponding displacement fields $\boldsymbol{u}(\boldsymbol{X})$ are shown for the undeformed and deformed configuration for: (a) Surface FEM, and (b) Trace FEM, respectively.

6.2.1 Surface FEM

As mentioned above, similar to the model problem in Section 3.3, a higher-order Surface FEM approach with C^0-continuous Lagrange elements is employed, see Fig. 6.2(a). The discrete displacements of the membrane are defined as $\boldsymbol{u}^h = u^{h,i}\boldsymbol{E}_i$, with $\boldsymbol{E}_i$ being Cartesian base vectors, $i = 1, 2, 3$ and $u^{h,i} = \boldsymbol{M}^{\mathrm{T}} \cdot \hat{\boldsymbol{u}}^i$. Based on Eq. 3.1, the following discrete test and trial function spaces are introduced

$$\mathcal{S}_{\boldsymbol{u}}^{\mathrm{M},h} = \left\{ \boldsymbol{v}^h \in \left[\mathcal{Q}^k_{\Gamma_{\boldsymbol{X}}}\right]^3 : \ \boldsymbol{v}^h|_{\partial\Gamma^h_{\boldsymbol{X},\mathrm{D}}} = \hat{\boldsymbol{G}} \right\}, \tag{6.42}$$

$$\mathcal{V}_{\boldsymbol{u}}^{\mathrm{M},h} = \left\{ \boldsymbol{v}^h \in \left[\mathcal{Q}^k_{\Gamma_{\boldsymbol{X}}}\right]^3 : \ \boldsymbol{v}^h|_{\partial\Gamma^h_{\boldsymbol{X},\mathrm{D}}} = \boldsymbol{0} \right\}. \tag{6.43}$$

The discrete weak form of Eq. 6.41 reads as follows: Given Lamé constants $(\lambda, \mu) \in \mathbb{R}^+$, body forces $\boldsymbol{F} \in \mathbb{R}^3$ on $\Gamma^h_{\boldsymbol{X}}$, tractions $\hat{\boldsymbol{H}} \in \mathbb{R}^3$ on $\partial\Gamma^h_{\boldsymbol{X},\mathrm{N}}$, find the displacement field $\boldsymbol{u}^h \in \mathcal{S}_{\boldsymbol{u}}^{\mathrm{M},h}$ such that for all test functions $\boldsymbol{v}^h \in \mathcal{V}_{\boldsymbol{u}}^{\mathrm{M},h}$ there holds in $\Gamma^h_{\boldsymbol{X}}$

$$t \int_{\Gamma^h_{\boldsymbol{X}}} \nabla^{\Gamma,\mathrm{dir}}_{\boldsymbol{X}} \boldsymbol{v}^h : \mathbf{K}\left(\boldsymbol{u}^h\right) \mathrm{d}A = t \int_{\Gamma^h_{\boldsymbol{X}}} \boldsymbol{v}^h \cdot \boldsymbol{F} \, \mathrm{d}A + \int_{\partial\Gamma^h_{\boldsymbol{X},\mathrm{N}}} \boldsymbol{v}^h \cdot \hat{\boldsymbol{H}} \, \mathrm{d}s \ . \tag{6.44}$$

The sought discrete displacement field $\boldsymbol{u}^h(\boldsymbol{X})$ is obtained solving a non-linear system of equations for the $n_{\mathrm{DOF}} = 3n$ nodal values (degrees of freedom) as usual in the context of finite strain theory.

In the following, an iterative scheme for the numerical solution of the obtained non-linear system of equations is sketched. With a set of n_{DOF} independent test functions $\tilde{\boldsymbol{v}}^h \in \{\boldsymbol{v}^{h,i}\}$, where $i = 1, \dots, n_{\mathrm{DOF}}$, Eq. 6.44 leads to a system of non-linear equations, which shall be solved with a Newton-Raphson iteration scheme. Therefore, the residuum from Eq. 6.44 is

$$\begin{aligned} \mathfrak{f}_{\mathrm{res}}(\underline{\hat{\boldsymbol{u}}}) := t \int_{\Gamma^h_{\boldsymbol{X}}} \nabla^{\Gamma,\mathrm{dir}}_{\boldsymbol{X}} \tilde{\boldsymbol{v}}^h : \mathbf{K}\left(\boldsymbol{u}^h(\underline{\hat{\boldsymbol{u}}})\right) \mathrm{d}A - t \int_{\Gamma^h_{\boldsymbol{X}}} \tilde{\boldsymbol{v}}^h \cdot \boldsymbol{F} \, \mathrm{d}A \\ - \int_{\partial\Gamma^h_{\boldsymbol{X},\mathrm{N}}} \tilde{\boldsymbol{v}}^h \cdot \hat{\boldsymbol{H}} \, \mathrm{d}s \overset{!}{=} \boldsymbol{0} \in \mathbb{R}^{n_{\mathrm{DOF}}} \ . \end{aligned} \tag{6.45}$$

With a suitable start-vector $\underline{\hat{\boldsymbol{u}}}_0$ and stop criterion the system of non-linear equations can be iteratively solved as

$$\mathbf{A}_b \cdot \Delta\underline{\hat{\boldsymbol{u}}}_{b+1} = -\mathfrak{f}_{\mathrm{res}}(\underline{\hat{\boldsymbol{u}}}_b) \ , \tag{6.46}$$

$$\underline{\hat{\boldsymbol{u}}}_{b+1} = \Delta\underline{\hat{\boldsymbol{u}}}_{b+1} + \underline{\hat{\boldsymbol{u}}}_b \ , \tag{6.47}$$

where $\mathbf{A}_b$ is the tangent stiffness matrix (Jacobi-matrix) at the iteration step b. The tangent stiffness matrix is determined by

$$[\mathbf{A}_b]_{ij} = \frac{[\partial \mathfrak{f}_{\mathrm{res}}(\underline{\hat{\boldsymbol{u}}}_b)]_i}{\partial \underline{\hat{u}}_j} \qquad \text{with } (i, j) \in \{1, \dots, n_{\mathrm{DOF}}\}^2 \ , \tag{6.48}$$

where the index i refers to the corresponding test function and j to the nodal value $\hat{u}_j$.

6.2.2 Trace FEM

In this section, the continuous weak form of the equilibrium, see Eq. 6.41, is discretized with the Trace FEM. The discrete function spaces for the trial and test functions of the membrane displacement field are

$$\bar{\mathcal{S}}_{\boldsymbol{u}}^{\mathrm{M},h} = \left\{ \boldsymbol{v}^h \in \left[\mathcal{T}_{\Gamma^h_{\boldsymbol{X}}}\right]^3 \right\} \ , \tag{6.49}$$

$$\bar{\mathcal{V}}_{\boldsymbol{u}}^{\mathrm{M},h} = \left\{ \boldsymbol{v}^h \in \left[\mathcal{T}_{\Gamma^h_{\boldsymbol{X}}}\right]^3 \right\} \ , \tag{6.50}$$

with $\mathcal{T}_{\Gamma^h_{\boldsymbol{X}}}$ from Eq. 3.7 where $\Gamma^h_{\boldsymbol{X}}$ refers to the undeformed domain. Note that the corresponding function spaces in the Trace FEM for the trial and test functions are denoted by a bar in comparison to their counterpart in the Surface FEM, see Eqs. (6.42) and (6.43). An example of a discrete displacement field in the Trace FEM is visualized in Fig. 6.2(b).

Enforcing the essential boundary conditions with the non-symmetric version of Nitsche's method, the discrete weak form of Eq. 6.41 with the Trace FEM reads as follows: Given Lamé constants $(\lambda, \mu) \in \mathbb{R}^+$, body forces $\boldsymbol{F} \in \mathbb{R}^3$ on $\Gamma^h_{\boldsymbol{X}}$, tractions $\hat{\boldsymbol{H}} \in \mathbb{R}^3$ on $\partial\Gamma^h_{\boldsymbol{X},\mathrm{N}}$, and stabilization parameter $\rho \in \mathbb{R}^+$ and boundary conditions $\hat{\boldsymbol{G}}$ on $\partial\Gamma^h_{\boldsymbol{X},\mathrm{D}}$, find the displacement field $\boldsymbol{u}^h \in \bar{\mathcal{S}}_{\boldsymbol{u}}^{\mathrm{M},h}$ such that for all test functions $\boldsymbol{v}^h \in \bar{\mathcal{V}}_{\boldsymbol{u}}^{\mathrm{M},h}$ there holds in $\Gamma^h_{\boldsymbol{X}}$

$$\begin{aligned} & t \int_{\Gamma^h_{\boldsymbol{X}}} \nabla^{\Gamma,\mathrm{dir}}_{\boldsymbol{X}} \boldsymbol{v}^h : \mathbf{K}\left(\boldsymbol{u}^h\right) \mathrm{d}A - \underbrace{\int_{\partial\Gamma^h_{\boldsymbol{X},\mathrm{D}}} \boldsymbol{v}^h \cdot \left[\mathbf{K}(\boldsymbol{u}^h) \cdot \boldsymbol{N}_{\partial\Gamma_{\boldsymbol{X}}}\right] \mathrm{d}s}_{\text{boundary term due to } \boldsymbol{v}^h \neq \boldsymbol{0} \text{ on } \partial\Gamma^h_{\boldsymbol{X},\mathrm{D}}} + \\ & \underbrace{\int_{\partial\Gamma^h_{\boldsymbol{X},\mathrm{D}}} \left(\boldsymbol{u}^h - \hat{\boldsymbol{G}}\right) \cdot \left[\mathbf{K}(\boldsymbol{v}^h) \cdot \boldsymbol{N}_{\partial\Gamma_{\boldsymbol{X}}}\right] \mathrm{d}s}_{\text{Nitsche term}} + \underbrace{\rho \int_{\Omega_{\Gamma^h_{\boldsymbol{X}}}} \left(\boldsymbol{N}^{\mathrm{e}} \cdot \nabla_{\boldsymbol{X}} \boldsymbol{u}^h\right) \cdot \left(\boldsymbol{N}^{\mathrm{e}} \cdot \nabla_{\boldsymbol{X}} \boldsymbol{v}^h\right) \mathrm{d}V}_{\text{stabilization term}} \\ & = t \int_{\Gamma^h_{\boldsymbol{X}}} \boldsymbol{v}^h \cdot \boldsymbol{F} \, \mathrm{d}\Gamma + \int_{\partial\Gamma^h_{\boldsymbol{X},\mathrm{N}}} \boldsymbol{v}^h \cdot \hat{\boldsymbol{H}} \, \mathrm{d}s \ , \end{aligned} \tag{6.51}$$

where $\Omega_{\Gamma^h_{\boldsymbol{X}}}$ is the undeformed, active background mesh. In comparison to Eq. 6.44, additional terms occur in the discrete weak form due to the weak enforcement of essential boundary conditions with Nitsche's method and the stabilization. The sought discrete displacement field $\boldsymbol{u}^h(\boldsymbol{X})$ is obtained just as above by solving a non-linear system of equations.

Note that the stabilization term is the only term which is not evaluated on the manifold $\Gamma^h_{\boldsymbol{X}}$ but in the volumetric, active background mesh $\Omega_{\Gamma^h_{\boldsymbol{X}}}$ (using standard Gauss integration). Therefore, one has to extend the normal vector $\boldsymbol{N}(\boldsymbol{X})$ from the undeformed manifold $\Gamma^h_{\boldsymbol{X}}$ to the neighborhood, resulting in $\boldsymbol{N}^{\mathrm{e}}(\boldsymbol{X})$ for all $\Omega_{\Gamma^h_{\boldsymbol{X}}}$. This is particularly simple for implicitly defined manifolds using $\boldsymbol{N}^{\mathrm{e}}(\boldsymbol{X}) = \frac{\nabla_{\boldsymbol{X}} \phi^h(\boldsymbol{X})}{\|\nabla_{\boldsymbol{X}} \phi^h(\boldsymbol{X})\|}$ for all $\boldsymbol{X} \in \Omega_{\Gamma^h_{\boldsymbol{X}}}$. Furthermore, in the stabilization term, the *classical* gradient operator $\nabla_{\boldsymbol{X}}$ is used instead of the *surface* operators used in the other terms. In [73], it is recommended that the stabilization parameter should be chosen in the range $O(h) \lesssim \rho \lesssim O(h^{-1})$, where h is the element size of the active background mesh.

A remark is added concerning *slip supports* because the above mentioned weak form rather expects that all displacement components are prescribed through $\hat{\boldsymbol{G}}$ along the Dirichlet boundary $\partial\Gamma^h_{\boldsymbol{X},\mathrm{D}}$. In the Nitsche's method, displacement constraints in selected, arbitrary unit directions $\boldsymbol{v}_d$ with magnitude $\hat{G}$ may be prescribed by replacing the corresponding terms in Eq. (6.51) with

$$\begin{aligned} &- \int_{\partial\Gamma^h_{\boldsymbol{X},\mathrm{D}}} \left(\boldsymbol{v}^h \cdot \boldsymbol{v}_d\right) \left[\mathbf{K}(\boldsymbol{u}^h) \cdot \boldsymbol{N}_{\partial\Gamma_{\boldsymbol{X}}}\right] \cdot \boldsymbol{v}_d \,\mathrm{d}s \\ &+ \int_{\partial\Gamma^h_{\boldsymbol{X},\mathrm{D}}} \left(\boldsymbol{u}^h \cdot \boldsymbol{v}_d - \hat{G}\right) \left[\mathbf{K}(\boldsymbol{v}^h) \cdot \boldsymbol{N}_{\partial\Gamma_{\boldsymbol{X}}}\right] \cdot \boldsymbol{v}_d \,\mathrm{d}s \;. \end{aligned} \tag{6.52}$$

Depending on the test case, robustness of the numerical scheme for the approximate solution of the sought displacement field $\boldsymbol{u}^h(\boldsymbol{X})$ becomes more important, especially if the quality of the initial guess $\hat{\underline{\boldsymbol{u}}}_0$ is not good. In this situation, it may be beneficial to enforce the essential boundary conditions with the penalty method, although the overall approach is inconsistent in this case. The discrete weak form of Eq. 6.41 with the penalty method reads as follows: Given Lamé constants $(\lambda, \mu) \in \mathbb{R}^+$, body forces $\boldsymbol{F} \in \mathbb{R}^3$ on $\Gamma^h_{\boldsymbol{X}}$, tractions $\hat{\boldsymbol{H}} \in \mathbb{R}^3$ on $\partial\Gamma^h_{\boldsymbol{X},\mathrm{N}}$, and stabilization parameter $\rho \in \mathbb{R}^+$, penalty parameter $\alpha \in \mathbb{R}^+$ and boundary conditions $\hat{\boldsymbol{G}}$ on $\partial\Gamma^h_{\boldsymbol{X},\mathrm{D}}$, find the displacement field $\boldsymbol{u}^h \in \bar{\mathcal{S}}^{\mathrm{M},h}_{\boldsymbol{u}}$ such that for all test functions $\boldsymbol{v}^h \in \bar{\mathcal{V}}^{\mathrm{M},h}_{\boldsymbol{u}}$ there holds in $\Gamma^h_{\boldsymbol{X}}$

$$\begin{aligned} t \int_{\Gamma^h_{\boldsymbol{X}}} \nabla^{\Gamma,\mathrm{dir}}_{\boldsymbol{X}} \boldsymbol{v}^h : \mathbf{K}\left(\boldsymbol{u}^h\right) \mathrm{d}A + &\underbrace{\alpha \int_{\partial\Gamma^h_{\boldsymbol{X},\mathrm{D}}} \boldsymbol{v}^h \cdot \left(\boldsymbol{u}^h - \hat{\boldsymbol{G}}\right) \mathrm{d}s}_{\text{penalty term}} \\ &\underbrace{+ \rho \int_{\Omega_{\Gamma^h_{\boldsymbol{X}}}} (\boldsymbol{N}^{\mathrm{e}} \cdot \nabla_{\boldsymbol{X}} \boldsymbol{u}^h) \cdot (\boldsymbol{N}^{\mathrm{e}} \cdot \nabla_{\boldsymbol{X}} \boldsymbol{v}^h) \,\mathrm{d}V}_{\text{stabilization term}} \\ &= t \int_{\Gamma^h_{\boldsymbol{X}}} \boldsymbol{v}^h \cdot \boldsymbol{F} \,\mathrm{d}\Gamma + \int_{\partial\Gamma^h_{\boldsymbol{X},\mathrm{N}}} \boldsymbol{v}^h \cdot \hat{\boldsymbol{H}} \,\mathrm{d}s \;. \end{aligned} \tag{6.53}$$

6.3 Numerical results

A number of test cases for membranes in three dimensions are considered in this section. The numerical results focus on the convergence rates for two different types of errors. The "energy error" $\varepsilon_{\mathfrak{e}}$ compares the approximated stored elastic energy with the analytical one,

$$\varepsilon_{\mathfrak{e}} = \left|\mathfrak{e}\left(\boldsymbol{u}\right) - \mathfrak{e}\left(\boldsymbol{u}_h\right)\right| \;, \tag{6.54}$$

with $\mathfrak{e}$ computed based on Eq. 6.30. The analytical energy $\mathfrak{e}(\boldsymbol{u})$ may also be computed by an overkill approximation, i.e., based on an extremely fine mesh with higher-order elements. Provided that geometry and boundary conditions allow for sufficiently smooth solutions, the expected convergence rates in this error norm are $p + 1$ with p being the order of the elements.

The "residual error" ε_{res} integrates the error in the equilibrium as stated in Eq. 6.32, that is,

$$\varepsilon_{\text{res}} = \sqrt{\sum_{\text{e}=1}^{n_{\text{el}}} \int_{\Gamma_{\boldsymbol{X}}^{h,\text{e}}} \mathfrak{r}\left(\boldsymbol{u}^h\right) \cdot \mathfrak{r}\left(\boldsymbol{u}^h\right) \, \mathrm{d}A} \, , \quad \text{with } \mathfrak{r}\left(\boldsymbol{u}^h\right) = \operatorname{div}_\Gamma \boldsymbol{\sigma}\left(\boldsymbol{u}^h\right) + \boldsymbol{f}(\boldsymbol{x}) \; . \tag{6.55}$$

This error obviously vanishes for the analytical solution. It is important to note that the integrand in (6.55) involves second-order derivatives. Therefore, the integral must not be carried out over the whole (discretized) domain $\Gamma_{\boldsymbol{X}}^h$ but integrated element by element as indicated by the summation. That is, element boundaries, where already the first derivatives of the C^0-continuous shape functions feature jumps, are neglected in computing ε_{res}. Due to the presence of second-order derivatives, the expected convergence rates are $p-1$ which also indicates that higher-order elements are crucial for convergence in ε_{res}.

6.3.1 Membrane with given deformation

In the first test case, a membrane in the shape of a half sphere with radius $r = 1.0$ undergoes a prescribed displacement and the stored elastic energy is computed from the viewpoint of the Surface FEM and the Trace FEM. That is, in the Surface FEM, *surface* meshes with different resolutions and element orders are generated. See Fig. 6.2(a) for some example mesh composed by quadratic elements. The displacements

$$\boldsymbol{u}(\boldsymbol{X}) = \begin{bmatrix} \frac{5}{2} + \frac{1}{5}\,(X+1) \\ -\frac{3}{2} \\ -\frac{1}{2}\left[1 - (X^2 + Y^2)\right] - \frac{3}{2} \end{bmatrix} \tag{6.56}$$

are evaluated at the nodes and interpolated based on the shape functions implied by the *surface* meshes, yielding $\boldsymbol{u}^h(\boldsymbol{X})$; see Fig. 6.2(a) for the resulting deformed membrane. Then, the elastic energy of the deformed configuration $\mathfrak{e}(\boldsymbol{u}^h)$ is computed with Eq. 6.30.

For the Trace FEM viewpoint, *background* meshes of different resolutions and orders are generated in $\Omega_{\boldsymbol{X}} = [-1,1] \times [-1,1] \times [0,1]$ and the geometry is defined based on the level-set function $\phi\left(\boldsymbol{X}\right) = \|\boldsymbol{X}\| - r$. See Fig. 6.2(b) for a sketch of the situation using quadratic background elements. Then, the (active) nodes of the background mesh are deformed by the given displacement field Eq. 6.56, yielding $\boldsymbol{u}^h(\boldsymbol{X})$ based on the shape functions implied by the *background* meshes. This displacement field living in the whole background mesh is only evaluated on the membrane surface in order to compute the stored energy $\mathfrak{e}(\boldsymbol{u}^h)$ according to the Trace FEM.

We set the Lamé constants to $\lambda = 3$ and $\mu = 2$. The resulting energy is given by the value $\mathfrak{e}(\boldsymbol{u}) = 1.642871443585262$. In Fig. 6.3, the convergence results for the various meshes are shown for the Surface and the Trace FEM. It is seen that in both cases *optimal* convergence results are achieved. The energy error converges one order higher than expected for even element orders. In the Trace FEM, the convergence curves are less smooth than in the Surface FEM because the approximation spaces are not nested upon refinement; this is well-known for results obtained with FDMs in general.

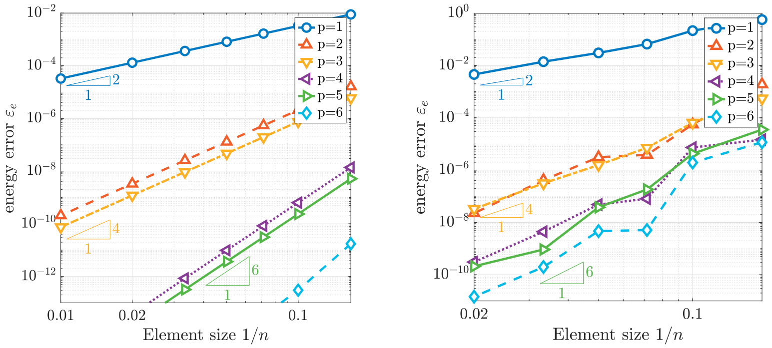

(a) Surface FEM, $\varepsilon_{\mathfrak{e}}$ **(b)** Trace FEM, $\varepsilon_{\mathfrak{e}}$

Fig. 6.3: Convergence results for test case 1: The energy error $\varepsilon_{\mathfrak{e}}$ for the (a) Surface FEM, and (b) Trace FEM.

It is thus seen that the Surface FEM as well as the Trace FEM have the potential to achieve optimal results. For all other test cases below, we shall now obtain the discrete displacement fields based on solving the non-linear systems of equations resulting from the weak forms given in Section 6.2.

6.3.2 Membrane with smooth boundaries

For the next test case, a membrane loaded by gravity with a smooth boundary is considered. Similar to the example before, numerical solutions are obtained with both Surface and Trace FEM. The undeformed membrane $\Gamma_{\boldsymbol{X}}$ is given by the parametrization

$$\boldsymbol{X}(\boldsymbol{r}) = \begin{bmatrix} \frac{3}{2}\,r \\ s \\ c\,\sin\left(r\,s\right) \end{bmatrix} , \quad \text{with} \quad \sqrt{r^2+s^2} \in [0,1] \ , \tag{6.57}$$

or implicitly by means of multiple level-set functions with

$$\phi(\boldsymbol{X}) = c\,\sin\left(\frac{2}{3}X\,Y\right) - Z \ , \quad \text{with} \quad \psi_1(\boldsymbol{X}) = \sqrt{\left(\frac{2X}{3}\right)^2 + Y^2} - 1 \ , \tag{6.58}$$

where $c \in \mathbb{R}$ is a scaling parameter in vertical direction. The resulting configurations for the explicit and implicit definition are visualized in Fig. 6.4(a) and Fig. 6.5(a) for $c = 0.4$, respectively. The thickness of the membrane is $t = 0.01$, Young's modulus is $E = 1\,000$ and Poisson's ratio $\nu = 0.3$, which is easily converted into the Lamé parameters. The loading is gravity acting on the membrane surface with $\boldsymbol{F}(\boldsymbol{X}) = [0, 0, -200\,t]^{\mathrm{T}}$ for all $\boldsymbol{X} \in \Gamma_{\boldsymbol{X}}$. The whole boundary is treated as a Dirichlet boundary with prescribed zero-displacements. The deformed configuration, obtained with Surface FEM, is displayed in Fig. 6.4(b) with computed von-Mises stresses based on the Cauchy stress tensor. The

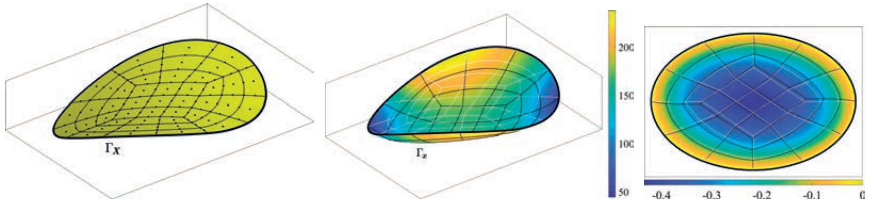

(a) undeformed conf. **(b)** deformed conf. **(c)** displacement u_z

Fig. 6.4: Sketch of test case 2 with the Surface FEM: (a) Shows the undeformed configuration $\Gamma^h_{\boldsymbol{X}}$ with example mesh composed by quadratic elements, (b) the deformed configuration $\Gamma^h_{\boldsymbol{x}}$ with von-Mises stresses, and (c) top view of the vertical displacement field u_z. White lines show element edges in $\Gamma^h_{\boldsymbol{X}}$, black lines in $\Gamma^h_{\boldsymbol{x}}$.

vertical displacement field is given in Fig. 6.4(c) in top view.

Employing the Trace FEM, equivalent results may be obtained. The situation in the frame of the Trace FEM is sketched in Fig. 6.5. In detail, Fig. 6.5(a) shows the active background mesh composed by the cut elements, Fig. 6.5(b) the automatically generated integration points as outlined in Section 3.2.2, and Fig. 6.5(c) the deformed zero-isosurface where colors on the surface refer to the Euclidean norm of the displacement field $\boldsymbol{u}$.

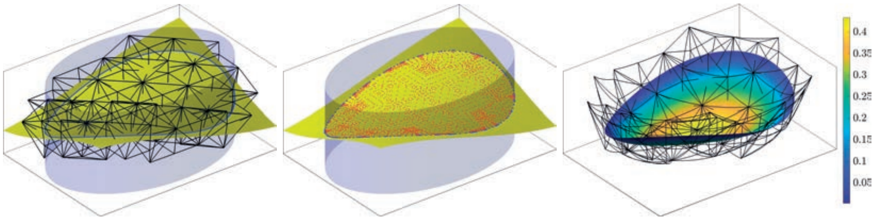

(a) active background mesh **(b)** integration points **(c)** displacement $\boldsymbol{u}$

Fig. 6.5: Sketch of test case 2 with the Trace FEM: (a) Active background mesh and zero-isosurfaces of ϕ and ψ_1, (b) automatically generated integration points in the domain (red) and on the boundary (blue), and (c) deformed zero isosurface.

Convergence results for the Surface FEM are given in Fig. 6.6. For this particular example, where the boundary is smooth, optimal convergence rates are found in the energy error $\varepsilon_{\mathfrak{e}}$ and residual error $\varepsilon_{\mathrm{res}}$.

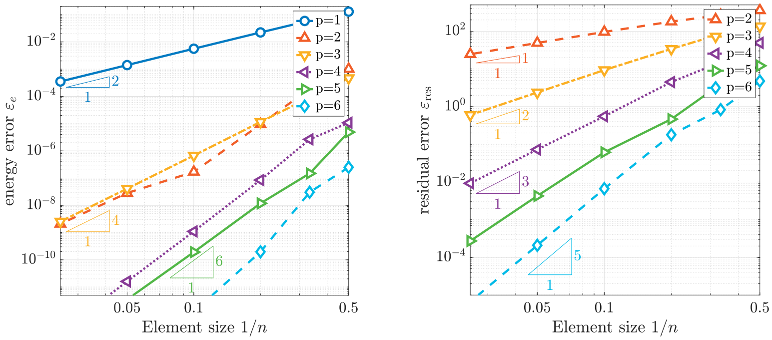

(a) energy error $\varepsilon_{\mathfrak{e}}$ **(b)** residual error ε_{res}

Fig. 6.6: Convergence results of the Surface FEM for test case 2 with $c = 0.4$: (a) Shows the results for the energy error $\varepsilon_{\mathfrak{e}}$, and (b) gives the residual error ε_{res}.

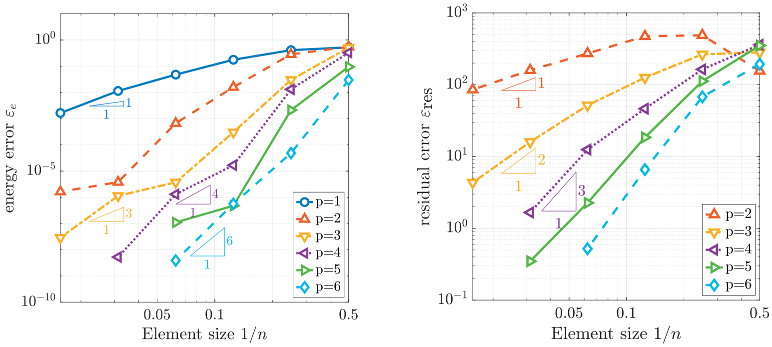

(a) energy error $\varepsilon_{\mathfrak{e}}$ **(b)** residual error ε_{res}

Fig. 6.7: Convergence results of the Trace FEM for test case 2 with $c = 0.4$: (a) Shows the results for the energy error $\varepsilon_{\mathfrak{e}}$, and (b) for the residual error ε_{res}.

The approximations with the Trace FEM are obtained with a stabilization parameter $\rho = \frac{Etp^4}{h}$. That is, as suggested in [72], also the order of the elements is considered in the scaling of the stabilization parameter. It was found that the scaling with Young's modulus E and the thickness t of the membrane is also useful. Furthermore, we found that using the penalty method instead of Nitsche's method for considering boundary conditions has a benefitial influence on the convergence behaviour of the Newton-Raphson scheme for solving the non-linear problem. The stopping criterion in the Newton-Raphson scheme is based on the relative change in the stored elastic energy rather than the relative changes in the primal variables. This is useful because for elements that are only cut slightly, the primal variables may change considerably (compared to the tolerance of 10^{-12} in the stopping criterion), yet with a negligible influence on the displacements and energy of the shell.

The results of the Trace FEM are presented in Fig. 6.7 with a penalty parameter $\alpha = 10^{10}$. In agreement to the results with the Surface FEM, see Fig. 6.6, it is confirmed that the expected optimal convergence rates are achieved. The convergence curves are not as straight as for the Surface FEM but feature small deviations as usual for FDMs.

6.3.3 Membrane with corners

Lastly, a membrane with corners is taken as an example. The shape of the mid-surface of the membrane, material parameters and boundary conditions are similar to the previous example. However, the parameter space and slave level-set functions are modified in order to change the shape of the boundary. In detail, the geometry is represented as

$$\boldsymbol{X}(\boldsymbol{r}) = \begin{bmatrix} \frac{3}{2}r \\ s \\ c\,\sin\left(r\,s\right) \end{bmatrix} , \qquad \text{with} \quad r,\, s \in [-1,1] \ , \tag{6.59}$$

$$\phi(\boldsymbol{X}) = c\,\sin\left(\frac{2}{3}X\,Y\right) - Z \ , \quad \text{with} \quad \psi_1 = X^2 - \frac{9}{4},\ \psi_2 = Y^2 - 1 \ . \tag{6.60}$$

The resulting membrane is illustrated for the explicit situation in Fig. 6.8(a). Similar to above, the deformed configuration, obtained with Surface FEM, is displayed in Fig. 6.8(b) with computed von-Mises stresses and the vertical displacement field is given in Fig. 6.8(c).

Convergence results for the Surface FEM are given in Fig. 6.9. In contrast to the example above, corners are present in the membrane geometry, it is seen that the convergence rates are bounded. Only linear and quadratic elements converge optimally in $\varepsilon_{\mathfrak{e}}$, higher orders improve the error level, however, not the convergence rates. It is thus confirmed that corners in membranes have the potential to reduce the convergence rates. We repeated the same study with the Trace FEM with the same findings than for the Surface FEM, that is, the corners hinder optimal convergence and are omitted for brevity.

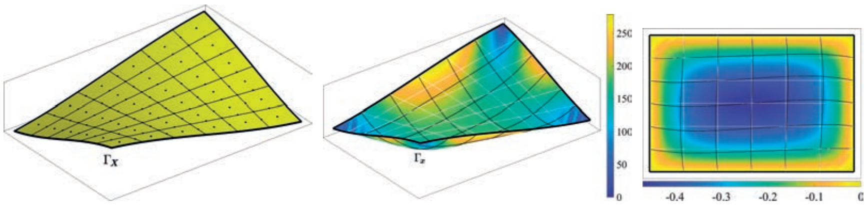

(a) undeformed conf. **(b)** deformed conf. **(c)** displacement u_z

Fig. 6.8: Sketch of test case 3 with the Surface FEM: (a) Shows the undeformed configuration $\Gamma^h_{\boldsymbol{X}}$ with example mesh composed by quadratic elements, (b) the deformed configuration $\Gamma^h_{\boldsymbol{x}}$ with von-Mises stresses, and (c) top view of the vertical displacement field u_z. White lines show element edges in $\Gamma^h_{\boldsymbol{X}}$, black lines in $\Gamma^h_{\boldsymbol{x}}$.

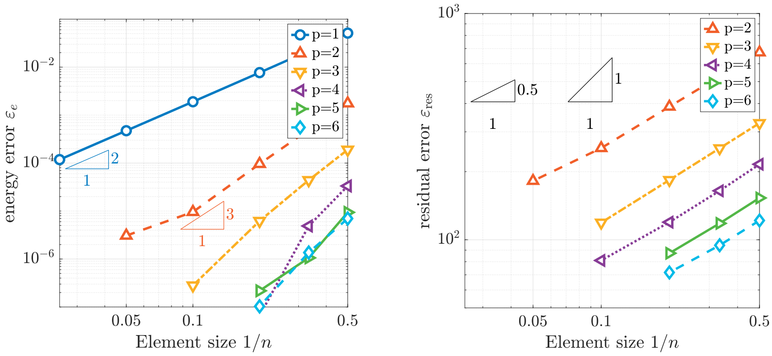

(a) energy error $\varepsilon_{\mathfrak{e}}$ **(b)** residual error ε_{res}

Fig. 6.9: Convergence results of the Surface FEM for test case 3 with $c = 0.1$: (a) Shows the results for the energy error $\varepsilon_{\mathfrak{e}}$, and (b) gives the residual error ε_{res}.

7 Conclusion and Outlook

7.1 Summary

In this thesis, higher-order accurate finite element schemes are presented for explicitly and implicitly defined thin-walled structures embedded in the three-dimensional space. In particular, a higher-order Surface FEM using Lagrange elements or isogeometric analysis and a higher-order accurate fictitious domain method, i.e., the Trace FEM, are elaborated in detail.

Both finite element approaches are introduced based on the employed function spaces. Most importantly, the Surface FEM uses two-dimensional shape functions whereas the Trace FEM employs background meshes implying three-dimensional shape functions. Major implementational aspects such as (i) higher-order accurate integration, (ii) stabilization and (iii) treatment of essential boundary conditions are discussed. For the integration on parametrized surfaces, standard Gauß-Legendre integration rules are employed as usual in the Surface FEM. For implicitly defined manifolds, based on (multiple) level-set functions, a higher-order accurate and robust procedure is used to identify the zero-isosurfaces and generate integration points. In the Trace FEM, the so-called "normal derivative volume stabilization" is employed to address stability issues common in FDMs. This stabilization technique easily enables higher-order accuracy, is straightforward in the implementation, the choice of the stabilization parameter is rather flexible, and the extension to vector-valued problems is trivial. Regarding the treatment of essential boundary conditions, different methods such as strong enforcement, Lagrange multipliers, penalty method, symmetric and non-symmetric versions of Nitsche's method are elaborated. The two fundamentally different finite element schemes, Surface and Trace FEM, are first applied to a simple model problem, the Poisson equation on compact and open manifolds, for comparisons w.r.t. accuracy, robustness and efficiency.

The next major part of the thesis is the recast of the classical shell models, such as Kirchhoff-Love shells and Reissner-Mindlin shells, and large deformation membranes in the frame of the tangential differential calculus (TDC). This framework, which is well-established in the context of transport and flow problems, enables the definition of differential surface operators in the global Cartesian coordinate system so that curvilinear coordinates are not necessarily required. As a consequence, the resulting surface PDEs are valid independently of the concrete geometry definition, enabling the analysis of explicitly *and* implicitly defined shells and membranes in a unified sense, whereas the classical approach is limited to parametrized surfaces. In this sense, the reformulated PDEs are more general than the classical theories and naturally yield in a symbolic notation, whereas the classical approach is typically formulated in index notation. Moreover, the formulation of the PDEs in the frame of the TDC enables a sharper split between finite element technology and the concrete application, which may be beneficial for multi-purpose finite element implementations.

The recast of the shell and membrane equations includes all relevant mechanical aspects. In particular, the equilibrium in strong form and all mechanical meaningful boundary conditions are derived. In addition, the stress resultants, such as normal forces, bending moments and transverse shear forces are formulated in the global Cartesian coordinate system and it is shown how (parametrization-)invariant quantities, e.g., principal moments are computed. The obtained boundary value problems are discretized with both higher-order Surface FEM and higher-order Trace FEM. The continuous and discrete weak forms are given. The essential boundary conditions are enforced with Lagrange multipliers in case of the Surface FEM and for the Trace FEM, the non-symmetric version of Nitsche's method or the penalty method are employed. The resulting implementations are tested on a set of classical and new benchmarks. In addition to the well-established code verification procedures in the context of shells and membranes, i.e., reference displacements at selected points or manufactured solutions, the concept of residual errors is employed. The residual errors are a suitable criteria for higher-order finite element schemes, where the error in the strong form of the equilibrium is measured. Provided that the involved mechanical fields are sufficiently smooth, optimal orders of convergence are achieved for shells and membranes independently of the numerical methodology.

In conclusion, the current thesis generalizes the classical shell and membrane theories and establishes a new numerical approach, the Trace FEM, in these applications. In particular, the analysis of implicitly defined geometries is enabled, yet the classical situation of parametrized surfaces is also covered. The generalized shell and membrane equations are discretized with higher-order Surface and Trace FEM and the numerical results confirm optimal higher-order converge rates for both methods.

7.2 Outlook

In future work, the presented reformulation of the shell equations within the linear theory may be extended to the *non*-linear situation of shells undergoing large deformations as already shown for structural membranes herein. We believe that the presented formulation has the potential to become the standard notation for shells and membranes and successively replaces the classical notation. This is justified because the new notation applies to explicit *and* implicit surfaces, and enables Surface *and* Trace FEM and is, therefore, more general.

The generalization of the shell and membrane equations offers a wide range of future applications. In the context of embedded domain methods or coupling, the reformulated shell and membrane equations may be implicitly embedded in the surrounding continuum, e.g., considering for a reinforcement or composite structures. The major advantage is that a parametrization of the embedded surfaces is not needed. The shape functions of the continuum are restricted to the manifold and the contribution to the stiffness matrix can be directly added to the global system. Then, of course, the displacement fields are not smooth near the embedded structures which could be covered in an XFEM-related approach. As an alternative, the implicitly defined structure in the continuum may be added in a diffusive (smeared) manner in order to avoid a sharp discontinuity. Another interesting application field is fluid-structure interaction. In particular, one may implicitly embed the structure into the fluid resulting into an unfitted fluid-structure interaction method for curved shells and membranes.

Bibliography

[1] A. Apostolatos, R. Schmidt, R. Wüchner, and K.U. Bletzinger, “A Nitsche-type formulation and comparison of the most common domain decomposition methods in isogeometric analysis”, *Internat. J. Numer. Methods Engrg.*, vol. 97, pp. 473–504, 2013. DOI: `10.1002/nme.4568`.

[2] J.H. Argyris and D.W. Scharpf, “The SHEBA Family of Shell Elements for the Matrix Displacement Method”, *The Aeronautical Journal*, vol. 72, pp. 873–883, 1968. DOI: `10.1017/S0001924000085250`.

[3] D.N. Arnold, F. Brezzi, B. Cockburn, and L.D. Marini, “Unified Analysis of Discontinuous Galerkin Methods for Elliptic Problems”, *SIAM J. Numer. Anal.*, vol. 39, pp. 1749–1779, 2002. DOI: `10.1137/s0036142901384162`.

[4] I. Babuška, “Error-bounds for finite element method”, *Numer. Math.*, vol. 16, pp. 322–333, 1971. DOI: `10.1007/BF02165003`.

[5] I. Babuška, “The finite element method with Lagrangian multipliers”, *Numer. Math.*, vol. 20, pp. 179–192, 1973. DOI: `10.1007/BF01436561`.

[6] I. Babuška, “The Finite Element Method with penalty”, *Math. Comput.*, vol. 27, pp. 221–228, 1973. DOI: `10.2307/2005611`.

[7] Y. Başar and W.B. Krätzig, *Mechanik der Flächentragwerke.* Braunschweig: Vieweg + Teubner Verlag, 1985. DOI: `10.1007/978-3-322-93983-8`.

[8] K.J. Bathe, A. Iosilevich, and D. Chapelle, “An evaluation of the MITC shell elements”, *Computers & Structures*, vol. 75, pp. 1–30, 2000. DOI: `10.1016/S0045-7949(99)00214-X`.

[9] T. Belytschko, H. Stolarski, W.K. Liu, N. Carpenter, and J.S.J Ong, “Stress projection for membrane and shear locking in shell finite elements”, *Comp. Methods Appl. Mech. Engrg.*, vol. 51, pp. 221–258, 1985. DOI: `10.1016/0045-7825(85)90035-0`.

[10] D.J. Benson, Y. Bazilevs, M.C. Hsu, and T.J.R. Hughes, “Isogeometric shell analysis: The Reissner-Mindlin shell”, *Comp. Methods Appl. Mech. Engrg.*, vol. 199, pp. 276–289, 2010. DOI: `10.1016/j.cma.2009.05.011`.

[11] J. Benzaken, J.A. Evans, S. McCormick, and R. Tamstorf, “Nitsche’s method for linear Kirchhoff–Love shells: Formulation, error analysis, and verification”, *Comp. Methods Appl. Mech. Engrg.*, vol. 374, p. 113 544, 2021. DOI: `10.1016/j.cma.2020.113544`.

[12] M. Bertalmio, L.T. Cheng, S. Osher, and G. Sapiro, “Variational Problems and Partial Differential Equations on Implicit Surfaces”, *J. Comput. Phys.*, vol. 174, pp. 759–780, 2001. DOI: `10.1006/jcph.2001.6937`.

[13] S. Bieber, B. Oesterle, E. Ramm, and M. Bischoff, “A variational method to avoid locking–independent of the discretization scheme”, *Internat. J. Numer. Methods Engrg.*, vol. 114, pp. 801–827, 2018. DOI: `10.1002/nme.5766`.

[14] M. Bischoff, E. Ramm, and J. Irslinger, “Models and Finite Elements for Thin-walled Structures”, in *Encyclopedia of Computational Mechanics (Second Edition)*, E. Stein, R. Borst, and T. J. Hughes, Eds., Chichester: John Wiley & Sons, 2017. DOI: `10.1002/9781119176817.ecm2026`.

[15] J. Blaauwendraad and J.H. Hoefakker, *Structural Shell Analysis*, ser. Solid Mechanics and Its Applications. Berlin: Springer, 2014, vol. 200.

[16] A. Bonito, A. Demlow, and R.H. Nochetto, “Chapter 1 - finite Element Methods for the Laplace-Beltrami Operator”, in *Geometric Partial Differential Equations - Part I*, ser. Handbook of Numerical Analysis, A. Bonito and R.H. Nochetto, Eds., vol. 21, Amsterdam: Elsevier, 2020, pp. 1–103. DOI: `10.1016/bs.hna.2019.06.002`.

[17] F. Brezzi, “On the existence, uniqueness and approximation of saddle-point problems arising from Lagrange multipliers”, *RAIRO Anal. Numér.*, vol. R-2, pp. 129–151, 1974. DOI: `10.1051/m2an/197408R201291`.

[18] H.-G. Bui, D. Schillinger, and G. Meschke, “Efficient cut-cell quadrature based on moment fitting for materially nonlinear analysis”, *Comp. Methods Appl. Mech. Engrg.*, vol. 366, p. 113 050, 2020. DOI: `10.1016/j.cma.2020.113050`.

[19] M. Burger, “Finite element approximation of elliptic partial differential equations on implicit surfaces”, *Comput. Vis.Sci.*, vol. 12, pp. 87–100, 2009. DOI: `10.1007/s00791-007-0081-x`.

[20] E. Burman, “A penalty-free nonsymmetric Nitsche-type method for the weak imposition of boundary conditions”, *SIAM J. Numer. Anal.*, vol. 50, pp. 1959–1981, 2012. DOI: `10.1137/10081784X`.

[21] E. Burman, S. Claus, P. Hansbo, M.G. Larson, and A. Massing, “CutFEM: Discretizing geometry and partial differential equations”, *Internat. J. Numer. Methods Engrg.*, vol. 104, pp. 472–501, 2015. DOI: `10.1002/nme.4823`.

[22] E. Burman, D. Elfverson, P. Hansbo, M.G. Larson, and K. Larsson, “Shape optimization using the cut finite element method”, *Comp. Methods Appl. Mech. Engrg.*, vol. 328, pp. 242–261, 2018. DOI: `10.1016/j.cma.2017.09.005`.

[23] E. Burman and P. Hansbo, “Fictitious domain finite element methods using cut elements: I. A stabilized Lagrange multiplier method”, *Comp. Methods Appl. Mech. Engrg.*, vol. 199, no. 41, pp. 2680–2686, 2010. DOI: `10.1016/j.cma.2010.05.011`.

[24] E. Burman, P. Hansbo, and M.G. Larson, “A stabilized cut finite element method for partial differential equations on surfaces: The Laplace-Beltrami operator”, *Comp. Methods Appl. Mech. Engrg.*, vol. 285, pp. 188–207, 2015. DOI: `10.1016/j.cma.2014.10.044`.

[25] E. Burman, P. Hansbo, M.G. Larson, K. Larsson, and A. Massing, “Finite Element Approximation of the Laplace-Beltrami Operator on a Surface with Boundary”, *Numer. Math.*, vol. 141, pp. 141–172, 2018. DOI: `10.1007/s00211-018-0990-2`.

[26] E. Burman, P. Hansbo, M.G. Larson, and A. Massing, “Cut finite element methods for partial differential equations on embedded manifolds of arbitrary codimensions”, *ESAIM: Mathematical Modelling and Numerical Analysis*, vol. 52, pp. 2247–2282, 2018. DOI: `10.1051/m2an/2018038`.

[27] C. R. Calladine, *Theory of Shell Structures*. Cambridge: Cambridge University Press, 1983.

[28] M. Cenanovic, P. Hansbo, and M.G. Larson, “Cut finite element modeling of linear membranes”, *Comp. Methods Appl. Mech. Engrg.*, vol. 310, pp. 98–111, 2016. DOI: `10.1016/j.cma.2016.05.018`.

[29] D. Chapelle and K.J. Bathe, “Fundamental considerations for the finite element analysis of shell structures”, *Computers & Structures*, vol. 66, pp. 19–36, 1998. DOI: `10.1016/S0045-7949(97)00078-3`.

[30] D. Chapelle and K.J. Bathe, *The Finite Element Analysis of Shells – Fundamentals*, ser. Computational Fluid and Solid Mechanics. Berlin: Springer, 2011.

[31] P.G. Ciarlet, *Mathematical Elasticity, III: Theory of Shells*. Amsterdam: Elsevier, 1997.

[32] F. Cirak and M. Ortiz, “Fully C1-conforming subdivision elements for finite deformation thin-shell analysis”, *Internat. J. Numer. Methods Engrg.*, vol. 51, pp. 813–833, 2001. DOI: `10.1002/nme.182.abs`.

[33] F. Cirak, M. Ortiz, and P. Schröder, “Subdivision surfaces: A new paradigm for thin-shell finite-element analysis”, *Internat. J. Numer. Methods Engrg.*, vol. 47, pp. 2039–2072, 2000. DOI: `10.1002/(SICI)1097-0207(20000430)47:12<2039::AID-NME872>3.0.CO;2-1`.

[34] J.A. Cottrell, T.J.R. Hughes, and Y. Bazilevs, *Isogeometric Analysis: Toward Integration of CAD and FEA*. Chichester: John Wiley & Sons, 2009. DOI: `10.1002/9780470749081`.

[35] F. de Prenter, C. Lehrenfeld, and A. Massing, “A note on the stability parameter in Nitsche’s method for unfitted boundary value problems”, *Comput Math Appl*, vol. 75, pp. 4322–4336, 2018. DOI: `10.1016/j.camwa.2018.03.032`.

[36] K. Deckelnick, G. Dziuk, C.M. Elliott, and C.J. Heine, “An h-narrow band finite-element method for elliptic equations on implicit surfaces”, *IMA J. Numer. Anal.*, vol. 30, pp. 351–376, 2010. DOI: `10.1093/imanum/drn049`.

[37] M.C. Delfour and J.P. Zolésio, “Shape Analysis via Oriented Distance Functions”, *J. Funct. Anal.*, vol. 123, pp. 129–201, 1994. DOI: `10.1006/jfan.1994.1086`.

[38] M.C. Delfour and J.P. Zolésio, “A Boundary Differential Equation for Thin Shells”, *J. Differential Equations*, vol. 119, pp. 426–449, 1995. DOI: `10.1006/jdeq.1995.1097`.

[39] M.C. Delfour and J.P. Zolésio, “Tangential Differential Equations for Dynamical Thin Shallow Shells”, *J. Differential Equations*, vol. 128, pp. 125–167, 1996. DOI: `10.1006/jdeq.1996.0092`.

[40] M.C. Delfour and J.P. Zolésio, “Differential equations for linear shells comparison between intrinsic and classical”, in *Advances in Mathematical Sciences: CRM’s 25 Years (Montreal, PQ, 1994), CRM Proc. Lecture Notes*, vol. 11, Providence, Rhode Island, 1997.

[41] M.C. Delfour and J.P. Zolésio, *Shapes and Geometries: Metrics, Analysis, Differential Calculus, and Optimization.* Philadelphia: SIAM, 2011.

[42] A. Demlow, “Higher-order finite element methods and pointwise error estimates for elliptic problems on surfaces”, *SIAM J. Numer. Anal.*, vol. 47, pp. 805–827, 2009. DOI: `10.1137/070708135`.

[43] A. Demlow and G. Dziuk, “An adaptive finite element method for the Laplace-Beltrami operator on implicitly defined surfaces”, *SIAM J. Numer. Anal.*, vol. 45, pp. 421–442, 2007. DOI: `10.1137/050642873`.

[44] A. Demlow and M.A. Olshanskii, “An adaptive surface finite element method based on volume meshes”, *SIAM J. Numer. Anal.*, vol. 50, pp. 1624–1647, 2012. DOI: `10.1137/110842235`.

[45] C. Denyer, *Nautilus shell cutaway*, licensed under CC0 1.0. [Online]. Available: `https://www.needpix.com/photo/1454160/` (visited on 11/21/2020).

[46] W. Dornisch and S. Klinkel, “Treatment of Reissner-Mindlin shells with kinks without the need for drilling rotation stabilization in an isogeometric framework”, *Comp. Methods Appl. Mech. Engrg.*, vol. 276, pp. 35–66, 2014. DOI: `10.1016/j.cma.2014.03.017`.

[47] W. Dornisch, S. Klinkel, and B. Simeon, “Isogeometric Reissner-Mindlin shell analysis with exactly calculated director vectors”, *Comp. Methods Appl. Mech. Engrg.*, vol. 253, pp. 491–504, 2013. DOI: `10.1016/j.cma.2012.09.010`.

[48] A. Düster, E. Rank, and B. Szabó, “The p-Version of the Finite Element and Finite Cell Methods”, in *Encyclopedia of Computational Mechanics (Second Edition)*, E. Stein, R. Borst, and T. J. Hughes, Eds., Chichester: John Wiley & Sons, 2017. DOI: `https://doi.org/10.1002/9781119176817.ecm2003g`.

[49] G. Dziuk, “Finite elements for the Beltrami operator on arbitrary surfaces”, in *Partial Differential Equations and Calculus of Variations.* Berlin: Springer, 1988, pp. 142–155. DOI: `10.1007/BFb0082865`.

[50] G. Dziuk and C.M. Elliott, “Finite elements on evolving surfaces”, *IMA J. Numer. Anal.*, vol. 27, pp. 262–292, 2007. DOI: `10.1093/imanum/drl023`.

[51] G. Dziuk and C.M. Elliott, “Eulerian finite element method for parabolic PDEs and on implicit surfaces”, *Interfaces Free Bound.*, vol. 10, 2008. DOI: `10.4171/IFB/182`.

[52] G. Dziuk and C.M. Elliott, “Finite element methods for surface PDEs”, *Acta Numerica*, vol. 22, pp. 289–396, 2013. DOI: `10.1017/S0962492913000056`.

[53] R. Echter, B. Oesterle, and M. Bischoff, “A hierarchic family of isogeometric shell finite elements”, *Comp. Methods Appl. Mech. Engrg.*, vol. 254, pp. 170–180, 2013. DOI: `10.1016/j.cma.2012.10.018`.

[54] D. Elfverson, M.G. Larson, and K. Larsson, “A new least squares stabilized Nitsche method for cut isogeometric analysis”, *Comp. Methods Appl. Mech. Engrg.*, vol. 349, pp. 1–16, 2019. DOI: `10.1016/j.cma.2019.02.011`.

[55] C.M. Elliott and B. Stinner, “Analysis of a diffuse interface approach to an advection diffusion equation on a moving surface”, *Mathematical Models and Methods in Applied Sciences*, vol. 19, pp. 787–802, 2009. DOI: `10.1142/S0218202509003620`.

[56] C.M. Elliott and V. Styles, “An ALE ESFEM for Solving PDEs on Evolving Surfaces”, *Milan Journal of Mathematics*, vol. 80, pp. 469–501, 2012. DOI: `10.1007/s00032-012-0195-6`.

[57] A. Embar, J. Dolbow, and I. Harari, “Imposing Dirichlet boundary conditions with Nitsche’s method and spline-based finite elements”, *Internat. J. Numer. Methods Engrg.*, vol. 83, pp. 877–898, 2010. DOI: `10.1002/nme.2863`.

[58] M. Farshad, *Design and Analysis of Shell Structures*. Berlin: Springer, 1992. DOI: `10.1007/978-94-017-1227-9`.

[59] S. Fernández-Méndez and A. Huerta, “Imposing essential boundary conditions in mesh-free methods”, *Comp. Methods Appl. Mech. Engrg.*, vol. 193, pp. 1257–1275, 2004. DOI: `10.1016/j.cma.2003.12.019`.

[60] L.P. Franca and T.J.R. Hughes, “Two classes of mixed finite element methods”, *Comp. Methods Appl. Mech. Engrg.*, vol. 69, pp. 89–129, 1988. DOI: `10.1016/0045-7825(88)90168-5`.

[61] T.P. Fries, “Higher-order conformal decomposition FEM (CDFEM)”, *Comp. Methods Appl. Mech. Engrg.*, vol. 328, pp. 75–98, 2018. DOI: `10.1016/j.cma.2017.08.046`.

[62] T.P. Fries, “Higher-order surface FEM for incompressible Navier-stokes flows on manifolds”, *Int. J. Numer. Methods Fluids*, vol. 88, pp. 55–78, 2018. DOI: `10.1002/fld.4510`.

[63] T.P. Fries and S. Omerović, “Higher-order accurate integration of implicit geometries”, *Internat. J. Numer. Methods Engrg.*, vol. 106, pp. 323–371, 2016. DOI: `10.1002/nme.5121`.

[64] T.P. Fries, S. Omerović, D. Schöllhammer, and J. Steidl, “Higher-order meshing of implicit geometries - Part I: Integration and interpolation in cut elements”, *Comp. Methods Appl. Mech. Engrg.*, vol. 313, pp. 759–784, 2017. DOI: `10.1016/j.cma.2016.10.019`.

[65] T.P. Fries and D. Schöllhammer, “Higher-order meshing of implicit geometries - Part II: Approximations on manifolds”, *Comp. Methods Appl. Mech. Engrg.*, vol. 326, pp. 270–297, 2017. DOI: `10.1016/j.cma.2017.07.037`.

[66] T.P. Fries and D. Schöllhammer, “A unified finite strain theory for membranes and ropes”, *Comp. Methods Appl. Mech. Engrg.*, vol. 365, p. 113 031, 2020. DOI: `10.1016/j.cma.2020.113031`.

[67] T.P. Fries and D. Schöllhammer, “Non-linear structural membranes and ropes based on tangential differential calculus”, in *Proc. Appl. Math. Mech.*, vol. 20, Chichester: John Wiley & Sons, 2020, e202000045. DOI: `10.1002/pamm.202000045`.

[68] T.P. Fries, S.Omerović, D.Schöllhammer, and J. Steidl, "A fictitious domain method with higher-order accurate integration in cut elements", in *6th European Congress on Computational Mechanics (ECCM VI) and 7th European Congress on Computational Fluid Dynamics (ECFD VII). E. Oñate, X. Oliver, and A. Huerta (eds.)*, Barcelona: International Centre for Numerical Methods in Engineering (CIMNE), 2018, pp. 3994–3405.

[69] M.H. Gfrerer, "A C^1-continuous Trace-Finite-Cell-Method for linear thin shell analysis on implicitly defined surfaces", *ArXiv e-prints*, 2020. arXiv: `2007.00075 [cs.CE]`.

[70] M.H. Gfrerer and M. Schanz, "High order exact geometry finite elements for seven-parameter shells with parametric and implicit reference surfaces", *Comput. Mech.*, vol. 64, pp. 133–145, 2019. DOI: `10.1007/s00466-018-1661-y`.

[71] F. Gibou, R. Fedkiw, and S. Osher, "A review of level-set methods and some recent applications", *J. Comput. Phys.*, vol. 353, pp. 82–109, 2018. DOI: `10.1016/j.jcp.2017.10.006`.

[72] J. Grande, C. Lehrenfeld, and A. Reusken, "Analysis of a high-order trace finite element method for PDEs on level set surfaces", *SIAM J. Numer. Anal.*, vol. 56, pp. 228–255, 2018. DOI: `10.1137/16M1102203`.

[73] J. Grande and A. Reusken, "A higher order finite element method for partial differential equations on surfaces", *SIAM*, vol. 54, pp. 388–414, 2016. DOI: `10.1137/14097820X`.

[74] S. Gross, T. Jankuhn, M.A. Olshanskii, and A. Reusken, "A trace finite element method for vector-laplacians on surfaces", *SIAM J. Numer. Anal.*, vol. 56, pp. 2406–2429, 2018. DOI: `10.1137/17M1146038`.

[75] S. Gross and A. Reusken, *Numerical Methods for Two-phase Incompressible Flows*, ser. Springer Series in Computational Mathematics. Berlin: Springer, 2011, vol. 40.

[76] Y. Guo, H. Do, and M. Ruess, "Isogeometric stability analysis of thin shells: From simple geometries to engineering models", *Internat. J. Numer. Methods Engrg.*, vol. 118, pp. 433–458, 2019. DOI: `10.1002/nme.6020`.

[77] Y. Guo and M. Ruess, "Nitsche's method for a coupling of isogeometric thin shells and blended shell structures", *Comp. Methods Appl. Mech. Engrg.*, vol. 284, pp. 881–905, 2015. DOI: `10.1016/j.cma.2014.11.014`.

[78] Y. Guo, M. Ruess, and D. Schillinger, "A parameter-free variational coupling approach for trimmed isogeometric thin shells", *Comput. Mech.*, vol. 59, pp. 693–715, 2017. DOI: `10.1007/s00466-016-1368-x`.

[79] M.E. Gurtin and I.A. Murdoch, "A continuum theory of elastic material surfaces", *Archive for Rational Mechanics and Analysis*, vol. 57, pp. 291–323, 1975. DOI: `10.1007/BF00261375`.

[80] A. Hansbo and P. Hansbo, "An unfitted finite element method, based on Nitsche's method, for elliptic interface problems", *Comp. Methods Appl. Mech. Engrg.*, vol. 191, pp. 5537–5552, 2002. DOI: `10.1016/S0045-7825(02)00524-8`.

[81] P. Hansbo and M.G. Larson, “Finite element modeling of a linear membrane shell problem using tangential differential calculus”, *Comp. Methods Appl. Mech. Engrg.*, vol. 270, pp. 1–14, 2014. DOI: `10.1016/j.cma.2013.11.016`.

[82] P. Hansbo and M.G. Larson, “Continuous/discontinuous finite element modelling of Kirchhoff plate structures in $\mathbb{R}^3$ using tangential differential calculus”, *Comput. Mech.*, vol. 60, pp. 693–702, 2017. DOI: `10.1007/s00466-017-1431-2`.

[83] P. Hansbo, M.G. Larson, and F. Larsson, “Tangential differential calculus and the finite element modeling of a large deformation elastic membrane problem”, *Comput. Mech.*, vol. 56, pp. 87–95, 2015. DOI: `10.1007/s00466-015-1158-x`.

[84] P. Hansbo, M.G. Larson, and K. Larsson, “Variational formulation of curved beams in global coordinates”, *Comput. Mech.*, vol. 53, pp. 611–623, 2014. DOI: `10.1007/s00466-013-0921-0`.

[85] P. Hansbo, M.G. Larson, and K. Larsson, “Analysis of Finite Element Methods for Vector Laplacians on Surfaces”, *IMA J. Numer. Anal.*, vol. 40, pp. 1652–1701, 2020. DOI: `10.1093/imanum/drz018`.

[86] Cygnusloop99, *Asu SkySong Innovation Center*, licensed under CC BY-SA 3.0. [Online]. Available: `https://commons.wikimedia.org/w/index.php?curid=9553141` (visited on 01/19/2021).

[87] F. Gabaldén, *L’Oceanogràfic*, licensed under Cc-by-2.0. [Online]. Available: `https://commons.wikimedia.org/wiki/File:L%27Oceanografic_(Valencia,_Spain)_01.jpg` (visited on 11/21/2020).

[88] T.J.R. Hughes, J.A. Cottrell, and Y. Bazilevs, “Isogeometric analysis: CAD, finite elements, NURBS, exact geometry and mesh refinement”, *Comp. Methods Appl. Mech. Engrg.*, vol. 194, pp. 4135–4195, 2005. DOI: `10.1016/j.cma.2004.10.008`.

[89] A. Ibrahimbegović and F. Gruttmann, “A consistent finite element formulation of nonlinear membrane shell theory with particular reference to elastic rubberlike material”, *Finite Elem. Anal. Des.*, vol. 13, pp. 75–86, 1993. DOI: `10.1016/0168-874X(93)90008-E`.

[90] T. Jankuhn, M.A. Olshanskii, and A. Reusken, “Incompressible Fluid Problems on Embedded Surfaces Modeling and Variational and Formulations”, *Interfaces Free Bound.*, vol. 20, pp. 353–377, 2018. DOI: `10.4171/ifb/405`.

[91] T. Jankuhn, M.A. Olshanskii, A. Reusken, and A. Zhiliako, “Error Analysis of Higher Order Trace Finite Element Methods for the Surface Stokes Equations”, *ArXiv e-prints*, 2020. arXiv: `2003.06972`.

[92] T. Jankuhn and A. Reusken, “Higher Order Trace Finite Element Methods for the Surface Stokes Equations”, *ArXiv e-prints*, 2019. arXiv: `1909.08327`.

[93] M. Jung and U. Langer, *Methode der finiten Elemente für Ingenieure: Eine Einführung in die numerischen Grundlagen und Computersimulation.* Berlin: Springer, 2013.

[94] J. Kiendl, K.-U. Bletzinger, J. Linhard, and R. Wüchner, “Isogeometric shell analysis with Kirchhoff-Love elements”, *Comp. Methods Appl. Mech. Engrg.*, vol. 198, pp. 3902–3914, 2009. DOI: `10.1016/j.cma.2009.08.013`.

[95] J. Kiendl, E. Marino, and L. De Lorenzis, "Isogeometric collocation for the Reissner-Mindlin shell problem", *Comp. Methods Appl. Mech. Engrg.*, vol. 325, pp. 645–665, 2017. DOI: `10.1016/j.cma.2017.07.023`.

[96] G. Kirchhoff, "Über das Gleichgewicht und die Bewegung einer elastischen Scheibe", *Journal für die reine und angewandte Mathematik (Crelles Journal)*, vol. 40, pp. 51–88, 1850. DOI: `10.1515/crll.1850.40.51`.

[97] Y. Ko, P.S. Lee, and K.J. Bathe, "A new MITC4+ shell element", *Computers & Structures*, vol. 182, pp. 404–418, 2017. DOI: `10.1016/j.compstruc.2016.11.004`.

[98] M.G. Larson and S. Zahedi, "Stabilization of high order cut finite element methods on surfaces", *IMA J. Numer. Anal.*, vol. 40, pp. 1702–1745, 2020. DOI: `10.1093/imanum/drz021`.

[99] C. Lebiedzik, "Exact boundary controllability of a shallow intrinsic shell model", *J. Math. Anal. Appl.*, vol. 335, pp. 584–614, 2007. DOI: `10.1016/j.jmaa.2007.01.061`.

[100] C. Lehrenfeld, "High order unfitted finite element methods on level set domains using isoparametric mappings", *Comp. Methods Appl. Mech. Engrg.*, vol. 300, pp. 716–733, 2016. DOI: `10.1016/j.cma.2015.12.005`.

[101] A.E.H. Love, "On the small vibrations and deformations of thin elastic shells", *Philos. Trans. R. Soc.*, vol. 179, 491ff, 1888.

[102] B. Müller, F. Kummer, and M. Oberlack, "Highly accurate surface and volume integration on implicit domains by means of moment-fitting", *Internat. J. Numer. Methods Engrg.*, vol. 96, pp. 512–528, 2013. DOI: `10.1002/nme.4569`.

[103] N. Nguyen-Thanh, K. Zhou, X. Zhuang, P. Areias, H. Nguyen-Xuan, Y. Bazilevs, and T. Rabczuk, "Isogeometric analysis of large-deformation thin shells using RHT-splines for multiple-patch coupling", *Comp. Methods Appl. Mech. Engrg.*, vol. 316, pp. 1157–1178, 2017. DOI: `10.1016/j.cma.2016.12.002`.

[104] J. Nitsche, "Über ein Variationsprinzip zur lösung von Dirichlet-Problemen bei Verwendung von Teilräumen, die keinen Randbedingungen unterworfen sind", *Abhandlungen aus dem Mathematischen Seminar der Universität Hamburg*, vol. 36, pp. 9–15, 1971. DOI: `10.1007/BF02995904`.

[105] B. Oesterle, E. Ramm, and M. Bischoff, "A shear deformable, rotation-free isogeometric shell formulation", *Comp. Methods Appl. Mech. Engrg.*, vol. 307, pp. 235–255, 2016. DOI: `10.1016/j.cma.2016.04.015`.

[106] B. Oesterle, R. Sachse, E. Ramm, and M. Bischoff, "Hierarchic isogeometric large rotation shell elements including linearized transverse shear parametrization", *Comp. Methods Appl. Mech. Engrg.*, vol. 321, pp. 383–405, 2017. DOI: `10.1016/j.cma.2017.03.031`.

[107] M.A. Olshanskii, A. Quaini, A. Reusken, and V. Yushutin, "A finite element method for the surface stokes problem", *SIAM J. Sci. Comput.*, vol. 40, A2492–A2518, 2018. DOI: `10.1137/18M1166183`.

[108] M.A. Olshanskii and A. Reusken, “A finite element method for surface PDEs: Matrix properties”, *Numer. Math.*, vol. 114, pp. 491–520, 2009. DOI: `10.1007/s00211-009-0260-4`.

[109] M.A. Olshanskii and A. Reusken, “Trace finite element methods for PDEs on surfaces”, *Lecture Notes in Computational Science and Engineering*, vol. 121, pp. 211–258, 2017. DOI: `10.1007/978-3-319-71431-8_7`.

[110] M.A. Olshanskii, A. Reusken, and J. Grande, “A finite element method for elliptic equations on surfaces”, *SIAM*, vol. 47, pp. 3339–3358, 2009. DOI: `10.1137/080717602`.

[111] M.A. Olshanskii and X. Xu, “A trace finite element method for PDEs on evolving surfaces”, *SIAM*, vol. 39, A1301–A1319, 2017. DOI: `10.1137/16M1099388`.

[112] E. Oñate, *Structural Analysis with the Finite Element Method Linear Statics*, ser. Lecture Notes on Numerical Methods in Engineering and Sciences. Berlin: Springer, 2013, vol. 2. Beams, Plates and Shells.

[113] T.M. van Opstal, E.H. van Brummelen, and G.J. van Zwieten, “A finite-element/boundary-element method for three-dimensional, large-displacement fluid-structure-interaction”, *Comp. Methods Appl. Mech. Engrg.*, vol. 284, pp. 637–663, 2015. DOI: `10.1016/j.cma.2014.09.037`.

[114] S. Osher and J.A. Sethian, “Fronts propagating with curvature-dependent speed: Algorithms based on Hamilton-Jacobi formulations”, *J. Comput. Phys.*, vol. 79, pp. 12–49, 1988. DOI: `10.1016/0021-9991(88)90002-2`.

[115] L. Piegl and W. Tiller, *The NURBS Book (Monographs in Visual Communication)*, 2nd. Berlin: Springer, 1997.

[116] M. Radwańska, A. Stankiewicz, A. Wosatko, and J. Pamin, *Plate and Shell Structures.* Chichester: John Wiley & Sons, 2017. DOI: `10.1002/9781118934531`.

[117] A. Rätz and A. Voigt, “PDE’s on surfaces - A diffues interface approach”, *Commun. Math. Sci.*, vol. 4, pp. 575–590, 2006.

[118] E. Reissner, “The effect of transverse shear deformation on the bending of elastic plates”, *ASME J. Appl. Mech.*, vol. 12, A69–77, 1945.

[119] A. Reusken, “Analysis of trace finite element methods for surface partial differential equations”, *IMA J. Numer. Anal.*, vol. 35, pp. 1568–1590, 2014. DOI: `10.1093/imanum/dru047`.

[120] M. Ruess, D. Schillinger, Y. Bazilevs, V. Varduhn, and E. Rank, “Weakly enforced essential boundary conditions for NURBS-embedded and trimmed NURBS geometries on the basis of the finite cell method”, *Internat. J. Numer. Methods Engrg.*, vol. 95, pp. 811–846, 2013. DOI: `10.1002/nme.4522`.

[121] D. Schillinger, I. Harari, M.C. Hsu, D. Kamensky, S.K.F. Stoter, Y. Yu, and Y. Zhao, “The non-symmetric Nitsche method for the parameter-free imposition of weak boundary and coupling conditions in immersed finite elements”, *Comp. Methods Appl. Mech. Engrg.*, vol. 309, pp. 625–652, 2016. DOI: `10.1016/j.cma.2016.06.026`.

[122] D. Schöllhammer and T.P. Fries, "Classical Shell Analysis in view of Tangential Differential Calculus", in *6th European Congress on Computational Mechanics (ECCM VI) and 7th European Congress on Computational Fluid Dynamics (ECFD VII). E. Oñate, X. Oliver, and A. Huerta (eds.)*, Barcelona: International Centre for Numerical Methods in Engineering (CIMNE), 2018, pp. 3646–3657.

[123] D. Schöllhammer and T.P. Fries, "Kirchhoff–Love shell theory based on Tangential Differential Calculus", in *Proc. Appl. Math. Mech.*, vol. 18, Chichester: John Wiley & Sons, 2018, e201800170. DOI: `10.1002/pamm.201800170`.

[124] D. Schöllhammer and T.P. Fries, "A unified approach for shell analysis on explicitly and implicitly defined surfaces", in *Form and Force: Proceedings of the IASS Symposium 2019 - Structural Membranes 2019, C. Lázaro, K.U. Bletzinger, E. Oñate (eds.)*, Barcelona: International Centre for Numerical Methods in Engineering (CIMNE), 2019, pp. 750–757.

[125] D. Schöllhammer and T.P. Fries, "Kirchhoff-Love shell theory based on tangential differential calculus", *Comput. Mech.*, vol. 64, pp. 113–131, 2019. DOI: `10.1007/s00466-018-1659-5`.

[126] D. Schöllhammer and T.P. Fries, "Reissner–Mindlin shell theory based on Tangential Differential Calculus", in *Proc. Appl. Math. Mech.*, vol. 19, Chichester: John Wiley & Sons, 2019, e201900099. DOI: `10.1002/pamm.201900099`.

[127] D. Schöllhammer and T.P. Fries, "Reissner–Mindlin shell theory based on tangential differential calculus", *Comp. Methods Appl. Mech. Engrg.*, vol. 352, pp. 172–188, 2019. DOI: `10.1016/j.cma.2019.04.018`.

[128] D. Schöllhammer and T.P. Fries, "A generalized formulation of classical shell models based on tangential differential calculus", in *Berichte der Fachtagung Baustatik - Baupraxis 14: 23. und 24. März 2020, Universität Stuttgart*, M. Bischoff, M. von Scheven, and B. Oesterle, Eds., vol. 14, Stuttgart: Institut für Baustatik und Baudynamik, Universität Stuttgart, 2020, pp. 431–438. DOI: `10.18419/opus-10762`.

[129] D. Schöllhammer and T.P. Fries, "A higher-order Trace finite element method for shells", *Internat. J. Numer. Methods Engrg.*, 2020. DOI: `10.1002/nme.6558`.

[130] D. Schöllhammer and T.P. Fries, "Implicit Analysis of Reissner–Mindlin shells with the Trace FEM", in *Proc. Appl. Math. Mech.*, vol. 20, Chichester: John Wiley & Sons, 2020, e202000049. DOI: `10.1002/pamm.202000049`.

[131] D. Schöllhammer, B. Marussig, and T.P. Fries, "A Consistent Higher-Order Isogeometric Shell Formulation", *Comp. Methods Appl. Mech. Engrg.*, 2020, submitted, Preprint on arXiv: 2012.11975.

[132] J.C. Simo and D.D. Fox, "On a stress resultant geometrically exact shell model. Part i: Formulation and optimal parametrization", *Comp. Methods Appl. Mech. Engrg.*, vol. 72, pp. 267–304, 1989. DOI: `10.1016/0045-7825(89)90002-9`.

[133] J.C. Simo, D.D. Fox, and M.S. Rifai, "On a stress resultant geometrically exact shell model. Part ii: The linear theory; Computational aspects", *Comp. Methods Appl. Mech. Engrg.*, vol. 73, pp. 53–92, 1989. DOI: `10.1016/0045-7825(89)90098-4`.

[134] A. Stavrev, L.H. Nguyen, R. Shen, V. Varduhn, M. Behr, S. Elgeti, and D. Schillinger, “Geometrically accurate, efficient, and flexible quadrature techniques for the tetrahedral finite cell method”, *Comp. Methods Appl. Mech. Engrg.*, vol. 310, pp. 646–673, 2016. DOI: `10.1016/j.cma.2016.07.041`.

[135] A.B. Tepole, H. Kabaria, K.U. Bletzinger, and E. Kuhl, “Isogeometric Kirchhoff-Love shell formulations for biological membranes”, *Comp. Methods Appl. Mech. Engrg.*, vol. 293, pp. 328–347, 2015. DOI: `10.1016/j.cma.2015.05.006`.

[136] S. Timoshenko and S. Woinowsky-Krieger, *Theory of Plates and Shells*, 2nd. New York: McGraw-Hill Book Company, Inc., 1959.

[137] S.P. Timoshenko, *History of Strength of Materials.* New York: McGraw-Hill Book Company, Inc., 1953.

[138] S.W. Walker, *The Shapes of Things: A Practical Guide to Differential Geometry and the Shape Derivative*, ser. Advances in Design and Control. Philadelphia: SIAM, 2015. DOI: `10.1137/1.9781611973969`.

[139] G. Wempner and D. Talaslidis, *Mechanics of Solids and Shells: Theories and Approximations.* Florida: CRC Press LLC, 2002.

[140] J.-J. Xu, Y. Yang, and J. Lowengrub, “A level-set continuum method for two-phase flows with insoluble surfactant”, *J. Comput. Phys.*, vol. 231, pp. 5897–5909, 2012. DOI: `10.1016/j.jcp.2012.05.014`.

[141] J.-J. Xu and H.-K. Zhao, “An Eulerian Formulation for Solving Partial Differential Equations along a Moving Interface”, *J. Sci. Comput.*, vol. 19, pp. 573–594, 2003. DOI: `10.1023/A:1025336916176`.

[142] H.T.Y. Yang, S. Saigal, A. Masud, and R.K. Kapania, “A survey of recent shell finite elements”, *Internat. J. Numer. Methods Engrg.*, vol. 47, pp. 101–127, 2000. DOI: `10.1002/(SICI)1097-0207(20000110/30)47:1/3<101::AID-NME763>3.0.CO;2-C`.

[143] P.F. Yao, “On shallow shell equations”, *Discrete Contin. Dyn. Syst. Ser. S*, vol. 2, pp. 697–722, 2009. DOI: `10.3934/dcdss.2009.2.697`.

[144] O. Zienkiewicz, R. Taylor, and J.Z. Zhu, *The Finite Element Method: Its Basis and Fundamentals: Seventh Edition*, 7th. Oxford: Elsevier LTD, 2013. DOI: `10.1016/C2009-0-24909-9`.

[145] A. Zingoni, *Shell Structures in Civil and Mechanical Engineering: Theory and analysis*, 2nd. London: ICE Publishing, 2018.

[146] Z. Zou, M.A. Scott, D. Miao, M. Bischoff, B. Oesterle, and W. Dornisch, “An isogeometric reissner–mindlin shell element based on bézier dual basis functions: Overcoming locking and improved coarse mesh accuracy”, *Comp. Methods Appl. Mech. Engrg.*, vol. 370, p. 113 283, 2020. DOI: `10.1016/j.cma.2020.113283`.

A Properties and auxiliary relations in the TDC

In the following, a summary of product rules, useful relations, and properties of important quantities in the frame of the TDC which are needed to the derive surface PDEs are presented.

Normal projector

$$\mathbf{P} = \mathbb{I} - \boldsymbol{n}_\Gamma \otimes \boldsymbol{n}_\Gamma \tag{A.1}$$

$$\mathbf{P} \cdot \mathbf{P} = \mathbf{P} \tag{A.2}$$

$$\mathbf{P} = \mathbf{P}^{\mathrm{T}} \tag{A.3}$$

$$\mathbf{P} \cdot \boldsymbol{n}_\Gamma = \mathbf{0} \tag{A.4}$$

$$\mathbf{P} \cdot \boldsymbol{t} = \boldsymbol{t} \qquad \text{iff } \boldsymbol{t} \cdot \boldsymbol{n}_\Gamma = 0 \tag{A.5}$$

$$\nabla^{\mathrm{cov}}_{\Gamma,i} \mathbf{P} = \mathbf{0} \qquad i = 1, 2, 3 \tag{A.6}$$

$$\mathrm{div}_\Gamma \mathbf{P} = -\varkappa \cdot \boldsymbol{n}_\Gamma \qquad \text{with Eq. A.13} \tag{A.7}$$

$$\mathrm{tr}\left(\mathbf{P} \cdot \mathbf{A} \cdot \mathbf{P}\right) = \mathbf{P} : \mathbf{A} = \mathbf{P} : \mathbf{A}^{\mathrm{T}} \qquad \forall\ \mathbf{A} \in \mathbb{R}^{3\times 3} \tag{A.8}$$

Weingarten map

$$\mathbf{H} = \nabla^{\mathrm{dir}}_\Gamma \boldsymbol{n}_\Gamma = \nabla^{\mathrm{cov}}_\Gamma \boldsymbol{n}_\Gamma \tag{A.9}$$

$$\mathbf{H} = \mathbf{H}^{\mathrm{T}} \tag{A.10}$$

$$\mathbf{H} = \mathbf{H} \cdot \mathbf{P} = \mathbf{P} \cdot \mathbf{H} = \mathbf{P} \cdot \mathbf{H} \cdot \mathbf{P} \tag{A.11}$$

$$\mathbf{H} \cdot \boldsymbol{n}_\Gamma = \boldsymbol{n}_\Gamma^{\mathrm{T}} \cdot \mathbf{H} = \mathbf{0} \tag{A.12}$$

$$\mathrm{tr}\left(\mathbf{H}\right) = \varkappa \tag{A.13}$$

$$-\,\mathrm{eig}\left(\mathbf{H}\right) = \kappa_i \qquad i = 1, 2\,, (\kappa_3 = 0) \tag{A.14}$$

$$\kappa_1 \cdot \kappa_2 = K \tag{A.15}$$

$$\mathbf{H} \cdot \nabla^{\mathrm{dir}}_\Gamma \boldsymbol{u} = \mathbf{H} \cdot \nabla^{\mathrm{cov}}_\Gamma \boldsymbol{u} \tag{A.16}$$

Tangential gradient of scalar-valued functions

$$\mathbf{P} \cdot \nabla_\Gamma f = \nabla_\Gamma f \tag{A.17}$$

$$\nabla_\Gamma f \cdot \boldsymbol{n}_\Gamma = 0 \tag{A.18}$$

Surface Hessian matrix

$$\mathbf{He}^{\mathrm{dir}} \neq \mathbf{He}^{\mathrm{dir}^{\mathrm{T}}} \tag{A.19}$$

$$\mathbf{He}^{\mathrm{cov}} = \mathbf{He}^{\mathrm{cov}^{\mathrm{T}}} \tag{A.20}$$

$$\mathbf{He}^{\mathrm{dir}} \neq \mathbf{He}^{\mathrm{cov}} \qquad \text{if } \Gamma \text{ is flat} \Rightarrow \mathbf{He}^{\mathrm{dir}} = \mathbf{He}^{\mathrm{cov}} \tag{A.21}$$

$$\mathrm{tr}(\mathbf{He}^{\mathrm{dir}}) = \mathrm{tr}(\mathbf{He}^{\mathrm{cov}}) \tag{A.22}$$

Directional gradient of vector-valued functions

$$\nabla_\Gamma^{\mathrm{dir}} \boldsymbol{v} \neq (\nabla_\Gamma^{\mathrm{dir}} \boldsymbol{v})^{\mathrm{T}} \tag{A.23}$$

$$\nabla_\Gamma^{\mathrm{dir}} \boldsymbol{v} \cdot \mathbf{P} = \nabla_\Gamma^{\mathrm{dir}} \boldsymbol{v} \tag{A.24}$$

$$\nabla_\Gamma^{\mathrm{dir}} \boldsymbol{v} \cdot \boldsymbol{n}_\Gamma = \mathbf{0} \tag{A.25}$$

$$(\nabla_\Gamma^{\mathrm{dir}} \boldsymbol{v})^{\mathrm{T}} \cdot \boldsymbol{n}_\Gamma = -\mathbf{H} \cdot \boldsymbol{v} + \nabla_\Gamma(\boldsymbol{v} \cdot \boldsymbol{n}_\Gamma) \tag{A.26}$$

$$\nabla_\Gamma^{\mathrm{dir}} \boldsymbol{n}_\Gamma = (\nabla_\Gamma^{\mathrm{dir}} \boldsymbol{n}_\Gamma)^{\mathrm{T}} \tag{A.27}$$

Covariant gradient of vector-valued functions

$$\nabla_\Gamma^{\mathrm{cov}} \boldsymbol{v} \neq (\nabla_\Gamma^{\mathrm{cov}} \boldsymbol{v})^{\mathrm{T}} \tag{A.28}$$

$$\nabla_\Gamma^{\mathrm{cov}} \boldsymbol{v} \cdot \boldsymbol{n}_\Gamma = \mathbf{0} \tag{A.29}$$

$$(\nabla_\Gamma^{\mathrm{cov}} \boldsymbol{v})^{\mathrm{T}} \cdot \boldsymbol{n}_\Gamma = \mathbf{0} \tag{A.30}$$

$$\nabla_\Gamma^{\mathrm{cov}} \boldsymbol{n}_\Gamma = (\nabla_\Gamma^{\mathrm{cov}} \boldsymbol{n}_\Gamma)^{\mathrm{T}} \tag{A.31}$$

Product rules of surface gradients

$$\nabla_\Gamma(fg) = \nabla_\Gamma(f)g + f\nabla_\Gamma(g) \tag{A.32}$$

$$\nabla_\Gamma(\boldsymbol{u}\cdot\boldsymbol{a}) = (\nabla_\Gamma^{\mathrm{dir}}\boldsymbol{u})^{\mathrm{T}}\cdot\boldsymbol{a} + (\nabla_\Gamma^{\mathrm{dir}}\boldsymbol{a})^{\mathrm{T}}\cdot\boldsymbol{u} \tag{A.33}$$

$$\nabla_\Gamma(\boldsymbol{u}\cdot\boldsymbol{n}_{\boldsymbol{\Gamma}}) = (\nabla_\Gamma^{\mathrm{dir}}\boldsymbol{u})^{\mathrm{T}}\cdot\boldsymbol{n}_{\boldsymbol{\Gamma}} + \mathbf{H}\cdot\boldsymbol{u} \tag{A.34}$$

$$\nabla_\Gamma^{\mathrm{dir}}(f\boldsymbol{u}) = f\nabla_\Gamma^{\mathrm{dir}}\boldsymbol{u} + \boldsymbol{u}\otimes\nabla_\Gamma f \tag{A.35}$$

$$\nabla_\Gamma^{\mathrm{cov}}(f\boldsymbol{u}) = f\nabla_\Gamma^{\mathrm{cov}}\boldsymbol{u} + \mathbf{P}\cdot\boldsymbol{u}\otimes\nabla_\Gamma f \tag{A.36}$$

$$\nabla_\Gamma^{\mathrm{dir}}(\mathbf{A}\cdot\boldsymbol{u}) = \left[\nabla_{\Gamma x}^{\mathrm{dir}}\mathbf{A}\cdot\boldsymbol{u} \quad \nabla_{\Gamma y}^{\mathrm{dir}}\mathbf{A}\cdot\boldsymbol{u} \quad \nabla_{\Gamma z}^{\mathrm{dir}}\mathbf{A}\cdot\boldsymbol{u}\right] + \mathbf{A}\cdot\nabla_\Gamma^{\mathrm{dir}}\boldsymbol{u} \tag{A.37}$$

$$\nabla_\Gamma^{\mathrm{cov}}(\mathbf{A}\cdot\boldsymbol{u}) = \mathbf{P}\cdot\left[\nabla_{\Gamma x}^{\mathrm{dir}}\mathbf{A}\cdot\boldsymbol{u} \quad \nabla_{\Gamma y}^{\mathrm{dir}}\mathbf{A}\cdot\boldsymbol{u} \quad \nabla_{\Gamma z}^{\mathrm{dir}}\mathbf{A}\cdot\boldsymbol{u}\right] + \mathbf{P}\cdot\mathbf{A}\cdot\nabla_\Gamma^{\mathrm{dir}}\boldsymbol{u} \tag{A.38}$$

$$\mathbf{P}\cdot\left(\mathbf{H}\cdot\nabla_\Gamma^{\mathrm{dir}}\boldsymbol{u}\right)\cdot\mathbf{P} = \mathbf{H}\cdot\nabla_\Gamma^{\mathrm{dir}}\boldsymbol{u} \tag{A.39}$$

$$\begin{aligned}\boldsymbol{n}_\Gamma\cdot&\left[\nabla_{\Gamma x}^{\mathrm{dir}}\mathbf{H}\cdot[\mathbf{A}]_{i1} \quad \nabla_{\Gamma y}^{\mathrm{dir}}\mathbf{H}\cdot[\mathbf{A}]_{i2} \quad \nabla_{\Gamma z}^{\mathrm{dir}}\mathbf{H}\cdot[\mathbf{A}]_{i3}\right] = \\ &= \left[\nabla_{\Gamma x}^{\mathrm{dir}}\mathbf{H}\cdot\boldsymbol{n}_\Gamma \quad \nabla_{\Gamma y}^{\mathrm{dir}}\mathbf{H}\cdot\boldsymbol{n}_\Gamma \quad \nabla_{\Gamma z}^{\mathrm{dir}}\mathbf{H}\cdot\boldsymbol{n}_\Gamma\right] : \mathbf{A} \\ &= -\mathbf{A} : (\mathbf{H}\cdot\mathbf{H}) = -\left(\mathbf{A}\cdot\mathbf{H}\right) : \mathbf{H} = -\left(\mathbf{H}\cdot\mathbf{A}\right) : \mathbf{H} \qquad \forall\ \mathbf{A}\in\mathbb{R}^{3\times3}\end{aligned} \tag{A.40}$$

Surface divergence

$$\mathrm{div}_\Gamma\boldsymbol{f} = \mathrm{tr}\left(\nabla_\Gamma^{\mathrm{dir}}\boldsymbol{f}\right) = \mathrm{tr}\left(\nabla_\Gamma^{\mathrm{cov}}\boldsymbol{f}\right) \tag{A.41}$$

$$\mathrm{div}_\Gamma(f\mathbf{P}) = \nabla_\Gamma f - f\varkappa\boldsymbol{n}_\Gamma \qquad \text{with Eq. A.13} \tag{A.42}$$

$$\mathbf{P}\cdot\mathrm{div}_\Gamma\mathbf{H} = \nabla_\Gamma\varkappa \qquad \text{with Eq. A.13} \tag{A.43}$$

$$\mathrm{div}_\Gamma(\mathbf{A}\cdot\mathbf{B}) = \mathbf{A}\cdot\mathrm{div}_\Gamma\mathbf{B} + \sum_{i=1}^{3}\sum_{k=1}^{3}[\mathbf{A}_{,i}]_{jk}[\mathbf{B}]_{ki} \tag{A.44}$$

$$\mathrm{div}_\Gamma(\mathbf{A}\cdot\boldsymbol{n}_\Gamma) = \mathrm{div}_\Gamma\mathbf{A}\cdot\boldsymbol{n}_\Gamma \qquad \text{with } \mathbf{A} = \mathbf{A}^{\mathrm{T}}, \mathrm{tr}(\mathbf{A}\cdot\mathbf{H}) = 0 \tag{A.45}$$

$$\boldsymbol{n}_\Gamma\mathrm{div}_\Gamma(\mathbf{A}\cdot\boldsymbol{n}_\Gamma) = \mathbf{Q}\cdot\mathrm{div}_\Gamma\mathbf{A} \qquad \text{with } \mathbf{A} = \mathbf{A}^{\mathrm{T}}, \mathrm{tr}(\mathbf{A}\cdot\mathbf{H}) = 0 \tag{A.46}$$

$$\boldsymbol{n}_\Gamma\cdot\mathrm{div}_\Gamma\mathbf{A} = -\mathbf{H} : \mathbf{A} \qquad \text{with } \mathbf{A} = \mathbf{P}\cdot\mathbf{A}\cdot\mathbf{P} \tag{A.47}$$

Properties for tangential vectors $\boldsymbol{v}\in T_P\Gamma$

$$(\nabla_\Gamma^{\mathrm{dir}}\boldsymbol{v})^{\mathrm{T}}\cdot\boldsymbol{n}_\Gamma = -\mathbf{H}\cdot\boldsymbol{v} \tag{A.48}$$

$$\mathbf{P}\cdot\mathrm{div}_\Gamma(\nabla_\Gamma^{\mathrm{cov}}v)^{\mathrm{T}} = \nabla_\Gamma\mathrm{div}_\Gamma\boldsymbol{v} + K\boldsymbol{v} \qquad \text{with Eq. A.15} \tag{A.49}$$

$$[\varkappa\mathbf{H} - \mathbf{H}\cdot\mathbf{H}]\cdot\boldsymbol{v} = K\boldsymbol{v} \qquad \text{with Eq. A.13, Eq. A.15} \tag{A.50}$$

Monographic Series TU Graz

Structural Analysis

Wolfgang Moser
Transient coupled BEM-BEM and BEM-FEM analyses
2006
ISBN 978-3-902465-54-2

Tatiana Ribeiro
Elastoplastic Boundary Element Method with adaptive cell generation
2007
ISBN 978-3-902465-55-9

Christian Dünser
Simulation of Sequential Tunnel Excavation with the Boundary Element Method
2007
ISBN 978-3-902465-65-8

André Pereira
Coupling BEM/FEM for fluid-soil-structure interaction
2008
ISBN 978-3-85125-010-7

Gudrun Stettner
Dynamic behavior of semi-rigid frames considering SSI
2009
ISBN 978-3-85125-064-0

Klaus Thöni
The Boundary Element Method for Non-Linear Problems
2009
ISBN 978-3-85125-078-7

Plínio Glauber Carvalho dos Prazeres
Simulation of NATM Tunnel Construction with the BEM
2010
ISBN 978-3-85125-088-6

Monographic Series TU Graz

Structural Analysis

Katharina Riederer
Modelling of Ground Support in Tunnelling using the BEM
2010
ISBN 978-3-85125-090-9

Jürgen Zechner
Fast elasto-plastic BEM with hierarchical matrices
2012
ISBN 978-3-85125-233-0

Benjamin Marussig
Seamless Integration of Design and Analysis through Boundary Integral Equations
2016
ISBN 978-3-85125-440-2

Daniel Schöllhammer
Unified modelling and higher-order accurate analysis of curved shells and membranes
2021
ISBN 978-3-85125-813-4